



DISSERTATION

**Ionization phases and electron angular
distributions of multi-electron atoms probed by
attosecond pulses**

Ausgeführt zum Zwecke der Erlangung des akademischen Grades eines
Doktors der technischen Wissenschaften unter der Leitung von

O.Univ.-Prof. Dipl.-Phys. Dr.rer.nat. Joachim Burgdörfer
Dipl.-Ing. Dr. techn. Iva Březinová
Institut für Theoretische Physik

eingereicht an der Technischen Universität Wien
Fakultät für Physik

von

Stefan Donsa

Matrikelnummer: 00925656
Bloch-Bauer Promenade 24/1/96
1100 Wien

Wien, October 4th 2019

Deutsche Kurzfassung

Die Entdeckung und Erklärung des photoelektrischen Effekts war einer der ersten Beweise der Lichtquantenhypothese. Darüber hinaus stellt die Absorption eines hochenergetischen Photons, und die darauf folgende Emission eines Elektrons, bis heute einen fundamentalen Baustein der Wechselwirkung von Licht mit Materie dar. Obwohl Photoionisation schon sehr genau untersucht worden ist, konnte seit der Jahrtausendwende mit Hilfe der *Attosekundenphysik* ein noch tiefergehendes Verständnis des photoelektrischen Effekts erzielt werden. So gelang es, unter anderem, die Zeit zu messen, die ein Elektron benötigt, um das Atom zu verlassen, nachdem es ein Photon absorbiert hat. Diese charakteristische Zeit ist in der komplexen Phase der quantenmechanischen Wellenfunktion des Elektrons eingepreist. Eine präzise Messung der Elektronenwellenfunktion nach der Ionisation, wie durch die *Attosekundenphysik* ermöglicht, erlaubt es direkte Rückschlüsse auf die zugrundeliegenden physikalischen Prozesse zu ziehen.

Die quantenmechanische Phase der Wellenfunktion ist allerdings nicht direkt experimentell bestimmbar, sondern kann nur mit Hilfe von aufwendigen Messprotokollen gemessen werden. Zusammen mit theoretischen Rechnungen und numerischen Simulationen, ist es jedoch oft möglich die korrelierte Elektronendynamik zu rekonstruieren. Die Untersuchung von einfachen atomaren Systemen, für die numerisch präzise Simulationen möglich sind, bilden die Grundlage unseres Verständnisses der Wechselwirkung von ultrakurzen und starken Laserpulsen mit Materie.

Wir untersuchen, teilweise in Kooperation mit experimentellen Arbeitsgruppen, unterschiedliche Photoionisationsmessprotokolle zur Charakterisierung von Photoionisation mit Hilfe von hochpräzisen *ab initio* Simulationen. Der Großteil der untersuchten Protokolle verwendet die Winkelverteilung der emittierten Elektronen als Observable zur Charakterisierung prototypischer Ionisierungsprozesse.

Im einfachsten Fall führt die Absorption eines hochenergetischen Photons zur Emission eines einzelnen Elektrons. Um die quantenmechanische Phase der ionisierten Elektronen zu bestimmen, wurden Messprotokolle entwickelt, bei denen das bereits ionisierte Elektron ein weiteres Photon absorbiert. Eben dieser Kontinuum-Kontinuum Übergang bewirkt eine zusätzliche Phasenverschiebung der Wellenfunktion, welche mit Hilfe des winkel aufgelösten Elektronenspektrums bestimmt werden kann. Neben der Anregung eines Einteilchenkontinuum-Zustandes kann die Absorption eines Photons auch die Anregung einer sogenannten Fano-Resonanz bewirken. Wir zeigen im Detail wie ultrakurze Laserpulse verwendet werden können, um die Streuphase in der Nähe einer solchen Resonanz zu bestimmen, und wie der zeitliche Aufbau der charakteristischen Absorptionslinie unter Einsatz von kurzen, aber starken, Laserpulsen verfolgt werden kann. Der Einfluss der Elektron-Elektron Wechselwirkung kann genau untersucht werden für den Fall von Dop-

pelionisation mit ultrakurzen Laserpulsen. Da in diesem Fall beide Elektronen das Atom nahezu gleichzeitig verlassen, enthüllt eine Messung der Winkelverteilung beider Elektronen den Einfluß der interelektronischen Coulomb-Wechselwirkung auf diesen Prozess. Um den Einfluss der Elektron-Elektron-Wechselwirkung auf den Doppelionisationsprozess zu quantifizieren, untersuchen wir den prototypischen Fall von Helium Doppelionisation mit zirkular polarisierten Laserfeldern.

Abstract

Photoionization, i.e. Einstein's photoelectric effect, often is one key ingredient to a broad variety of physical phenomena. Complementary to previous methods, attosecond metrology has provided the means to measure the time associated with the photoelectric effect. Neither is photoionization instantaneous nor is there a universal time associated with this process. Rather the exact emission time depends on the energy of the liberated electron and the details of the system it is leaving. The observed photoionization time delay (or advance) is imprinted on the quantum mechanical wave function as a variation of the phase shift. Being able to retrieve this scattering phase constitutes one major opportunity provided by attosecond metrology. Since the acquired quantum mechanical phase shift depends on the ionized system the measurement of photoionization phases can be used to probe and study matter.

Even though the quantum mechanical phase carries a large amount of information it is, unfortunately, not directly accessible in experiment. Often, intricate detection schemes are necessary to retrieve phase information. Furthermore, in many cases theoretical calculations and analytical models are additionally needed to fully reconstruct the electronic dynamics from the measured phase information. Thus, theoretical calculations and experiments on simple atomic systems serve as backbone of our understanding and provide the playing ground for the exploration of more complex phenomena in, e.g., solids and topological materials.

Within this thesis we numerically explore, in close collaboration with experimental groups, various measurement setups to investigate photoionization of atoms by ultrashort laser pulses using highly accurate *ab initio* simulations. We will mainly focus on the phases which can be obtained from the measurement of angular resolved electron spectra (angular distributions) for three prototypical ionization regimes and highlight which information can be gained by the different techniques.

The simplest scenario we investigate is single ionization by high energetic ultrashort laser pulses. The phase acquired within this process can be determined with measurement protocols that require at least one additional photon absorption by the quasi-free electron after absorption of the high-energy photon. Within this thesis we will accurately determine the phase acquired within this free-free transition. As a second scenario, we investigate the quantum mechanical scattering phase near atomic Fano resonances, whose existence is a direct consequence of electron-electron correlation. We will determine in detail how this phase can be measured using attosecond pulses. Furthermore, we will show how strong few-cycle light fields can be used to projectively measure ultrafast electronic processes such as the build-up of the asymmetric Fano line shape. As a further application, we will show that angular distributions serve as ideal candidates to pin down electronic correlations for

double ionization of atomic helium by circularly polarized light fields.

Contents

Deutsche Kurzfassung	i
Abstract	iii
List of Acronyms	ix
1. Introduction	3
2. Theoretical methods	7
2.1. Hamiltonian	7
2.1.1. Interaction with electromagnetic fields	8
2.2. Computational methods	9
2.2.1. Single-active electron approximation	9
2.2.2. Two-active electron systems	10
2.2.3. Newstock code package: simulating single ionization of many-electron atoms	13
3. Observing, steering and controlling ultrafast electronic processes	15
3.1. Attosecond metrology - overview	15
3.2. RABBITT	17
3.3. Attosecond transient absorption spectroscopy	22
4. Angle resolved RABBITT	25
4.1. Angle dependence of time delays	25
4.1.1. Angle dependence of the continuum-continuum delay τ_{cc}	27
4.1.2. Angle dependence of the photoionization time delay for shake-up states in helium	35
4.2. Analyzing RABBITT traces for overlapping channels	43
4.3. Measuring phase differences between different continuum-continuum transitions	44
4.3.1. Photoelectron angular distributions for single ionization of helium	45
4.3.2. Extracting phase differences between continuum-continuum transitions to different final angular momenta	47

5. Measuring the phase of Fano resonances	53
5.1. Fano resonances	53
5.1.1. Fano resonances in atoms	57
5.2. Direct measurement of the one-photon Fano phase	58
5.2.1. RABBITT with even and odd harmonics	59
5.2.2. Circular holographic ionization phase meter (CHIP)	65
5.3. Excursus: Wavelength scanning of resonances in atomic argon	75
5.3.1. Phases retrieved with wavelength scanning	75
6. Monitoring the build-up of a Fano resonance in the time-domain	81
6.1. Time dependent Fano wavefunction	81
6.2. Projective measurement	85
6.3. <i>Ab initio</i> treatment of the depletion process	87
7. Time-resolved coupling between Fano resonances	93
7.1. Coupling doubly excited states with few-cycle light fields	93
7.2. Reconstructing the time-dependent dipole moment	98
7.2.1. Reconstruction of dynamics for non time-translation invariant systems	100
7.3. Application to Rabi flopping between doubly excited states in helium	102
7.3.1. Comparison of dipole oscillations with occupations of doubly excited states	102
7.3.2. Retrieving dynamics of doubly excited states from experimental data	103
7.3.3. Strong field dynamics	110
8. Two-photon double ionization with elliptically polarized light fields	113
8.1. Sequential and nonsequential two-photon double ionization	114
8.2. Cross sections for TPDI	115
8.2.1. Spectrally nonsequential two-photon double ionization	117
8.2.2. Temporally nonsequential TPDI	119
8.3. XUV-XUV pump-probe sequence with elliptically polarized pulses	123
8.3.1. Doubly differential energy distributions	123
8.3.2. Singly differential energy distributions	127
8.3.3. Joint angular distributions	129
9. Summary & Outlook	133
A. LOPT RABBITT spectrum	139
B. Differences and similarities between RABBITT and streaking	141
B.1. Relation between the continuum-continuum delay and the Coulomb-laser coupling	141
B.2. Comparing time delays obtained from RABBITT and streaking	142
C. Calculation of the electron spectrum close to resonances	145

D. Additional information on RABBITT with even and odd harmonics	147
D.1. Beating of the asymmetry \mathcal{C} in RABBITT with even and odd harmonics	147
D.2. Phases retrieved by RABBITT with even and odd harmonics as function of the intensity of the harmonics	149
D.3. Angle-integrated RABBITT with even and odd harmonics	151
E. Derivation of the CHIP beating formula and the phase shear term	155
E.1. Lowest-order perturbation theory for CHIP	155
E.2. Finite pulse duration effects	156
F. Argon basis	159
F.1. Determination of basis quality	161
F.2. Pulse parameters	163
G. Derivation of the time-dependent dipole moment for an impulsively excited Fano resonance	165
H. Interference pattern of $P(E_1, E_2)$ for XUV-XUV pump probe sequences	167
I. Doubly excited states in helium	173
J. Parameters for the different simulations	175
J.1. Single-active electron calculations	175
J.1.1. Parameters for Fig. 4.1	175
J.1.2. Parameters for Fig. 4.3	176
J.1.3. Parameters for Fig. 4.6	176
J.2. Two-active electron calculations	177
J.2.1. Parameters for Fig. 4.9	177
J.2.2. Parameters for Fig. 4.16	177
J.2.3. Parameters for the simulations in section 4.3	178
J.2.4. Parameters for Fig. 5.4a	178
J.2.5. Parameters for Fig. 5.5b	179
J.2.6. Parameters for section 5.2.2	180
J.2.7. Parameters for section 6.3	180
J.2.8. Parameters for section 7.1	181
J.2.9. Parameters for section 7.3.1	181
J.2.10. Parameters for section 7.3.2	182
J.2.11. Parameters for chapter 8	182
Bibliography	185

List of Acronyms

APT Attosecond pulse train

ATAS Attosecond transient absorption spectroscopy

CC Continuum-continuum (phase)

CEP Carrier-envelope phase

CLC Coulomb-laser coupling

COLTRIMS Cold target recoil ion momentum spectroscopy

CHIP Circular holographic ionization phase meter

ECS Exterior complex scaling

EWS Eisenbud-Wigner-Smith (time delay)

FEDVR Finite element discrete variable representation

FEL Free-electron laser

FWHM Full width at half maximum

HHG High-harmonic Generation

IR Infrared

LCP Left-circularly polarized

LOPT Lowest-order perturbation theory

MB Mainband

MIR Mid-infrared

NIR Near-infrared

RABBITT Reconstruction of attosecond beating by interference of two-photon transitions

RABBITT-*evo* RABBITT with even and odd harmonics

- RCP** Right-circularly polarized
- SAE** Single-active electron
- SB** Sideband
- TDCC** Time-dependent close coupling
- TDCS** Triply-differential cross section
- TDDM** Time-dependent dipole moment
- TDSE** Time-dependent Schrödinger equation
- TPDI** Two-photon double ionization
- VMI** Velocity map imaging
- XUV** Extreme ultraviolet

1. Introduction

Multiple breakthroughs in the generation and characterization of optical light fields at the end of the last century have paved the way to generate phase controlled few-cycle laser pulses in the near infrared (NIR) wavelength regime [1, 2]. This technological advance has made it possible to generate light pulses with durations approaching few hundreds of attoseconds¹ in the extreme ultraviolet (XUV) regime via high-harmonic generation (HHG) [3–14]. The first experimental demonstration of laser pulses with durations below one femtosecond with table-top light sources has been achieved by focusing intense infrared light fields into atomic gas jets [12]. Nowadays, ultrashort XUV light pulses can be produced efficiently from many different targets including molecules [15, 16], liquids [17], solids [18] and two-dimensional materials [19]. The highest energetic XUV pulses produced to date have energies in the keV regime [20, 21] and durations of less than 100 as [22, 23]. Since the XUV pulses are generated by the interaction of the strong few-cycle NIR light field with the target, the XUV and NIR pulses are locked in phase with respect to each other and can thus be used to perform pump-probe experiments similar to what has been done in femtochemistry [24], however on the attosecond scale. The XUV pulses are more energetic and shorter, providing therefore access to physical processes different to those involved in femtosecond chemistry. In other words, being able to generate and control light pulses with durations comparable to the time scale of valence electron motion in atoms, molecules and solids has opened up many possibilities to investigate, characterize and steer electronic motion on its natural timescale, attoseconds.

To achieve the ultimate goal of attosecond metrology to observe and control electronic motion in solids and complex systems, it is necessary to understand the fundamental physical processes underlying the light-matter interaction at ultrashort timescales. This poses significant challenges to, both, experiment and theory. Only when a detailed understanding of the involved processes is gained from systems where accurate theoretical predictions are possible, reliable applications of the methods to more complex systems are in reach.

Along these lines we exploit highly accurate numerical simulations for the prototypical systems of hydrogen, helium, and argon. These comparatively small systems allow for highly accurate numerical predictions and are, thus, ideal candidates to increase our knowledge about the fundamentals of light-matter interaction.

One of the most intensively investigated processes is photoionization of atoms (Einstein’s photoelectric effect) in the presence of an ionizing XUV and a probing NIR field. Complementary to measurements of ionization cross sections attosecond metrology allows to

¹ 1 as = 10⁻¹⁸s

measure phases and, thus, time information. Hence, its use enabled the precise characterization of the ultrashort light pulses generated by HHG [13, 25], and it was possible to measure the timing of the photoelectric effect itself [26–29]. Theoretical studies have shown that the measured photoionization delay between the XUV absorption and the electron emission can be decomposed [30, 31] into two different contributions. One originates from the absorption of the XUV photon and the other from the subsequent transitions in the continuum caused by the NIR field. While the first contribution can be shown to be exactly the scattering time delay between XUV absorption and electron emission (Eisenbud-Wigner-Smith time delay) [30], the latter one is caused by the propagation of the quasi-free electron in the residual Coulombic potential and its interaction with the NIR field. This contribution was theoretically approximated for very low NIR intensities in a perturbative fashion [27, 31, 32] and for moderate intensities by classical analysis [33]. Recent experiments and calculations [34, 35] have shown that exactly this time delay involves a dependence on the electron emission angle, so far not yet accounted for by either of these approximations. Obtaining a better understanding of the angle dependence of the photoionization time delay for hydrogen and shake-up ionization in helium is thus one of the objectives of this thesis.

While photoionization phases (or time delays) are well understood for the structureless continuum (i.e. in the absence of resonances), the experimental characterization of the spectral phase close to Fano resonances (structured continuum) is still an active field of research. Fano resonances are quasi-bound states which are embedded in the continuum. The interaction between the quasi-bound resonance with the adjacent continuum leads to a superposition of electrons which are ionized directly to the continuum and electrons which populate the resonance and decay exponentially into the continuum. Interference of these two paths leads to the formation of characteristic asymmetric absorption and electron spectra [36–38]. Fano resonances are a ubiquitous feature and emerge in many different areas all around physics as, e.g. in mie scattering of plasmonics [39], scattering in photonic nanocavities [40], or in quantum transport in microwave billiards [41] and as such, play a fundamental role in nuclear, atomic, and molecular science, condensed-matter physics, and photonics, see e.g. [42–51]. The only physical property necessary is a quasi-bound state which is coupled to an energetically degenerate continuum.

While the imprint of the spectral phase of atomic Fano resonances on the ionization phases retrieved with RABBITT (reconstruction of attosecond bursts by two-photon transitions) has been measured by several groups [52–55], the direct measurement of the one-photon Fano phase has not been achieved. Within this thesis we will introduce two methods to directly measure the one-photon Fano phase using the full photoelectron angular distribution [56]. Complementary to the phase measurement we also show how to observe the ultrafast build-up of the asymmetric line shape in experiment [57] which has been the topic of multiple theoretical works [58–62].

Beyond the possibility to resolve Fano resonances in the time and spectral domain few-cycle NIR fields can couple atomic resonances (once they are excited) near resonantly [63–69]. Depending on the field strength either Rabi cycling between the different states or strong-field ionization dominates. Within this thesis we develop a new method to directly

recover the Rabi flopping dynamics of multiple resonances in helium coupled by few-cycle IR fields [70] and study the transition between the Rabi cycling and the strong-field ionization regime.

In the last part of this thesis we proceed from the single ionization continuum to the double ionization continuum for the prototypical case of atomic helium. We investigate two-photon double ionization (TPDI) with elliptically polarized XUV pulses, which can now be routinely produced [71–87]. We show that the additional polarization control of the light field allows to obtain closer insights into the electronic correlations associated with sequential and nonsequential TPDI, previously investigated with linearly polarized fields, e.g. [58, 88–97].

For this thesis to be self-contained we review a few aspects of the numerical implementation discussed in detail in [98–100]. Parts of this thesis have already been published in journal articles and conference proceedings [56, 57, 70, 101–104].

Unless mentioned explicitly we use atomic units ([a.u.]) throughout this thesis.

2. Theoretical methods

Modeling and understanding the time-dependent response of atomic and molecular systems to strong laser fields has been the subject of tremendous effort from many researchers both with analytical models and numerical implementations. While analytical models are very important to understand the basic physics underlying the observed processes they quickly reach the limit of validity once the processes can not be treated perturbatively any more. Numerical simulations might be still possible, however, their interpretation is often equally complicated as analyzing experimental data. Many times, only the combination of experimental results, numerical calculations, and analytical models makes it possible to disentangle different physical processes and deepen our knowledge about nature.

Within this chapter we will briefly review the theoretical principles and computational methods used to obtain the results presented within this thesis.

2.1. Hamiltonian

Within this work we consider many-electron atoms at non-relativistic energies subject to ultrashort laser fields. The field-free dynamics is captured by the non-relativistic Hamiltonian for the N electron (charge $-e$) system with nuclear charge Z

$$\hat{H}_0 = \frac{\hat{\mathbf{p}}_n^2}{2m_n} + \sum_{i=1}^N \frac{\hat{\mathbf{p}}_{e,i}^2}{2m_e} - \sum_{i=1}^N \frac{Ze^2}{|\hat{\mathbf{r}}_{e,i} - \hat{\mathbf{r}}_n|} + \sum_{i<j} \frac{e^2}{|\hat{\mathbf{r}}_{e,i} - \hat{\mathbf{r}}_{e,j}|}, \quad (2.1)$$

where $\hat{\mathbf{r}}_n, \hat{\mathbf{p}}_n$ and $\hat{\mathbf{r}}_{e,i}, \hat{\mathbf{p}}_{e,i}$ are the position and momentum operators of the nucleus and electrons, m_n is the mass of the nucleus, and m_e is the electron mass. Introducing center-of-mass coordinates we can write the Hamiltonian for the relative coordinates $\hat{\mathbf{r}}_i$ as

$$\hat{H}_0 = \sum_{i=1}^N \left[\frac{\hat{\mathbf{p}}_i^2}{2\mu} - \frac{Ze^2}{r_i} \right] + \sum_{i<j} \frac{e^2}{|\hat{\mathbf{r}}_i - \hat{\mathbf{r}}_j|}, \quad (2.2)$$

with $\mu = \frac{m_n m_e}{m_n + m_e}$ being the relative mass which we approximate with the electron mass $\mu \approx m_e$. In deriving Eq. (2.2) we ignored the mass polarization term $\frac{\hat{\mathbf{p}}_i \hat{\mathbf{p}}_j}{2m_n}$ which is suppressed by the mass of the nucleus. The last term in Eq. (2.2) describes the electron-electron interaction and makes the Hamiltonian and, hence, also the time-dependent Schrödinger equation (TDSE)

$$i\hbar \frac{\partial}{\partial t} |\Psi\rangle = \hat{H} |\Psi\rangle \quad (2.3)$$

which governs the time-dependent dynamics of the electrons, non-separable.

2.1.1. Interaction with electromagnetic fields

The field-driven dynamics of a free electron (charge $-e$) is governed by the *minimal coupling* Hamiltonian

$$\hat{H}_{mc} = \frac{[\hat{\mathbf{p}} + \frac{e}{c}\mathbf{A}(\hat{\mathbf{r}}, t)]^2}{2m_e} - e\Phi(\hat{\mathbf{r}}, t), \quad (2.4)$$

where the canonical momentum is given by $\hat{\mathbf{p}} = \hat{\mathbf{p}}_{kin} + \frac{e}{c}\mathbf{A}(\hat{\mathbf{r}}, t)$. The vector potential \mathbf{A} and the corresponding magnetic field \mathbf{B} are treated as classical fields. Approximating the involved fields to be classical is reasonable due to the high intensities of the considered pulses. In the following we use the Coulomb gauge ($\nabla \cdot \mathbf{A} = 0, \Phi = 0$) which defines the electric field as $\mathbf{E} = -\frac{1}{c}\partial_t\mathbf{A}$.

Considering the large length scale of the field (ten's to hundred's of nanometers) compared to the length scale of the atomic wave function (\AA 's) we can neglect the spatial dependence of the vector field

$$\mathbf{A}(\mathbf{r}, t) = \mathbf{A}(t)e^{i\mathbf{k}\mathbf{r} - i\omega t} + c.c. \approx \mathbf{A}(t)e^{-i\omega t} + c.c., \quad (2.5)$$

which amounts the dipole approximation². This implies $\mathbf{B} = 0$.

Using these assumptions the field dependent part of the minimal coupling Hamiltonian \hat{H}_{mc} in (so called) velocity gauge is

$$\hat{H}_{em} = \frac{e^2}{2m_e c^2} \mathbf{A}^2(t) + \frac{e}{m_e c} \hat{\mathbf{p}} \mathbf{A}(t). \quad (2.6)$$

The quadratic term contains no operator and can be included as global phase factor into the wave function. The final form of the electron-laser interaction Hamiltonian in velocity gauge is

$$\hat{H}_{em}^V = \frac{e}{m_e c} \hat{\mathbf{p}} \mathbf{A}(t). \quad (2.7)$$

Performing the unitary Göppert-Mayer transformation \hat{U}^{GM} onto the wave function in velocity gauge $|\Psi^V\rangle$

$$|\Psi^L\rangle = \hat{U}^{\text{GM}} |\Psi^V\rangle = e^{i\frac{e}{\hbar c}\mathbf{A}(t)\hat{\mathbf{r}}} |\Psi^V\rangle \quad (2.8)$$

we obtain the wave function in length gauge $|\Psi^L\rangle$. Inserting $|\Psi^L\rangle$ into the TDSE we obtain the electron-laser interaction in length gauge

$$\hat{H}_{em}^L = e\hat{\mathbf{r}}\mathbf{E}(t). \quad (2.9)$$

Observables are gauge-independent but within the numerical implementation the convergence behavior can be very different. Comparing both gauges can thus be used as accurate

² However, over the last years many researchers have become interested into non-dipole effects [105–108] and investigate for example the momentum shift the ionized electrons get into the propagation direction of the light field due to the photon pressure during photoionization [109].

check of numerical convergence [110]. For many-electron atoms the interaction of all electrons with the electromagnetic field is given by

$$\hat{H}_{em}^V = \frac{\hat{\mu}^V}{c} \mathbf{A}(t) = \frac{1}{c} \sum_{i=1}^N \frac{e}{m_e} \hat{\mathbf{p}}_i \mathbf{A}(t) \quad (2.10)$$

in velocity gauge and

$$\hat{H}_{em}^L = \hat{\mu}^L \mathbf{E}(t) = \sum_{i=1}^N e \hat{\mathbf{r}}_i \mathbf{E}(t) \quad (2.11)$$

in length gauge. The full Hamiltonian is then given by $\hat{H} = \hat{H}_0 + \hat{H}_{em}^{V/L}$.

2.2. Computational methods

To treat the interaction of many-electron systems with laser fields there exists a variety of methods. If the dynamics can be reduced to the dynamics of a single electron we use the single-active electron approximation (SAE) where only one electron is treated explicitly while all others are incorporated via a mean-field potential.

For effective two-electron systems, e.g. helium or the hydrogen anion, we solve the Schrödinger equation from first principles within the time-dependent close-coupling method [111]. Increasing the number of electrons beyond two makes the direct solution of the TDSE computationally impossible and only approximate solutions seem possible [112, 113]. We will briefly introduce the concepts of the `newstock` code package which is suited to treat single-ionization of many-electron atoms very efficiently and accurately.

2.2.1. Single-active electron approximation

Within the single-active electron approximation the TDSE for one electron moving in a model potential is solved. The model potential is chosen such that the ionization potential and some of the bound states are accurately represented, see e.g. [114, 115] for typical model potentials. Our computational method is based on the pseudo-spectral split-operator method [116]. We employ a low-order split-step method, and split the full Hamiltonian into \hat{H}_0 and \hat{H}_{em} . \hat{H}_0 can be evaluated easily within the energy eigenbasis of the field free Hamiltonian \hat{H}_0 , and \hat{H}_{em} can be evaluated numerically very efficiently in coordinate space employing the length gauge. The energy eigenstates are obtained by diagonalizing \hat{H}_0 . The computationally demanding operations are, thus, the transformations between the eigenbasis of \hat{H}_0 and the coordinate space. We expand the three-dimensional wave function into spherical harmonics Y_ℓ^m

$$\psi(\mathbf{r}, t) = \sum_{\ell=0}^{\infty} \sum_{m=-\ell}^{\ell} \frac{R^{\ell m}(r, t)}{r} Y_\ell^m(\theta, \phi), \quad (2.12)$$

and discretize the r coordinate on a grid using a finite-element discrete-variable representation (FEDVR) [117–120] based on Gauss-Lobatto quadratures. In the numerical implementation the sum over ℓ in Eq. (2.12) is truncated at sufficiently high values L_{\max} . For linearly polarized light fields along \hat{z} the magnetic quantum number is not changed during the interaction, which reduces the numerical complexity of the problem.

2.2.2. Two-active electron systems

Solving the time-dependent Schrödinger equation in its full dimensionality including the full electron-electron interaction for an effective two-electron system is computationally manageable [121–127]. In the present implementation we expand the two-electron wave function in coupled spherical harmonics

$$\Psi(\mathbf{r}_1, \mathbf{r}_2, t) = \sum_{L,M} \sum_{l_1, l_2} \frac{R_{l_1, l_2}^{L,M}(r_1, r_2, t)}{r_1 r_2} \mathcal{Y}_{l_1, l_2}^{L,M}(\Omega_1, \Omega_2), \quad (2.13)$$

with

$$\begin{aligned} \mathcal{Y}_{l_1, l_2}^{L,M}(\Omega_1, \Omega_2) = \\ \sum_{m_1, m_2} \langle l_1 m_1 l_2 m_2 | l_1 l_2 LM \rangle Y_{l_1}^{m_1}(\Omega_1) Y_{l_2}^{m_2}(\Omega_2). \end{aligned} \quad (2.14)$$

Inserting this expansion into the TDSE yields the time-dependent close coupling (TDCC) equations [88, 91, 92, 111]. The time-dependent close-coupling equations can be written as

$$\begin{aligned} i \frac{\partial}{\partial t} R_{l_1, l_2}^{L,M}(r_1, r_2, t) = & T_{l_1, l_2}(r_1, r_2) R_{l_1, l_2}^{L,M}(r_1, r_2, t) \\ & + \sum_{\ell'_1, \ell'_2, L', M'} V_{l_1, l_2, \ell'_1, \ell'_2}^{L, M, L', M'}(r_1, r_2, t) R_{\ell'_1, \ell'_2}^{L', M'}(r_1, r_2, t) \\ & + \sum_{\ell'_1, \ell'_2} W_{l_1, l_2, \ell'_1, \ell'_2}^L(r_1, r_2, t) R_{\ell'_1, \ell'_2}^{L, M}(r_1, r_2, t), \end{aligned} \quad (2.15)$$

where T_{l_1, l_2} is the one-electron operator containing the kinetic terms and the interaction with the nucleus, $V_{l_1, l_2, \ell'_1, \ell'_2}^{L, M, L', M'}$ is the interaction operator with the electro-magnetic field and $W_{l_1, l_2, \ell'_1, \ell'_2}^L$ is the electron-electron interaction. Within this thesis we have extended our TDCC approach [89, 98] previously limited to the case of linearly polarized light fields to arbitrarily polarized fields. Accordingly, the total magnetic quantum number M is no longer a conserved quantity. This substantially increases the number of coupled (L, M) channels for the same maximum total angular momentum L_{\max} and thereby the numerical complexity. The number of contributing (L, M) channels increases from $(L_{\max} + 1)$ for linear polarized light fields to $\frac{(L_{\max} + 1)(L_{\max} + 2)}{2}$ for laser-fields polarized in the $\hat{x} - \hat{y}$ plane by exploiting the reflection symmetry ($\hat{z} \rightarrow -\hat{z}$). The one-particle kinetic and electron-nucleus interaction T_{l_1, l_2} is not changed when going from linear to arbitrary field polarization.

Also the electron-electron interaction $W_{\ell_1, \ell_2, \ell'_1, \ell'_2}^L$ does not depend on the total magnetic quantum number M . The interaction of the electrons with the laser field $V_{\ell_1, \ell_2, \ell'_1, \ell'_2}^{L, M, L', M'}$, however, changes substantially. In the present implementation we expand the interaction with the field in spherical tensor components

$$\hat{\boldsymbol{\mu}} \cdot \mathbf{F}(t) = \sum_{q=-1}^1 (-1)^q \hat{\mu}_q F_{-q}, \quad (2.16)$$

where the spherical tensor components are defined as $\hat{T}_{+1} = -(\hat{T}_x + i\hat{T}_y)/\sqrt{2}$, $\hat{T}_{-1} = (\hat{T}_x - i\hat{T}_y)/\sqrt{2}$, $\hat{T}_0 = \hat{T}_z$ and $\hat{\boldsymbol{\mu}}$ is the interaction operator, \mathbf{F} is the electric field or vector potential depending on the chosen gauge. The spherical tensor components are directly proportional to the spherical harmonics, i.e. $\hat{T}_m \propto Y_{\ell=1}^m$. We thus have to calculate the transition matrix elements $\langle \ell_1, \ell_2, L, M | Y_1^m | \ell'_1, \ell'_2, L', M' \rangle$ which are found to be [128]

$$\begin{aligned} \langle \ell_1, \ell_2, L, M | Y_1^m | \ell'_1, \ell'_2, L', M' \rangle &= -\sqrt{\frac{3}{4\pi}} (-1)^{(\ell_2 - M)} \begin{pmatrix} \ell_1 & 1 & \ell'_1 \\ 0 & 0 & 0 \end{pmatrix} \delta_{\ell_2, \ell'_2} \\ &\times [(2L + 1)(2L' + 1)(2\ell_1 + 1)(2\ell'_1 + 1)]^{1/2} \begin{Bmatrix} L & L' & 1 \\ \ell'_1 & \ell_1 & \ell'_2 \end{Bmatrix} \begin{pmatrix} L & L' & 1 \\ -M & M' & -m \end{pmatrix} \delta_{M', M+m}. \end{aligned} \quad (2.17)$$

Inserting Eq. (2.17) together with the other terms into the close-coupling equations [Eq. (2.15)] yields coupled equations which can be numerically implemented analogously to our previous approach [98, 128]. The radial wave functions $R_{\ell_1, \ell_2}^{L, M}(r_1, r_2, t)$ are discretized on a spatial grid using FEDVR [117–120]. For the temporal propagation we use the short-iterative Lanczos algorithm with adaptive time step control [126, 129, 130].

Calculating single- and double-ionization spectra

Our calculation of single- and double-ionization spectra relies on the projection of the time-dependent wave function onto Coulomb waves after the interaction with the laser fields. In the absence of a closed solution for the asymptotic double continuum functions we neglect the influence of the electron-electron interaction onto the continuum waves. To account for this error the wave function has to be propagated sufficiently long after the end the pulses to ensure accurate spectra [89, 98].

To extract the spectral information for single ionization of helium we construct the single continuum as a symmetrized product state of a bound state with $\Phi_{n, \ell, m}(\mathbf{r})$ of the He^+ ion and a spherical Coulomb wave $\psi_{\mathbf{k}}(\mathbf{r})$ normalized either in momentum or energy space

$$\Xi_{n, \ell, m, \mathbf{k}}^{SC}(\mathbf{r}_1, \mathbf{r}_2) = \frac{1}{\sqrt{2}} [\Phi_{n, \ell, m}(\mathbf{r}_1) \psi_{\mathbf{k}}(\mathbf{r}_2) + \Phi_{n, \ell, m}(\mathbf{r}_2) \psi_{\mathbf{k}}(\mathbf{r}_1)]. \quad (2.18)$$

To obtain angle-resolved spectra we use the partial wave expansion to express $\psi_{\mathbf{k}}(\mathbf{r})$ as

$$\psi_{\mathbf{k}}(\mathbf{r}) = \sum_{\ell=0}^{\infty} \sum_{m=-\ell}^{\ell} i^{\ell} e^{-i\sigma_{\ell}} [Y_{\ell}^m(\Omega)]^* \Phi_{k, \ell}(\mathbf{r}), \quad (2.19)$$

where

$$\Phi_{k,\ell}(\mathbf{r}) = \frac{\phi_{k,\ell}(r)}{r} Y_\ell^m(\Omega) = \frac{1}{r} \sqrt{\frac{2}{\pi}} F_\ell(\eta, kr) Y_\ell^m(\Omega). \quad (2.20)$$

In Eq. (2.19) $\sigma_\ell = \arg\{\Gamma(1 + \ell - i\eta)\}$ is the Coulomb phase shift, $F_\ell(\eta, kr)$ the regular radial Coulomb functions [131] and the Coulomb parameter $\eta = -\frac{Z}{k}$. We use incoming boundary conditions as appropriate for extracting ionization probabilities [132]. Inserting the partial expansion for the bound states we obtain

$$\Phi_{n,\ell,m}(\mathbf{r}) = \frac{\chi_{n,\ell}(r)}{r} Y_\ell^m(\Omega), \quad (2.21)$$

where $\chi_{n,\ell}(r)$ is the radial part of the bound Coulomb eigenfunctions [131]. The fully differential single ionization probability is obtained by projecting the six-dimensional wave function $|\Psi\rangle$ onto the single continuum states

$$\begin{aligned} P^{SI}(n, l, m, \mathbf{k}) &= \left| \langle \Xi_{n,l,m,\mathbf{k}}^{SC} | \Psi \rangle \right| \quad (2.22) \\ &= \left| \sum_{L,M} \sum_{\ell_k=0}^{\infty} \sum_{m_k=-\ell_k}^{\ell_k} (-i)^{\ell_k} e^{i\sigma_{\ell_k}} Y_{m_k}^{\ell_k}(\Omega_k) \langle \ell m \ell_k m_k | \ell \ell_k L M \rangle c_{\ell,\ell_k}^{L,M}(n, k) \right|^2, \end{aligned}$$

with

$$c_{\ell,\ell_k}^{L,M}(n, k) = \sqrt{2} \int_0^\infty \int_0^\infty dr_1 dr_2 R_{\ell,\ell_k}^{L,M}(r_1, r_2) \chi_{n,\ell}^*(r_1) \phi_{k,\ell_k}^*(r_2). \quad (2.23)$$

Similarly, we define the double continuum wave function as symmetrized product state of two Coulomb waves with charge $Z = 2$. For $\mathbf{k}_1 \neq \mathbf{k}_2$ these states are given by

$$\Xi_{\mathbf{k}_1, \mathbf{k}_2}^{DC}(\mathbf{r}_1, \mathbf{r}_2) = \frac{1}{\sqrt{2}} [\psi_{\mathbf{k}_1}(\mathbf{r}_1) \psi_{\mathbf{k}_2}(\mathbf{r}_2) + \psi_{\mathbf{k}_1}(\mathbf{r}_2) \psi_{\mathbf{k}_2}(\mathbf{r}_1)]. \quad (2.24)$$

The full spectral distribution for double ionization is given by

$$P^{DI}(\mathbf{k}_1, \mathbf{k}_2) = \left| \sum_{L,M} \sum_{\ell_1, \ell_2} i^{-\ell_1 - \ell_2} e^{i(\sigma_{\ell_1} + \sigma_{\ell_2})} \mathcal{Y}_{\ell_1, \ell_2}^{L,M}(\Omega_1, \Omega_2) c_{\ell_1, \ell_2}^{L,M}(k_1, k_2) \right|^2, \quad (2.25)$$

with

$$c_{\ell_1, \ell_2}^{L,M}(k_1, k_2) = \sqrt{2} \int_0^\infty \int_0^\infty dr_1 dr_2 R_{\ell_1, \ell_2}^{L,M}(r_1, r_2) \phi_{k_1, \ell_1}^*(r_1) \phi_{k_2, \ell_2}^*(r_2). \quad (2.26)$$

For a more detailed discussion of the numerical implementation and the extraction of spectra we refer the reader to [60, 89, 98–100].

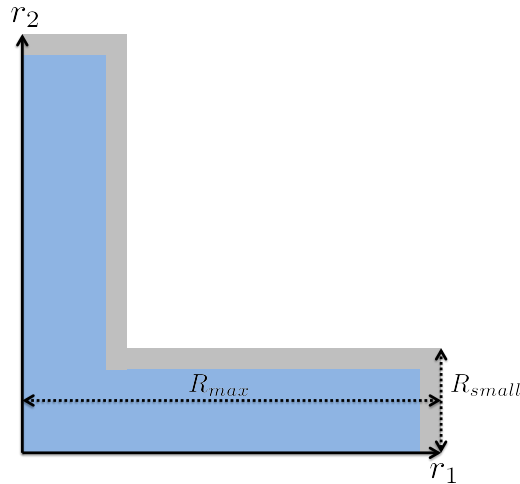


Figure 2.1.: Sketch of the asymmetric box used for the two-active electron simulations of single ionization. R_{max} is the radial box size for the ionized electron and R_{small} the radial box size for the electron which stays in the vicinity of the core. The gray shaded area represents the radial region where a complex absorbing potential prevents reflections of the wave function at the boundaries of the box.

Asymmetric boxes for single ionization

While for the investigation of double ionization the maximal radius for both electrons (r_1, r_2) is typically chosen to be the same, for single ionization only one electron transverses far away from the core and the other one stays close to it. We exploit this by using an asymmetric box with two different radii for the ionized electron (R_{max}) and the bound electron (R_{small}) in simulating single ionization spectra, see Fig. 2.1. Choosing an asymmetric box drastically reduces the computational complexity and enables us to simulate relatively long ionization pulses.

2.2.3. Newstock code package: simulating single ionization of many-electron atoms

For more than two electrons the direct solution of the TDSE is computationally not feasible any more. In the following we very briefly describe the fundamentals of the `newstock` code package which is developed by Luca Argenti and Eva Lindroth [102, 133] to treat single ionization of many electron atoms with high accuracy³.

The N -electron time-dependent wave function of the atom is expressed by a set of $(N - 1)$ electron states (ions) which are coupled to a large set of one-particle states (departing electron) using the TDCC scheme giving rise to a N particle state. To better account for electronic correlations these coupled states are complemented by a set of localized N electron bound states.

³ `newstock` is based on an extension of the multi-electron close-coupling atomic "Stockholm" code [134].

The time dependent Hamiltonian $\hat{H}(t)$ is given by the sum of the field-free non-relativistic Hamiltonian \hat{H}_0 and the dipole-interaction Hamiltonian \hat{H}_I in velocity gauge

$$\begin{aligned}\hat{H}(t) &= \hat{H}_0 + \hat{H}_I(t) \\ &= \hat{H}_0 + \alpha \mathbf{A}(t) \cdot \sum_i \hat{\mathbf{p}}_i\end{aligned}\quad (2.27)$$

where α is the fine structure constant. Doing so all relativistic corrections are neglected⁴. The one-particle radial orbitals of the departing electron are represented as linear combinations of B-splines [136–138], whereas the correlated parent ions are expanded over a finite number of configuration-state functions which are obtained from the ATSP2K package [139–141]. The initial ground state is obtained by diagonalization of the \hat{H}_0 in the $^1S^e$ sector of the full close-coupling space. To calculate the photoelectron spectrum after the end of the pulse sequence the probability amplitude $\mathcal{A}_{a;\varepsilon\hat{\Omega}\sigma}$ for detecting in coincidence the parent ion in the oriented (M_a, Σ_a) state a with energy E_a and the photoelectron with energy ε , along the direction $\hat{\Omega}$, and with spin projection σ , is computed as

$$\mathcal{A}_{a;\varepsilon\hat{\Omega}\sigma} = e^{i(E_a+\varepsilon)t} \langle \Psi_{a;\varepsilon\hat{\Omega}\sigma}^- | \Psi(t) \rangle, \quad (2.28)$$

where $\Psi_{a;\varepsilon\hat{\Omega}\sigma}^-$ is a scattering state in which the parent ion and the photoelectron are not angularly or spin coupled fulfilling incoming boundary conditions [132]. The scattering states are normalized as $\langle \Psi_{a;\varepsilon\hat{\Omega}\sigma}^- | \Psi_{b;\varepsilon'\hat{\Omega}'\sigma'}^- \rangle = \delta_{ab} \delta^{(2)}(\hat{\Omega} - \hat{\Omega}') \delta_{\sigma\sigma'}$. To obtain the energy and angularly resolved distribution of a photoelectron entangled with a parent ion in state a we sum over all the possible orientations of the final ion, spin orientations of the photoelectron, and average over the orientations of the initial neutral target (M_0, Σ_0)

$$\frac{dP_a}{dEd\Omega} = \frac{\sum_{M_0\Sigma_0} \sum_{M_a\Sigma_a\sigma} |\mathcal{A}_{a;\varepsilon\hat{\Omega}\sigma}|^2}{(2L_0 + 1)(2S_0 + 1)}. \quad (2.29)$$

⁴ For heavy atoms like argon this is already a severe approximation, since the $^2P^o$ ground state of the Ar^+ parent ion exhibits a 0.18 eV spin-orbit splitting that is comparable to the Auger width of many relevant resonances in the photoionization spectrum of the atom [135].

3. Observing, steering and controlling ultrafast electronic processes

The most important building block to investigate and control the time evolution of any process is the ability to clock and measure it on its natural timescale. For atomic and molecular processes this time scale corresponds to femto- or even attoseconds. Ahmed Zewail [24] and others have pioneered the use of pump-probe setups containing (at least) two laser pulses to investigate the dynamics of chemical reactions happening on the femtosecond timescale. Typically, a first pump pulse is used to excite the system out of its ground state into an excited state. After some time a second time-delayed probe pulse manipulates the excited state and through its response it is possible to retrieve information about the primary excitation process. This simple scheme has been generalized to an arbitrary number of pulses and targets.

Within this thesis we will focus on even shorter timescales, namely attoseconds. We consider ultrashort excitation times and a high level of control achieved by many experimental groups [1, 2, 142].

In this chapter, we will briefly review a small subset of attosecond metrology techniques used today and describe RABBITT and attosecond transient absorption spectroscopy in detail, as they are employed within this thesis.

3.1. Attosecond metrology - overview

Attosecond metrology combines a large spectral bandwidth with ultrafast temporal resolution. This is achieved by the ultrashort excitation time of extreme-ultraviolet (XUV) light fields with attosecond duration [2, 12–14, 69, 143–150]. Together with the advances in producing and controlling few-cycle near-infrared (NIR) to mid-infrared (MIR) light fields [151–154], attosecond metrology has opened the way to manipulate and control electron dynamics. Typically the XUV is used to pump the system under investigation while the few-cycle NIR field ranging from low to high intensities is used as probe. The NIR and XUV light field are perfectly synchronized given the former generates the latter via high-harmonic generation (HHG) [3, 4, 6, 9–11].

To time resolve dynamics of ultrafast processes by optical methods many different schemes have been suggested and applied in recent years. Among those, three prominent methods are attosecond streaking [155, 156], RABBITT (Reconstruction of attosecond bursts by

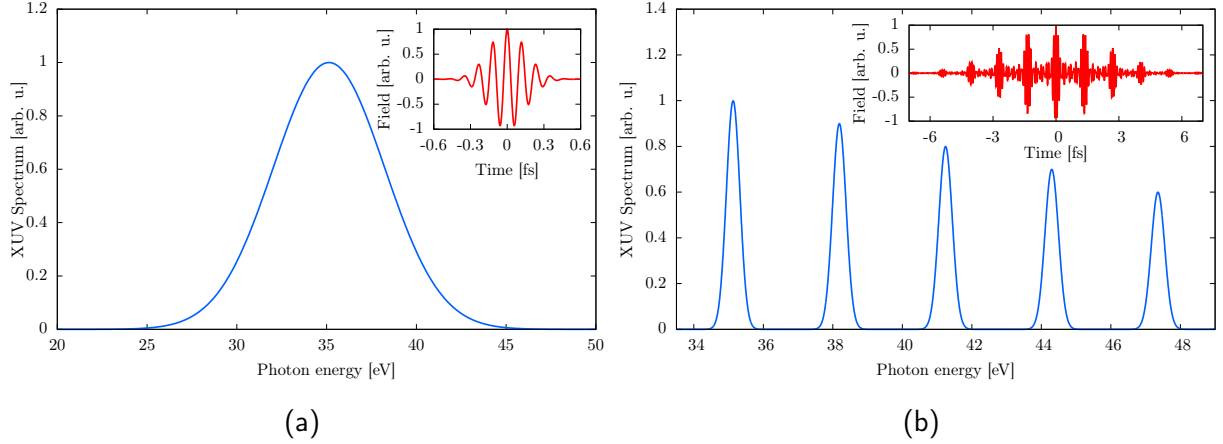


Figure 3.1.: (a) Prototypical spectrum of a single attosecond pulse with an intensity full-width at half maximum (FWHM) duration of 250 as, commonly employed in streaking. The inset shows the temporal profile of this pulse. (b) Prototypical spectrum of an attosecond pulse train consisting of five different harmonics as employed in RABBITT. Each harmonic has an intensity FWHM duration of 4 fs. The inset shows the temporal profile of this pulse.

interference of two-photon transitions) [25, 157, 158] and attosecond transient absorption spectroscopy (ATAS) [147, 159–161].

In attosecond streaking [155, 156] the target is ionized by absorption of one photon from an ultrashort (< 500 as) single attosecond XUV pulse [see Fig. 3.1 a for a sketch of a typical spectral profile] constituting the pump. A second moderately intense, phase-controlled few-cycle NIR laser pulse is used to probe the XUV-driven dynamics. Varying the time delay between the pump and the probe pulse and studying the resulting photoelectron spectrum as a function of this time delay allows to investigate the XUV initiated dynamics of the electron wavepacket.

RABBITT [25, 27, 31, 157] uses an attosecond pulse train (APT) (typical duration < 20 fs) together with a weak replica of the fundamental low-energetic (typically NIR) laser field used to generate the APT as probe pulse to ionize the target. The APT consists of multiple XUV pulses with frequencies of odd multiples of the energy of the fundamental field ω_{IR} as pump pulse [see Fig. 3.1 b for a sketch of a typical spectral profile]. Due to the interference of two-photon transitions, where one XUV photon is absorbed and one IR photon is absorbed or emitted, peaks appear at energies which are even multiples of ω_{IR} [162, 163], so called sidebands. As they are formed by interference of two paths a relative phase measurement is possible [158].

ATAS [159–161] focuses on the measurement of the transmission spectrum of an optical light field through a medium. The target is illuminated by an XUV laser pulse combined with an IR field which perturbs the system. The role of the pump and probe is thus interchanged as compared to the previous cases.

Of course the methods described above are not the only techniques commonly used in the

field of ultrafast metrology. Others are, e.g., high-harmonic spectroscopy [15, 164, 165], the combination of a strong IR field with its second harmonic [166], the use of circularly polarized IR fields to investigate tunnel ionization [167–169], or the detection of the different ions present after the interaction with the light field [170] to name just a few.

3.2. RABBITT

Following the first experiments showing HHG from gases [3, 4, 6] many independent investigations started to measure the duration and characteristics of the generated attosecond pulse trains, e.g. [162, 163]. Building up on these early experiments, the RABBITT technique was developed to retrieve not only the duration but also the spectral phases of the single XUV harmonics [25, 157, 158, 171] and thus succeeded to fully characterize the APT. RABBITT relies on the interference of two two-photon transitions at the same final energy, as can be seen for the simple example of an APT consisting of just harmonic H_{2n-1} and H_{2n+1} with photon energy $(2n-1)\hbar\omega_{\text{IR}}$ and $(2n+1)\hbar\omega_{\text{IR}}$ [Fig. 3.2a]. Here ω_{IR} is the frequency of the fundamental IR used to create the APT via HHG. A prototypical example for the photoelectron spectrum produced for one specific time delay by the pulse setup specified in Fig. 3.2a is shown in Fig. 3.2b. The blue lines correspond to absorption of one photon from the XUV harmonics which are commonly called mainbands (MB). The red line indicates the peak which appears, if the APT is dressed by its fundamental field, due to a two-photon transition involving the absorption of one photon out of the APT and the absorption or emission of one photon from the fundamental field [sidebands (SB)]. If the time delay between the APT and the fundamental IR field is varied, the SB amplitudes vary as function of the delay with frequency $2\omega_{\text{IR}}$, see Fig. 3.2c.

The oscillations of the sidebands can be understood within second-order perturbation theory [27, 31, 32, 158]. The wave function at each sideband energy H_{2n} can be described as a superposition of two paths, namely absorption of one photon of the harmonic below H_{2n-1} the sideband, followed by absorption of one photon of the fundamental IR field and absorption of one photon of the harmonic above H_{2n+1} the sideband followed by stimulated emission of one IR. Both paths are included in the full two-photon amplitudes which can be determined as transition from the initial state $|i\rangle$ to the final state $|f\rangle$ [172]

$$\mathcal{A}_{f \leftarrow i}^{(2)} = -i \int_{-\infty}^{\infty} d\varepsilon \tilde{A}_{\text{IR}}(\omega_{fi} - \varepsilon) \tilde{A}_{\text{APT}}(\varepsilon) \mathcal{M}_{fi}(\varepsilon) \quad (3.1)$$

with

$$\mathcal{M}_{fi}(\varepsilon) = \alpha^2 \langle f | \hat{p}_z G_0^+(E_i + \varepsilon) \hat{p}_z | i \rangle \quad (3.2)$$

being the monochromatic two-photon transition amplitude in velocity gauge and α is the fine structure constant⁵. $\tilde{A}_{\text{IR/APT}}(\varepsilon)$ are the Fourier transforms of the vector fields associated with the fundamental IR and the APT, and $\omega_{fi} = E_f - E_i$ is the energy difference between the initial and the final state. $G_0^+(E_i + \varepsilon)$ is the retarded Green's function of the

⁵ We assumed linear polarization of the APT and the IR field along \hat{z} for simplicity.

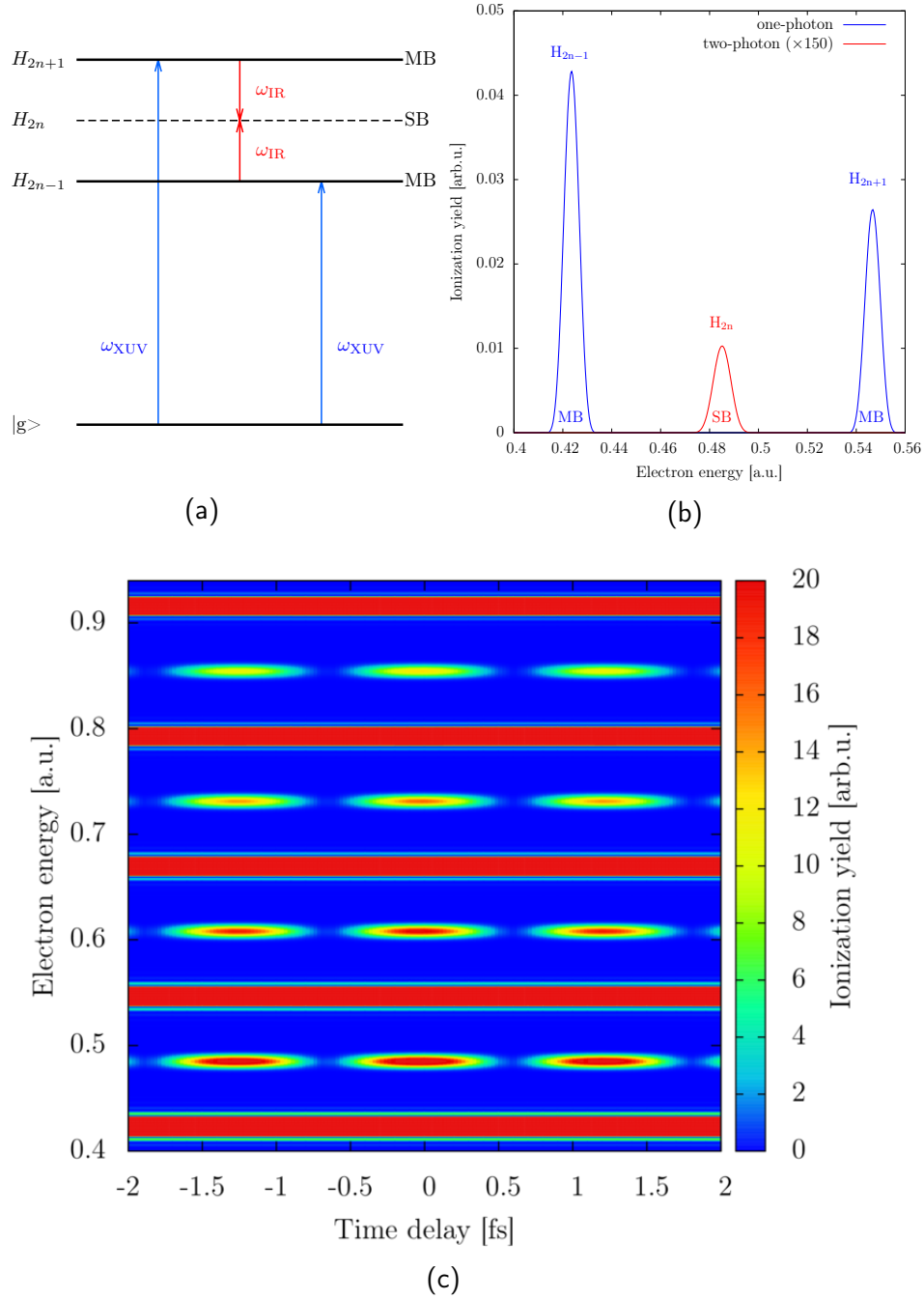


Figure 3.2.: Sketch of the RABBITT scheme: (a) Energy diagram of the interfering two-photon transitions inducing a $2\omega_{IR}$ -beating in the fully angle integrated electron spectrum in the sidebands (SB) (energy region, where the even harmonics would be). (b) Photoionization spectrum of hydrogen for two harmonics dressed by the fundamental IR as depicted in (a). The peaks corresponding to the absorption of one XUV photon are referred to as mainbands (MB) and the peaks which are caused by a two-photon process (one XUV absorption and one IR absorption or emission) are referred to as sidebands. (c) Prototypical RABBITT spectrum for ionization of hydrogen as a function of the final photoelectron energy and the time delay between the APT and the fundamental IR field. The parameters for the RABBITT simulations of hydrogen shown in (b) and (c) are given in App. J.1.1.

field-free Hamiltonian and \hat{p}_z is the electron momentum operator which is proportional to the interaction operator in velocity gauge.

To derive an analytic expression for the RABBITT spectrum we separate the full two-photon amplitude [Eq. (3.1)] into the two paths depicted in Fig. 3.2a leading to the same sideband

$$\mathcal{A}_{f \leftarrow i}^{(2)}(H_{2n}) = \mathcal{A}_{H_{2n-1} + \omega_{\text{IR}}}^{(2)} + \mathcal{A}_{H_{2n+1} - \omega_{\text{IR}}}^{(2)}. \quad (3.3)$$

The terms $\mathcal{A}_{H_{2n-1} + \omega_{\text{IR}}}^{(2)}$ and $\mathcal{A}_{H_{2n+1} - \omega_{\text{IR}}}^{(2)}$ represent the path involving absorption and emission of an IR photon. In the limit of monochromatic IR fields and in the case where the intermediate state reached via XUV absorption is a structureless continuum state, the two components of the two-photon transition $\mathcal{A}_{f \leftarrow i}^{(2)}$ are written as [27, 31, 32, 158, 173]

$$\mathcal{A}_{H_{2n \pm 1} \mp \omega_{\text{IR}}}^{(2)} = \sum_{\lambda} \sum_{\ell = \lambda \pm 1} \left| \mathcal{A}_{H_{2n \pm 1} \mp \omega_{\text{IR}}, \lambda \ell}^{(2)} \right| e^{i\eta_{\lambda}(\varepsilon_{2n \pm 1})} e^{i\phi_{cc, \lambda \ell}^{\mp}} e^{\mp i\omega_{\text{IR}}\tau} e^{i\pi(1-\lambda/2)} Y_{\ell}^m(\theta, \varphi), \quad (3.4)$$

where λ, ℓ are the angular momenta of the intermediate and final state. The magnitude of the two-photon matrix element $\left| \mathcal{A}_{H_{2n \pm 1} \mp \omega_{\text{IR}}, \lambda \ell}^{(2)} \right|$ depends explicitly on all involved angular momenta, energies and whether the IR photon is absorbed or emitted [173, 174]. $\eta_{\lambda}(\varepsilon_{2n \pm 1})$ is the phase acquired by the XUV driven one-photon transition to the intermediate continuum state with energy $\varepsilon_{2n \pm 1}$ and angular momentum λ . It can be calculated from scattering theory in first-order perturbation theory and its interpretation as photoionization time delay has been studied intensively, see [30, 32, 175]. The factor $\exp(\mp i\omega_{\text{IR}}\tau)$ stems from the absorption (emission) of one IR photon. The time delay τ is given by the difference between the peak time of the IR and the APT, i.e. $\tau = \tau_{\text{IR}} - \tau_{\text{APT}}$. The continuum-continuum phase $\phi_{cc, \lambda \ell}^{\pm}$ arises due to the absorption (emission) of an IR photon in the presence of the Coulomb potential and imposes an additional phase onto the electron wave packet [27, 31, 32]. In general, the continuum-continuum phase depends on the energy and angular momentum of the intermediate and final state. Performing an asymptotic expansion for high electron energies and large distances from the core an analytic expression can be derived [27, 31, 32] for $\phi_{cc, \lambda \ell}^{\pm}$ which does not depend on the angular momenta of the intermediate or final state of the wave packet. The difference between absorption and emission is only implicitly included via the intermediate momentum κ reached via the XUV transition and the final momentum k :

$$\phi_{cc}(k, \kappa) = \arg \left\{ \frac{(2\kappa)^{iZ/\kappa} \Gamma[2 + iZ(1/\kappa - 1/k) + \gamma(k, \kappa)]}{(2k)^{iZ/k} (\kappa - k)^{iZ(1/\kappa - 1/k)}} \right\}, \quad (3.5)$$

with

$$\gamma(k, \kappa) = iZ \frac{(\kappa - k)(\kappa^2 + k^2)}{2\kappa^2 k^2} \Gamma[1 + iZ(1/\kappa - 1/k)], \quad (3.6)$$

and Z being the asymptotic charge of the residual ion⁶. Numerical calculations, however, show that for low photoelectron energies $\phi_{cc, \lambda \ell}^{\pm}$ does depend on the angular momentum

⁶ We use Eq. [100] from [31], which is the most accurate analytic expression, as it includes also long-range amplitude corrections.

of the final state [31, 32]. Ignoring the dependence on the angular momenta [Eq. (3.5)] the continuum-continuum phases for an electron with final energy E are given by energy conservation

$$\phi_{cc}^+ = \phi_{cc} \left(\sqrt{2E}, \sqrt{2E - \omega_{\text{IR}}} \right), \quad (3.7)$$

$$\phi_{cc}^- = \phi_{cc} \left(\sqrt{2E}, \sqrt{2E + \omega_{\text{IR}}} \right). \quad (3.8)$$

For a short-ranged potential as provided by Yukawa potentials, or negative ions ϕ_{cc} is strictly zero. For high energies $\phi_{cc}(k, \kappa)$ is universal for different atomic species and does not depend on the specific form of the potential close to the core. If any of the intermediate states has a resonant contribution the factorization as employed in Eq. 3.4 is not applicable [52, 53, 172, 176, 177]⁷.

Assuming without loss of generality that all fields are linearly polarized along \hat{z} the angle-integrated RABBITT spectrum is given by

$$\begin{aligned} |\psi(E = H_{2n})|^2 &= \int d\theta \sin(\theta) |\psi(E = H_{2n}, \theta)|^2 \\ &= \int d\theta \sin(\theta) \left| \mathcal{A}_{2n-1+\omega_{\text{IR}}}^{(2)} + \mathcal{A}_{2n+1-\omega_{\text{IR}}}^{(2)} \right|^2 \\ &= A + B \cos(2\omega_{\text{IR}}\tau + \Delta\phi) \\ &= A + B \cos(2\omega_{\text{IR}}[\tau - \tau_R]), \end{aligned} \quad (3.9)$$

with $\tau_R = -\frac{\Delta\phi}{2\omega_{\text{IR}}}$ being the approximate time delay as retrieved by RABBITT. For more details see App. A.

Higher-order transitions, e.g. absorption or emission of three or five IR photons, would contribute by the admixture of oscillations with frequencies $4\omega_{\text{IR}}$ or $6\omega_{\text{IR}}$, etc. which is discussed, e.g., in [178].

To extract the time delays τ_R from RABBITT spectra we integrate each sideband separately in energy over the spectral width of the sideband [Fig. 3.3a] for each time delay. The resulting data is fitted to a function $A + B \cos(2\omega_{\text{IR}}\tau + \Delta\phi)$, see Fig. 3.3b. τ_R can also be retrieved by comparing the fitted curve to a $\cos(2\omega_{\text{IR}}\tau)$ oscillation without phase offset from the peak difference between the two curves.

A similar treatment as the one discussed here can also be used to describe the oscillations which are observed within the mainbands [171]. Their interpretation is, however, not as straightforward as for the sidebands, since there are three different interfering paths, i.e. the interference of one one-photon and two three-photon transitions, at the same final energy.

Within this thesis we will explicitly show how the recently found angle-dependence of the photoemission time delay in atoms [34, 35, 179] can be understood, see Sec. 4.1. We also explore the influence of polarizable targets on angle-resolved RABBITT measurements.

⁷ An extensive treatment of intermediate resonances and finite pulse duration effects can be found in [176].

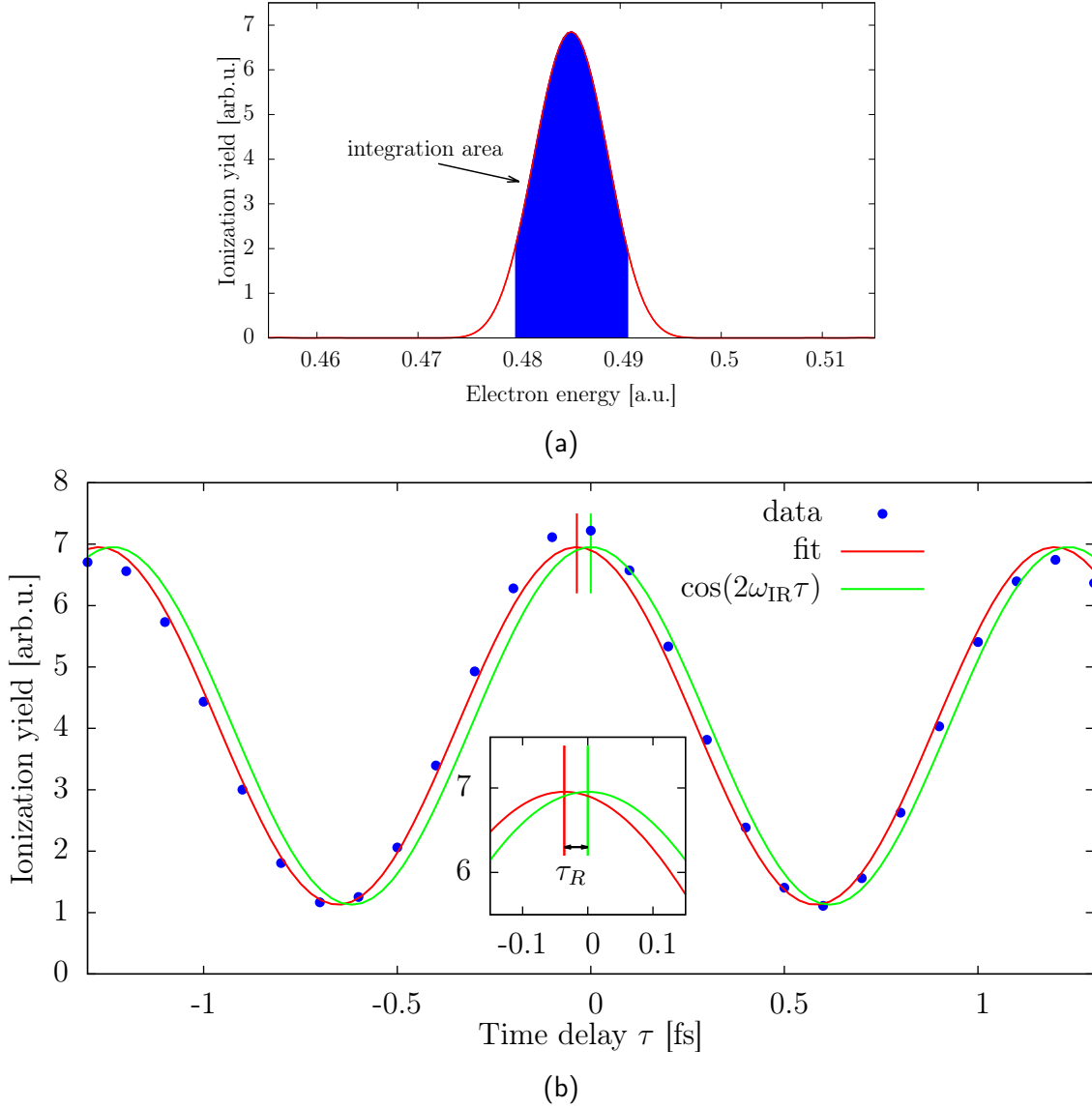


Figure 3.3.: (a) Illustration of the typical area (spectral width) over which the RABBITT sideband is integrated to obtain τ_R from RABBITT traces. (b) Oscillation of the lowest energetic SB shown in Fig. 3.2c integrated over the harmonic width as function of the time delay between the IR field and the APT (blue points). The red line represents a fit to the data with $A + B \cos(2\omega_{\text{IR}}\tau + \Delta\phi)$ and the green line shows the same function without a phase shift, i.e. $\Delta\phi = 0$. The inset shows how the RABBITT time delay τ_R can be extracted by comparing with a $\cos(2\omega_{\text{IR}}\tau)$ oscillation without phase offset.

Further we will explicitly quantify the dependence of the continuum-continuum phase $\phi_{cc,\lambda\ell}^{\pm}$ on the final angular momentum ℓ of the photoelectron using the full information provided by angle-resolved RABBITT measurements, see Sec. 4.3.

3.3. Attosecond transient absorption spectroscopy

In attosecond transient absorption spectroscopy (ATAS), the target is probed by an optical field and the transmitted signal $I_1(\omega)$ is measured. The main observable is the optical density (OD) of the target which is given by

$$\text{OD}(\omega) = -\log\left(\frac{I_1(\omega)}{I_0(\omega)}\right), \quad (3.10)$$

where $I_0(\omega)$ is the photon spectrum of the pulse measured without passing through a target. In ATAS the target is typically ionized by a sequence of at least two pulses which can be delayed in time with respect to each other. Typically, a rather short XUV pump pulse is used to initiate dynamics in the target, which is subsequently probed, modified and controlled by a longer-wavelength IR field. Performing a time delay scan between the fields the optical density becomes a function of frequency and delay time between the two pulses $\text{OD}(\omega, \tau)$.

To calculate the transient absorption spectrum from first principles we start by calculating the energy ΔE which the target (in our case atom) loses (gains) after the interaction with the laser pulse sequence [159, 160]

$$\Delta E = \int_{-\infty}^{\infty} dt \frac{dE(t)}{dt}, \quad (3.11)$$

where $E(t)$ is the time-dependent energy of the target in the laser field. The rate at which energy is transferred to (from) the target $\frac{dE(t)}{dt}$ can be obtained from the solution of the time-dependent Schrödinger equation by calculating the dipole moment $\langle \hat{\mathbf{r}} \rangle = \mathbf{r}(t)$

$$\frac{dE}{dt} = \frac{d}{dt} \langle \psi | \hat{H} | \psi \rangle = \left\langle \psi \left| \frac{\partial \hat{H}}{\partial t} \right| \psi \right\rangle = \langle \psi | \hat{\mathbf{r}} | \psi \rangle \frac{\partial \mathbf{F}}{\partial t} = \mathbf{r}(t) \frac{\partial \mathbf{F}}{\partial t}. \quad (3.12)$$

In Eq. (3.12) we assumed that the Hamiltonian has no time dependence apart from the driving electric field $\mathbf{F}(t)$ and we use length gauge. Inserting Eq. (3.11) into Eq. (3.12) and

representing the dipole moment and the field in Fourier-space we find

$$\begin{aligned}
\Delta E &= \int_{-\infty}^{\infty} dt \langle \hat{\mathbf{r}} \rangle \frac{\partial \mathbf{F}}{\partial t} \\
&= \frac{1}{2\pi} \int_{-\infty}^{\infty} dt \int_{-\infty}^{\infty} d\omega_1 \int_{-\infty}^{\infty} d\omega_2 \tilde{\mathbf{r}}(\omega_1) e^{-i\omega_1 t} \partial_t \tilde{\mathbf{F}}(\omega_2) e^{-i\omega_2 t} \\
&= \frac{-i}{2\pi} \int_{-\infty}^{\infty} dt \int_{-\infty}^{\infty} d\omega_1 \int_{-\infty}^{\infty} d\omega_2 \tilde{\mathbf{r}}(\omega_1) e^{-i\omega_1 t} \omega_2 \tilde{\mathbf{F}}(\omega_2) e^{-i\omega_2 t} \\
&= i \int_{-\infty}^{\infty} d\omega_1 \tilde{\mathbf{r}}(\omega_1) \omega_1 \tilde{\mathbf{F}}(-\omega_1) = \int_{-\infty}^{\infty} d\omega i\omega \Lambda(\omega), \tag{3.13}
\end{aligned}$$

with $\Lambda(\omega) = \tilde{\mathbf{r}}(\omega) \tilde{\mathbf{F}}(-\omega) = \tilde{\mathbf{r}}(\omega) [\tilde{\mathbf{F}}(\omega)]^*$ using that the electric field $\mathbf{F}(t)$ is a real function, i.e., $\tilde{\mathbf{F}}(-\omega) = [\tilde{\mathbf{F}}(\omega)]^*$. This leads to

$$\Delta E = - \int_{-\infty}^{\infty} d\omega \omega \text{Im} [\Lambda(\omega)] = \int_{-\infty}^{\infty} d\omega \omega S(\omega), \tag{3.14}$$

where $S(\omega) = -\text{Im} \left(\tilde{\mathbf{r}}(\omega) [\tilde{\mathbf{F}}(\omega)]^* \right)$ is the single atom response. Positive (negative) values of S correspond to energy gained (lost) by the target from (to) the field.

To calculate the macroscopic optical density we calculate the polarization

$$P(\omega) = \rho \tilde{\mathbf{r}}(\omega) \tag{3.15}$$

which acts as a source term in Maxwell's equations and thus the macroscopic response is calculated by solving the coupled TDSE and Maxwell's equations. However, it was shown that within the linear-response limit (e.g. dilute gas target) [160] the generalized cross section $\sigma(\omega)$ for the XUV absorption as can be obtained just from the energy-gain per unit frequency [Eq. (3.13)] at the level of single-atom response

$$\sigma(\omega) = \frac{\omega \text{Im} \{ \Lambda(\omega) \}}{I(\omega)}, \tag{3.16}$$

where $I(\omega) = |\tilde{\mathbf{F}}(\omega)|^2 / 4\pi\alpha$ is the incoming flux of the field. In the numerical implementation it is (similar to HHG simulations) numerically more stable to calculate the expectation value of the dipole acceleration $\mathbf{a}(t) = \frac{d^2 \mathbf{r}(t)}{dt^2}$ instead of the dipole moment and use the Fourier identity $\tilde{\mathbf{r}}(\omega) = -\tilde{\mathbf{a}}(\omega) / \omega^2$ [180].

ATAS has been used in previous studies to measure the decay of autoionizing resonances in atoms [181, 182], or to characterize ultrafast phase transitions in strongly correlated materials [183]. Contrary to streaking and RABBITT, ATAS can also be used to resolve bound electron dynamics [143, 153, 184] since it does not rely on photoionization. Within this thesis we will employ ATAS to monitor the time-dependent build-up of Fano resonances (Chap. 6) and to investigate the field driven coupling between autoionizing resonances (Chap. 7).

4. Angle dependence of photoionization time delays and phases probed by RABBITT

One key quantity used to characterize the single ionization continuum is the phase photoelectrons acquire upon ionization and imprinted into this phase the photoionization time delay. The first experiments and theoretical calculations investigating photoionization time delays have either been performed just for emission of electrons into one specific direction in a streaking geometry, e.g. [26, 185], or for angle-integrated photoelectron spectra with RABBITT [27, 186–188]. Recently, however, there has been considerable interest into measuring time delays as a function of the emission angle of the electrons with respect to the laser polarization direction in RABBITT [34, 35, 173, 177, 179, 189]. Doing so for single ionization of atomic helium, a strong angular dependence of the measured delay was observed accompanied with theoretical calculations validating these findings [34]. Indeed, similar effects were also found in studies employing streaking [190, 191]⁸.

In this chapter we will focus on time delays obtained from angle-resolved RABBITT traces. We will show that the retrieved time delays can still be separated into three different contributions (scattering, continuum-continuum and polarization delay), where all three can be angle dependent.

Further we will compare our results with experiments, which measure the phase difference between continuum-continuum transitions involving different angular momenta using the full information provided by angle-resolved RABBITT.

In the following chapter we will restrict ourselves to investigations of the unstructured (flat) single-ionization continuum. The imprint of resonances onto the single-ionization continuum will be discussed in detail in chapter 5.

4.1. Angle dependence of time delays

Within this thesis we assume that the angle-dependent observed time delay $\tau_R(\theta)$ can be decomposed into three different contributions [30]

$$\tau_R(\theta) = \tau_{\text{EWS}}(\theta) + \tau_{\text{cc}}(\theta) + \tau_{\text{dipole}}(\theta). \quad (4.1)$$

⁸ In addition it was proposed that one could use a non-collinear streaking setup where the IR field is not collinear with the ionizing XUV but polarized into the direction in which the electron spectrum is collected. This allows to measure angle-dependent scattering phase shifts without the need to redefine the Coulomb-laser coupling [190, 191].

The first term, the one-photon Eisenbud-Wigner-Smith time delay

$$\tau_{\text{EWS}}(\theta) = \frac{\partial}{\partial \varepsilon} \arg \{ \langle \alpha, \varepsilon, \theta | \hat{z} | g \rangle \} \quad (4.2)$$

is associated with the half-scattering ionization event from the groundstate $|g\rangle$ to the intermediate continuum state $|\alpha\rangle$ with energy ε reached via the XUV transition. In RABBITT, therefore, the spectral derivative τ_{EWS} is not probed exactly, but only approximately in terms of a finite difference

$$\tau_{\text{EWS}}(\theta) \approx \frac{\arg \{ \langle \alpha, \varepsilon + \omega_{\text{IR}}, \theta | \hat{z} | g \rangle \} - \arg \{ \langle \alpha, \varepsilon - \omega_{\text{IR}}, \theta | \hat{z} | g \rangle \}}{2\omega_{\text{IR}}}. \quad (4.3)$$

If the intermediate state α is a single partial wave (e.g. ionization of an initial s electron to a p wave as for hydrogen) τ_{EWS} has no intrinsic angle dependence. If, however, the intermediate state is a superposition of different partial waves with different angular momenta (e.g. ionization of an electron out of the $2p$ shell in neon to a superposition of an s and d wave) the scattering delay associated with the XUV transition itself is already angle-dependent and Eq. (4.2) has to be generalized to

$$\tau_{\text{EWS}}(\theta) = \frac{\sum_{i=1}^N \sigma_{\alpha_i} \frac{\partial}{\partial \varepsilon} \arg \{ \langle \alpha_i, \varepsilon, \theta | \hat{z} | g \rangle \}}{\sum_{i=1}^N \sigma_{\alpha_i}}, \quad (4.4)$$

where $\sigma_{\alpha_i} = |\langle \alpha_i, \varepsilon, \theta | \hat{z} | g \rangle|^2$ is the partial amplitude cross-section and the sum runs over all relevant intermediate states $|\alpha_i\rangle$. We will revisit Eq. 4.4 in Sec. 4.2.

The second contribution in Eq. (4.1), the continuum-continuum delay $\tau_{\text{cc}}(\theta)$ ⁹, is caused by the phase shift the outgoing electron wave-packet encounters in interacting with the IR field in the Coulomb field of the residual ion [27] [Sec. 3.2]. According to the asymptotic expansion for large values of kr performed in [31, 32] the continuum-continuum phase, τ_{cc} does not depend on the angular momenta of the intermediate or final state [Eqs. (3.7) and (3.8)] and is given by

$$\tau_{\text{cc}} = -\frac{\phi_{\text{cc}}^- - \phi_{\text{cc}}^+}{2\omega_{\text{IR}}}, \quad (4.5)$$

Thus, if the dependence on the angular momenta can be ignored, τ_{cc} does not depend on the emission angle θ of the electron. If, however, the dependence of continuum-continuum phase $\phi_{\text{cc},\lambda\ell}^\pm$ on the angular momenta of the intermediate (λ) and final state ℓ [Eq. 3.4] is treated explicitly the continuum-continuum delay depends on θ .

The third term $\tau_{\text{dipole}}(\theta)$ is caused by the polarization state (with dipole moment \mathbf{d}) of the residual ion [28, 29, 192]. It can be expressed as

$$\tau_{\text{dipole}}(\theta) = \frac{1}{\omega_{\text{IR}}} \text{atan} \left(-\omega_{\text{IR}} \frac{\mathbf{d} \cdot \boldsymbol{\sigma}_{\text{IR}}}{\mathbf{k} \cdot \boldsymbol{\sigma}_{\text{IR}}} \right) = \frac{1}{\omega_{\text{IR}}} \text{atan} \left(-\omega_{\text{IR}} \frac{d_z}{k \cos(\theta)} \right), \quad (4.6)$$

⁹ τ_{cc} is closely related to the Coulomb laser coupling (CLC) delay τ_{CLC} encountered in streaking [33], see App. B.1.

where $\boldsymbol{\sigma}_{\text{IR}}$ is the polarization direction of the IR field, d_z is the dipole moment along \hat{z} direction and we have assumed that the IR field is linearly polarized along \hat{z} direction. For streaking experiments, where the emitted photoelectrons are only measured in forward direction, Eq. (4.6) has been shown to be very accurate for the prototypical example of shake-up ionization in helium [28, 29].

Eq. (4.6) predicts an explicit dependence of the retrieved time-delay on the emission angle θ , if the residual ion has a dipole moment [192]. However, a polarization induced time delay τ_{dipole} does not only arise if the residual ion has a permanent dipole moment, but also if the ion is easily polarized due to (quasi)-degenerate energy levels, e.g. $2s, 2p_0$ states in He^+ [100, 193]. The effective dipole moment along \hat{z} for these states is given by

$$\langle d_{\text{eff},z}^{m\ell} \rangle (\theta) = \sum_k d_k |\alpha_{nk\ell}|^2 \frac{|c_{nk}|^2}{|c_{n\ell}|^2} \quad (4.7)$$

where $\alpha_{nk\ell} = \langle nk | n\ell \rangle$ are the expansion coefficients of the Stark states $|nk\rangle$ of the subshell n into the eigenstates $|n\ell\rangle$ of the ion, $c_{nj} = \langle E, \theta | \hat{z} | nj \rangle$ is the dipole-transition matrix element to either Stark $|nk\rangle$ or angular momentum eigenstates $|n\ell\rangle$ and $d_k = \langle nk | \hat{z} | nk \rangle$ is the dipole-moment of the respective Stark states [30, 100].

In addition to the contributions discussed above one more time delay can be part of τ_R . If the neighboring XUV harmonics have a different relative spectral phase this phase difference is part of the retrieved phase difference [25, 157, 158, 171], see App. A. In this thesis, however, we do not consider time delays stemming from different spectral phases of the XUV harmonics and, thus, ignore this contribution in the following.

4.1.1. Angle dependence of the continuum-continuum delay τ_{cc}

A recent experiment by Heuser et al. [34] showed that the photoionization time delay for single-ionization from the ground state of the helium atom is strongly angle dependent for electron emission angles $\theta > 60^\circ$ relative to the polarization direction of the linearly polarized laser field. This was also confirmed by accompanying single-active electron and *ab initio* calculations. For this specific case τ_{EWS} is not angle dependent as the XUV populates only one partial wave channel, i.e., $|\text{He}^+(1s), \varepsilon p_0\rangle$ and the residual ion is not polarizable by the weak IR field, i.e. $\tau_{\text{dipole}} = 0$. Hence the angle-dependence of τ_R is caused purely by the IR induced continuum-continuum transition and thus enters only into τ_{cc} .

To shed more light onto the origin of this angle dependence we perform calculations for hydrogen and compare these results to calculations for a short-ranged Yukawa potential ($V(r) = \frac{Z}{r} e^{-r/a}$) with the same ground state energy, but no additional bound states and also no Coulomb tail¹⁰.

For the Coulomb potential the scattering time delay τ_{EWS} is given purely by the Coulomb phase shift of the p wave $\sigma_1(E) = \arg \left\{ \Gamma \left(2 - \frac{i}{k} \right) \right\}$. The scattering time delay for the Yukawa potential was calculated numerically. For both potentials we use the same pulse

¹⁰ The parameters for the Yukawa potential are $Z = 1.90831$ and $a = 1$ [168].

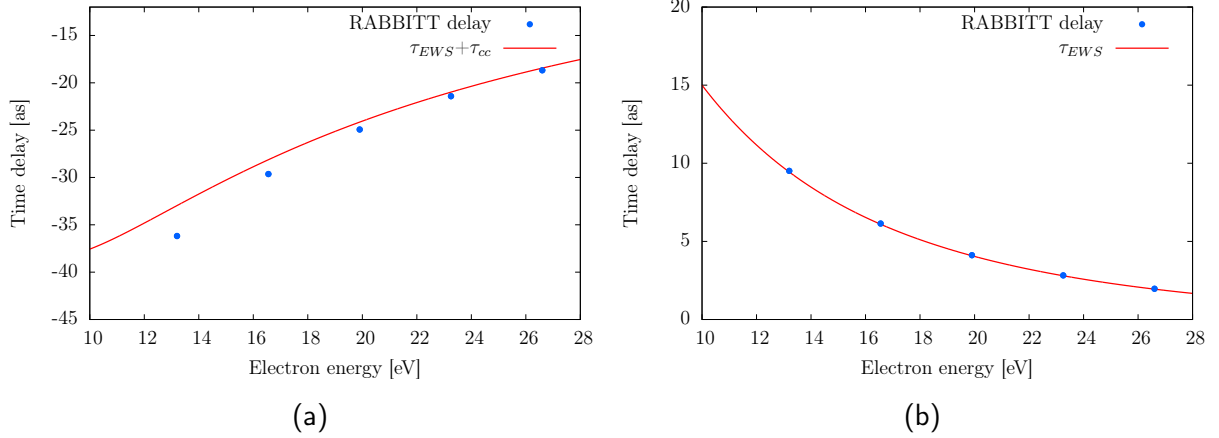


Figure 4.1.: Time delays τ_R obtained from RABBITT traces evaluated in forward direction $\theta = 0^\circ$ for (a) a hydrogen potential and (b) a Yukawa-potential which has the same ionization potential as the hydrogen atom. Both simulations are compared against the analytic prediction [Eq. (4.1)]. The wavelength of the fundamental IR field is $\lambda_{\text{IR}} = 740\text{nm}$. The FWHM duration of the IR and the APT are 20 fs and 15 fs. The exact pulse and convergence parameters are given in App. J.1.1.

sequence of IR and APT [Tab. J.1].

Evaluating the time delay from RABBITT traces in forward direction ($\theta = 0^\circ$) and integrating the electron signal within each sideband in energy [Fig. 3.3a] the retrieved time delays coincide very well with the analytic prediction [Eq. 4.1] for hydrogen, Fig. 4.1a. The remaining discrepancies between the numerical results and the analytic prediction at low energies are not caused by the finite difference approximation of τ_{EWS} , Eq. (4.3), as this error amounts to ≈ 0.2 as, whereas the discrepancy is ≈ 2 as for the lowest energy [$E \approx 13.2$ eV]. The error stems from the asymptotic expansion with respect to kr in deriving τ_{cc} , Eq. (4.5), which is not accurate for low photoelectron energies [31, 32]. The results obtained for the Yukawa potential (range $a = 1$), Fig. 4.1b, are in excellent agreement with the analytic prediction [$\tau_R = \tau_{\text{EWS}}$] as there is no additional time delay due to the continuum-continuum transition, validating our previous assumption that the discrepancy for low energies is caused by τ_{cc} .

To characterize the angle dependence of the time delay $\tau_R(\theta)$ we focus centered on the sideband at 16.5 eV (the other sidebands show a very similar behavior). The time delay obtained for the Yukawa potential shows almost no angle dependence until $\theta \approx 75^\circ$ followed by a rapid phase jump of π (corresponding to approximately 617 as), Fig. 4.2. Slightly different to that, the Coulomb potential shows a strong but smooth phase variation close to the angle of the phase jump observed for the Yukawa potential. While for the Yukawa potential the RABBITT phase $\Delta\phi$ jumps by π between $\theta = 0^\circ$ and $\theta = 90^\circ$ the phase variation for the Coulomb potential is considerably smaller (roughly 0.92π , corresponding to a relative time delay of 572 as for $\lambda_{\text{IR}} = 740$ nm). Increasing the fundamental wavelength of the IR field, but keeping the final electron energy nearly constant, the relative phase

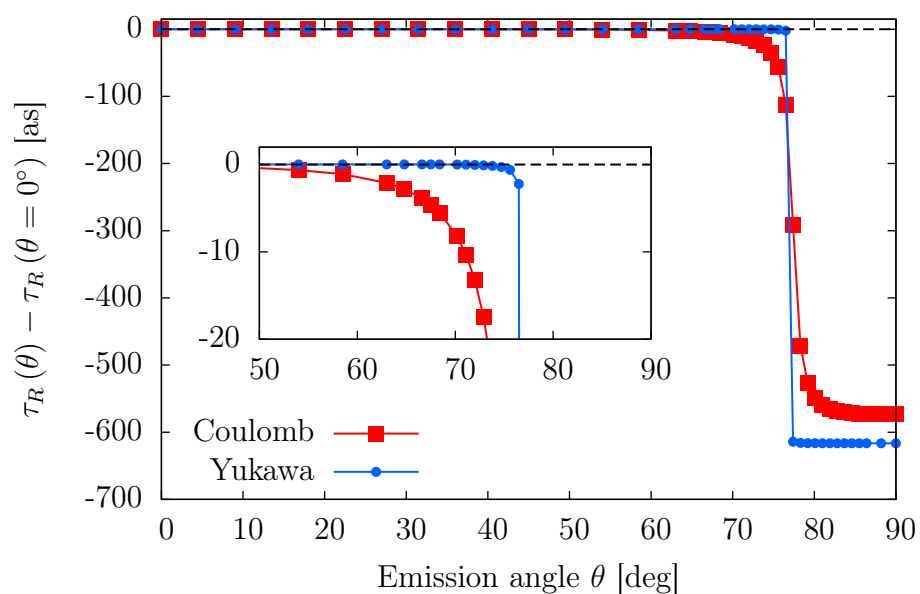


Figure 4.2.: Angle resolved time delay τ_R for the SB centered at $E = 16.5$ eV for the Yukawa potential (\bullet) and hydrogen (\blacksquare). The fundamental wavelength of the IR is $\lambda_{\text{IR}} = 740$ nm. The time delay at $\theta = 0^\circ$ is subtracted for all points to enhance the visibility of the angle dependence

shift between emission parallel and perpendicular to the laser field polarization direction increases and approaches π , see Fig. 4.3a. Further, the emission angle at which the phase jump occurs increases with the IR wavelength. Keeping the IR wavelength fixed and analyzing the different sidebands (and thus different final electron energies), both the angle at which the rapid phase variation occurs as well as the absolute magnitude of it increase with the final energy of the photoelectron, see Fig. 4.3b.

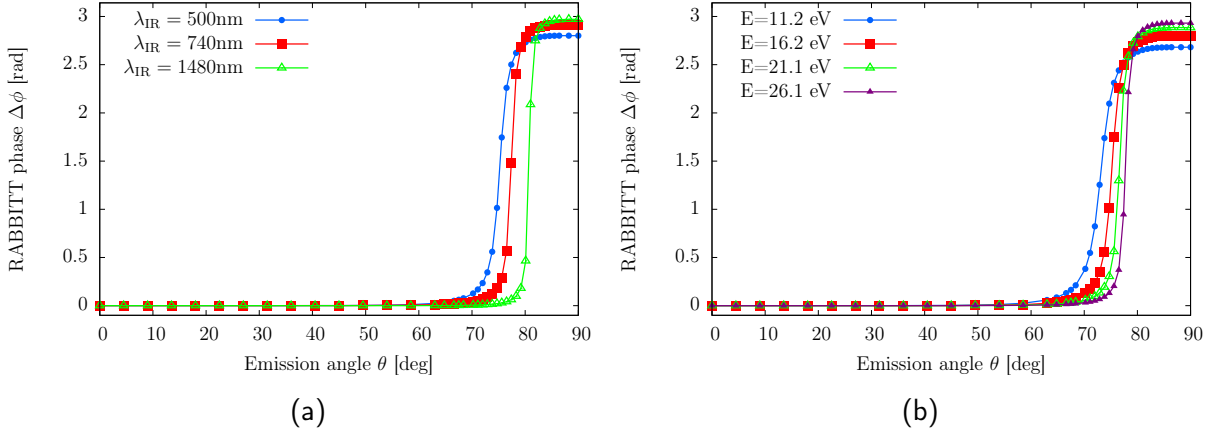


Figure 4.3.: (a) Angle resolved RABBITT phase $\Delta\phi$ obtained from RABBITT traces for ionization of hydrogen by three different APTs and fundamental IR fields. The final electron energy in the considered sideband is 16.15 eV for $\lambda_{\text{IR}} = 500$ nm and 16.5 eV for $\lambda_{\text{IR}}=740$ nm and 1480 nm. (b) Angle resolved RABBITT phase obtained for ionization of hydrogen for $\lambda_{\text{IR}} = 500$ nm analyzed for different SB energies E . The pulse parameters are the same as in (a) for $\lambda_{\text{IR}} = 500$ nm. $\Delta\phi(\theta = 0^\circ)$ is subtracted for all points in (a) and (b) to enhance the visibility of the angle dependence. The numerical parameters are given in App. J.1.1 and J.1.2

To illustrate the origin of the rapid phase jump for ionization from the s ground state of the Yukawa potential we write the wave function at each side band in lowest-order perturbation theory (LOPT) for absorption of one XUV photon and subsequent absorption (emission) of an IR photon [Eq. (3.4)] [31, 173]

$$\Psi(E, \tau, \theta) = \sum_{L=0,2} e^{i\frac{\pi}{2}} Y_L^0(\theta) \left\{ \left| \mathcal{A}_{pL}^{(+)} \right| e^{i[\omega_{\text{IR}}\tau + \eta_p^{(+)}(E - \omega_{\text{IR}})]} + \left| \mathcal{A}_{pL}^{(-)} \right| e^{i[-\omega_{\text{IR}}\tau + \eta_p^{(-)}(E + \omega_{\text{IR}})]} \right\}, \quad (4.8)$$

where $\eta_p^{(\pm)}(E \mp \omega_{\text{IR}})$ is the scattering phase of the intermediate p wave before absorbing (emitting) the IR photon. The two-photon transition amplitude for absorption of one XUV photon to angular momentum 1 (p wave) and subsequent absorption (emission) of an IR

photon and to the final electron angular momentum L , $\mathcal{A}_{pL}^{(\pm)}$, is obtained from $\mathcal{A}_{2n\pm 1\mp\omega_{\text{IR}}}^{(2)}$ [Eq. (3.4)]

$$\begin{aligned}\mathcal{A}_{H_{2n\pm 1\mp\omega_{\text{IR}}}^{(2)}} &= \sum_{L=0,2} e^{i\frac{\pi}{2}} \left| \mathcal{A}_{H_{2n\pm 1\mp\omega_{\text{IR}},pL}^{(\mp)}} \right| e^{\mp i\omega_{\text{IR}}\tau} e^{i\eta_p^{(\pm)}(E\mp\omega_{\text{IR}})} e^{i\phi_{\text{cc},\lambda L}^{\pm}} Y_L^0(\theta) \\ &= \sum_{L=0,2} e^{i\frac{\pi}{2}} \left| \mathcal{A}_{pL}^{(\mp)} \right| e^{\mp i\omega_{\text{IR}}\tau} e^{i\eta_p^{(\pm)}(E\mp\omega_{\text{IR}})} Y_L^0(\theta),\end{aligned}\quad (4.9)$$

using the fact that for the short-ranged Yukawa potential the continuum-continuum phase vanishes, i.e. $\phi_{\text{cc},\lambda L}^{\pm} = 0$. We assume that all fields are linearly polarized along \hat{z} and hence all magnetic quantum numbers are $m = 0$.

The photoelectron spectrum for the sideband is given by

$$\begin{aligned}|\Psi(E, \tau, \theta)|^2 &= \left(\left| \mathcal{A}_{p0}^{(+)} \right|^2 + \left| \mathcal{A}_{p0}^{(-)} \right|^2 \right) Y_0^0(\theta)^2 + \left(\left| \mathcal{A}_{p2}^{(+)} \right|^2 + \left| \mathcal{A}_{p2}^{(-)} \right|^2 \right) Y_2^0(\theta)^2 \\ &\quad + \left(\left| \mathcal{A}_{p0}^{(+)} \right| \left| \mathcal{A}_{p2}^{(+)} \right| + \left| \mathcal{A}_{p0}^{(-)} \right| \left| \mathcal{A}_{p2}^{(-)} \right| \right) Y_0^0(\theta) Y_2^0(\theta) \\ &\quad + 2 \left[\left| \mathcal{A}_{p0}^{(+)} \right| \left| \mathcal{A}_{p0}^{(-)} \right| Y_0^0(\theta)^2 + \left| \mathcal{A}_{p2}^{(+)} \right| \left| \mathcal{A}_{p2}^{(-)} \right| Y_2^0(\theta)^2 \right] \text{Re} \left\{ e^{i(\omega_{\text{IR}}\tau + \eta_p^{(+)})} e^{-i(-\omega_{\text{IR}}\tau + \eta_p^{(-)})} \right\} \\ &\quad + 2Y_0^0(\theta) Y_2^0(\theta) \left[\left| \mathcal{A}_{p0}^{(+)} \right| \left| \mathcal{A}_{p2}^{(-)} \right| + \left| \mathcal{A}_{p0}^{(-)} \right| \left| \mathcal{A}_{p2}^{(+)} \right| \right] \text{Re} \left\{ e^{i(\omega_{\text{IR}}\tau + \eta_p^{(+)})} e^{-i(-\omega_{\text{IR}}\tau + \eta_p^{(-)})} \right\} \\ &= A(\theta) + 2 \left| \mathcal{A}_{p0}^{(+)} \right|^2 B(\theta) \cos(2\omega_{\text{IR}}\tau - [\eta_p^{(-)} - \eta_p^{(+)}]) \\ &= A(\theta) + 2 \left| \mathcal{A}_{p0}^{(+)} \right|^2 B(\theta) \cos(2\omega_{\text{IR}}\tau + \Delta\eta_p).\end{aligned}\quad (4.10)$$

The term A in Eq. (4.10) is constant with respect to the delay τ and

$$B(\theta) = aY_0^0(\theta)^2 + bc^2Y_2^0(\theta)^2 + Y_0^0(\theta)Y_2^0(\theta)c(1+ab) \quad (4.11)$$

is the angle dependent pre-factor of the $\cos(2\omega_{\text{IR}}\tau + \Delta\eta_p)$ oscillation. The factors a, b, c are defined as

$$a = \left| \mathcal{A}_{p0}^{(-)} \right| / \left| \mathcal{A}_{p0}^{(+)} \right|, \quad (4.12)$$

$$b = \left| \mathcal{A}_{p2}^{(+)} \right| / \left| \mathcal{A}_{p2}^{(-)} \right|, \quad (4.13)$$

$$c = \left| \mathcal{A}_{p2}^{(-)} \right| / \left| \mathcal{A}_{p0}^{(+)} \right|. \quad (4.14)$$

Following Fano's propensity rules¹¹ [173, 174] a and b are > 1 . Eq. (4.11) shows that $B(\theta)$ can change the sign from positive to negative for $\theta > 58^\circ$ due to the node in

¹¹ Fano's propensity rules: Upon absorption of a photon the probability that the angular momentum of the electron ℓ is increased, is bigger than the probability to decrease ℓ . Conversely, for emission of a photon the probability to decrease ℓ is bigger [174].

$Y_2^0(\theta) \propto [3 \cos^2(\theta) - 1]$. The sign change of $B(\theta)$ results in a phase jump of the retrieved phase, which is exactly what we observe in Fig. 4.2 for the Yukawa potential. The angle at which $B(\theta)$ changes its sign for photoionization of helium depends strongly on both the final photoelectron energy and the undetermined parameter $c = \left| \mathcal{A}_{p2}^{(-)} \right| / \left| \mathcal{A}_{p0}^{(+)} \right|$, Fig. 4.4. For the specific case shown in Fig. 4.4 the angle at which the jump occurs increases mono-

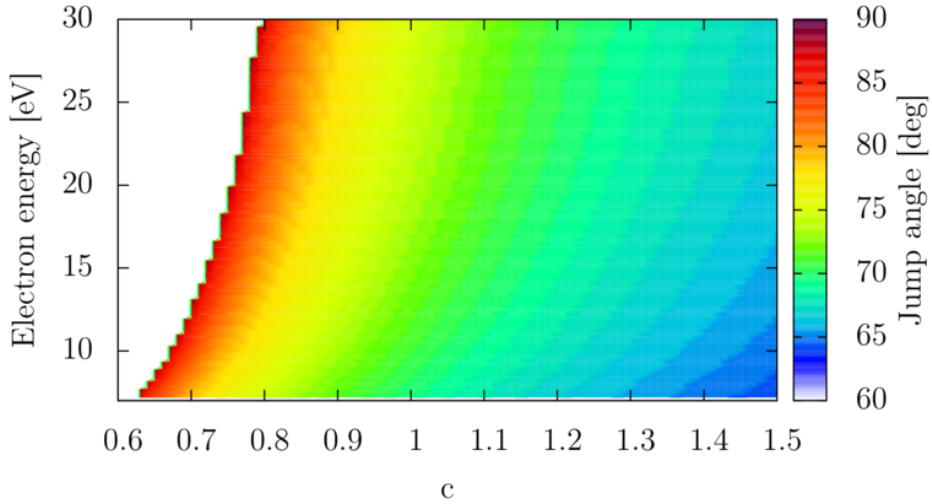


Figure 4.4.: Angle at which $B(\theta)$ [Eq. (4.11)] changes sign as function of the final photoelectron energy and the parameter c . a and b are extracted from [173] for ionization of helium. The white area represents the parameter range where Eq. (4.11) predicts no phase jump.

tonically with the final energy for fixed value of c . Conversely, the angle decreases for constant final energy if c is increased, which is plausible due to the bigger weight of the d partial wave. If the s wave is more dominant compared to the d wave no phase jump is visible (white area in Fig. 4.4).

To be able to extract a jump angle for both considered potentials we define the jump angle for the Coulomb potential at the middle of the observed symmetric drop. As already seen in Fig. 4.3b, the position of the phase jump increases monotonically with the final photoelectron energy for both potentials [Fig. 4.5]. Interestingly, the position is in almost perfect agreement for the two potentials. This indicates that first, the parameter c is very similar for the two potentials, and second, although the Coulomb potential shows a much smoother variation of the time delay with the angle, the position of the rapid change is not altered. The monotonic increase of the jump angle with the final electron energy is observed for all considered wavelengths.

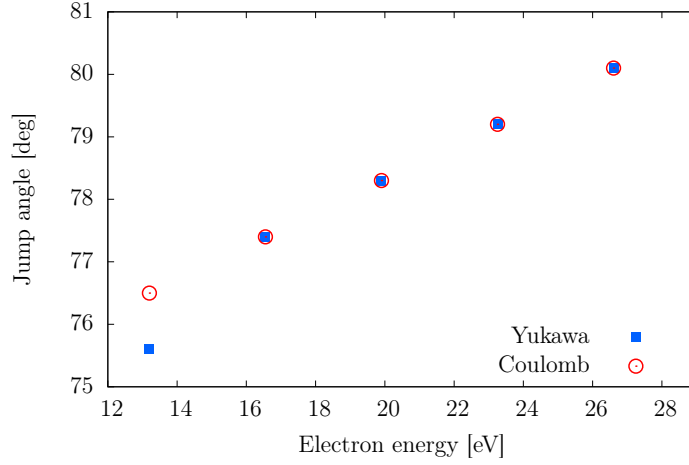


Figure 4.5.: Angle at which the time delay exhibits a rapid jump for the Yukawa and the Coulomb potential (hydrogen). The wavelength of the fundamental IR field is $\lambda_{\text{IR}} = 740$ nm. The pulse parameters are the same as for the results shown in Fig. 4.3 a for this wavelength. For details see text.

The blurring of the phase jump for the Coulomb potential as compared to the Yukawa potential, can most likely be explained by the modification of Eq. (4.8) for the long-range potential

$$\Psi(E, \tau, \theta) = \sum_{L=0,2} e^{i\frac{\pi}{2}L} Y_L^0(\theta) \left[\left| \mathcal{A}_{pL}^{(+)} \right| e^{i(\omega_{\text{IR}}\tau + \eta_p^{(+)} + \phi_{cc,pL}^+)} + \left| \mathcal{A}_{pL}^{(-)} \right| e^{i(\omega_{\text{IR}}\tau + \eta_p^{(-)} + \phi_{cc,pL}^-)} \right], \quad (4.15)$$

as given by Eq. 3.4 for an intermediate state with $\lambda = 1$ (p wave). Indications of a dependence of the continuum-continuum phase $\phi_{cc,\lambda L}^{\pm}$ on the final angular momentum L have already been seen in [31, 32]. This dependence cancels, however, almost completely if only the difference between $\phi_{cc,pL}^+$ and $\phi_{cc,pL}^-$ for the same L is considered. This is the case for angle-integrated RABBITT spectra where all terms of Eq. (4.10) proportional to $Y_0^0 Y_2^0$ vanish. If the difference between continuum-continuum phases $\phi_{cc,\lambda L}^{\pm}$ for different final angular momenta L contributes, as for angle-resolved RABBITT spectra, the angular momentum dependence of $\phi_{cc,pL}^{\pm}$ becomes clearly visible, see also Sec. 4.3. The observation that the total phase variation is smaller for increasing IR wavelengths [Fig. 4.3] can be attributed to larger values of the continuum-continuum coupling $\phi_{cc,pL}^{\pm}$ for increasing IR wavelength.

So far we have always considered ionization from an initial s electron, which leads to a superposition of an s and d wave for the photoelectron wave packet produced by the RABBITT technique. Considering instead ionization from an initial p_0 electron the final two-photon photoelectron wave packet consists of a superposition of p_0 and f_0 waves which

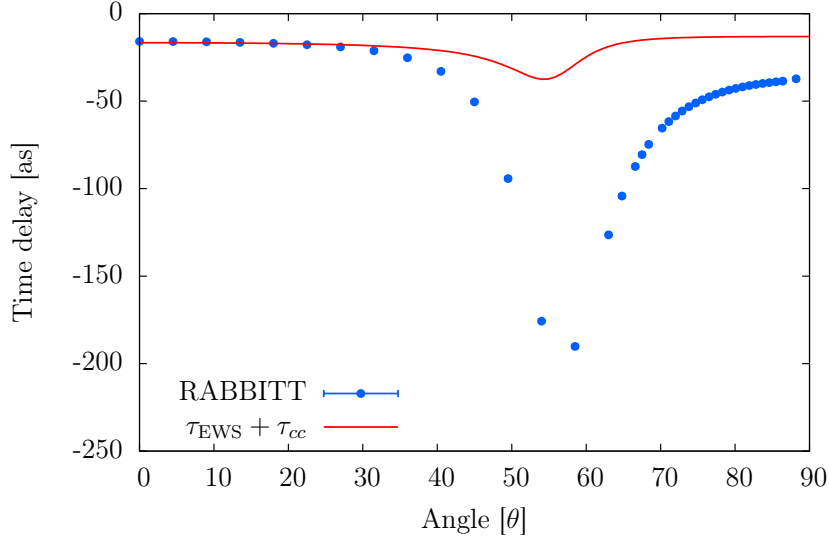


Figure 4.6.: Angle resolved RABBITT time delay for ionization of the $2p_0$ shell of neon within the single-active electron approximation compared to the analytic prediction Eq. (4.1). The final electron energy is 21.98 eV. The numerical parameters are given in App. J.1.3.

implicates a very different combination of partial waves in Eq. (4.15) with final angular momenta $L = 1, 3$. Thus we expect a qualitatively different angle dependence of τ_{cc} as compared to ionization of an electron from an s shell, e.g. hydrogen, for electrons ionized from different shells. We illustrate this by analyzing the angle dependence of the RABBITT time delay obtained for photoionization of neon from the $2p_0$ shell. We treat the neon atom in the single-active electron approximation using the model potential given in [114]. The IR wavelength is $\lambda_{\text{IR}} = 800\text{nm}$ and the APT is formed from the 29th and 31st harmonic. For emission angles $\theta < 30^\circ$ we find good agreement between the analytical prediction [Eq. 4.1] and the obtained delay, while for larger emission angles the overall shape looks similar but the absolute magnitude of the variation is not captured correctly, see Fig. 4.6. The variation of the analytical prediction is due to the angle-dependent scattering delay τ_{EWS} , since we use an angle independent formula for τ_{cc} , Eq. (4.5).

Concluding, we find that the interference of the different partial waves populated by the two-photon transitions inherent in RABBITT leads to an angle-dependent variation of the retrieved time delay. The functional form of this variation depends strongly on the initial angular momentum of the ionized electron. A recent study has drawn very similar conclusions [173].

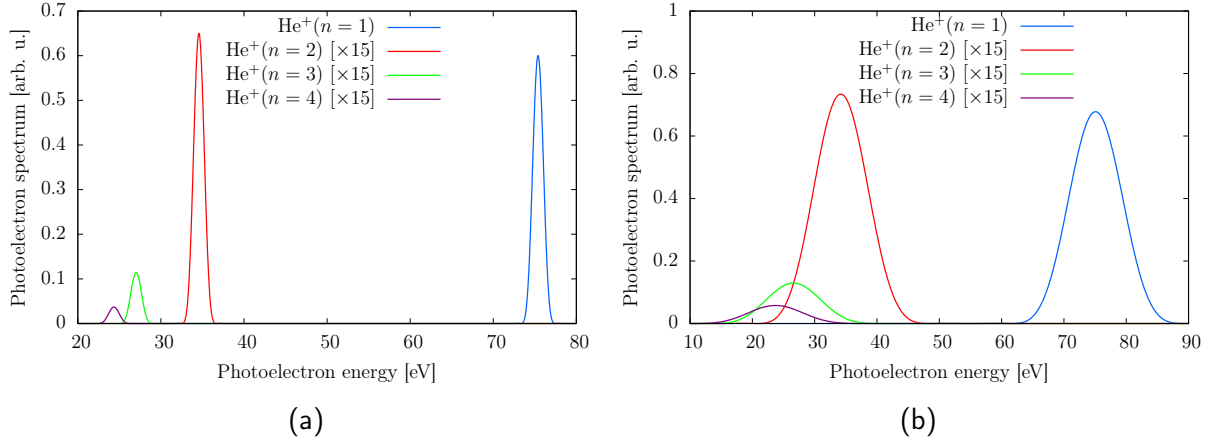


Figure 4.7.: (a) Electron spectrum of the different He⁺(n = k) shake-up channels for photoionization of helium by a 2 fs FWHM duration XUV pulse with a central photon energy of 100 eV. (b) Electron spectrum of the different shake-up channels in helium after ionization by a 0.3 fs FWHM duration XUV pulse with a central photon energy of 100 eV.

To be able to compare the ionization yields of the different channels, the spectra for all channels apart for the shake-down channel [He⁺(n = 1)] are multiplied by 15.

4.1.2. Angle dependence of the photoionization time delay for shake-up states in helium

During shake-up ionization of a multi-electron system the ionized electron interacts with the residual electron via electron-electron interaction and thus can promote excitations of the ion. If such an excitation takes place the energy of the ionized electron is smaller compared to an ionization event where the residual ion stays in the ground state (shake-off ionization). For the prototypical system of atomic helium this leads to multiple peaks in the single-photon ionization spectrum at energies

$$\begin{aligned}
 E_s &= E_\gamma - I_{p,1} - (E_{\text{He}^+(n=s)} - E_{\text{He}^+(n=0)}) \\
 &= E_\gamma - I_{p,1} - 2\frac{s^2 - 1}{s^2},
 \end{aligned} \tag{4.16}$$

if the spectral width of the ionizing pulse is small enough for the peaks not to overlap, see Fig. 4.7a. E_γ is the energy of the absorbed photon, $I_{p,1}$ is the first ionization potential for helium (0.904 a.u.), and $E_{\text{He}^+(n=s)} = -\frac{2}{s^2}$ a.u. is the energy of the He⁺(n = s) residual ion. Even though the timing of shake-up ionization has already been investigated in depth with streaking experiments and calculations [26, 28–30, 100, 193–195] it is worthwhile revisiting this process with RABBITT for a multitude of reasons.

First, the spectral width of the single attosecond pulse used for streaking is too broad to

analyze the $n = 2$ shake-up channel isolated from the $n > 2$ channels, since the spectral overlap of the peaks intertwines the information of the different channels. This can be seen explicitly in Fig. 4.7b where we use an XUV with FWHM duration of 300 as typically used in streaking [28]. While the $\text{He}^+(n = 1)$ channel is clearly separated from the shake-up channels $\text{He}^+(n \geq 2)$ all shake-up channels overlap spectrally. This makes the analysis of streaking spectra in presence of overlapping channels quite difficult as was seen, e.g., for photoionization of neon [26, 193]. In RABBITT, it is possible to energetically separate the different channels and analyze them separately [196], see also Fig. 4.7a. Second, the interpretation of angle-resolved spectra is more intuitive for RABBITT as geometric effects due to the directionality of the momentum shift caused by the moderately strong IR field beyond the dipole approximation do not need to be considered [190, 191]. Third, shake-up ionization of helium provides a prototypical example to compare RABBITT and streaking (when still feasible) and to check whether both techniques extract the same photoionization time delays for polarizable targets.

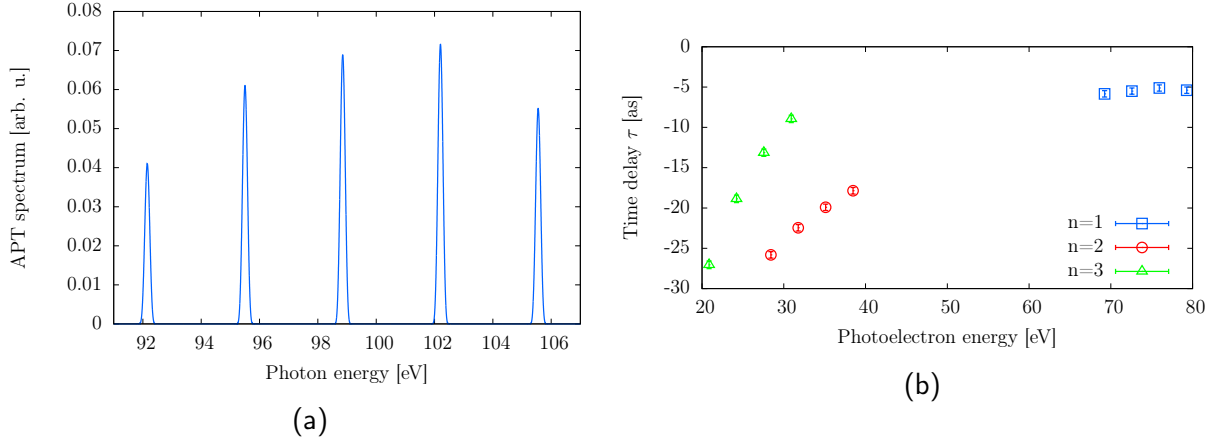


Figure 4.8.: (a) Spectrum of the APT used for all simulations shown in Sec. 4.1.2. (b) Time delays τ_R obtained from fully angle-integrated RABBITT traces resolved for the $n=1,2$ and 3 shells upon ionization by the APT shown in (a).

The wavelength of the fundamental IR is $\lambda_{\text{IR}} = 740\text{nm}$ with a peak intensity of $2 \times 10^9 \text{ W/cm}^2$. The FWHM duration of the IR and the APT are 20 fs and 15 fs.

Throughout this subsection we use an IR with wavelength $\lambda_{\text{IR}} = 740\text{nm}$, FWHM duration of 20fs and peak intensity of $2 \times 10^9 \text{ W/cm}^2$. The APT consists of the 55th, 57th, 59th, 61st and 63rd harmonic of the fundamental with a FWHM duration of 15fs and peak intensities between 10^{10} W/cm^2 and 10^{12} W/cm^2 , see Fig. 4.8a. For more details on the numerical parameters see App. J.2.1. A typical RABBITT trace from which the photoionization time delays τ_R are obtained is shown in Fig. 4.9b. To avoid any influence of overlapping channels we analyze all RABBITT traces separately for each channel, unless stated otherwise.

Due to the high spectral resolution of RABBITT the final electron energies are well separated for the three-lowest energetic residual ions [Fig. 4.9a]. For the prototypical case where the residual ion is in the groundstate, $\text{He}^+(n = 1)$, i.e. the shake-down channel, the

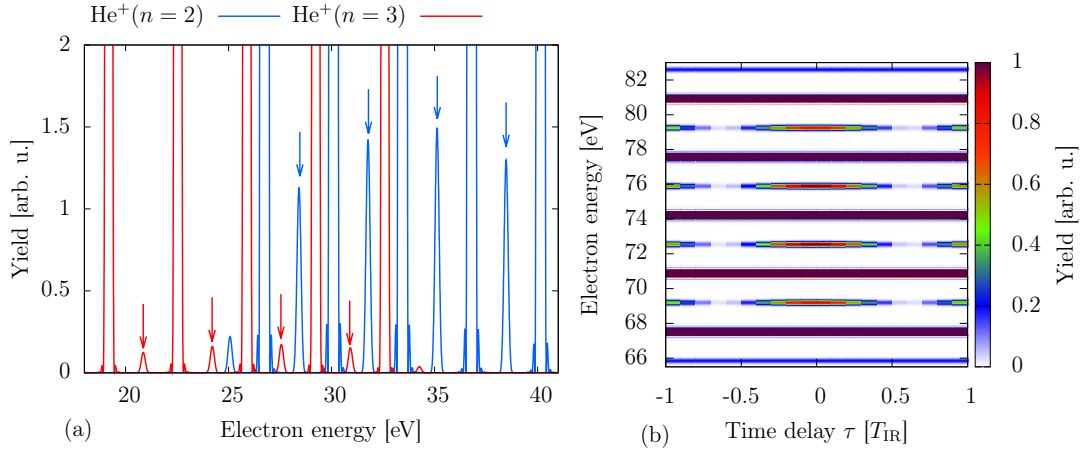


Figure 4.9.: (a) Fully angle-integrated photoelectron spectrum upon ionization by the APT shown in Fig. 4.8a for vanishing time delay between the APT and the fundamental IR ($\tau = 0$) centered on the energy region of the $n = 2, 3$ shake-up channels. The high spectral resolution provided by RABBITT allows to clearly distinguish the different sidebands (marked by arrows) of the two shake-up channels. (b) Fully angle-integrated RABBITT trace for the $\text{He}^+(n = 1)$ shake-down channel. The wavelength of the fundamental IR is $\lambda_{\text{IR}} = 740\text{nm}$ with a peak intensity of $2 \times 10^9 \text{ W/cm}^2$. The FWHM duration of the IR and the APT are 20 fs and 15 fs.

retrieved delays τ_R depends only very weakly on the final electron energies, see Fig. 4.8b. The absolute values obtained from the angle-integrated RABBITT traces are in very good agreement with streaking calculations and measurements [28, 29, 100]. Furthermore, the photoionization delays are also in very good agreement with single active electron calculations showing that electronic correlations do not influence the photoionization time delay in the shake-down channel for high photon energies [30, 100]. The time delays for the shake-up channels, however, show a much stronger dependence on the final electron energy.

The experimentally measured time delays employing attosecond streaking between shake-down ionization [$\text{He}^+(n = 1)$] and shake-up ionization [$\text{He}^+(n \geq 2)$]

$$\tau^{(n \geq 2)} - \tau^{(n=1)} \quad (4.17)$$

agree very well with streaking simulations extracted from literature [28]. Comparing those values, however, to $\tau_R^{(n=2)} - \tau_R^{(n=1)}$ obtained from angle-integrated RABBITT traces we find a striking difference of approximately 7 as [Fig. 4.10] between the RABBITT calculations and the streaking results (theory and experiment). This difference is not caused by the slightly different IR wavelength which alters only the time delay caused by the IR transition (τ_{cc} or τ_{CLC}) by less than 1 as. Rather the difference can be attributed to two fundamentally different effects. First, in streaking, due to the spectral width of the ionizing XUV pulse, it is experimentally not possible to separate the contributions from the

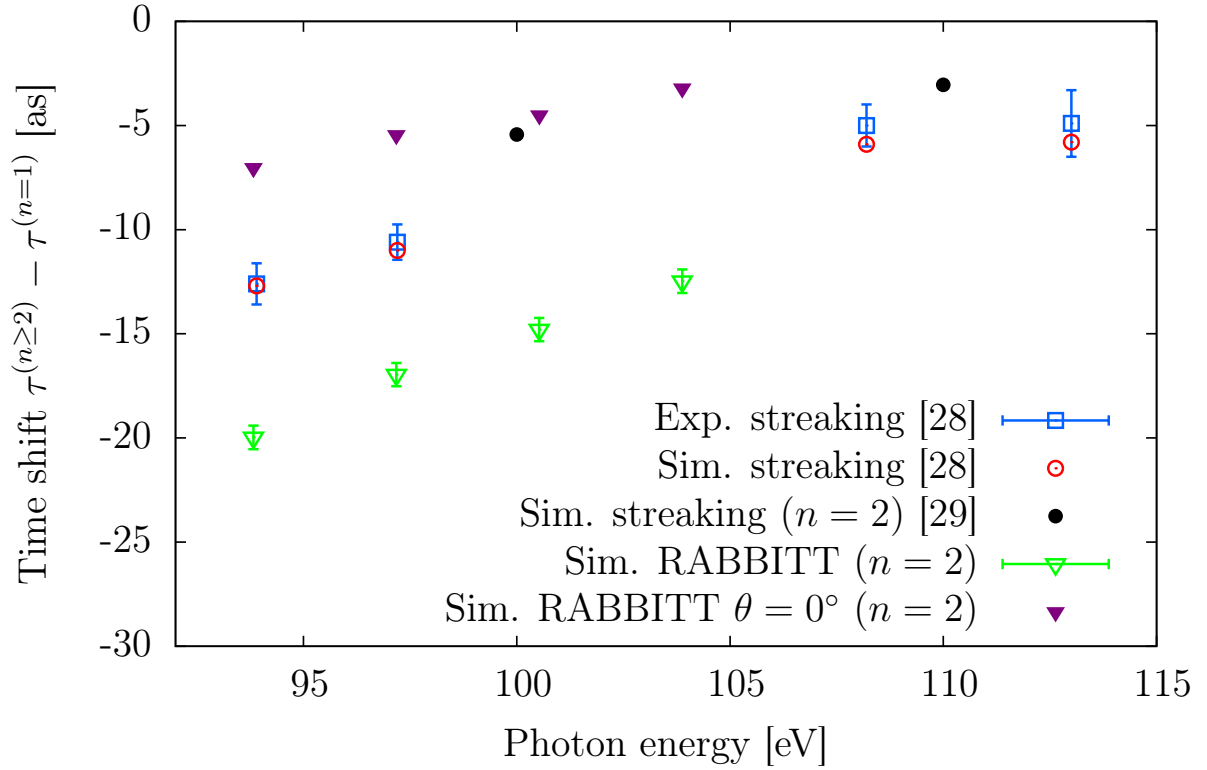


Figure 4.10.: Comparison of the relative photoionization time delay $\tau^{(n \geq 2)} - \tau^{(n=1)}$ between electrons in the shake-up channels [$\text{He}^+ (n > 2)$] and in the shake-down channel [$\text{He}^+ (n = 1)$] for streaking and RABBITT. The experimental (boxes) and simulation results (empty circles) including all shake-up channels for streaking are extracted from [28]. The simulation results including only the $\text{He}^+ (n = 2)$ shake-up channel (full circles) for streaking are extracted from [29]. RABBITT allows to directly retrieve the time delays for the $\text{He}^+ (n = 2)$ shake-up channel as the higher channels are spectrally separated. We retrieve $\tau_R^{(n=2)} - \tau_R^{(n=1)}$ from fully angle-integrated RABBITT traces (empty green triangles) and RABBITT traces evaluated just in forward direction, i.e. $\theta = 0^\circ$ (filled purple triangles). The numerical parameters are given in J.2.1.

He^+ ($n = 2$) and He^+ ($n > 2$) channels. This mixing leads to a larger time delay between shake-down and shake-up ionization [29]. RABBITT circumvents this problem as the better spectral resolution allows to separate the different channels. Second the retrieved time delay is not isotropic for the shake-up channels and thus a difference between the time delay obtained from an angle-integrated RABBITT trace and a streaking trace which is evaluated in forward direction ($\theta = 0^\circ$) has to be expected. Taking these two difference into account the time delay difference $\tau_R^{(n=2)} - \tau_R^{(n=1)}$ obtained from RABBITT traces evaluated just in forward direction ($\theta = 0^\circ$) agrees very well with streaking calculations for the same quantity, i.e. selecting only the $n = 2$ shake-up channel. A more detailed comparison between RABBITT and streaking is given in appendix B.2.

The influence of the angular momentum of the residual ion is revealed by calculating the time delays not only for the full He^+ ($n = 2$) shell, but also for the He^+ ($2s$) and He^+ ($2p$) states as well as for the two parabolic Stark states He^+ ($n = 2, k = \pm 1$) separately, see Fig. 4.11a.

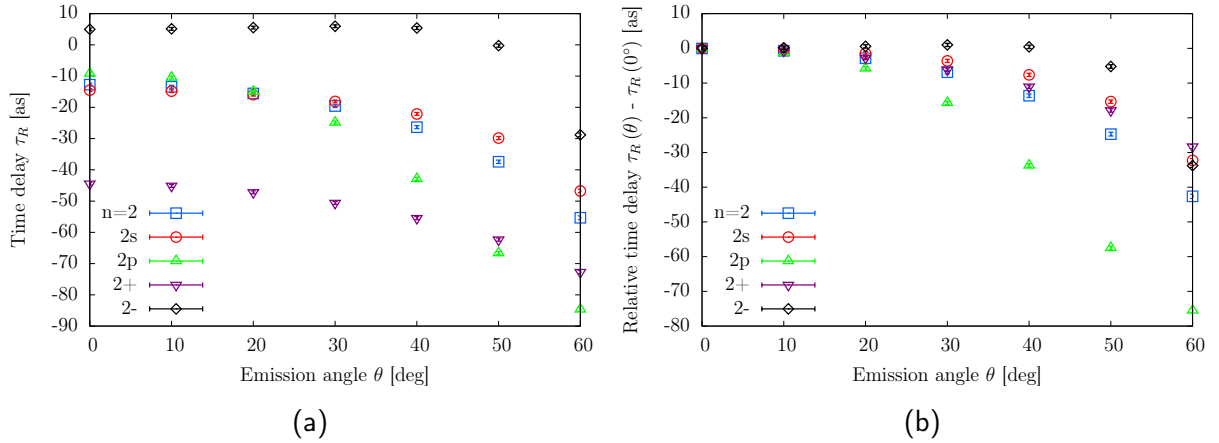


Figure 4.11.: Angle dependence of the retrieved delays for the $n = 2$ shake-up channel with RABBITT. For brevity, we only show results for the lowest energetic sideband [$E \approx 28.4$ eV]. We checked that the other sidebands show similar results. (a) Absolute time delay as function of the electron emission angle relative to the laser polarization axis θ . (b) Relative time delay with respect to emission along $\theta = 0^\circ$.

The considerable variation of the time delays for the different residual ions for emission along $\theta = 0^\circ$ was observed and explained before by the different scattering delay τ_{EWS} and the different effective dipole moment d_{eff} [Eq. 4.7] and hence different dipole delay τ_{dipole} [29]. The contribution from the continuum-continuum transition is the same for all channels along $\theta = 0^\circ$.

Close inspection of the relative time delay $\tau(\theta) - \tau(\theta = 0^\circ)$ reveals that the functional form of the angle-variation is quite different for the different channels as was to be expected based on the results from Sec. 4.1.1, see Fig. 4.11b. The $|k = -1\rangle$ state shows a very slight increase until $\theta \approx 40^\circ$ before the delay decreases rapidly while the time delay for the $2p$ state decreases monotonically. The three other states show a similar behavior of the relative

time delay variation with the emission angle. The angle dependence shown in Fig. 4.11 cannot be explained by the small variation of the scattering delay τ_{EWS} [Fig. 4.12 a], as the variation of τ_{EWS} is drastically smaller compared to the variation observed for $\tau_R(\theta)$. To compare our numerical results to the analytic prediction [Eq. (4.1)] we explicitly take the angle dependence of τ_{EWS} and of the dipole delay τ_{dipole} [Eq. (4.6)] into account. In the absence of an analytic prediction for the angle dependence of τ_{cc} , we use Eq. (4.5). Doing so we obtain reasonable agreement for the $n=2$ shell between the numerical results and the analytic prediction [blue line and points in Fig. 4.12b]. For the $\text{He}^+(2s)$ channel the analytical prediction matches the numerical results almost perfectly. In the case of the $\text{He}^+(2p)$ channel the analytical prediction deviates for $\theta > 20^\circ$. Nevertheless, with the near perfect agreement for the $\text{He}^+(2s)$ residual ion we are able to confirm the prediction of the angle-dependence for $\tau_{\text{dipole}}(\theta)$, as this is the only angle-dependent contribution in the analytical prediction and correctly describes the variation of the time delay by 35as. The good agreement for the full $\text{He}^+(n=2)$ shell is due to the dominance of the $\text{He}^+(2s)$ over the $\text{He}^+(2p)$ channel for the considered emission angles.

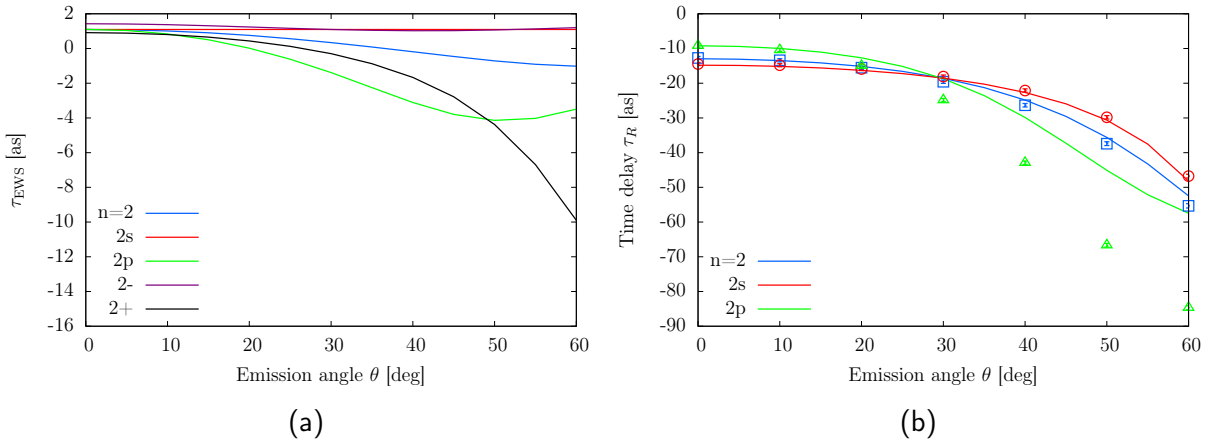


Figure 4.12.: (a) Variation of the scattering delay τ_{EWS} with the emission angle. (b) Comparison of the retrieved photoemission time delay (points) for RABBITT with the analytic prediction given by Eq. (4.1) (solid lines) by taking into account the angle-dependence of the scattering delay τ_{EWS} and of the polarization delay τ_{dipole} . For brevity, we only show results for the lowest energetic sideband [$E \approx 28.4$ eV]. We checked that the other sidebands show similar results.

For the $n=3$ shake-up states [Fig. 4.13] the retrieved time delays vary up to 200as within the considered range of emission angles. Similar to the $\text{He}^+(n=2)$ shell the retrieved time delays for the $n=3$ shake-up channels decrease monotonically with increasing emission angle θ . This qualitative trend is also reflected by the analytic prediction. For the $\text{He}^+(n=3)$ shake-up channels differences (especially for the $3d$ channel) between the calculated time delays and the analytical prediction are already visible for emission along $\theta = 0^\circ$. One possible explanation for this is that, the $\text{He}^+(n=3)$ shake-up channels are energetically

already quite close to the $\text{He}^+(n = 4)$ channels ($\Delta E \approx 2.6\text{eV}$). It has been shown that already such a near degeneracy introduces a dipole delay to the retrieved time delays [100]. Our prediction for the dipole delay [Eq. (4.6)] does include, however, only contributions from fully degenerate states. To develop a proper prediction for the dipole delay including the influence of nearly degenerate states modifications of Eq. (4.6) would be necessary. This goes beyond the scope of this thesis, but is an interesting further direction to study photoemission time delays from more complex targets, e.g. molecules, where the energy levels can be expected to be much more dense compared to He^+ .

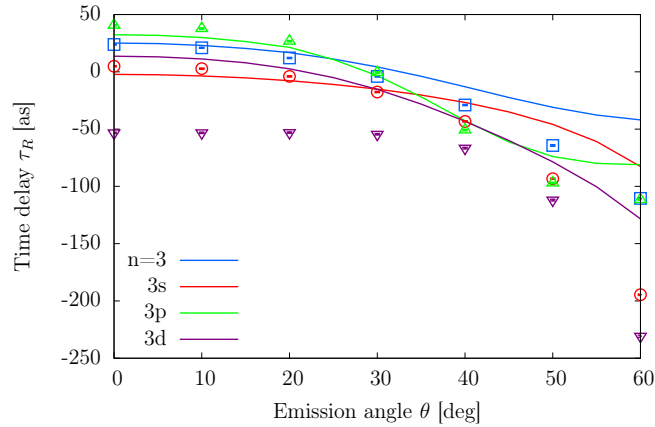


Figure 4.13.: Angle dependence of the $\text{He}^+(n = 3)$ shake-up states. We consider the lowest energetic sideband which corresponds to an photoelectron energy of approximately 21 eV. The solid lines represent the analytic prediction [Eq. (4.1)] and the points the simulation results.

An alternative approach to study the angle-dependence of time delays is to expand the measured electron spectrum into spherical harmonics

$$|\Psi(E, \theta)|^2 = \sum_{j=0}^{J_{max}} \beta_j(E) Y_j^0(\theta) \quad (4.18)$$

where β_j ¹² are anisotropy parameters [35, 177, 197–199]. This approach can be seen as an extension of standard angular resolved photoelectron spectroscopy. All odd β_j are 0 as long as we only consider sufficiently long APTs and, hence, avoid the spectral overlap (and hence interference) of main- and sidebands. All even β_j oscillate with the same frequency as the full spectrum.

Comparing the time delays retrieved from the oscillating β_j 's for the different residual ions we observe that the shake-down channel yields the same time delays for β_0 , β_2 , and β_4 , Fig. 4.14. For the shake-up channels we observe that the different β_j parameters experience

¹² β_0 is directly proportional to the angle-integrated signal, due to the orthogonality relation of the spherical harmonics.

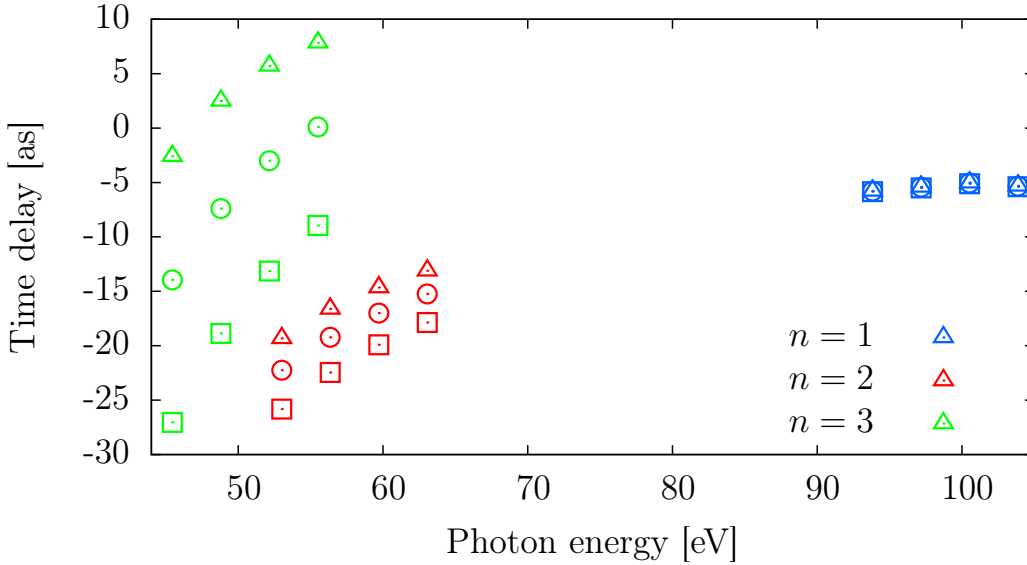


Figure 4.14.: Time delays obtained from analyzing the oscillation of the β_j parameters [Eq. (4.18)] for the $n=1,2,3$ shake-up channels separately. β_0 : (\square), β_2 : (\circ), β_4 : (\triangle).

strongly differing delays which is an indication of the different partial wave mixing. To connect the delays obtained from angle-integrated RABBITT traces with angle-resolved time delays calculated within this thesis we also investigate how the RABBITT spectra depend on the opening angle Θ_{\max} up to which the spectra are integrated over. As expected from our previous results the time delays retrieved from partially angle integrated spectra do not depend on the opening angle Θ_{\max} for the shake-down channel, but show a pronounced angle dependence for the shake-up channels, Fig. 4.15. The non-monotonic variation of the time-delay with increasing opening angle Θ_{\max} arises due to the forward-backward symmetry of the retrieved time delays.

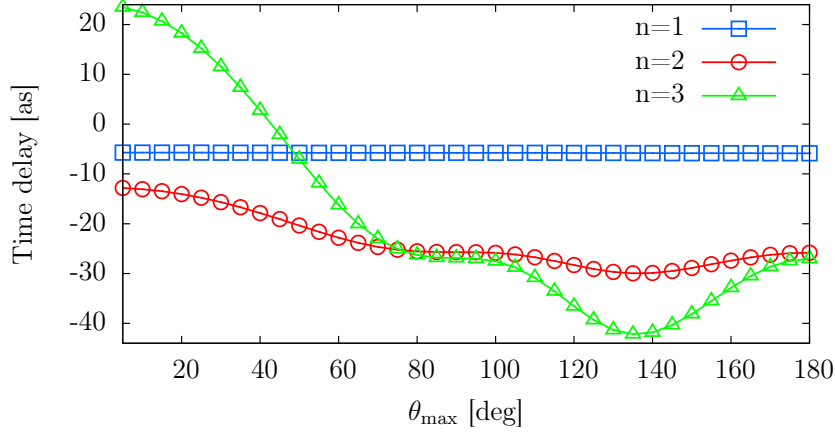


Figure 4.15.: Retrieved delays for the different shake-up channels retrieved from partially angle integrated RABBITT spectra up to opening angle Θ_{\max} for the lowest energetic sideband. The final electron energy is approximately 69.2 eV for the $\text{He}^+(n = 1)$ channel, 28.4 eV for the $\text{He}^+(n = 2)$ channel and 20.8 eV for the $\text{He}^+(n = 3)$ channel.

4.2. Analyzing RABBITT traces for overlapping channels¹³

So far we have considered well isolated ionization channels. Unfortunately, this is not the typical case. Instead in multi-electron systems many ionization channels overlap at each considered energy. This becomes especially problematic for attosecond metrology techniques where the energy resolution is limited by the considerable spectral width of the exciting XUV pulses. Overlapping channels and hence a convoluted retrieved phase information was also identified [193] as probable reason for the disagreement between the experimentally observed [26] and theoretically predicted [193, 195, 200] time delay between photoionization from the neon $2s$ and $2p$ subshell. A recent RABBITT experiment managed to spectrally separate the signal from the $2s$ subshell and nearby shake-up satellite within their experiment and found good agreement with various theoretical calculations [196], thereby showing the potential of the high energy resolution provided by RABBITT. In the remainder of this subsection, we will focus on the more general case where the spectral resolution of RABBITT is not sufficient to disentangle the different ionization channels in the electron spectrum. To do so we choose a scenario where the sidebands for the $\text{He}^+(n = 2)$ and the $\text{He}^+(n = 3)$ channels are directly on top of each other, see Fig. 4.16a. The exact parameters employed in the simulations are given in App. J.2.2. We can analyze the spectral RABBITT traces for the $\text{He}^+(n = 2)$ and the $\text{He}^+(n = 3)$

¹³ The calculations shown in this section were performed in collaboration with Manuel Ederer in the course of his master thesis.

channels separately and obtain the corresponding time delay for each channel. The delay of the spectrum for the overlapping channels is expected to be given by the incoherent sum

$$\tau_{\text{avg}}(\theta) = \frac{\sigma_{n=2}(\theta)\tau_{n=2}(\theta) + \sigma_{n=3}(\theta)\tau_{n=3}(\theta)}{\sigma_{n=2}(\theta) + \sigma_{n=3}(\theta)}, \quad (4.19)$$

where $\sigma_{n=k}(\theta)$ is the angle-dependent single-photon ionization cross section and $\tau_{n=k}(\theta)$ the respective time delay for the $\text{He}^+(n=k)$ channel, see also Eq. (4.4). Comparing the delay obtained from Eq. (4.19) to the numerical results obtained from analyzing the spectrum with overlapping channels we see almost perfect agreement for a large range of electron emission angles, Fig. 4.16b. Although we have considered in this scenario only two overlapping channels we have no doubt that this can be generalized to an arbitrary number of channels.

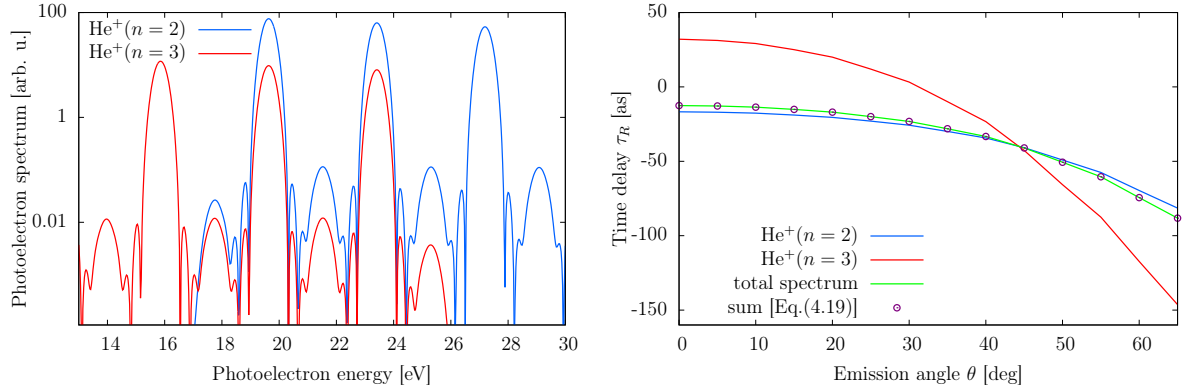


Figure 4.16.: (a) Single-ionization spectra for the $\text{He}^+(n=2,3)$ sub-shell after IR assisted XUV ionization (RABBITT) for time delay $\tau = 0$ between the IR and the APT. (b) Time delays obtained from RABBITT spectra calculated for the separate $\text{He}^+(n=2,3)$ sub-shells and the total spectrum including all channels compared to the time delays obtained via incoherent summation [Eq. (4.19)].

The numerical parameters are given in App. J.2.2.

4.3. Measuring phase differences between different continuum-continuum transitions

In the final section of this chapter we investigate the continuum-continuum phase $\phi_{cc,\lambda\ell}^\pm$ in more detail and propose a scheme to measure it accurately. We discuss a joint experimental and theoretical work where angle and energy resolved RABBITT traces are used to extract the dependence of $\phi_{cc,\lambda\ell}^\pm$ on the final angular momentum ℓ [Eq. 3.4] for the prototypical case

of helium¹⁴ [101]. The full angular distribution allows to retrieve the relative two-photon phase between final states with the same energy but different angular momenta involving the same intermediate state. This is complementary to conventional RABBITT, where phase differences between paths involving different intermediate states are measured, see Fig. 4.17. We note that this work is similar to complete single-photon ionization experiments [201] and the detection of phase differences with angle-resolved spin polarization measurements [202–204].

4.3.1. Photoelectron angular distributions for single ionization of helium

For ionization from the ground state s -shell of helium, four main quantum pathways contribute to each RABBITT sideband, namely, the transitions $s \rightarrow p \rightarrow s$ and $s \rightarrow p \rightarrow d$, for both the absorption [Fig. 4.17a] and stimulated emission [Fig. 4.17b] of the IR photon. In the weak-field regime, the s ($\ell = 0$) and d ($\ell = 2$) photoionization amplitudes at the sideband with energy E_f can be expressed, within lowest-order of perturbation theory, by the well-known two-photon-transition formula Eq. (3.3) [176]. To disentangle the phases

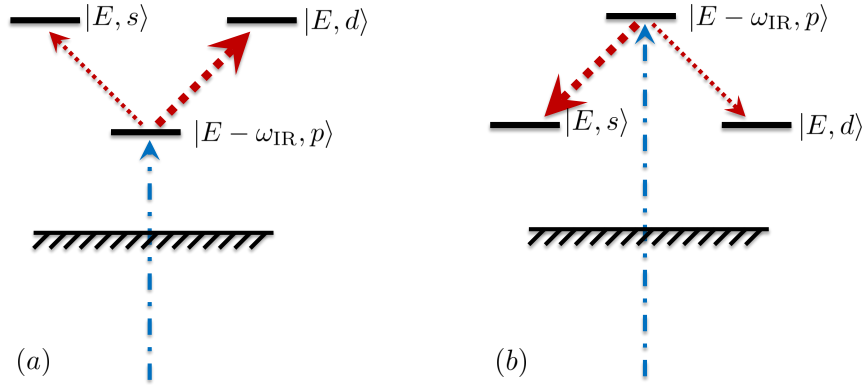


Figure 4.17.: Sketch of the possible two-photon pathways for ionization from an s electron for absorption of one XUV photon and (a) absorption or (b) emission of an IR photon. The wider arrow indicates the preferred transition from the intermediate to the final state due to Fano's propensity rules [173, 174].

of the different partial waves we use a decomposition in the spirit of Eq. (3.4) [27, 31, 32]

$$\mathcal{A}_{H_{2n\pm 1\mp\omega_{\text{IR}},\lambda\ell}}^{(2)} = \left| \mathcal{A}_{\ell}^{(2\pm)} \right| e^{i(\phi_{\lambda\ell}^{(2\pm)} \pm \omega_{\text{IR}}\tau)}, \quad (4.20)$$

¹⁴ The experiments were performed in the group of Ursula Keller at the ETH Zürich. The single-active electron calculations were performed by Nicolas Douguet in the group of Luca Argenti at the University of Central Florida.

where we do not decompose the two-photon phase $\phi_{\lambda\ell}^{(2\pm)}$ explicitly into a scattering phase η_λ and a continuum-continuum phase $\phi_{cc,\lambda\ell}^\pm$ as done in Eq. (3.4). As we are considering single-ionization of helium close to the single-ionization threshold the intermediate state is always a p wave and thus we will drop the dependency on the intermediate angular momentum λ in the following, as it is the same for all quantities. The photoelectron yield at each sideband is given by

$$\begin{aligned} P(\theta, \tau) &= \left| (\mathcal{A}_s^{(2+)} + \mathcal{A}_s^{(2-)}) Y_0^0(\theta) + (\mathcal{A}_d^{(2+)} + \mathcal{A}_d^{(2-)}) Y_2^0(\theta) \right|^2 \\ &= \sum_{j=0}^4 \beta_j(\tau) Y_j^0(\theta). \end{aligned} \quad (4.21)$$

where θ is the angle between the laser polarization axis. The anisotropy parameters β_j obtained from Eq. (4.21) are given by

$$\begin{aligned} \beta_0 &= \frac{1}{\sqrt{4\pi}} \left\{ |\mathcal{A}_s^{(2+)}|^2 + |\mathcal{A}_s^{(2-)}|^2 + 2 |\mathcal{A}_s^{(2+)}| |\mathcal{A}_s^{(2-)}| \cos(2\omega_{\text{IR}}\tau + \phi_s^{(2+)} - \phi_s^{(2-)}) \right. \\ &\quad \left. + |\mathcal{A}_d^{(2+)}|^2 + |\mathcal{A}_d^{(2-)}|^2 + 2 |\mathcal{A}_d^{(2+)}| |\mathcal{A}_d^{(2-)}| \cos(2\omega_{\text{IR}}\tau + \phi_d^{(2+)} - \phi_d^{(2-)}) \right\}, \end{aligned} \quad (4.22)$$

$$\begin{aligned} \beta_2 &= \frac{\sqrt{5}}{7\sqrt{\pi}} \left[|\mathcal{A}_d^{(2+)}|^2 + 2 |\mathcal{A}_d^{(2-)}|^2 + |\mathcal{A}_d^{(2+)}| |\mathcal{A}_d^{(2-)}| \cos(2\omega_{\text{IR}}\tau + \phi_d^{(2+)} - \phi_d^{(2-)}) \right] \\ &\quad + \frac{2}{\sqrt{\pi}} \left[|\mathcal{A}_s^{(2+)}| |\mathcal{A}_d^{(2+)}| \cos(\phi_s^{(2+)} - \phi_d^{(2+)}) \right. \\ &\quad \left. + |\mathcal{A}_s^{(2-)}| |\mathcal{A}_d^{(2-)}| \cos(\phi_s^{(2-)} - \phi_d^{(2-)}) \right. \\ &\quad \left. + |\mathcal{A}_s^{(2+)}| |\mathcal{A}_d^{(2-)}| \cos(2\omega_{\text{IR}}\tau + \phi_s^{(2+)} - \phi_d^{(2-)}) \right. \\ &\quad \left. + |\mathcal{A}_s^{(2-)}| |\mathcal{A}_d^{(2+)}| \cos(2\omega_{\text{IR}}\tau + \phi_d^{(2+)} - \phi_s^{(2-)}) \right], \end{aligned} \quad (4.23)$$

$$\beta_4 = \frac{3}{7\sqrt{\pi}} \left[|\mathcal{A}_d^{(2+)}|^2 + |\mathcal{A}_d^{(2-)}|^2 + 2 |\mathcal{A}_d^{(2+)}| |\mathcal{A}_d^{(2-)}| \cos(2\omega_{\text{IR}}\tau + \phi_d^{(2+)} - \phi_d^{(2-)}) \right]. \quad (4.24)$$

The two-photon phases

$$\begin{aligned} \phi_\ell^{(2\pm)} &= \phi_{cc,\ell}^\pm(E, \omega_{\text{IR}}) + \phi_{bc}^{(1)}(E \mp \omega_{\text{IR}}) \\ &= \phi_{cc,\ell}^\pm(E, \omega_{\text{IR}}) + \eta_p(E \mp \omega_{\text{IR}}) + \phi_{\text{XUV}}(E \mp \omega_{\text{IR}}) \end{aligned} \quad (4.25)$$

contain both the phase $\phi_{cc,\ell}^\pm$ of the continuum-continuum transition and the phase $\phi_{bc}^{(1)}$ associated with the preceding ionization [bound-continuum (bc) transition] by the APT.

The latter one contains the phase of the ionizing XUV pulse ϕ^{XUV} and the atomic phase η_p for the half-scattering process of the outgoing electron wavepacket at the atomic potential [see also Eq. (A.5)]. As discussed before the spectral derivative of the one-photon scattering phase $d\eta_p(E)/dE$ is the EWS delay for single photon ionization [30]. Analogously, $d\phi_{cc,\ell}^{\pm}(E, \omega_{\text{IR}})/dE$ can be interpreted as the delay of continuum-continuum transitions. However, since the IR-driven cc-transition occurs primarily at large distances from the atomic core [27], the accumulated phase, unlike for one-photon ionization does not account for the full half-scattering phase. Rather the continuum-continuum phase originates only from the propagation in the long-range tail of the atomic potential. Therefore, the influence of the centrifugal potential $L^2/2r^2$ on the cc-phase was previously neglected [27]. As shown in section 4.1 this approximation is not valid anymore if RABBITT spectra are analyzed for large electron emission angles.

4.3.2. Extracting phase differences between continuum-continuum transitions to different final angular momenta

Each of the three β_j parameters [Eqs. (4.22) – (4.24)] oscillates at twice the IR frequency

$$\beta_j(\tau) = a + b \cos(2\omega_{\text{IR}}\tau - \phi), \quad (4.26)$$

with a well defined offset a , amplitude b , and phase ϕ , which are directly related to the parameters in Eq. (4.21) and can all be unambiguously extracted from the measurement. The system of Eqs. (4.22) – (4.24) has 4 unknown amplitudes and 4 unknown phases. The phases appear in differences only, and are thus only determined up to an overall constant, allowing us to set one of the phases to zero without loss of generality. The experimentally unknown absolute time zero is subtracted out hereby. The remaining variables can then be fitted simultaneously to the system of equations using a least square minimization routine based on the Levenberg-Marquardt-algorithm [205].

Making use of both the angle-dependent phase and amplitude of the RABBITT interference pattern we can thus determine the amplitudes and relative phases of all four quantum paths contributing to any given sideband. In particular, the relative phase between the two pathways which lead to different angular momenta, is for the absorption

$$\begin{aligned} \phi_s^{(2+)}(E, \omega_{\text{IR}}) - \phi_d^{(2+)}(E, \omega_{\text{IR}}) &= \phi_{cc,s}^+(E, \omega_{\text{IR}}) + \phi_{bc}^{(1)}(E - \omega_{\text{IR}}) \\ &\quad - \phi_{cc,d}^+(E, \omega_{\text{IR}}) - \phi_{bc}^{(1)}(E - \omega_{\text{IR}}) \\ &= \phi_{cc,s}^+(E, \omega_{\text{IR}}) + \eta_p(E - \omega_{\text{IR}}) + \phi^{\text{XUV}}(E - \omega_{\text{IR}}) \\ &\quad - \phi_{cc,d}^+(E, \omega_{\text{IR}}) - \eta_p(E - \omega_{\text{IR}}) - \phi^{\text{XUV}}(E - \omega_{\text{IR}}) \\ &= \phi_{cc,s}^+(E, \omega_{\text{IR}}) - \phi_{cc,d}^+(E, \omega_{\text{IR}}), \end{aligned} \quad (4.27)$$

and for stimulated emission of an IR photon

$$\begin{aligned} \phi_s^{(2-)}(E, \omega_{\text{IR}}) - \phi_d^{(2-)}(E, \omega_{\text{IR}}) &= \phi_{cc,s}^-(E, \omega_{\text{IR}}) + \phi_{bc}^{(1)}(E + \omega_{\text{IR}}) \\ &\quad - \phi_{cc,d}^-(E, \omega_{\text{IR}}) - \phi_{bc}^{(1)}(E + \omega_{\text{IR}}) \\ &= \phi_{cc,s}^-(E, \omega_{\text{IR}}) - \phi_{cc,d}^-(E, \omega_{\text{IR}}), \end{aligned} \quad (4.28)$$

This enables to directly measure the influence of the final-state angular momentum on the cc-phase independent of the preceding one-photon bound-continuum transition. Indeed, in each case, we retrieve the phase difference between pathways involving the same intermediate state, i.e., cc-transitions following the absorption of the same XUV photon. Consequently, the phase of the bc-transition $\phi_{bc}^{(1)}$, which includes both XUV phase ϕ_{XUV} (or chirp) and the p -wave scattering phase η_p , cancels out, such that the remaining phase difference is purely due to the one-photon transition in the continuum, see Fig. 4.17. In contrast to traditional RABBITT [25, 27, 171], where phase differences $\phi(E + \omega_{\text{IR}}) - \phi(E - \omega_{\text{IR}})$ are extracted in order to approximate the phase derivative, this approach yields an (absolute) phase difference at a fixed energy.

Experiment

The experimental data was collected by the group of Ursula Keller (ETH Zürich) using a COLTRIMS detector [206] in combination with an XUV-IR pump-probe setup. The fundamental IR has a central wavelength of $\lambda_{\text{IR}} = 790$ nm and 29 fs FWHM duration and 0.7 mJ total energy. The APT train consists of the harmonics 13 to 25, corresponding to an energy range from 20 to 40 eV, created by high harmonic generation [10, 11]. For details on the experimental setup the reader is referred to [207].

Simulations

In order to prove the validity of the proposed extraction method, we apply the same fitting procedure to RABBITT traces obtained from two independent theoretical simulations, employing the single-active electron approximation and a full *ab initio* calculation. The parameters of the APT (Tab. 4.1) for the single-active electron and the *ab initio* simulation were chosen to match the experimental XUV spectra and are identical for both calculations. The numerical parameters of both simulations are given in App. J.2.3. The IR field in the experiment has a FWHM duration of 29 fs which is approximately 3.5 times longer than the IR used in the simulations (FWHM duration of 8 fs) for computational reasons. SAE simulations for an IR pulse duration of 20 fs give practically identical results to simulations for an IR pulse duration of 8 fs. Thus, we conclude that the IR duration has no influence on the retrieved phase difference [Eqs. (4.27) and (4.28)].

The phase difference $\phi_s^{(2\pm)} - \phi_d^{(2\pm)}$ can also be directly retrieved, i.e. without fitting, from theory by using only a single harmonic (Tab. 4.1) together with the IR field with vanishing time delay between the two fields. From these calculations we directly extract the two-photon phase of the s - and d -partial waves at the sidebands neighboring the single harmonic from the full *ab initio* simulations. The result for $\phi_s^{(2\pm)} - \phi_d^{(2\pm)}$ is labeled “direct *ab initio*” in Fig. 4.18.

In addition to the results for helium, we report calculations for the hydrogen atom, for which harmonics from the 9th to the 17th order are used to generate the XUV spectrum, such that the electron kinetic energy remains in the same range as for helium.

λ [nm]	ω [eV]	Peak intensity [W/cm ²]	FWHM duration [fs]	CEP [π]
790	1.57	1×10^{11}	8	0
53.01	23.39	1.04×10^{10}	3.6	-0.11
46.68	26.56	3.40×10^{10}	2.6	-0.06
41.60	29.80	6.38×10^{10}	2.0	-0.04
37.67	32.91	5.01×10^{10}	1.9	-0.06
34.33	36.11	3.65×10^{10}	2.0	-0.11
31.50	39.36	3.16×10^{10}	1.8	-0.18
29.22	42.43	1.46×10^{10}	1.6	-0.29
27.35	45.33	0.47×10^{10}	1.5	-0.44

Table 4.1.: Pulse parameters used in the SAE and the *ab initio* simulations. All but the first pulse form the attosecond pulse train (APT) used to ionize the helium atom.

Retrieved phase differences

We observe a remarkable quantitative agreement between experiment and the theoretical values for the phase difference $\phi_{cc,s}^{\pm} - \phi_{cc,d}^{\pm}$ for electron energies $2 \text{ eV} \leq E \leq 14 \text{ eV}$ (sideband 18 – 24). The agreement between the single-active electron simulation and the full *ab initio* calculation allows the conclusion that in the investigated energy range the effect of electron correlation on the continuum-continuum transition is either negligible or, though present, identical for each of the two pathways. In addition our results obtained for hydrogen exactly follow the helium trend. This supports the argument of negligible influence from both electron correlation effects and the helium short-range potential on the investigated cc-transition phases. The excellent agreement between the theoretical phase differences obtained from the fitting routine and the “direct” determination shows that the proposed fitting algorithm faithfully reproduces the observable we are interested in.

Our observations can be summarized by three points, which we will explain and discuss in more detail in the following:

1. The relative phase difference between *s*- and *d*-wave electrons converges to zero for increasing kinetic energy.
2. The relative phase between *s*- and *d*-wave photoelectrons is ubiquitously positive and decreases with energy, both for transitions involving absorption and stimulated emission at all kinetic energies.
3. In all sidebands, the absolute values of the phase difference between *s*- and *d*-wave are fairly equal for absorption and stimulated emission. The difference lies far below the experimentally accessible precision. The theoretical values indicate slightly larger delays for the absorption transition $\phi_{cc,s}^+ - \phi_{cc,d}^+$, see Fig. 4.18c.

Although the observed phase differences have previously not been recognized and analyzed, they were, in fact, noticeable also in earlier numerical simulations [31, 32]. Qualitatively

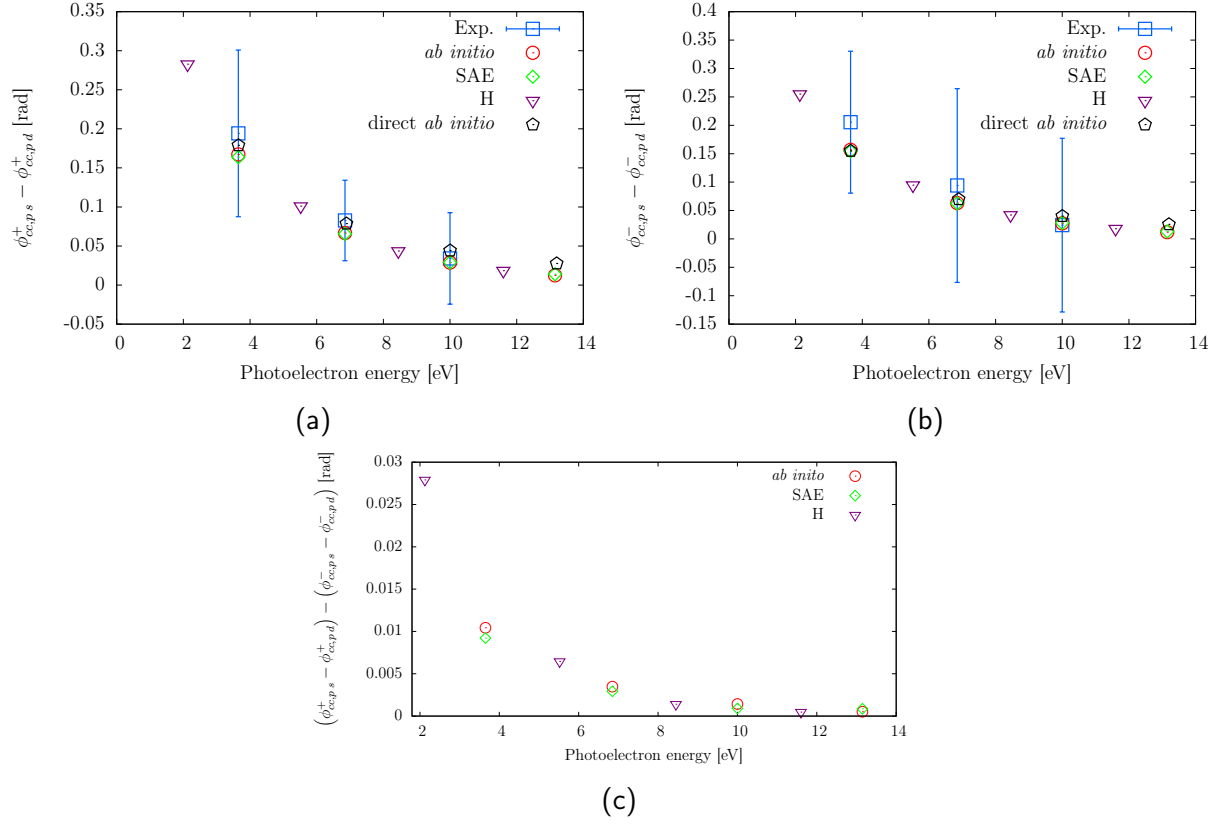


Figure 4.18.: Phase difference between the continuum-continuum transition to an s or d state in for (a) stimulated absorption and (b) stimulated emission of an IR photon. (c) Difference between phase differences for stimulated absorption ($\phi_{cc,ps}^+ - \phi_{cc,pd}^+$) and stimulated emission ($\phi_{cc,ps}^- - \phi_{cc,pd}^-$) shown in panel (a) and (b). The pulse profile of the employed pulses for the *ab initio* and the single-active electron (SAE) calculation are given in Tab. 4.1. The experimental and theoretical APT spectrum coincides but the FWHM duration of the IR field used in the experiment is approximately 29 fs compared to 8 fs in the theoretical simulations. The values reported for hydrogen (labeled “H”) are extracted from a simulation employing the odd orders of the 9th to 17th harmonic of $\lambda_{\text{IR}} = 790$ nm. All values, apart from the data labeled “direct *ab initio*”, are extracted by employing the fitting procedure described in the text. The data labeled “direct *ab initio*” is obtained from a full *ab initio* simulation employing only a single harmonic dressed by the fundamental IR field, where the phase difference is extracted by directly comparing the partial waves amplitudes in the s and d channel in the sidebands neighboring the used harmonic.

our results mirror the trend obtained for time-integral but angle- and spin-resolved photoemission [202–204]. All observations are fully consistent with the influence of the final-state centrifugal potential on the continuum scattering phase and on the Eisenbud-Wigner-Smith time delay, in the present case for continuum-continuum transitions.

Observation (1) is the obvious consequence of the decreasing effect of the underlying potential energy landscape on the escaping electron. With increasing kinetic energy the wave function tends towards the behavior of a free spherical wave. Moreover, with increasing momentum of the outgoing wavepacket, the cc-transition is effectively shifted to larger distances from the ionic core at which the centrifugal potential $\propto 1/r^2$ becomes negligible compared to the Coulomb potential. The latter was the underpinning of the previous analytical estimates of the cc-phase and time delay in which the angular momentum dependence was neglected [27].

Observation (2) clearly shows that the cc-phase is, in fact, directly related to the EWS phase for continuum-continuum scattering. This is supported by the observation that the phase and corresponding delay qualitatively resembles the EWS delay for bound-continuum transitions to different angular momentum states [202–204]. The fact that the retrieved phases are significantly smaller (by a factor 3 to 4) with respect to the scattering phase is due to the fact that, unlike for the bound-continuum transition, the continuum-continuum transition in the two-photon scenario probes the potential landscape not for the full radial range of half-scattering but only at large distances where the centrifugal potential is weaker. Nevertheless, the centrifugal potential still leads to clearly resolvable effects at low energies.

Observation (3) confirms the fact that the relevant phase is accumulated at distances where the Coulomb potential ($1/r$) dominates, the centrifugal potential provides a (small) correction, and the short-ranged contributions are entirely negligible. Therefore, the observed phases are universal, i.e. independent of the atomic species, and slightly larger for absorption than for emission. The latter is in line with the fact that the outgoing wavepacket after the bound-continuum transition propagates initially slower before absorption (but faster before emission) thereby enhancing (diminishing) the influence of the centrifugal potential on the subsequent cc-transition.

For larger atoms or molecules, where electron correlation effects become dominant, a deviation from such a universal trend might be expected. At lower kinetic energies, even larger delays can be expected. These were not measured in the experiment due to the limited tunability of the XUV spectrum in the present experiment. Sideband 16 in principle would lie just above the helium ionisation threshold and could be analysed in a similar fashion. However, Rydberg states of the neutral helium atom come into play here [208]. To analyze the latter sideband one would need to separate the intermediate states into a sum over intermediate bound and continuum states separately which goes beyond the scope of this work. A detailed theoretical treatment of this can, e.g., be found in [209].

5. Measuring the phase of Fano resonances

Continuing from the previous chapter, where we investigated the spectral phase of the structureless continuum, we characterize in this chapter the spectral phase in the vicinity of Fano resonances. Fano resonances generally occur in the course of excitation of discrete quantum states embedded in and coupled to a continuum [36–38, 210]. The cross section of atomic Fano resonances is very well characterized by numerous experiments and their spectral phase [134, 172, 176] as well as their temporal formation [59, 61, 211] was studied in great detail within theoretical works. Nevertheless, neither the spectral phase of the one-photon transition nor the temporal formation of the line shape has been measured for the simple prototypical system provided by many-electron atoms.

Within this chapter we focus on measurement protocols for the spectral phase of Fano resonances and discuss the temporal formation of the line shape in the next chapter, Chap. 6. We will briefly review the theoretical underpinning of Fano resonances before introducing two independent methods to measure the spectral phase of the doubly excited states in helium. In a short digression at the end of this chapter we show a joint theoretical and experimental study measuring the modulated two-photon transition phase in argon for the case of intermediate resonance states confirming and extending previous results [52–55, 188].

5.1. Fano resonances

Characteristic asymmetric absorption line shapes have first been discovered in noble gases [36, 212]. The asymmetry of the lines was explained by Ugo Fano [37, 38, 210] as signature of metastable states within the ionization spectrum. Within his approach the full Hamiltonian is decomposed into two parts: $H = H_0 + V_{CI}$. The first one is the unperturbed component H_0 which features the groundstate $|0\rangle$, continuum states $|\varepsilon\rangle$, and one (or more) bound states $|a\rangle$ embedded into the continuum. The second component is the “configuration interaction” V_{CI} which couples the bound state to the adjacent continuum states:

$$\langle 0 | H_0 | 0 \rangle = E_0 \tag{5.1}$$

$$\langle a | H_0 | a \rangle = E_a \tag{5.2}$$

$$\langle \varepsilon | H_0 | \varepsilon \rangle = \varepsilon \tag{5.3}$$

$$\langle a | V_{CI} | \varepsilon \rangle = \langle \varepsilon | V_{CI} | a \rangle^* = V_{a\varepsilon}. \tag{5.4}$$

All eigenstates of H_0 are orthogonal to each other and normalized $\langle 0|0\rangle = 1$, $\langle a|a\rangle = 1$, $\langle a|0\rangle = 0$, $\langle \varepsilon|\varepsilon'\rangle = \delta(\varepsilon - \varepsilon')$. The qualitative effect of the ‘‘configuration interaction’’, i.e. the coupling between discrete and continuum states, is that the exact eigenstate will be a superposition of $|a\rangle$ and continuum eigenstates $|\varepsilon\rangle$. A quantitative description amounts to solving the time-independent Schrödinger equation

$$H|\psi_E\rangle = E|\psi_E\rangle, \quad (5.5)$$

where E is the exact energy of the new eigenstate and

$$|\psi_E\rangle = b_E|a\rangle + \int |\varepsilon\rangle c_{\varepsilon,E} d\varepsilon. \quad (5.6)$$

The solution for the new eigenstate $|\psi_E\rangle$ is given by

$$|\psi_E\rangle = \frac{V_{aE}}{E - E_R(E)} |\tilde{a}\rangle + \frac{E - \tilde{E}_R(E)}{E - E_R(E)} |E\rangle. \quad (5.7)$$

$\tilde{E}_R(E) = \text{Re}[E_R(E)]$ is the real part of the complex resonance energy

$$E_R(E) = E_a + \Delta_a(E) - i\frac{\Gamma_a(E)}{2}, \quad (5.8)$$

with the coupling induced energy shift $\Delta_a(E) = P \int \frac{V_{a\varepsilon}V_{\varepsilon a}}{E - \varepsilon} d\varepsilon$ and the resonance width $\Gamma_a(E) = 2\pi |V_{aE}|^2$. The dressed resonance state $|\tilde{a}\rangle$ is written in the following way

$$|\tilde{a}\rangle = |a\rangle + P \int d\varepsilon |\varepsilon\rangle \frac{V_{\varepsilon a}}{E - \varepsilon}. \quad (5.9)$$

The eigenfunction $|\psi_E\rangle$ [Eq. (5.7)] can be conveniently written as

$$|\psi_E\rangle = |E\rangle \frac{\epsilon}{\epsilon + i} + |\tilde{a}\rangle \frac{1}{\pi V_{Ea}} \frac{1}{\epsilon + i}, \quad (5.10)$$

where $\epsilon(E)$ is the rescaled energy

$$\epsilon(E) = \frac{E - \tilde{E}_R(E)}{\Gamma_a(E)/2}. \quad (5.11)$$

Both, the shifted resonance energy $\tilde{E}_R(E)$ and the width $\Gamma_a(E)$ depend explicitly on energy. Assuming that \tilde{E}_R and Γ_a are slowly varying close to the resonance energy their value is commonly approximated with the value at $E = E_a$.

We can now calculate the photoabsorption cross section from the groundstate $|0\rangle$ to the new continuum states $|\psi_E\rangle$ with the dipole operator $\hat{\mathcal{O}} = \hat{n} \cdot \hat{\mathbf{p}}$

$$\sigma_E = \frac{4\pi^2}{c\omega_\gamma} \left| \langle \psi_E | \hat{\mathcal{O}} | 0 \rangle \right|^2, \quad (5.12)$$

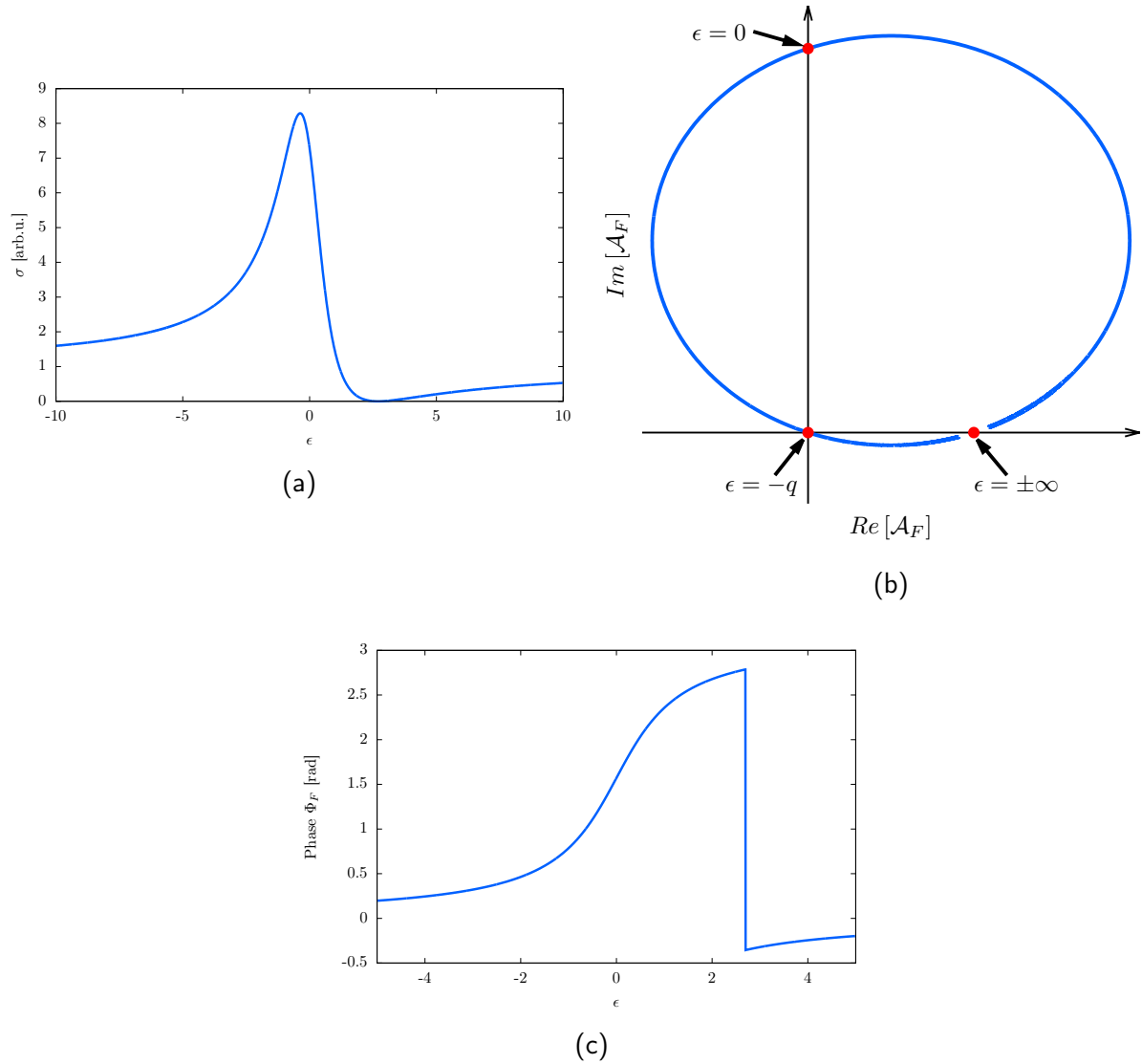


Figure 5.1.: (a) Cross section according to Eq. (5.16) for $q = -2.7$ to mimic the He(2s2p) resonance. (b) Trajectory of the Fano amplitude \mathcal{A}_F [Eq. (5.14)] in the complex plane. (c) Phase Φ_F [Eq. (5.17)] of the Fano amplitude \mathcal{A}_F as function of the rescaled energy ϵ .

where c is the speed of light, ω_γ is the frequency of the incident photon and \hat{n} is the polarization vector of the photon. The transition matrix element is given by

$$\begin{aligned}\langle 0 | \hat{\mathcal{O}} | \psi_E \rangle &= \mathcal{O}_{0E} \frac{\epsilon}{\epsilon + i} + \frac{\mathcal{O}_{0\tilde{a}}}{\pi V_{Ea}} \frac{1}{\epsilon + i} \\ &= \mathcal{O}_{0E} \frac{\epsilon + q}{\epsilon + i} = \mathcal{O}_{0E} \mathcal{A}_F,\end{aligned}\quad (5.13)$$

with $\mathcal{O}_{0\tilde{a}} = \langle 0 | \hat{\mathcal{O}} | \tilde{a} \rangle$, $\mathcal{O}_{0E} = \langle 0 | \hat{\mathcal{O}} | E \rangle$ and defining the Fano amplitude \mathcal{A}_F as

$$\mathcal{A}_F = \frac{\epsilon + q}{\epsilon + i}.\quad (5.14)$$

In Eq. (5.14) q is the Fano parameter

$$q = \frac{\mathcal{O}_{0\tilde{a}}}{\pi V_{Ea} \mathcal{O}_{0E}}.\quad (5.15)$$

If the Fano resonance is excited by absorption of one photon the q parameter is real as all involved continuum phases cancel and the absorption process is time-reversal symmetric. Taking the absolute magnitude of the transition matrix element gives the well known Fano profile

$$\sigma_E = \sigma_{bg}(E) \frac{(\epsilon + q)^2}{\epsilon^2 + 1},\quad (5.16)$$

where $\sigma_{bg}(E) = \frac{4\pi^2}{c\omega_\gamma} |\mathcal{O}_{0E}|^2$ is the smoothly varying cross section of the non-resonant background. Eq. (5.16) clearly indicates that a resonance which is coupled to a continuum yields an asymmetric cross section with respect to the resonance energy $\epsilon = 0$. The cross section vanishes for $\epsilon = -q$ [see Fig. 5.1a, where we use $q = -2.7$ to mimic the 2s2p resonance in helium [213]].

The Fano amplitude $\mathcal{A}_F(\epsilon)$ [Eq. (5.14)] forms a circle in the complex plane if the rescaled energy ϵ is scanned from $-\infty$ to $+\infty$ (Fig. 5.1b). At $\epsilon = -q$, \mathcal{A}_F changes from the second to the fourth quadrant of the complex plane, which is accompanied by a phase jump of π (Fig. 5.1c). Its phase is called Fano phase

$$\Phi_F(\epsilon) = \arg \{ \mathcal{A}_F(\epsilon) \} = \arg \left\{ \frac{\epsilon + q}{\epsilon + i} \right\}.\quad (5.17)$$

While conventional photoionization cross section measurements are not able to retrieve the phase variation of the photoionization amplitude, attosecond metrology, in principle, provides access to the phase information of electron wave packets. Recently, several RABBITT experiments [52–55] have taken a step towards measuring the phase of Fano resonances by tuning the harmonic energies such that they coincide with the resonance energy. By recording the phase energy resolved in adjacent sidebands [53, 54] or by finely varying the fundamental wavelength [52, 55], and thus the harmonic energies, these experiments have

notation	E_R (eV)	τ (fs)	q	Symmetry
$(2s)^2$	57.85	5.3	-	$^1S^e$
$(2p)^2$	59.91	10.2	-	$^1D^e$
$(2s2p)$	60.15	17.5	-2.7	$^1P^o$
$(2p)^2$	62.09	112.2	-	$^1S^e$
$(2s3p)$	63.66	79.3	-2.5	$^1P^o$

Table 5.1.: List of doubly excited states in helium most frequently used in this thesis with their resonance energy E_R , lifetime τ , Fano q parameter, and their symmetry [213, 215–217]. The value of the q parameter is given only for resonances which can be accessed via one-photon transitions.

measured the phase variation caused by Fano resonances. Due to the two-photon transition the measured phase is not the one expected from Eq. (5.14) but a convolution with the IR bandwidth [172, 176]. This convolution leads to a broadening of the one-photon phase and reduces phase contrast [52, 53, 176].

We propose in the following two independent methods to directly measure the one-photon Fano phase Φ_F [Eq. (5.17)], which both rely on the interference of one- and two-photon transitions. The first method employs a RABBITT like scheme with an APT consisting of even and odd harmonics and analyzes the interference of one- and two-photon transitions in each band created by the APT, thereby accessing the Fano phase directly. The second method exploits the recent technological advance to generate bi-circular XUV combs [77, 78] to retrieve the one-photon phase holographically from the fully angle-resolved photoelectron spectrum obtained from a single time delay measurement.

5.1.1. Fano resonances in atoms

Doubly excited states in helium

Fano resonances in helium are called doubly excited states¹⁵. In this thesis they serve as prototypical cases to study the spectral phase and the time-dependent build-up of the Fano profile [Chap. 6]. Also the coupling between different auto-ionizing states can be studied [Chap. 7], which is a long standing problem within atomic theory [63, 64, 66, 67, 69, 147, 214]. In Tab. 5.1 we list the energetically lowest lying and most prominent Fano resonances in helium in the $^1S^e$, $^1P^o$ and $^1D^e$ symmetry with their associated parameters, which we will refer to in this thesis.

¹⁵ In the first attempts to classify Fano resonances in helium independent particle models were used where the $2s2p$ resonance was described as superposition of the “doubly excited” $|2s2p\rangle$ and $|2p2s\rangle$ states [212].

Multi-channel resonances in argon

The second system where we will consider resonances is atomic argon. An important difference to helium is that argon comprises multi-channel resonances as compared to single channel resonances, see e.g. [52, 134] for a detailed treatment. The lowest energetic $3s^{-1}np$ resonances are created by ionization of an electron from the $3p$ shell and hence the outgoing electron has either angular momentum $\ell = 0$ or $\ell = 2$. Neither of the two electron angular momentum channels can be fully characterized by a Fano-amplitude [Eq. (5.14)] due to interchannel coupling. Close to the resonance however, it is possible to create a resonant channel by a unitary transformation [52, 134]. Coupling the two angular momentum channels $|\ell = 0, 2\rangle$, a resonant channel $|R\rangle$ and a non-resonant channel $|N\rangle$ can be formed

$$|R\rangle = |\ell = 0\rangle C_{s,R} + |\ell = 2\rangle C_{d,R}, \quad (5.18)$$

$$|N\rangle = |\ell = 0\rangle C_{s,N} + |\ell = 2\rangle C_{d,N}, \quad (5.19)$$

where $C_{s,R}$, $C_{d,R}$, $C_{s,N}$ and $C_{d,N}$ are energy-dependent coefficients. The resonant channel $|R\rangle$ exhibits the same phase and amplitude variation as a single channel resonance and the decoupled channel $|N\rangle$ shows no rapid phase variation close the resonance energy. The one-photon transition amplitude from the groundstate $|0\rangle$ to the final state $|\psi_E\rangle$ can then be written as

$$\langle 0 | \hat{O} | \psi_E \rangle = C_1 + C_2 \frac{q_a + \epsilon}{\epsilon + i}, \quad (5.20)$$

where C_1 and C_2 are background transition amplitudes for the non-resonant $|N\rangle$ and resonant $|R\rangle$ channel, respectively [52], and q_a is the Fano parameter of the considered resonance.

This parametrization is, of course, equivalent to the original formulation by Fano [38, 210] for the interaction of one resonant state with multiple continua where the cross section is given by

$$\sigma(\epsilon) = \sigma_a \frac{(q_a + \epsilon)^2}{\epsilon^2 + 1} + \sigma_b \quad (5.21)$$

with σ_a and σ_b being the (background) cross sections corresponding to the continuum which interacts, or does not interact with the resonant state, respectively. The prominent $3s^{-1}4p$ resonance in argon, which we will study in detail in Sec. 5.3 has a resonance energy of 26.60eV, a width of 0.080eV and a q -parameter of -0.286 [218, 219].

5.2. Direct measurement of the one-photon Fano phase

As shown in chapter 4, RABBITT is a powerful method to retrieve photoionization time delays of electronic wave packets far away from resonances [27, 186–188, 196, 220] and a powerful tool to characterize the spectral phase and duration of APTs [25, 157, 171]. If the

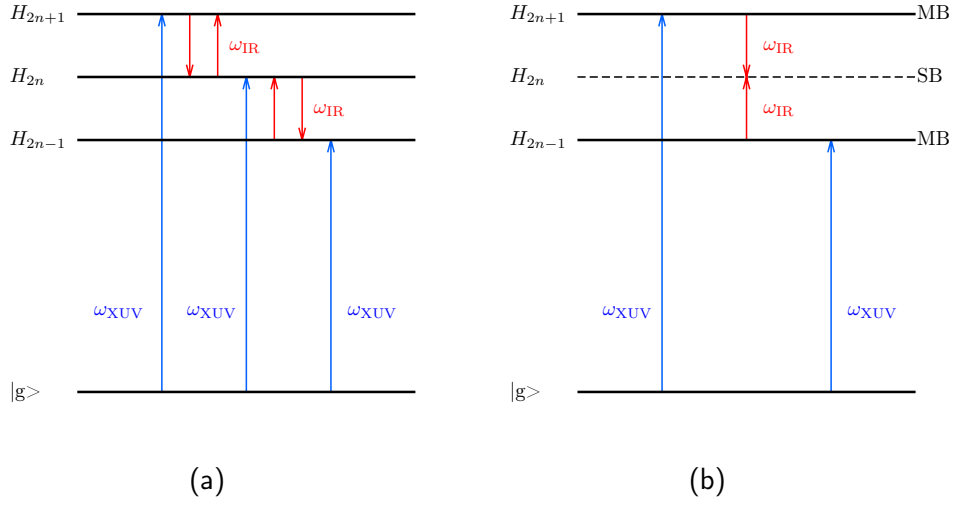


Figure 5.2.: (a) Sketch of the RABBITT with even and odd harmonics scheme, which induces an ω_{IR} beating in the asymmetry \mathcal{C} of every harmonic. (b) Sketch of the conventional RABBITT scheme which induces a $2\omega_{\text{IR}}$ within the angle-integrated photoelectron spectrum of each SB.

intermediate or final state is close to a resonance, however, the retrieved phase can not be directly related to the scattering time delay probed in the structureless continuum. Rather the phase of the sideband oscillation is given by a convolution of the sharp variation caused by the resonance with the IR mediated second order transition [52–54, 172, 176]. Thereby the characteristic phase jump expected in the one-photon amplitude close to a resonance, Fig. 5.1c, is smeared out, where the strength of this smearing is controlled by the spectral profile of the IR pulse.

To overcome this limitation we, first, present a scheme similar to RABBITT where the APT now consists not only of odd, but of both even and odd harmonics. Second, we propose the circular holographic ionization phase (CHIP) meter, which exploits a bi-circular APT to retrieve relative phase differences from the azimuthal photoelectron distribution without the need to perform a time-delay scan.

5.2.1. RABBITT with even and odd harmonics

Basic principles of RABBITT with even and odd harmonics

Typical APTs used within the RABBITT technique are produced by focusing a strong single-color laser pulse with duration < 100 fs into a gas target and the APT is generated via HHG [3, 4, 6, 9–11]. If the target is inversion symmetric the APT consists only of odd harmonics of the fundamental field. The inversion symmetry can, however, be broken easily by, e.g., using a single cycle IR pulse [153] or by focusing the fundamental together

with its second harmonic onto the target, which, in turn, leads to the generation of an APT consisting of even and odd harmonics [165, 197, 221]. Using such an APT together with a weak replica of the fundamental field leads to a mixture of energy-degenerate even and odd parity states in the continuum. The ionized electron wave packet is formed by the interference of one- and two-photon transitions leading to an asymmetry in the electron emission along the direction of the polarization vector [197, 222–224]. A pioneering experiment [197] showed that the asymmetry

$$\mathcal{C}(E, \tau) = P_{up}(E, \tau) - P_{down}(E, \tau) = \int_0^{2\pi} d\Omega P(E, \tau, \Omega) - \int_{2\pi}^{4\pi} d\Omega P(E, \tau, \Omega) \quad (5.22)$$

of the photoelectron spectrum shows a beating with the frequency of the fundamental field ω_{IR} ,¹⁶ with Ω being the solid angle. The beating of \mathcal{C} is caused by the interference of the direct XUV one-photon amplitude $\mathcal{A}_{E \leftarrow i}^{(1)}$ with the two-photon amplitude to the same final energy E via absorption of the energetically higher (lower) XUV photon and subsequent emission (absorption) of an additional IR photon $\mathcal{A}_{E \leftarrow E \pm \omega_{IR} \leftarrow i}^{(2)}$

$$\begin{aligned} \psi(E, \tau) &= \mathcal{A}_{E \leftarrow i}^{(1)} + \mathcal{A}_{E \leftarrow E + \omega_{IR} \leftarrow i}^{(2)} e^{-i\omega_{IR}\tau} + \mathcal{A}_{E \leftarrow E - \omega_{IR} \leftarrow i}^{(2)} e^{i\omega_{IR}\tau} \\ &= \sum_{L=\lambda \pm 1} \sum_{\lambda} \left| \mathcal{A}_{E \leftarrow i, \lambda}^{(1)} \right| e^{i\phi_{\lambda}^{(1)}(E)} Y_{\lambda}^0(\theta) \\ &\quad + \left| \mathcal{A}_{E, L \leftarrow E + \omega_{IR}, \lambda \leftarrow i}^{(2)} \right| e^{i[\phi_{\lambda, L}^{(2-)}(E) - \omega_{IR}\tau]} Y_L^0(\theta) \\ &\quad + \left| \mathcal{A}_{E, L \leftarrow E - \omega_{IR}, \lambda \leftarrow i}^{(2)} \right| e^{i[\phi_{\lambda, L}^{(2+)}(E) + \omega_{IR}\tau]} Y_L^0(\theta) \end{aligned} \quad (5.23)$$

as depicted in Fig. 5.2a. $\phi_{\lambda}^{(1)}(E)$ is the one-photon phase acquired by the XUV absorption to a state with angular momentum λ and $\phi_{\lambda, L}^{(2\pm)}(E)$ is the two-photon phase imprinted onto the wavepacket by the two photon-process where one IR photon is absorbed (emitted) together with the absorption of the XUV photon. L corresponds to the final angular momentum after the two-photon transition. For simplicity we assumed the fields to be linearly polarized along \hat{z} in Eq. (5.23).

Calculating the asymmetry \mathcal{C} [Eq. (5.22)] from Eq. (5.23) we find

$$\begin{aligned} \mathcal{C} &= \sum_{L=\lambda \pm 1} \sum_{\lambda, \lambda'} C_{L, \lambda} \\ &\quad \times \left\{ \left| \mathcal{A}_{E \leftarrow i, \lambda}^{(1)} \right| \left| \mathcal{A}_{E, L \leftarrow E + \omega_{IR}, \lambda' \leftarrow i}^{(2)} \right| \cos \left[\omega_{IR}\tau + \left(\phi_{\lambda}^{(1)} - \phi_{\lambda', L}^{(2-)} \right) \right] \right. \\ &\quad \left. + \left| \mathcal{A}_{E \leftarrow i, \lambda}^{(1)} \right| \left| \mathcal{A}_{E, L \leftarrow E - \omega_{IR}, \lambda' \leftarrow i}^{(2)} \right| \cos \left[-\omega_{IR}\tau + \left(\phi_{\lambda}^{(1)} - \phi_{\lambda', L}^{(2+)} \right) \right] \right\}, \end{aligned} \quad (5.24)$$

where the angular momentum dependent coefficient $C_{L, \lambda}$ is given by

$$C_{L, \lambda} = 8\pi \int_0^{\pi/2} d\theta \sin(\theta) Y_L^0(\theta) Y_{\lambda}^0(\theta). \quad (5.25)$$

¹⁶ Very similar such a beating has also been observed for above-threshold ionization with a two-color (fundamental and second harmonic) laser field [166].

The sum in Eq. (5.24) runs over all allowed intermediate angular momenta for λ and λ' . A derivation of Eq. (5.24) can be found in App. D.1.

Although the constant terms and terms with oscillation frequency of $2\omega_{\text{IR}}$ disappear in the asymmetry \mathcal{C} they would be present in the angle-integrated spectrum. Conversely, the terms oscillating with frequency ω_{IR} disappear in the angle-integrated spectrum.

While RABBITT with even and odd harmonics appears to be conceptually very similar to RABBITT there are important differences. The first big difference is that the phase of the oscillation is not the phase difference between two two-photon phases but between a one-photon and two-photon phase which, in general, have different angular momenta. Second, in traditional RABBITT two paths interfere at each considered sideband [Fig. 5.2b], whereas in the RABBITT with even and odd harmonics technique to same order in perturbation theory three paths interfere within each harmonic [Fig. 5.2a] giving rise to the superposition of a $\cos(\omega_{\text{IR}}\tau)$ and a $\cos(-\omega_{\text{IR}}\tau)$ term [Eq. (5.24)]. To be more precise Eq. (5.24) can be rewritten as

$$\begin{aligned}\mathcal{C} &= A_1 \cos(\omega_{\text{IR}}\tau + \Delta\phi_1) + A_2 \cos(-\omega_{\text{IR}}\tau + \Delta\phi_2) \\ &= A_3 \cos(\omega_{\text{IR}}\tau + \Delta\phi_3).\end{aligned}\tag{5.26}$$

The coefficients A_1, A_2, A_3 and the phase $\Delta\phi_1, \Delta\phi_2, \Delta\phi_3$ depend on the magnitude of the two-photon amplitudes $\left| \mathcal{A}_{E, L \leftarrow E \pm \omega_{\text{IR}}, \lambda' \leftarrow i}^{(2)} \right|$ and the phase differences $\phi_{\lambda}^{(1)} - \phi_{\lambda', L}^{(2\pm)}$ in a non-linear fashion via trigonometric relations. This complicates the interpretation of the retrieved phases as we will see in this section. Furthermore, there is no distinction between mainbands and sidebands anymore, as the asymmetry of every harmonic can be used to retrieve spectral information. This effectively doubles the spectral resolution in this technique compared to conventional RABBITT, since phase information can be retrieved from all harmonics and not just from the SBs.

In addition, the spectral contrast is improved compared to RABBITT, since the oscillation of \mathcal{C} in RABBITT with even and odd harmonics is caused by a three-photon process (two XUV photons and one IR photon), while in conventional RABBITT the oscillation of the angle-integrated spectrum is caused by a four-photon process (two XUV photons and two IR photons). Hence the oscillation amplitude of the asymmetry scales with the amplitude of the IR field in contrast to the intensity of the IR in conventional RABBITT. RABBITT with even and odd harmonics is very similar to a recently proposed variant of RABBITT where an APT formed of odd harmonics is dressed with the second harmonic of the fundamental field [225]. Schematically, this leads to the same interference scheme as for RABBITT with even and odd harmonics [Fig. 5.2a], however the spectral resolution is not improved over traditional RABBITT.

Within this section we will investigate RABBITT with even and odd harmonics and show how it can be used to retrieve one-photon ionization phases close to resonant transitions in the continuum. We will discuss explicitly how the interference of the oscillations with $\cos(\omega_{\text{IR}}\tau)$ and $\cos(-\omega_{\text{IR}}\tau)$ [Eq. (5.26)] complicates the retrieval of the phase of the electron wave packet and present a way to circumvent this problem in the following section, Sec. 5.2.2.

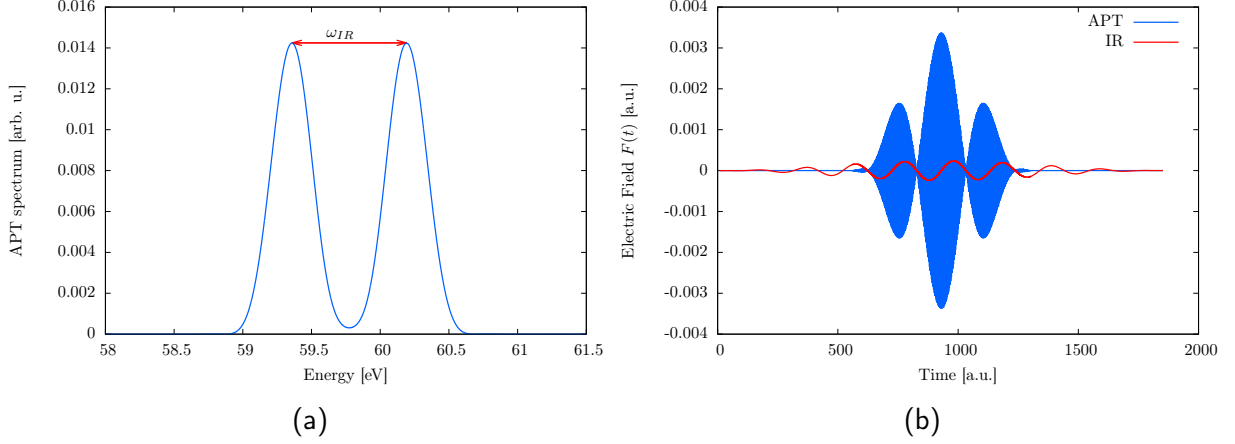


Figure 5.3.: (a) Energy spectrum of the APT used for the ionization of helium with just two adjacent harmonics. (b) Electric field as a function of time for time delay $\tau = 0$ between the IR and the APT.

RABBITT with even and odd harmonics for an APT with two harmonics

To illustrate the potential of this new spectroscopic technique we retrieve the Fano phase for the prototypical system of atomic helium with an APT consisting just of two neighboring harmonics, where the higher energetic harmonic is centered exactly at the $2s2p$ resonance energy in helium ($E_{2s2p} = 60.15$ eV) [Tab. 5.1], see Fig. 5.3a. Fig. 5.3b shows the electric fields for time-delay $\tau = 0$ between the APT and the IR. The numerical parameters are given in J.2.4.

Calculating the asymmetry \mathcal{C} for this case from [Eq. (5.24)] we obtain

$$\begin{aligned}
 \mathcal{C}(E, \tau) &= B_1 \cos(-\omega_{\text{IR}}\tau + \phi_p^{(1)} - \phi_{p,s}^{(2+)}) + B_2 \cos(-\omega_{\text{IR}}\tau + \phi_p^{(1)} - \phi_{p,d}^{(2+)}) \\
 &= B_1 \cos(-\omega_{\text{IR}}\tau + \Phi_F + \frac{\pi}{2}) + B_2 \cos(-\omega_{\text{IR}}\tau + \Phi_F + \frac{\pi}{2}) \\
 &= B_3 \sin(-\omega_{\text{IR}}\tau + \Phi_F),
 \end{aligned} \tag{5.27}$$

with B_1, B_2, B_3 being coefficients depending on the one- and two-photon amplitudes $\mathcal{A}^{(1)}$ and $\mathcal{A}^{(2)}$. In deriving Eq. (5.27) we neglected all contributions from the continuum-continuum phases $\phi_{cc,\lambda L}^\pm$ and the non-resonant one-photon scattering phase of the two-photon transition, since they are all much smaller compared to the Fano phase Φ_F of the resonant one-photon transition.

Performing a time-delay scan between the APT and the IR we observe an oscillation of the photoelectron emission asymmetry \mathcal{C} [Eq. (5.22)] with ω_{IR} [197, 223], see Fig. 5.4a. The asymmetry \mathcal{C} shows a pronounced variation of the phase of the oscillation as a function of the photoelectron energy. To extract the phase of this oscillation we fit $\mathcal{C}(E, \tau)$ with $A \sin(-\omega_{\text{IR}}\tau + \phi)$ for every energy and extract the phase ϕ . Comparing the retrieved phase to the numerically exact phase of the one-photon transition obtained by exterior-complex

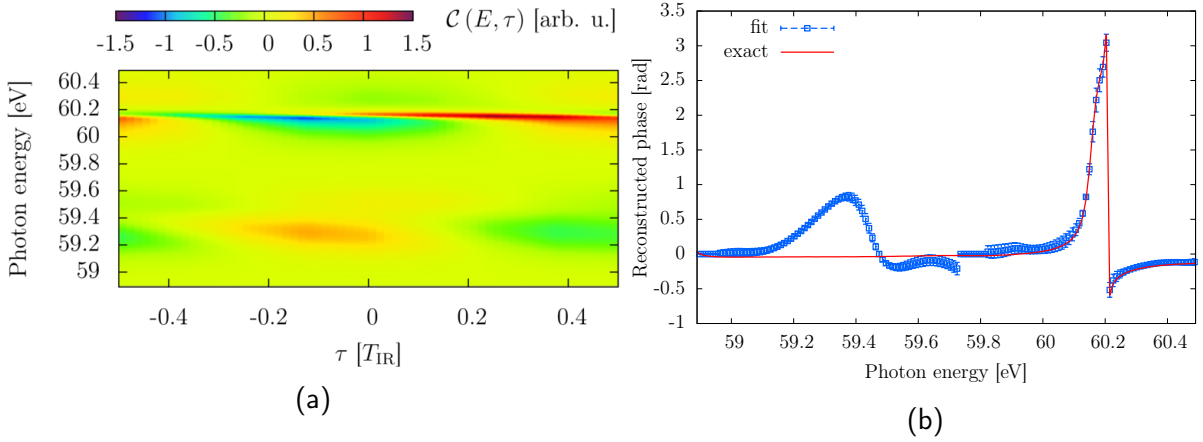


Figure 5.4.: (a) Asymmetry \mathcal{C} as function of the photon energy and the time delay τ . (b) Reconstructed phase of the ω_{IR} beating of $\mathcal{C}(E, \tau)$ employing an energy resolved fit with $\sin(-\omega_{\text{IR}}\tau + \phi)$ (blue points), compared to the “exact” one-phase retrieved from the calculation (red line).

scaling [60] we find near perfect agreement as expected from Eq. (5.27) [Fig. 5.4b]. The phase variation visible within the lower harmonic is in line with the recently measured RABBITT phase with intermediate resonant states [52–54].

This simple example shows that RABBITT with even and odd harmonics is a powerful method that can be used to measure one- and two-photon ionization phases involving resonant states. However, to exploit this method in experiments we need to verify that it also works in the generic case, where not only two, but many more harmonics are present, which will show in the following.

RABBITT with even and odd harmonics using a realistic APT and performing wavelength scanning

We thus investigate the RABBITT with even and odd harmonics scheme with a more realistic APT spanning from the 67th to the 75th harmonic, see Fig. 5.5a for the used pulse profile at $\lambda_{\text{IR}} = 1464\text{nm}$. The spectral phase of every harmonic was chosen to be 0. To follow the common experimental procedure used in RABBITT, we do not retrieve the phase for every energy point but integrate every harmonic over an energy region of ≈ 0.6 eV around its center and retrieve just one phase for each harmonic [Fig. 3.3b]. To retrieve the spectral phase variation we smoothly vary the wavelength of the fundamental field (and thus the energy of the harmonics of the APT) which allows the retrieval of ionization phases over a large spectral range [52, 55].

This procedure requires very good control of the fundamental wavelength, but poses less stringent criteria on the necessary energy resolution of the photoelectron detector. The fundamental field has a FWHM duration of approximately 22 fs and the APT duration

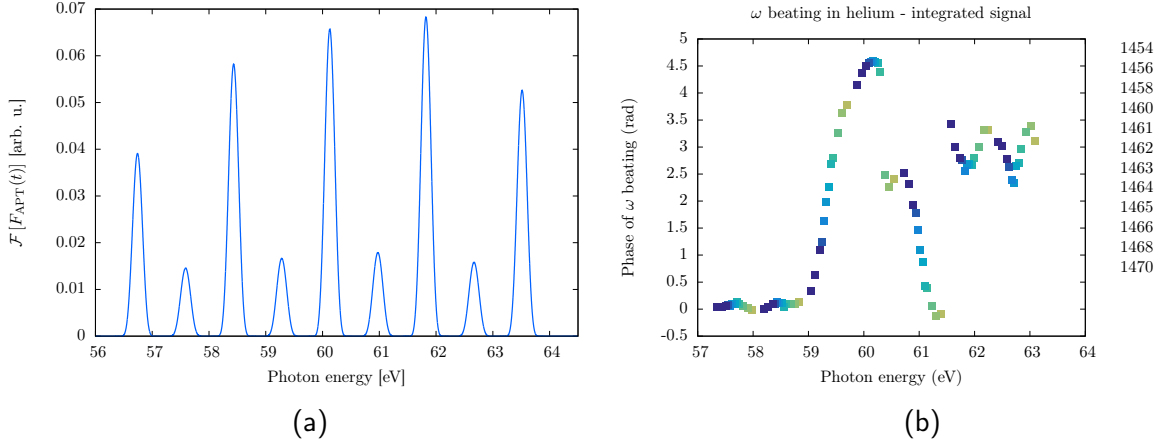


Figure 5.5.: (a) Spectral profile of the APT for $\lambda_{\text{IR}} = 1464\text{nm}$. (b) Retrieved phase of the ω_{IR} beating of the asymmetry \mathcal{C} integrated over the harmonic width for different fundamental wavelengths.

is roughly 14.5 fs, resulting in spectrally broad harmonics, see Fig. 5.5a. We smoothly vary the fundamental wavelength λ_{IR} from 1456nm to 1470nm, see J.2.5 for the numerical parameters used. For $\lambda_{\text{IR}} = 1464\text{nm}$ the 71st harmonic is almost resonant with the 2s2p resonance in helium.

The retrieved phase landscape for this realistic APT clearly does not resemble the results we observe for just two harmonics, compare Figs. 5.5b, 5.4b. For the realistic APT the retrieved phase varies drastically across the investigated energy region. The phase variation is almost continuous from 57 eV up to 60.2 eV, where it jumps by π . This jump can unambiguously be attributed to the 2s2p resonance. The position of the phase jump is shifted from the expected position due to the energy integration within each harmonic. Close to 61.5 eV the retrieved phase exhibits another jump by π . We can, however, not attribute this phase jump to a resonance as there is no resonance in this energy region. Even higher up in energy two pronounced continuous phase variations are observed which most likely are caused by the next resonances in the $^2\text{S}^e(62.1\text{eV})$ and in the $^2\text{P}^o(63.7\text{eV})$ symmetry, see Tab. 5.1

On the left and right hand side of the 2s2p resonance we observe strong, almost linear, phase variations with positive and negative slope, respectively. This is similar to results obtained with RABBITT [52–54, 176] for the retrieved phases in the sidebands neighboring a resonant harmonic. Such a modulation can also be seen in the nonresonant harmonic in Fig. 5.4b. Interestingly however, the observed phase variation in Fig. 5.5b is larger than for just two harmonics (Fig. 5.4b) and the measured two-photon phase from RABBITT [53, 54].

The reason for the large discrepancy with the results shown in the previous section is that we observe a three-path interference in every harmonic leading to a superposition of two independent oscillations considerably altering the results [Eq. (5.26)]. As example we

consider the extreme case where the two oscillations in Eq. (5.26) have equal amplitude, i.e. $B_1 = B_2$. In this case the asymmetry in the resonant harmonic is given by

$$\begin{aligned} \mathcal{C}(E, \tau) &= B_1 \cos(-\omega_{\text{IR}}\tau + \Delta_1) + B_1 \cos(\omega_{\text{IR}}\tau + \Delta_2) \\ &= 2B_1 \cos\left(\frac{\Delta_2 + \Delta_1}{2}\right) \cos\left(\omega_{\text{IR}}\tau + \frac{\Delta_2 - \Delta_1}{2}\right). \end{aligned} \quad (5.28)$$

Neglecting further all contributions of $\phi_{cc,\lambda L}^\pm$ and all nonresonant scattering phases (η_λ) the two phases Δ_1 and Δ_2 are identical, i.e. $\Delta_1 = \Delta_2 = \Phi_F + \pi/2$, and Eq. (5.28) simplifies further

$$\begin{aligned} \mathcal{C}(E, \tau) &= 2B_1 \cos\left(\Phi_F + \frac{\pi}{2}\right) \cos(\omega_{\text{IR}}\tau) \\ &= -2B_1 \sin(\Phi_F) \cos(\omega_{\text{IR}}\tau) \end{aligned} \quad (5.29)$$

In this case, the phase of the oscillation does not vary with energy. Instead the amplitude of the oscillation is modulated and changes sign at the resonance position. To reconstruct the Fano phase under these conditions it is necessary to measure the amplitude variation in addition to the phase variation, which is a severe complication for experiment.

Even though the analysis shown above relies on many assumptions we can conclude that the extracted phase does not necessarily coincide with the difference between the one- and two-photon phase, but modified in a nonlinear way. A systematic study of the retrieved phase as function of the amplitude of the harmonics neighboring the resonance is given in App. D.2.

5.2.2. Circular holographic ionization phase meter (CHIP)

Having shown in Sec. 5.2.1 that the retrieval of resonant and non-resonant ionization phases from RABBITT with even and odd harmonics is complicated due to the three path interference at each harmonic [Fig. 5.2a], we propose in this section a different approach to retrieve resonant ionization phases. We present the circular holographic ionization phase meter (CHIP), a pump-probe protocol, based on a bi-circular APT, that allows to directly retrieve the energy-resolved phase of either the one- or two-photon ionization amplitudes without the need for a time-delay scan [56].

The first key aspect of this method is the holographic read-out of a rapidly varying ionization phase in one arm of the interferometer, e.g., in proximity of a Fano resonance, relative to a smooth or nearly constant reference phase of the second arm. The second key ingredient of CHIP is the use of a bi-circular APT in combination with a co- or counter-rotating IR pulse (Fig. 5.6 b). In CHIP the photoelectron phase is encoded in the photoemission angle instead of a time-delay scan of the signal beating as in streaking, RABBITT, or high-harmonic spectroscopy. The proposed scheme requires high-resolution measurement of the angular resolved photoelectron energy distribution as recorded by, e.g. COLTRIMS detection [226].

CHIP involves isolated pairs of consecutive circular harmonics $3n + k$ ($k = 1, 2$) of the

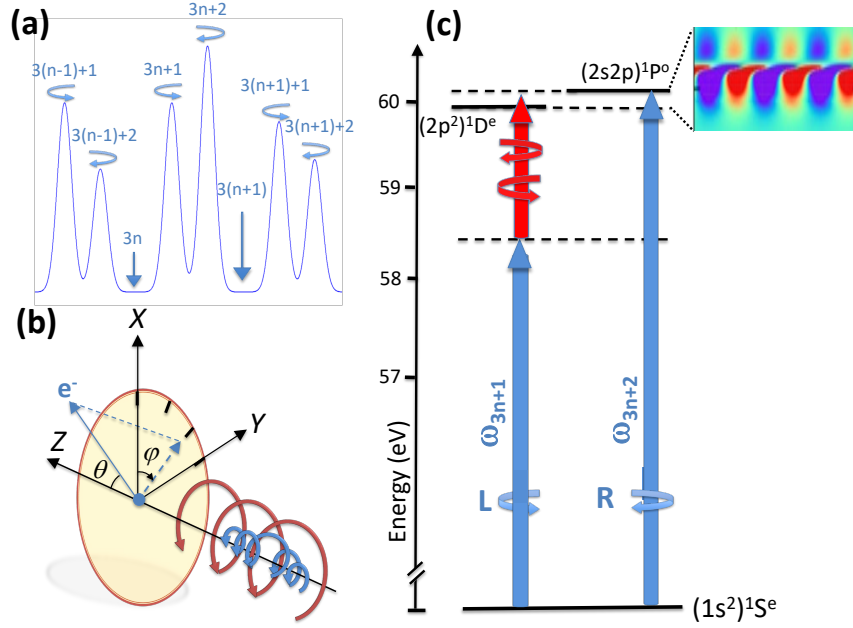


Figure 5.6.: (a) Typical spectrum of an APT generated by counter-rotating bichromatic fields, featuring isolated consecutive pairs of counter-rotating IR harmonics, $\omega_k = (3n + k) \omega_{\text{IR}}$, $k = 1, 2$ [77, 78]. (b) Geometry of the angularly resolved detection in CHIP. (c) Principle of CHIP (the IR probe is either co- or counter-rotating with the lower harmonic in the pair), and an example of photoelectron momentum distribution (inset) as a function of the emission angle (horizontal axis) and energy (vertical axis), for the co-rotating case with the upper harmonics populating the $(2s2p)^1P^o$ helium resonant state.

XUV APT (Fig. 5.6 a,b) with opposite helicity. Assuming, e.g., the helicity of the lower harmonic $3n + 1$ to be positive (or left-circularly polarized [LCP]) and the helicity of the upper harmonic $3n + 2$ to be negative (or right-circular [RCP]), the electric field for light propagating in positive \hat{z} direction is given by

$$\mathbf{F}^{(k)}(t) = F_0^{(k)} f(t) \begin{pmatrix} \cos(\omega_k t) \\ \nu_k \sin(\omega_k t) \\ 0 \end{pmatrix}, \quad (5.30)$$

where $f(t)$ is the pulse envelope, $F_0^{(k)}$ is the peak field strength, $\nu_k = (-1)^{k+1}$ is the light helicity and $\omega_k = (3n + k) \omega_{\text{IR}}$. The IR probe pulse can be chosen to be either co-rotating ($\nu_{\text{IR}} = +1$) or counter-rotating ($\nu_{\text{IR}} = -1$) with the lower harmonic ($k = 1$), allowing to control the interference between one- and two-photon amplitudes.

Employing *ab initio* simulations for helium, we demonstrate that the photoelectron angular distribution faithfully reproduces the energy dependence of the one-photon ionization amplitude of the atom near autoionizing resonances.

CHIP applied to doubly excited states in helium

One-photon ionization of helium from its ground-state by the upper harmonic ($k = 2$) creates a continuum wave at an energy $E = (3n + 2)\omega_{\text{IR}} - I_{p,1}$ with angular momentum quantum numbers $\ell = 1, m = -1$ [$Y_{\ell=1}^{m=-1}(\theta, \varphi)$]. The same energy can be reached via a two-photon absorption involving the lower harmonic ($k = 1$) and an IR photon. If the IR is co-rotating with the lower APT harmonic, the angular dependence of the continuum wave populated by the two-photon path is just $Y_2^2(\theta, \varphi)$. The interference between the one-photon and two-photon paths is proportional to $\left| a_{1-1}^{(1)} Y_1^{-1}(\theta, \varphi) + a_{22}^{(2)} Y_2^2(\theta, \varphi) \right|$, where $a_{\ell m}^{(1)}$ and $a_{\ell m}^{(2)}$ are the one-photon and two-photon amplitudes, respectively. This interference, therefore, depends on the azimuthal angle φ as $\cos(3\varphi - \Delta_{\text{LCP}})$, where Δ_{LCP} is the relative phase between the one- and the two-photon amplitude,

$$\Delta_{\text{LCP}}(E) = \delta^{(1)}(E) - \delta_{\text{LCP}}^{(2)}(E). \quad (5.31)$$

With a counter-rotating IR photon, the two-photon ionization populates a superposition of s and d waves with $m = 0$, corresponding to an angular dependence of $Y_0^0(\theta, \varphi)$ and $Y_2^0(\theta, \varphi)$. In this case the probability distribution

$$\left| a_{1-1}^{(1)} Y_1^{-1}(\theta, \varphi) + a_{00}^{(2)} Y_0^0(\theta, \varphi) + a_{20}^{(2)} Y_2^0(\theta, \varphi) \right|, \quad (5.32)$$

depends on φ as $\sim \cos(\varphi - \Delta_{\text{RCP}})$ ¹⁷. In CHIP, therefore, the interference between waves with $\ell = 0, 1, 2$, gives access to the ionization amplitudes and phases for dipole-forbidden or mixed-parity states. Thanks to the short duration of the APT, a single photoelectron spectrum is sufficiently broad to record the full excursion of the scattering phases across a resonance. The interference between two different paths to two different partial waves is key to the holographic mapping of a single ionization phase. If the phases of the two-photon transition $\mathcal{A}_{E,\ell m}^{(2)}$ are almost constant across a dipole-allowed resonance, for example, they can serve as holographic reference to measure a rapidly varying one-photon ionization phase $\arg[\mathcal{A}_{E,\ell m}^{(1)}]$ of the one-photon transition amplitude $\mathcal{A}_{E,\ell m}^{(1)}$.

We illustrate the capabilities of this concept with *ab initio* simulations of two prototypical examples (Fig. 5.6 c): the one-photon ionization phase near the dipole allowed doubly excited resonance $(2s2p)^1\text{P}^\circ$ and the ionization phase for the dipole-forbidden $(2p^2)^1\text{D}^\circ$ resonance of helium [see Tab. 5.1]. We employ an APT that comprises $3n + 1$ LCP and $3n + 2$ RCP harmonics of the fundamental wavelength $\lambda_{\text{IR}} = 783$ nm, with $n = 11, 12$, and 13 , as shown in Fig. 5.6 (b). The 38th harmonic is tuned to the optically allowed $(2s2p)^1\text{P}^\circ$ resonance. See App. J.2.6 for the numerical parameters. We explore a wide range of IR intensities, from $I_{\text{IR}} = 10^9$ W/cm², at which LOPT makes accurate predictions, to moderately strong fields $I_{\text{IR}} = 10^{11}$ W/cm², typical used in streaking settings. For the highest employed IR intensities the interference contrast is strongly enhanced albeit deviations from LOPT estimates appear.

¹⁷ For more details see App. E.1.

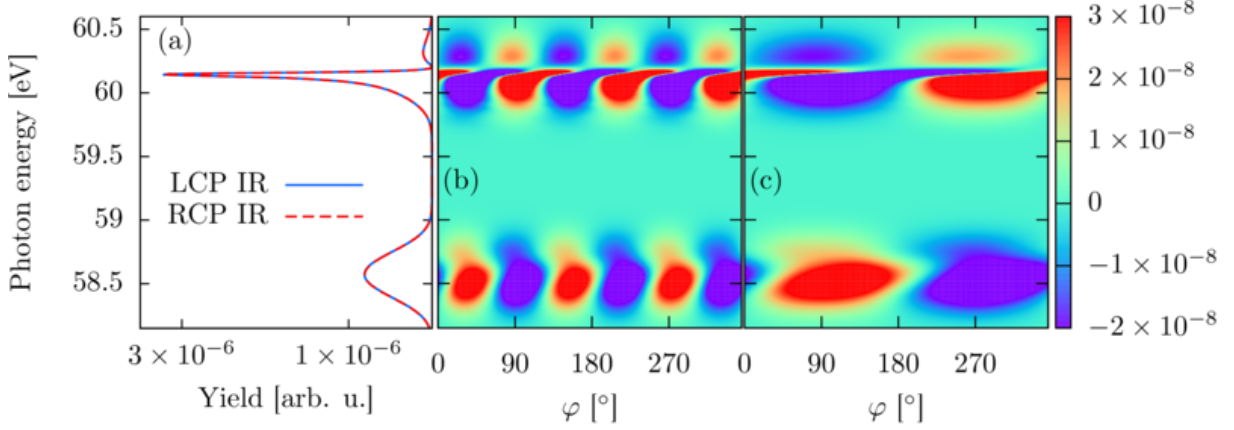


Figure 5.7.: Single ionization spectrum of atomic helium ionized by a bi-circular APT and a co- or counter-rotating IR pulse ($I_{\text{APT}} = 10^{11} \text{W/cm}^2$ and $5 \times 10^{11} \text{W/cm}^2$ for the even and odd harmonics, respectively, $I_{\text{IR}} = 10^9 \text{W/cm}^2$, $\tau_{\text{IR}} \approx 13 \text{fs}$, $\tau_{\text{APT}} \approx 5 \text{fs}$, $\theta = \pi/2$). (a) Spectrum at fixed azimuthal angle $\varphi = 0^\circ$ in the polarization plane $\theta = \pi/2$. Angular resolved photoemission spectrum with IR pulse (b) co-rotating with lower harmonic and (c) counter-rotating with the lower harmonic. A constant background was subtracted to enhance the contrast.

Whereas the photoelectron energy distributions for $\theta = \pi/2$, $\varphi = 0^\circ$ in the energy range between 58 and 60.5 eV are indistinguishable for the co- (LCP) and counter-rotating (RCP) IR pulses [Fig. 5.7a], their variations with φ are drastically different, featuring a $\cos(3\varphi - \Delta_{\text{LCP}})$ and a $\cos(\varphi - \Delta_{\text{RCP}})$ dependence (see Fig. 5.7b,c). At moderate IR intensities the angular-modulation fringes become clearly visible even without subtracting the average signal (Fig. 5.8) since their contrast increases linearly with the field strength (or $I_{\text{IR}}^{1/2}$). The angular-beating phase $\Delta(E) = \phi^{(1)}(E) - \phi^{(2)}(E)$, which contains the ionization phases, can be readily retrieved by Fourier analysis of the signal (Fig. 5.7b,c). The phase $\phi^{(1)}(E)$ across the $(2s2p)^1\text{P}^o$ resonance at $E = 60.15 \text{eV}$ (Fig. 5.9) exhibits the characteristic strong excursion with a discontinuous jump predicted by Fano's theory for resonant one-photon transitions [37, 38],

$$\phi^{(1)}(E) = \phi_{\text{bg}}^{(1)}(E) + \arg[(\epsilon + q)/(\epsilon + i)], \quad (5.33)$$

where $\phi_{\text{bg}}^{(1)}$ is the smooth background phase. As long as the reference phase $\phi^{(2)}(E)$ is approximately constant across the resonance, which is indeed the case here (Fig. 5.9), the angular-beating offset coincides with the ionization phase $\phi^{(1)}(E)$, up to an overall constant. Indeed, our simulations convincingly demonstrate that the Fano phase Φ_F of the optically allowed $(2s2p)^1\text{P}^o$ resonance can be directly retrieved from CHIP with a high degree of accuracy.

We turn now to the dipole forbidden resonance $(2p^2)^1\text{D}^e$ at $E = 59.91 \text{eV}$ which is simultaneously accessible within the bandwidth of the same harmonic of the ultrashort pulse (Fig. 5.6c). Here the two-photon transition involving the lower ($k = 1$) APT harmonic and the IR photon scans the resonance while the one-photon transition by the higher ($k = 2$)

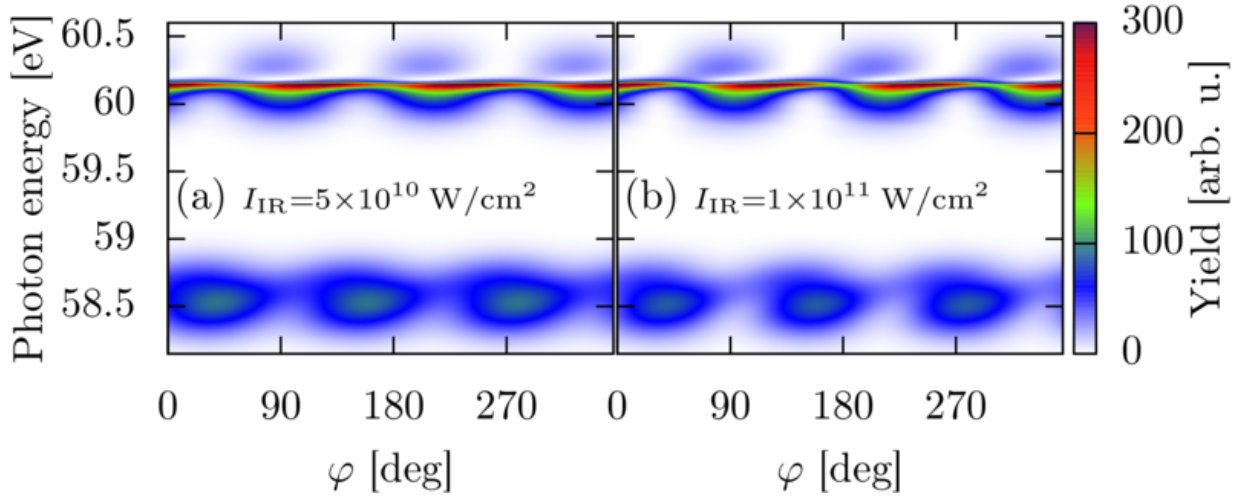


Figure 5.8.: Same as Fig. 5.7b but without background subtraction and (a) $I_{\text{IR}} = 5 \times 10^{10} \text{ W/cm}^2$, (b) $I_{\text{IR}} = 1 \times 10^{11} \text{ W/cm}^2$.

APT harmonic, far from the $(2s2p)^1\text{P}^o$ state, provides the nearly constant reference phase. In contrast to the one-photon resonance, we observe a pronounced dependence of the two-photon resonance phase on the IR polarization. For the co-rotating case, the two-photon ionization path exclusively populates $^1\text{D}^e$ states, whereas for the counter-rotating case both the resonant $\ell = 2$ and the non-resonant $\ell = 0$ states are populated, reducing the resonant contrast. For the dipole-forbidden resonance, the ionization path does not exhibit the same excursion as the one-photon resonant scattering phase [Eq. (5.17)]. This is because, in a two-photon process, the dipole transition to the final D resonant state $|1s, E, \ell = 2, m = 2\rangle$, proceeds by an intermediate P wave with outgoing character

$$\langle 1s, E, 2, 2 | \hat{T}^{(2)} | g \rangle = \langle 1s, E, 2, 2 | \hat{D}_1^1 \int dE' \frac{|1s, E', 1, 1\rangle \langle 1s, E', 1, 1 | \hat{D}_1^1 | g \rangle}{E - E' - \omega_{\text{IR}} + i\eta}, \quad (5.34)$$

which is not an eigenstate of the time-reversal operator and hence cannot be expressed as a purely real function [176]. In Eq. (5.34), \hat{D}_1^1 is the irreducible tensor component dipole operator for LCP. Consequently, the Fano q parameter for a resonance populated by a two-photon transition is inherently complex and the phase jump is blurred. Fitting the amplitude of the resonant ($\ell = 2, m = 2$) channel to $|(\epsilon + q)/(\epsilon + i)|^2$ (with $q \in \mathbb{C}$) yields $q \approx -0.07 + 0.99i$, inline with the analytical prediction $q = i$ [172] expected for long IR pulses. The two-photon continuum state in the counter-rotating case is a superposition of an s and a d wave, and hence it is possible to disentangle their contribution as they have a known dependence on θ . For example, since the d wave vanishes at the magic angle $\theta_m \approx 54.74^\circ$, i.e., $Y_2^0(\theta_m, \varphi) = 0$, CHIP at θ_m directly measures the $\ell = 0$ ionization phase relative to the one-photon reference.

In CHIP, the angular modulation is inherently and rigorously sinusoidal. Measurements

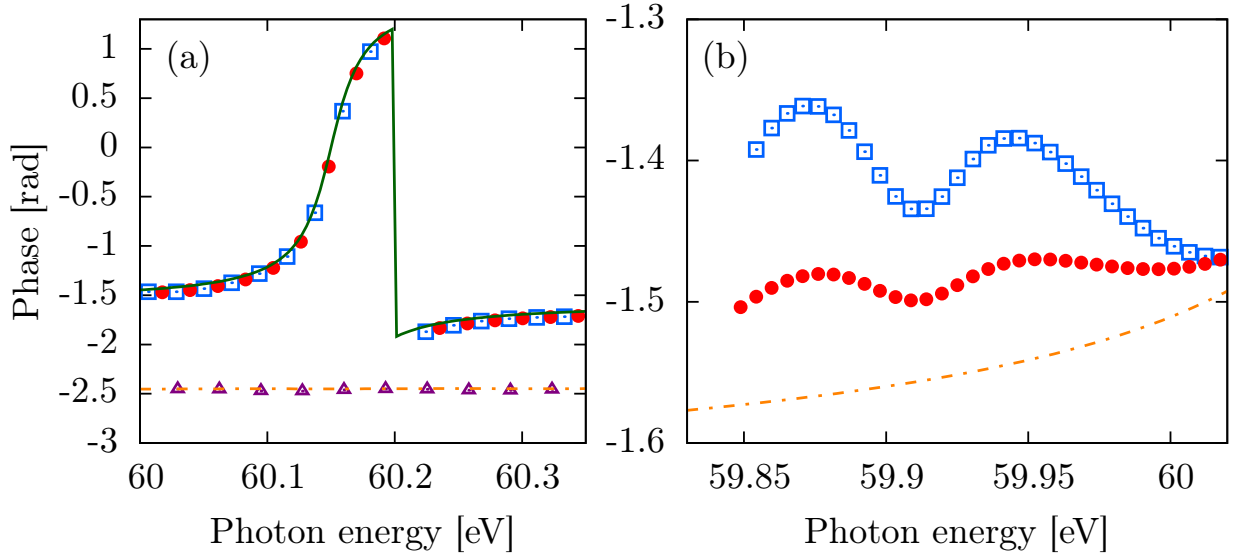


Figure 5.9.: Ionization phases near the doubly-excited state resonances (a) $(2s2p)^1P^o$ at $E = 60.15$ eV and (b) $(2p^2)^1D^e$ at $E = 59.91$ eV for an IR pulse either co-rotating (blue squares) or counter-rotating (red bullets) with the lower harmonic $(3n + 1)\omega_{\text{IR}}$. In (a) we show in addition the analytic prediction Eq. (5.17) (green solid line) for the phase jump near the $(2s2p)^1P^o$ resonance and the smooth two-photon reference phase $\phi^{(2)}$ for the s (orange dashed-dotted line) and d (purple triangles) partial waves separately. In (b) we also show the one-photon reference phase $\phi^{(1)}$ which originates from the p (orange dashed-dotted line) partial wave.

at only a few azimuthal angles (e.g., $\varphi = 15^\circ, 60^\circ, 170^\circ, 240^\circ$), therefore, are sufficient to completely characterize it [Fig. (5.10a)]. Furthermore, the ionization phases can be reconstructed with an energy resolution that is limited only by that of the spectrometer but not by the spectral width of the IR. To quantify the effect of the limited energy resolution on the extraction of ionization phases, we convolute the spectrum with instrumental resolutions of 20 meV and 50 meV width [Fig. (5.10a)]. At 20 meV the phase excursion of the narrow $(2s2p)^1P^o$ resonance is accurately reproduced, whereas at 50 meV the phase jump is significantly smoothed. The only main challenge in the implementation of CHIP, therefore, is to measure the angularly resolved photoelectron spectrum with a sufficiently high energy resolution. On the other hand, high-energy resolution is required only in the comparatively narrow width of a single harmonic, which can be easily achieved with a velocity-map imaging (VMI) detector in combination with tunable retardation plates [227]. Furthermore, while for the narrow $(2s2p)^1P^o$ resonance a high spectral resolution is required, for broader resonances (e.g. in argon or xenon), the requirements on the spectral resolution are less demanding and hence CHIP is ideally suited to reconstruct their phase. Finally, in the co-rotating configuration with a 3φ angular dependence the technique is insensitive to dipolar and quadrupolar distortions in the detection of the angular distribution due to, e.g., an imperfect beam alignment.

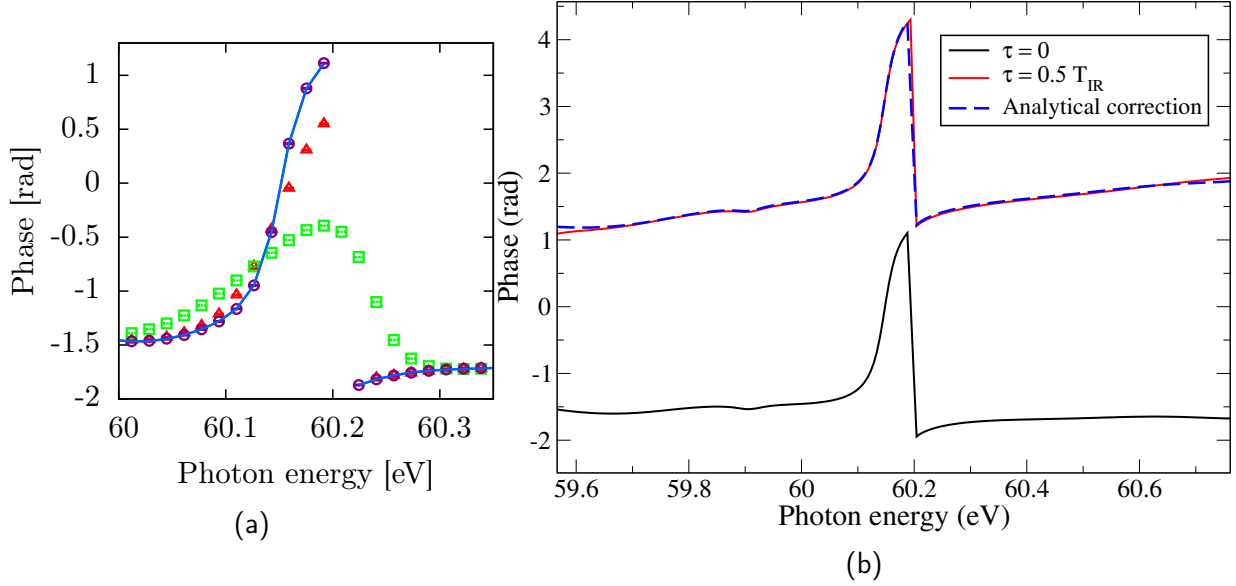


Figure 5.10.: (a) Dependence of the retrieved ionization phase of the $(2s2p)^1P^0$ Fano resonance on the angular and energy resolution ΔE of the detector. blue solid line: infinite resolution, purple circles (\circ): reconstructed phase for only four values of $\varphi \in \{15^\circ, 60^\circ, 170^\circ, 240^\circ\}$, red triangles (\triangle): $\Delta E = 20$ meV, green squares (\square): $\Delta E = 50$ meV.

(b) Comparison of the phase profile for zero (black solid line) and finite (red solid line) time delay between the IR and the APT. Apart for the global vertical shift, the two curves differ by a small slope, which is accurately described by Eq. (E.17). The blue dashed line represents the phase profile calculated for the time delay $\tau = 0.5T_{\text{IR}}$ from the phase profile for $\tau = 0$ employing Eq. (E.17). The FWHM pulse duration of the IR field was approximately 6.5 fs using a \cos^4 envelope for the vector potential.

Effects of non vanishing time delay between the APT and the IR and finite IR pulse duration

In the present *ab initio* simulations we have used zero time delay ($\tau = 0$) between the ATP pump and IR probe. As long as the pump and probe overlap, however, temporally any other time delay can be chosen, without altering the one-photon phase information. For monochromatic IR pulses a nonzero delay τ induces a trivial overall rotation of the angular distribution by $\Delta\phi = \omega_{\text{IR}}\tau$. Finite duration of the IR gives rise to an additional linear offset in the angular beating, on top of the global rotation. This shear term $\Delta\phi$ which is to a good approximation linear in both the time delay τ and the energy difference $\xi_e = E - \omega_k$ from the nominal center of the two-photon signal, is given by

$$\Delta\phi(\tau, \delta) = \frac{-1}{1 + \sigma_{\text{XUV}}^2/\sigma_{\text{IR}}^2} \xi_e \tau, \quad (5.35)$$

where σ_{XUV} and σ_{IR} are the standard deviation of the amplitudes of the XUV pump and the IR probe pulse, see App. E.2 for the derivation of Eq. 5.35. Notice that for an IR pulse with duration much longer than the XUV ($\sigma_{\text{IR}} \ll \sigma_{\text{XUV}}$) $\Delta\phi$ becomes negligible.

The accuracy of the analytical formula Eq. (5.35) is assessed by computing the linear distortion and shift of the phase at a nonzero time delay around the $(2s2p)^1P^o$ resonance. For the results shown in Fig. 5.10b we chose an IR pulse half as long as for the results shown in Fig. 5.9 to amplify the effect of a finite delay, which otherwise would be hardly visible. The spectral widths $\sigma_{\text{XUV}} = 0.4$ eV and $\sigma_{\text{IR}} = 0.29$ eV are obtained by taking the spectral FWHM of the pulses used for the simulation with a \cos^4 envelope of the vector potential. Using Eq. (5.35), we calculate the phase at $\tau = T_{\text{IR}}/2$ and find excellent agreement with *ab initio* calculations performed at the same time delay (Fig. 5.10b). The specific shape of the pulse (in Eq. (5.35) assumed to be Gaussian) thus plays a minor role.

The shear effect [Eq. (5.35)], which is quantitatively confirmed in our simulations, can be easily accounted for in the analysis of experimental data where linear and even quadratic background (attochirp) are commonplace.

Influence of elliptically polarized attosecond pulse trains

As recent measurements suggest that bi-circular APTs produced from $\omega - 2\omega$ fields can be elliptically polarized or even slightly depolarized [228, 229], we explicitly investigate how the CHIP scheme is affected by elliptically polarized harmonics. For brevity we restrict ourselves to the case of a co-rotating circularly polarized IR pulse with the lower harmonic. For this purpose, the elliptically polarized electric field of harmonic $(3n + k)$ is parametrized as follows

$$\mathbf{F}^{(k)}(t) = F_0^{(k)} f(t) \begin{pmatrix} \cos(\omega_k t) \\ (-1)^{k+1} \varepsilon \sin(\omega_k t) \\ 0 \end{pmatrix}, \quad (5.36)$$

where ε is the degree of ellipticity. Non-perfect ellipticity ($\varepsilon \neq 1$) of the harmonics leads to a superposition of three frequency components in the azimuthal beating of the angular

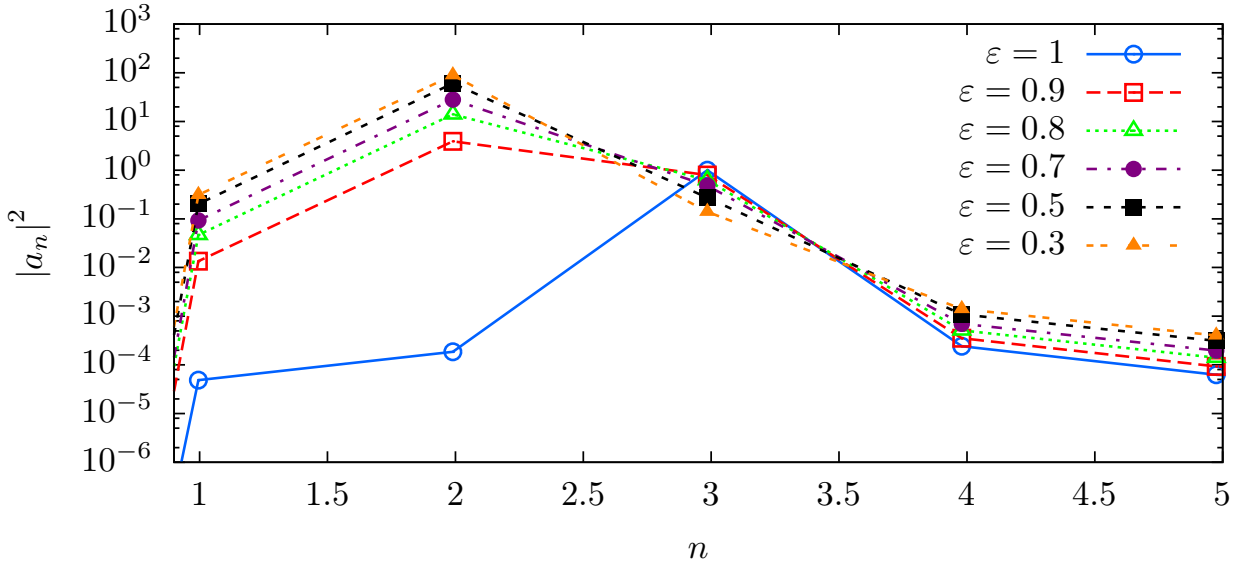


Figure 5.11.: Absolute magnitude squared of the Fourier transform of the angular distribution $P(E, \theta = \pi/2, \varphi) = \sum_{n>0} [a_n \cos(n\varphi - \Delta_n)]$ at photon energy $E = 60.15$ eV as a function of the APT ellipticity ε . The intensity of the IR is in the perturbative regime ($I_{\text{IR}} = 10^9$ W/cm²) for all APT ellipticities.

distribution $P(E, \theta = \pi/2, \varphi)$ instead of just one. The three components can be isolated by Fourier analysis of the angular distribution with respect to the azimuthal angle φ (see Fig. 5.11). As the ellipticity is gradually decreased from $\varepsilon = 1$ to $\varepsilon = 0.3$, in addition to the CHIP characteristic 3φ beating, two new beatings at φ and 2φ appear. The 2φ beating originates from the interference between the ionization amplitudes associated with the left- and right-circularly polarized components of the same harmonic. The appearance of the φ beating is accompanied by a decrease of the strength of the 3φ beating as ε decreases. The phase of the 2φ component vanishes across the full harmonic, which confirms that it is only caused by the interference of the one-photon transitions (see Fig. 5.12). Comparing the phase for the 3φ component with $\varepsilon = 0.8$ to the “reference” phase for a bi-circular APT ($\varepsilon = 1$), it is clear that it accurately reproduces the reference phase. Indeed, only a single circular component of each harmonic contributes to the 3φ oscillation. The co-rotating CHIP configuration therefore, is unaffected by the deviations from perfect circular polarization of the bi-circular APT, whereas in the counter-rotating CHIP the phase of the φ oscillation is affected by ellipticity. As a consequence all the contributions to the 3φ oscillation add up coherently. Therefore, co-rotating CHIP remains accurate even with partially depolarized harmonics, provided that the harmonics are not completely depolarized¹⁸.

¹⁸ We note that with the knowledge of both the Fourier magnitudes and phases, a complete characterization of the polarization and the harmonic phase of bi-circular APTs might be possible. However, the demonstration of this complete characterization goes beyond the scope of the present work.

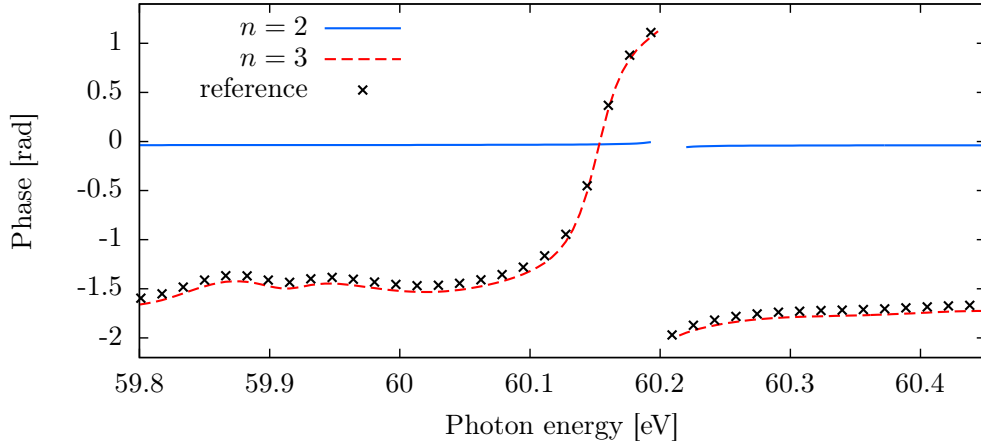


Figure 5.12.: Retrieved phase from the Fourier transformation of the angular distribution $P(E, \theta = \pi/2, \varphi)$ for the 2φ ($n = 2$) and the 3φ ($n = 3$) oscillation in the resonant harmonic for $\varepsilon = 0.8$ compared the phase of the 3φ oscillation extracted for CHIP with bi-circularly polarized ($\varepsilon = 1$) APT (reference: black crosses). Near 60.2 eV the Fourier amplitude for $n = 2$ vanishes and hence we do not show values for the retrieved phase in this region. The IR intensity was chosen to be in the perturbative regime $I_{\text{IR}} = 10^9 \text{ W/cm}^2$.

Phase retrieval for stronger IR fields

The contrast of the CHIP beating can be drastically enhanced by increasing the IR intensity (see Fig. 5.8). Here, we examine how IR intensities beyond the perturbative regime affect the retrieval of the one-photon phase in the CHIP scheme. We consider in the following only the co-rotating CHIP scheme employing the same APT as for Fig. 5.7 but for different intensities of the dressing IR field, ranging from the perturbative regime ($I_{\text{IR}} = 10^9 \text{ W/cm}^2$) to moderate intensities ($I_{\text{IR}} = 10^{11} \text{ W/cm}^2$). The extracted phases coincide with the perturbation theory up to $I_{\text{IR}} = 10^{10} \text{ W/cm}^2$ (see Fig. 5.13). At higher intensities the phase exhibits a full 2π excursion, as it has already been hypothesized for multi-channel resonances [52]. The strong IR field opens new radiative decay channels for the metastable state in which the autoionization decay is accompanied by the absorption or emission of one (or more) IR photons. Under the present conditions, we have ascertained numerically that the two-photon reference phase does not change as a function of intensity. This means that CHIP is, in principle, able to retrieve the phases even of laser-dressed autoionizing states. Fourier analysis shows that, even for IR intensities as high as 10^{11} W/cm^2 , the only relevant modulation of the azimuthal distribution is given by the 3φ beating.

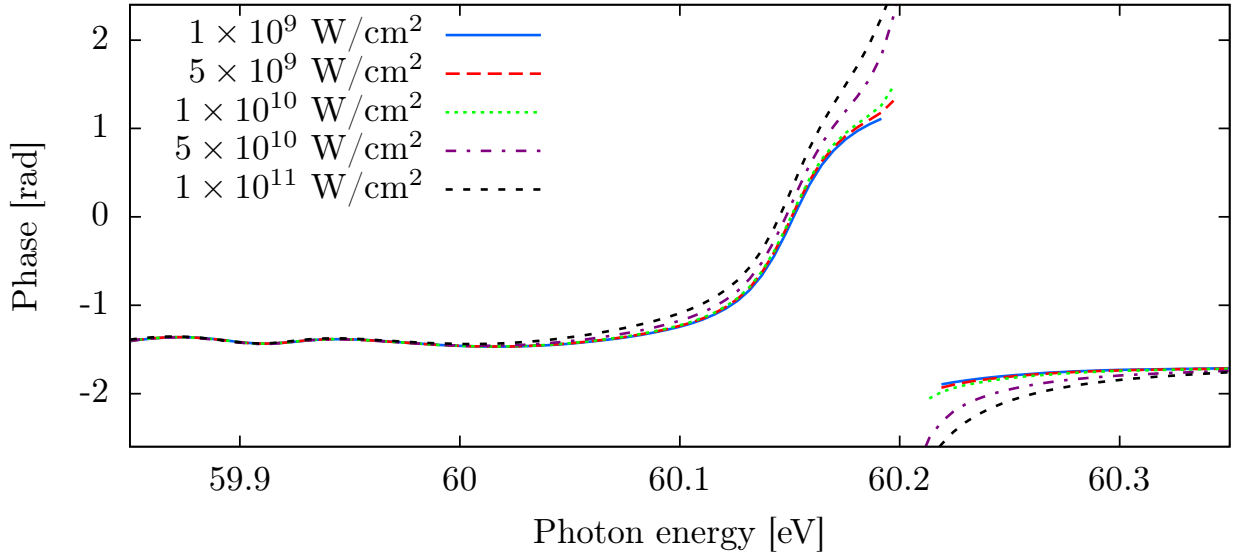


Figure 5.13.: Retrieved phase from the angular distribution $P(E, \theta = \pi/2, \varphi)$ for different IR intensities ranging from the perturbative ($I_{\text{IR}} = 10^9 \text{ W/cm}^2$) to the streaking regime ($I_{\text{IR}} = 10^{11} \text{ W/cm}^2$). We employ CHIP in the co-rotating configuration and extract the phase by fitting the azimuthal oscillation to $\cos(3\varphi - \Delta)$.

5.3. Excursus: Wavelength scanning of resonances in atomic argon

Even though we focused on the measurement of one-photon phases in this chapter we now make a small digression to discuss the influence of Fano resonances on the phases retrieved with angle-integrated RABBITT. These phases show a characteristic modulation [52–55] due to intermediate resonant states. In this excursus we present a joint theoretical and experimental study of XUV photoionization of atomic argon close to autoionizing resonances for photonenergies of 24–40 eV ¹⁹.

The present results achieve two primary goals. First, they provide a confirmation of the measurement from Kotur [52] in the spectral phase of the $3s^{-1}4p$ resonance at 26.7 eV. Second, we identify a previously unobserved phase structure of one (or more) autoionizing resonances centered near 34 eV which is not well-represented in the calculation shown in the following and, as such, evades definitive assignment.

5.3.1. Phases retrieved with wavelength scanning

We employ RABBITT to scan the phase variation in the sidebands caused by resonances in the intermediate states excited by the APT. This is achieved by performing multiple RABBITT measurements, each with a slightly different IR wavelength [52, 55]. Indeed,

¹⁹ The calculations were performed with the `newstock` code. The experiments were performed in the group of Louis DiMaurio at Ohio State University.

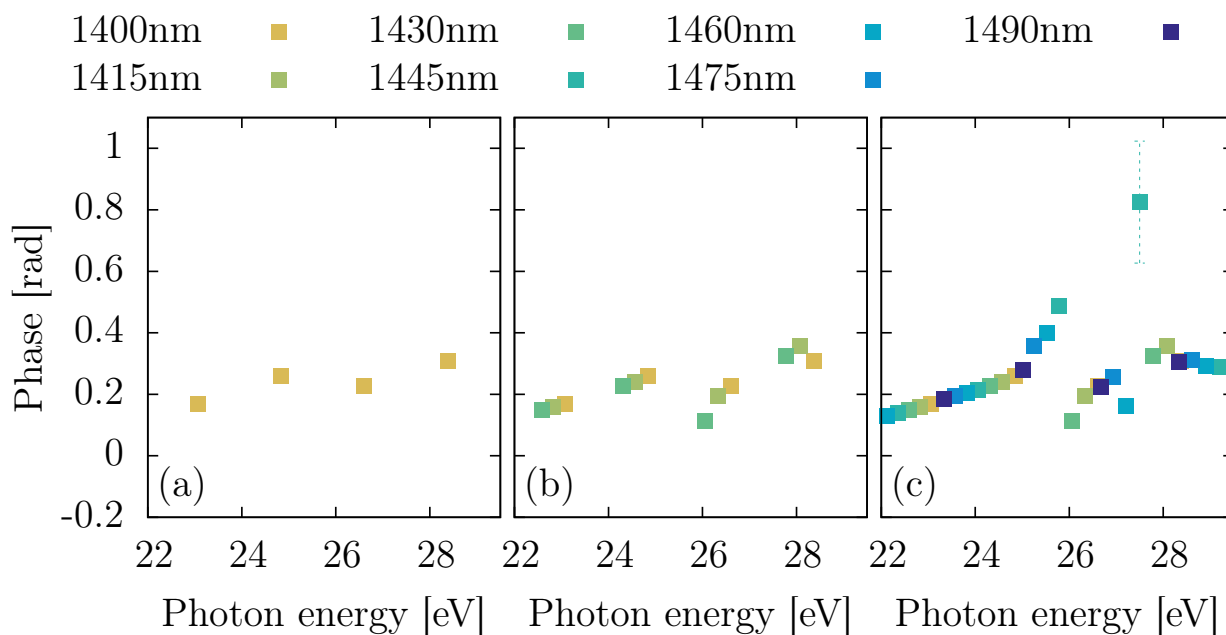


Figure 5.14.: Sequence of plots on how wavelength scanning with RABBITT can be used to map out the two-photon phase structure in atoms. (a) Retrieved phases from one RABBITT trace for $\lambda_{\text{IR}} = 1400$ nm by integrating the sideband across the harmonic width. (b) Changing the fundamental wavelength generates an APT which is shifted in energy and hence different energies of the two-photon phase are probed via RABBITT. (c) If the fundamental wavelength is changed over a sufficiently large range the full energy dependence of the two-photon phase can be accessed via RABBITT. The energy resolution is only limited by the energy integration over the width of the sidebands.

the experiment employs an optical parametric amplifier which allows tuning of the central wavelength over hundreds of nanometers in the mid-infrared, instead of using the output of a Ti:sapphire system, and CH₄ as generation gas for HHG. From every RABBITT trace the phase of the oscillation with the time delay τ is retrieved, see Fig. 5.14a. Analyzing the phases just from one RABBITT trace is sufficient if the phase structure is expected to be smoothly varying but not close to resonances, where sharp phase structures are expected. To resolve those sharp phase variations one combines the phases from RABBITT traces performed for different fundamental wavelength and thus also different harmonic energies, see Fig. 5.14b. If the wavelength is scanned over a large enough range, such that all energy regions are sampled and the difference between subsequent wavelengths is small enough to resolve the phase variation the full energy dependence of the two-photon phase can be accessed with this technique. We will call this approach wavelength scanning in the following [55, 102]. Using wavelength scanning the energy resolution is only limited by the energy integration over the width of the sidebands.

To resolve the phase close to the $3s^{-1}4p$ resonance in argon we perform multiple RABBITT simulations for different wavelengths of the fundamental field from $\lambda_{\text{IR}} = 1400$ nm to $\lambda_{\text{IR}} = 1500$ nm in steps of 5 nm in the theoretical calculations for two different bases (CSF-low and CSF-mid), see App. F for details on the basis used for `newstock`. The RABBITT phases are calculated by the integrating the electron yield within each sideband over an energy range of approximately 100 meV and fitting the time delay oscillations within an interval of $\tau \in [-0.5T_{\text{IR}} : 0.5T_{\text{IR}}]$.

The experimental data clearly reveals the two-photon phase variation in the energy region next the $3s^{-1}4p$ resonance [Fig. 5.15]. Similar to previous results [52, 53] we observe that the phase structures above and below the resonance resemble each other closely apart for an overall sign. Both `newstock` bases accurately reproduce the phase structure caused by the $3s^{-1}4p$ resonance, as well as the measured phase at lower energies, Fig. 5.15. Indeed, the theoretical calculations also show the dip in the phase right below 29 eV, which is most likely due to the high number of resonances right below the threshold opening. The quantitative disagreement between experiment and theory close to 27.5 eV might be caused by the wrong relative position of the $3s^{-1}5p$ resonance and by neglecting spin-orbit splitting in the theoretical calculations.

For photonenergies above 29eV many different single-ionization channels open for argon and due to inter-channel coupling and the presence of many resonances, modulations of the two-photon phase are expected. Previous streaking experiments and theoretical calculations resulted in strongly disagreeing predictions in this energy region [188, 230]. The experimental results obtained from wavelength scanning show a “W”-like structure in the energy region between 33 and 35 eV on top of a rather strongly oscillating phase landscape [Fig. 5.16]. Comparison with the theoretically obtained phase yields, unfortunately, rather bad agreement. The theoretical results do not reproduce the experimentally observed “W”-structure nor the other structures visible, apart from the qualitative agreement on the magnitude of the phase excursion. Possible explanations for this disagreement are among others the absence of spin-orbit splitting in the theoretical calculations, or the inaccurate description of the atomic structure in the CSF-mid basis.

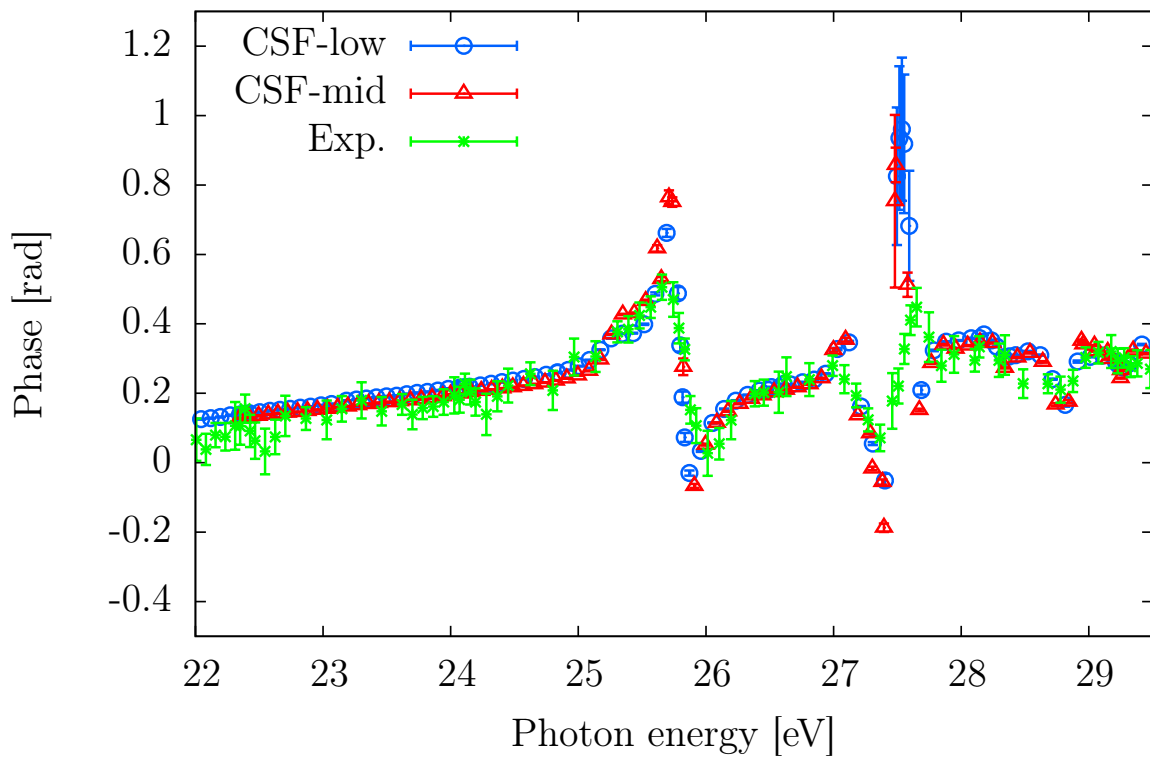


Figure 5.15.: Comparison between the theoretically and experimentally obtained phase variation below the second ionization threshold of argon (approximately 29.24 eV) by finely tuning the fundamental wavelength used to generate the APT over approximately 100 nm. The theoretical pulse parameters are given in App. F.2.

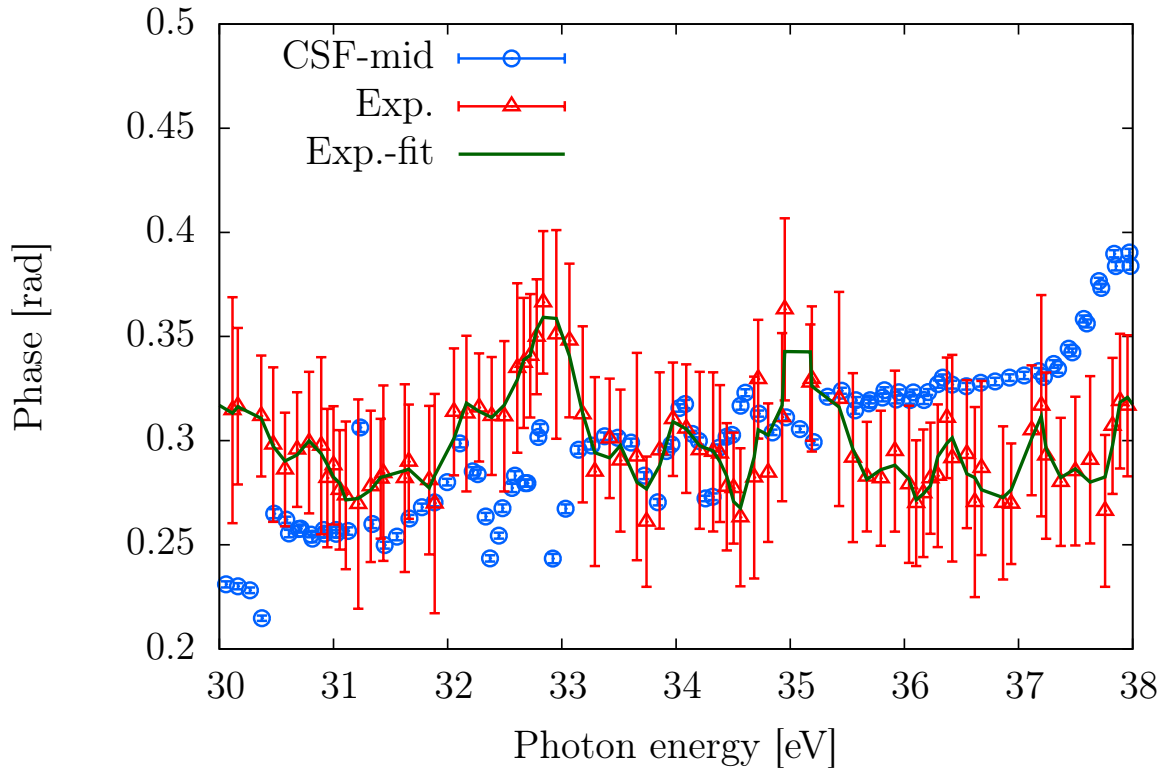


Figure 5.16.: Comparison between the theoretically and experimentally obtained phase variation by finely tuning the fundamental wavelength used to generate the APT over approximately 100 nm for the photon energy range 30 – 38 eV. Within this energy region many different ionization channels are accessible. The solid dark green line is an interpolated curve through the experimental data points to show the “W”-like structure between 33 and 35 eV.

Concluding, from the present theoretical data we are not able to attribute the experimentally observed “W”-structure between 33 and 35 eV to a single resonance or to the opening of an ionization threshold.

6. Monitoring the build-up of a Fano resonance in the time-domain

In the previous chapter we discussed in detail how the one-photon phase of Fano resonances can be measured in experiment. Attosecond metrology, however, also gives us the opportunity to resolve ultrafast processes in time. Accordingly several theoretical calculations have predicted the time-dependent formation of Fano resonances [59–62, 211, 231–234] and experiments have been able to measure lifetimes of atomic resonances [181, 182]. Until recently however, no experiment has been able to measure the time-domain build up of the Fano lineshape for atoms [53, 57].

In this chapter we show how attosecond transient absorption spectroscopy can be used to monitor the time-domain build up of the Fano line shape for the prototypical system of helium²⁰.

6.1. Time dependent Fano wavefunction

While the previous chapter focused on the time-independent Fano profile [Sec. 5.1] we now turn to a time-dependent formulation as investigated in many theoretical publications [59–62, 211, 231–234].

Assuming that the resonance $|a\rangle$ is excited at $t = 0$ with a delta-like XUV pulse the singly-ionized wave function for $t > 0$ is given by

$$|\psi(t)\rangle \approx \frac{1}{\sqrt{N}} \left(e^{-iE_0 t} |0\rangle + C_a(t) |a\rangle + \int C_\varepsilon(t) |\varepsilon\rangle d\varepsilon \right), \quad (6.1)$$

where N is a normalization factor. The time-dependent coefficients of the resonance $C_a(t)$ and the continuum states $C_\varepsilon(t)$ evolve according to the time-dependent Schrödinger equation, which yields

$$i\dot{C}_a(t) = E_a C_a(t) + \int C_\varepsilon(t) V_{a\varepsilon} d\varepsilon \quad (6.2)$$

$$i\dot{C}_\varepsilon(t) = V_{a\varepsilon}^* C_a(t) + \varepsilon C_\varepsilon(t). \quad (6.3)$$

By approximating the configuration interaction matrix element $V_{a\varepsilon}$ as real and constant in the energy range close to the resonance energy E_a Eqs. (6.2) and (6.3) can be solved

²⁰ This work was performed in collaboration with the experimental group of Thomas Pfeifer at the Max-Planck Institute for Nuclear Physics.

analytically assuming that the initial populations at $t = 0$ ($C_a^{(0)}$ and $C_\varepsilon^{(0)}$) are known [57, 59]:

$$C_a(t) = C_a^{(0)} \left(1 - \frac{i}{q}\right) e^{-\Gamma_a/2t}, \quad (6.4)$$

$$C_\varepsilon(t) = \frac{C_\varepsilon^{(0)}}{\varepsilon + i} [(q + \varepsilon) e^{-i(\varepsilon - E_a)t} - (q - i) e^{-\Gamma_a/2t}]. \quad (6.5)$$

In the limit $t \rightarrow \infty$, the coefficients are $C_a(t \rightarrow \infty) = 0$ and $C_\varepsilon(t \rightarrow \infty) = C_\varepsilon^{(0)} \frac{\varepsilon + q}{\varepsilon + i} e^{-i(\varepsilon - E_a)t}$. The time-dependent build-up of the electron wavepacket can be calculated as the absolute square of $C_\varepsilon(t)$ [59, 60, 231]

$$|C_\varepsilon(t)|^2 = \frac{|C_\varepsilon^{(0)}|^2}{\varepsilon^2 + 1} \{ (q + \varepsilon)^2 + (q^2 + 1) e^{-\Gamma_a t} - 2e^{-\frac{\Gamma_a t}{2}} [(q^2 + \varepsilon q) \cos((E - E_a)t) + (q + \varepsilon) \sin((E - E_a)t)] \} \quad (6.6)$$

The absolute square $|C_\varepsilon(t \rightarrow \infty)|^2$ is directly proportional to the time-independent Fano cross section Eq. (5.16).

Atomic resonances decay on a time scale of femtoseconds and thus the build-up of the Fano profile can not be recorded in real time.

To address this problem we propose to sample the time-dependent evolution of the asymmetric Fano line shape by performing a projective measurement at time T [57, 60]. The projective measurement stops the interference of the decaying resonance channel $|a\rangle$ and the already ionized part of the electron wave packet centered around the resonance energy E_a at the time of projection. Thus we can record the temporal evolution of the wavepacket if the projection time T is varied. The observed wave function is given by the projection of the full wave function onto continuum eigenstates at the moment of projection: $T |\langle \varepsilon | \psi(T) \rangle|^2$ [60, 231].

To observe the characteristic build-up using attosecond transient absorption spectroscopy we calculate the transient absorption cross section σ [57] following Eq. 3.16. The time-dependent dipole moment $d(t)$ (assuming already the rotating wave approximation) is given by

$$d(t) = \langle \psi(t) | z | \psi(t) \rangle \propto i \left\{ 2\delta(t) + \frac{\Gamma_a}{2} (q - i)^2 e^{-i(E_a - E_0)t} e^{-\frac{\Gamma_a}{2}t} \right\}. \quad (6.7)$$

For a derivation of Eq. (6.7) see App. G. Calculating the single-atom response [Eq. (3.16)] and considering only the small energy region close to the resonance energy E_a we can ignore

the prefactor ω to calculate the absorption cross section at the projection time T

$$\begin{aligned}
\sigma(E, T) &\propto \text{Im} \left\{ \int_0^T dt d(t) \right\} \\
&\propto \text{Re} \left\{ 1 + \frac{\Gamma_a}{2} (q - i)^2 \int_0^T dt e^{i[E - (E_a - E_0)]t} e^{-\frac{\Gamma_a}{2}t} \right\} \\
&\propto \text{Re} \left\{ 1 + \frac{(q - i)^2}{1 - i\epsilon} \left(1 - e^{-\frac{\Gamma_a}{2}(1 - i\epsilon)T} \right) \right\}. \tag{6.8}
\end{aligned}$$

In the following, we show experimental and theoretical results which show the transient build up of the Fano line-profile of the $2s2p$ resonance in helium using attosecond transient absorption spectroscopy [57].

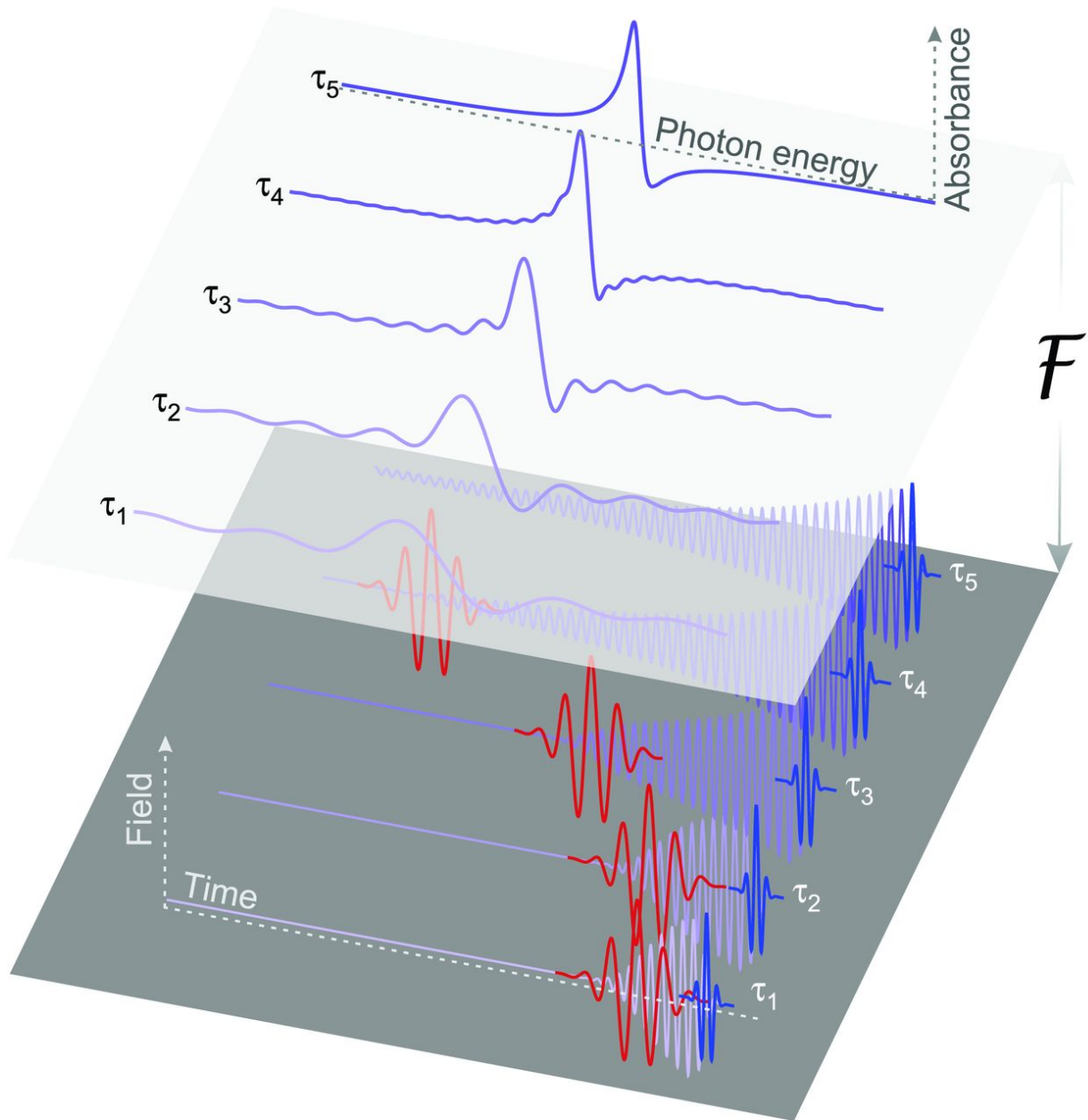


Figure 6.1.: Time-dependent formation of a Fano profile. The top (spectral domain) and the bottom (time domain) planes schematically show the connection between the measured absorption line shape and the temporal evolution of the dipole response (purple) for five time delays τ_1 to τ_5 . After excitation of the autoionizing state by the XUV pulse (blue), the autoionizing state decays exponentially, until the interference is blocked by a projective measurement. This projective measurement is realized by strong-field ionization of the excited state by an intense few-cycle NIR field (red). Controlling the time delay between the XUV excitation (start) and strong-field ionization (stop) allows to monitor the build up of the asymmetric line shape in the time domain.

6.2. Projective measurement

The transient build-up of the $2s2p$ resonance is revealed by measuring the transmission of an ultrashort XUV pulse through helium accompanied by an intense few-cycle (NIR) light field. To be able to resolve the time-dependent line shape we use the fact that optical spectrometers obtain a better energy resolution compared to photoelectron spectrometers, allowing for the tracking of small changes within the absorption spectrum. After the excitation of the resonance by a single ultrashort XUV pulse the formation of the Fano line is sampled by a projective measurement employing an intense ultrashort few-cycle NIR laser pulse. The projective measurement stops the interference between the directly ionized channel and the decaying auto-ionizing state at the time of projection [60]. Strong-field ionization (SFI) of the atom due to the intense NIR laser field blocks the coherent dipole response acting as temporal gate for the formation of the decaying Fano resonance. Varying the time delay between the XUV and the NIR pulse, and hence the projection time, with sub-femtosecond precision, allows to track the evolution of the Fano line shape in real time (see Fig 6.1 for a sketch). To facilitate the complete depletion of the resonant state, very high NIR intensities are needed, whereas lower NIR intensities have been previously used to alter the Fano q parameter [44] or to measure the lifetime of atomic resonances [70, 181].

Fig. 6.2 shows the experimentally observed transient absorption signal which reveals the time-dependent formation of the $2s2p$ Fano absorption line [for positive time delays τ the terminating NIR pulse arrives after the XUV excitation pulse]. For the unperturbed case, i.e. in the absence of the NIR pulse as depicted in Fig. 6.2 (gray line), the original Fano line shape is measured. The intensity of the 7 fs FWHM NIR pulse is high enough (approximately 20 TW/cm²) that the doubly excited states are completely ionized. As the projective measurement due to strong-field ionization is considerably shorter than the lifetime of the $2s2p$ state (17fs) the time-dependent formation of the line shape can be monitored [235].

In the case where the projection time τ is small compared to the state's lifetime, the short duration in which radiation is emitted by the XUV-triggered dipole oscillation is insufficient to form a well-defined Fano line as can be seen in Figs. 6.2 and 6.4C for $\tau < 10$ fs. At $\tau \approx 6$ fs the effect of the NIR is strongest and the spectral line is smeared out completely. When the autoionizing state is immediately depopulated after its excitation, the spectral response is mainly determined by the excitation process driven by the broadband single attosecond XUV pulse and spans several eV. This result agrees with several theoretical studies [59–61, 232] performed for the photoelectron spectrum showing that the energy distribution of the electrons ejected within 1/3 of the state lifetime (corresponding to 6 fs in the case of the $2s2p$ resonance in helium) after the initial excitation is governed by the frequency range of the excitation pulse (see also [173]). Increasing the time delay τ between excitation and ionization, the doubly excited state decays and the interference with the directly ionized electrons forms the characteristic asymmetric line shape. This gives rise to a narrower spectral line with the details of the autoionization process encoded in it. After approximately one lifetime, the Fano spectral signature is already recognizable and

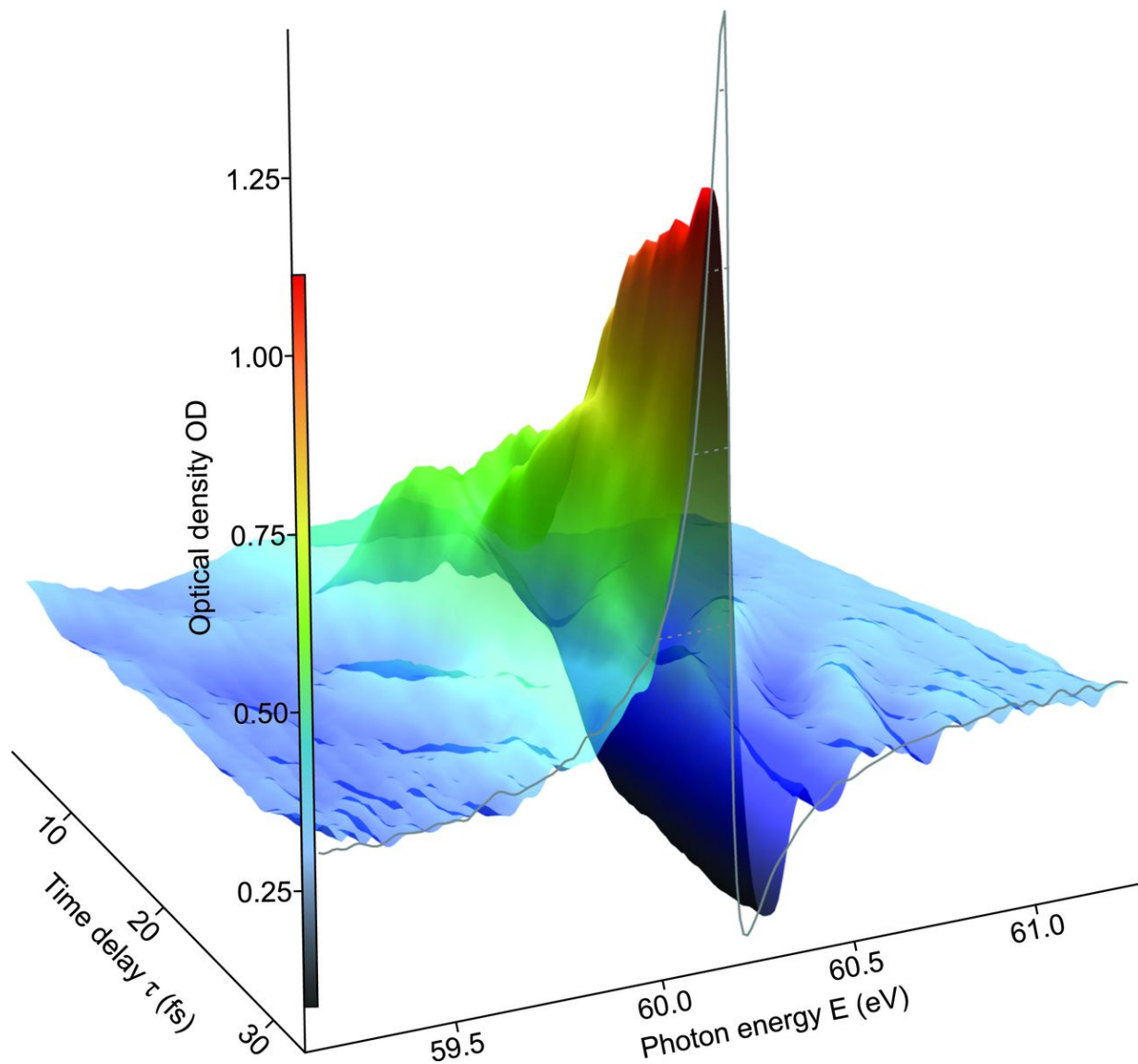


Figure 6.2.: Experimental attosecond transient absorption spectrum in terms of the optical density (OD) of the helium target (vertical axis) as a function of the XUV photon energy E and time delay $\tau \geq 0$ between XUV excitation and subsequent NIR ionization of the $2s2p$ state. The reference spectrum (gray line; dashed bars indicate the OD values from 0.5 to 1.25) shows the unperturbed $2s2p$ line, which corresponds to the limit for $\tau \rightarrow \infty$. The experimental data were averaged over one optical cycle in order to suppress the fast oscillation of the $2s2p$ state absorbance due to two-photon coupling to the $2s3p$ state [68] and to increase the signal to noise ratio.

continuously narrows down as the time delay is increased. For time delays significantly longer than the lifetime, the asymptotic Fano absorption profile is eventually recovered. At the end of the delay range presented in Fig. 6.2 the measured line shape already closely resembles the Fano line. However, this comparison is affected by the finite experimental spectrometer resolution (50 meV FWHM), which has a noticeable effect on the narrow unperturbed line. According to analytic theory, e.g. [59–61, 232], it takes roughly 100 fs (140 fs) for the 2s2p Fano line to reach 95% (99%) of the $\tau \rightarrow \infty$ peak amplitude. The experimental results shown here capture the most significant changes in the line shape, however it is not possible to extend the time delay to larger values with the current experimental setup.

6.3. *Ab initio* treatment of the depletion process

To analyze the experimental result in more detail we perform full *ab initio* calculations to simulate the proposed projective measurement scheme. For the numerical parameters employed in the simulation see App. J.2.7

We verify the temporal gating mechanism by studying the residual population of the 2s2p state after SFI as a function of the time delay for an NIR intensity of 2×10^{13} W/cm² (Fig. 6.3a). The residual population is obtained by projecting the wave function 40.5 fs after excitation by the XUV (Fig. 6.3b) onto the field-free quasi-bound 2s2p state²¹. For large negative time delays, i.e. the NIR arrives considerably before the XUV excites the resonance, the population remains unaffected. Already at $\tau \approx -5$ fs less than 10 % of the population remains bound because of SFI in the rising flank of the intense NIR pulse. Near-complete depletion to well below 1% is first reached around $\tau \approx 4$ to 5 fs in good agreement with the experimental observation. With a fall time (10% to 90% depletion) of about 4 fs, the efficiency of the sudden projective measurement (relative to the resonance life time) is confirmed. Moreover, as can be expected for a strong-field ionization process, the depletion of the excited state depends exponentially on the applied field strength (see inset in Fig. 6.3a).

We now compare both experiment and *ab initio* calculation to the analytic description of an isolated Fano resonance which is excited and depleted impulsively [Eq. (6.8)]. The existing analytical predictions describe the photoelectron spectrum in different scenarios, i.e. either the time-dependent build-up of the continuum component of the Fano resonance [59, 61, 232], or the final distribution of photoelectrons after a sudden removal of the bound population [60]. We explicitly verified that allresulting photoelectron spectra are identical in the case of an isolated Fano resonance and an infinitely short gating pulse. To directly compare the analytic prediction to experiment and the *ab initio* simulation we assume that the time delay τ between the XUV and the NIR pulse is the time T of the projective measurement by strong-field ionization. For the present experimental data this is an approximation as most of the strong-field ionization already takes place during the

²¹ The projection time was chosen large enough to ensure that the NIR field is over for all time delays considered.

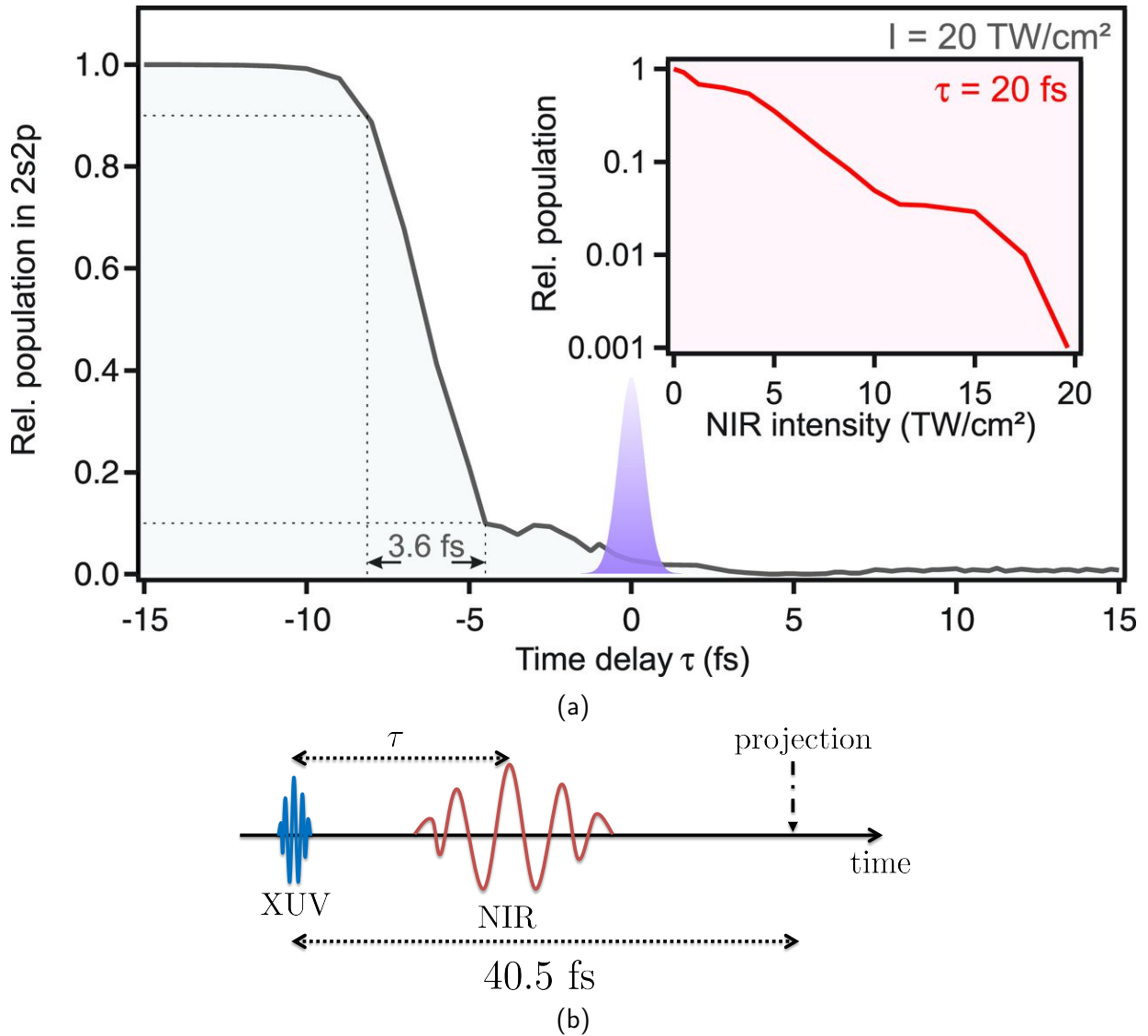


Figure 6.3.: (a) Calculated occupation of the 2s2p state after strong-field ionization. For each time delay τ between the XUV and the strong NIR pulse ($20 \text{ TW}/\text{cm}^2$), the occupation is obtained through projection onto the field-free quasi-bound state at a fixed time of 40.5 fs after the excitation by the XUV pulse.

Inset: Occupation of the 2s2p level for a fixed time delay between the XUV and NIR peak time $\tau = 20$ fs and varying NIR peak intensity. The purple pulse indicates the arrival of the XUV pulse with respect to which the NIR is delayed by τ .

(b) Illustration of the time at which the 2s2p population [shown in (a)] is obtained. The projection time of 40.5 fs after excitation is chosen such that the NIR field is over for all time delays.

rising flank of the NIR field [Fig. 6.3]. Figure 6.4 shows the build-up of the Fano resonance as predicted by Eq. (6.8) (A) (parameters of the 2s2p line are taken from [216]), compared to the numerical *ab initio* calculation (B) and to the experimental data (C). Conceptually, the main difference between the analytic prediction and the *ab initio* simulation is that in Fig. 6.4A the depletion is treated instantaneously. This implies that the quantum system remains unperturbed up to the strong-field ionization event, whereas a finite-duration NIR laser pulse is applied in (B), to model the experimental scenario (C). Moreover, the experimental spectra are additionally affected by a deviation of the laser pulse shape from a clean Gaussian pulse used in Fig. 6.4B.

The experimental NIR laser pulse is accompanied by a moderately strong pre-pulse which arrives approximately 15 fs before the main laser pulse. This pre-pulse is also a possible explanation for the observable dip within the optical density shown in Fig. 6.2 around $\tau = 15$ fs. Still, the experimental spectra clearly resolve the build up of the Fano resonance, validating the employed time-gating technique by a projective measurement. The three spectra agree well with respect to their shapes and peak-to-baseline ratios, especially at later stages of the build-up (darker colors). As the experimental laser pulse profile deviates from an ideal Gaussian pulse used in the simulations, we cannot expect perfect quantitative agreement.

Directly at the beginning of the build-up (lighter colors) all spectra share a smeared-out appearance reflecting the time/energy Fourier uncertainty relation. The *ab initio* calculation and the experiment agree particularly well also at these early times as they both exhibit broad wings with a similar structure, whereas the analytic spectrum is virtually flat. The discrepancy compared with the analytic theory shows that in the region of temporal overlap the strong NIR field has a noticeable effect on the measured line shape as the NIR field is not included in the analytic model. Among other effects the 2s2p state itself is modified by the strong field if the XUV and NIR field overlap temporally (e.g. by strong coupling to other doubly excited states [63, 64, 67]). Thus the simplified sequential picture of excitation of the 2s2p resonance by the XUV pulse and subsequent depletion by the strong NIR field does not apply in this case. An experimental approach to reduce the pulse overlap issue would be to use NIR laser pulses with shorter duration allowing smaller time delays without a significant overlap of the XUV and NIR.

The present *ab initio* simulations allow us to take a closer look into the depletion process. As already visible in the inset of Fig. 6.3a, a very high intensity for the strong-field ionizing NIR pulse is needed to obtain a perfect projective measurement. If the projective measurement does not deplete the 2s2p resonance completely the formation of the line-shape is only partially stopped and a complicated pattern emerges in the optical density, Fig. 6.5a. For an NIR intensity of 10^{12} W/cm² the optical density is only marginally modified as compared to the optical density observed without depletion by an NIR pulse. Increasing the intensity to 5×10^{12} W/cm² the resonance line starts to split into two separate lines, which is a characteristic sign of the Autler-Townes effect [160]. Only for the highest intensity shown SFI fully depletes the autoionizing state and the temporal formation of the line shape can be stopped [Eq. 6.8].

On top of strong-field ionization, the different doubly excited states [Tab. 5.1] are cou-

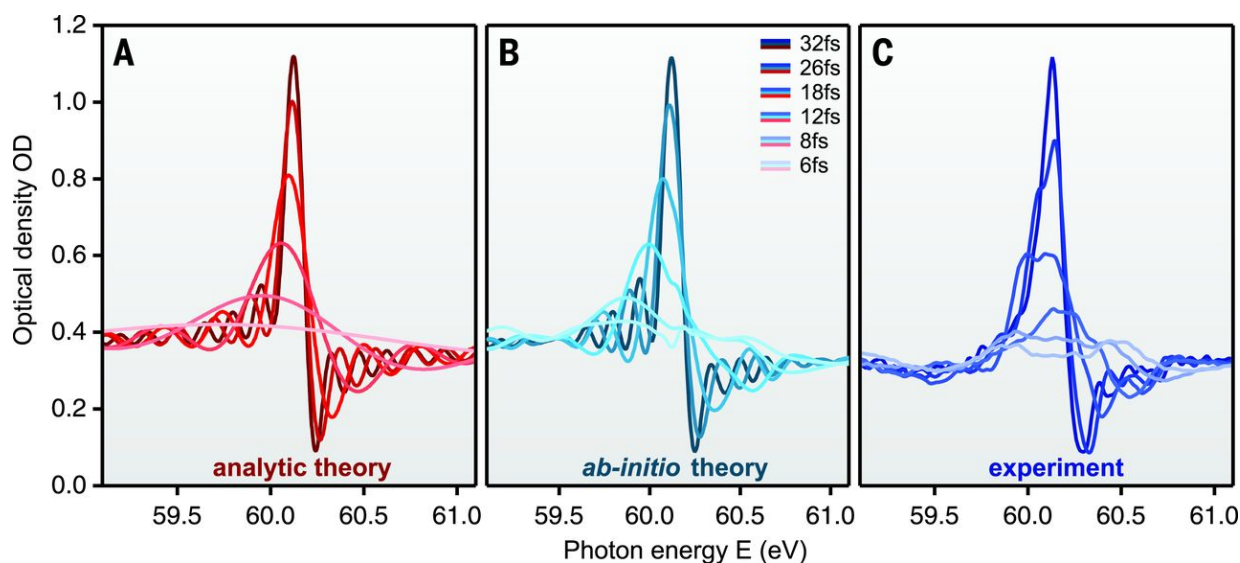


Figure 6.4.: Comparison between analytic theory, *ab initio* calculation, and experimental results for the helium 2s2p Fano line formation. (A) Absorption spectra calculated for a series of time delays between XUV and NIR according to the analytic expression [Eq. (6.8)]. (B) Numerically simulated absorption spectra for a 7-fs FWHM NIR pulse, with peak intensity of 20 TW/cm². (C) Experimentally recorded spectra. The theoretical spectral amplitudes in (A) and (B) are scaled to match the experimental peak and valley at 32 fs. Because of the finite duration of the NIR pulse in (B) and (C), the effective beginning of the line formation is not at $\tau = 0$. Thus, the analytic spectra are shifted by 4.5 fs in time delay in order to ensure comparability among the three data sets.

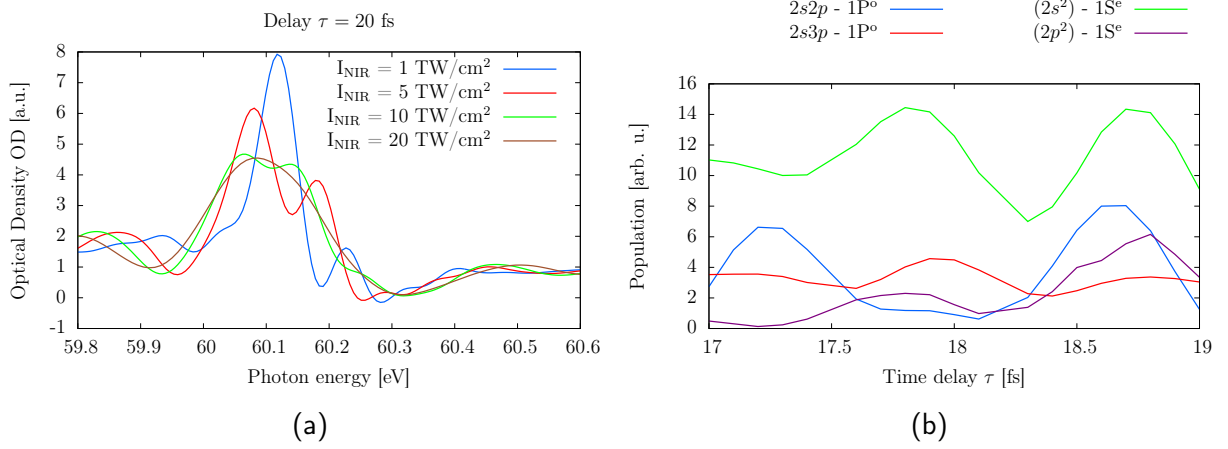


Figure 6.5.: (a) Optical density for a time delay of $\tau = 20$ fs between the exciting XUV pulse and the NIR pulse for different peak NIR intensities. (b) Population of the doubly excited states in helium 40.5 fs after excitation [Fig. 6.3b] and subsequent interaction with the NIR ($I_{\text{NIR}} = 2 \times 10^{13}$ W/cm²) as function of the time delay between the XUV and NIR pulse.

pled (almost) resonantly by the NIR field [63, 64, 67]. This coupling is responsible for the oscillations of the final state occupation of the $2s2p$ resonance and the nearby doubly excited states as function of the time delay τ , see Fig. 6.5b. This is a clear signature of Rabi oscillations [236] driven by the NIR laser pulse.

To obtain a more detailed understanding of the depletion by strong-field ionization we calculate the occupation of the $2s2p$ resonance as a function of real time by projecting the time-dependent wave function on the field free eigenstates at the times where the electric field is zero. Although this observable is experimentally not directly accessible it is useful to analyze the dynamics induced by strong NIR laser fields. Rabi oscillations are clearly observable within the time-dependent population of the resonance for a wide range of NIR intensities, see Fig. 6.6. For high intensities, however, strong-field ionization becomes the dominant process and only very weak oscillations can be observed. We will examine the interplay between resonant coupling of the doubly excited states and strong-field ionization in more detail in the next chapter (Chap. 7).

The last point we want to address in this subsection is the question whether it is possible to obtain the time at which the projective measurement happened from the absorption spectrum. From Eq. (6.8) one obtains

$$\sigma(\epsilon, \tau) \propto \mathcal{V} + \frac{e^{-\frac{\Gamma}{2}\tau}}{\epsilon^2 + 1} \{ \mathcal{W}_1 \cos[(E - E_R)\tau] + \mathcal{W}_2 \sin[(E - E_R)\tau] \}, \quad (6.9)$$

where \mathcal{V} , \mathcal{W}_1 and \mathcal{W}_2 are constants that depend only on ϵ and q . Oscillations with respect to $(E - E_R)$ are clearly visible in Fig. 6.4A and B to the left and to the right of the resonance energy. If the projective measurement takes place fast enough, the projection time is in principle imprinted in the oscillation period T of the fringes. Eq. (6.9), however,

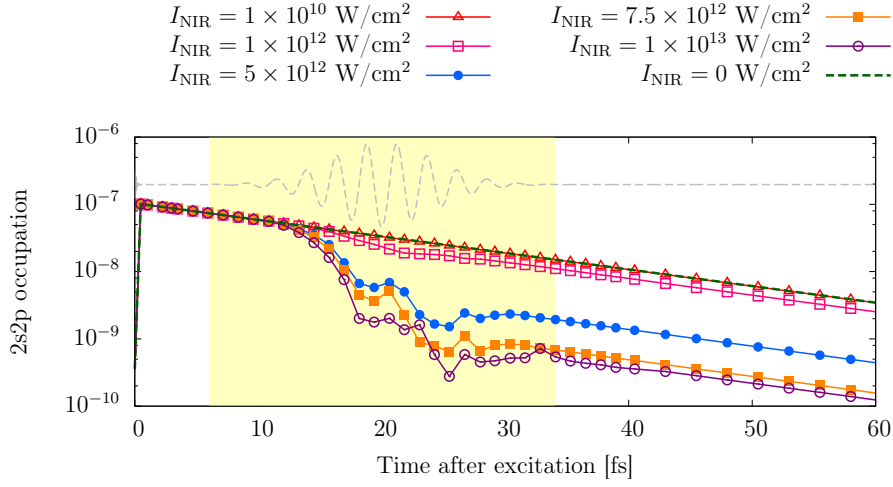


Figure 6.6.: Occupation of the 2s2p doubly excited state obtained by projection of the time-dependent wave function onto the field-free quasi-bound state as function of projection time and intensity of the NIR field. The projection times were chosen at the zero crossings of the electric field. The time delay between the XUV excitation and the projective measurement ($\tau = 20$ fs) was chosen such that the two pulses are not overlapping in time. The dashed gray line symbolizes the combined electric field of the XUV and the NIR and the yellow shaded area highlights the interaction time of the atom with the NIR field.

neglects all influences of longer pulses and requires a very sensitive measurement of the absorption spectrum rendering experimental verification challenging.

7. Time-resolved coupling between Fano resonances

Based on the results shown in the previous chapter we investigate in detail the interplay between strong-field ionization and the field-driven coupling of resonances by few-cycle light fields. Whereas we showed in chapter 5 and 6 how a combination of XUV and IR fields can be used to characterize Fano resonances in time and frequency domain, we study in this chapter the interaction of several resonances with IR fields over a wide range of intensities. Our intention is to develop a better understanding of the occupation oscillations shown in Fig. 6.5b employing *ab initio* simulations for the prototypical system of helium.

As first step towards achieving this aim, we analyze the residual occupation of the doubly excited states in helium after excitation by an ultrashort XUV laser pulse and subsequent driving with a few-cycle laser field. Variation of the wavelength of the driving few-cycle pulse, its intensity, and the time delay between the exciting XUV and the driving NIR field leads to pronounced modifications of the occupation of the double-excited states.

Subsequently, we will introduce a new method which allows to retrieve the full time-resolved dipole response of a strongly driven time-dependent system from a single absorption spectrum²². The only requirement is that the excitation is caused by a sufficiently short pulse. We use this scheme to observe Rabi oscillations between doubly excited states in helium occurring on the few-femtosecond time scale. In contrast to conventional pump-probe schemes, there is no need for scanning time delays in order to access real-time information.

7.1. Coupling doubly excited states with few-cycle light fields

Coupling of bound states by light fields is one of the building blocks of quantum optics. The occupation transfer between different coupled states driven by (near)resonant light fields has been studied in detail for various systems and is very well understood. In the context of just two levels which are coupled the light induced population transfer is often referred to as Rabi flopping [236, 237]. Within this simple model the light field induces not only a periodic population transfer between the two (or more) levels, but also imposes a characteristic phase shift onto the wavefunction.

²² The experiments shown in this chapter were performed in the group of Thomas Pfeifer at the Max-Planck Institute for Nuclear Physics. The results were analyzed and modeled in collaboration with the groups of Thomas Pfeifer and Christoph Keitel at the Max-Planck Institute for Nuclear Physics.

transition	ΔE (eV)	λ (nm)	transition dipole matrix element μ (a.u.)
$(2s2p) {}^1P^o - (2s^2) {}^1S^e$	-2.3	539	-1.56
$(2s2p) {}^1P^o - (2p^2) {}^1S^e$	1.94	639	2.17
$(2s3p) {}^1P^o - (2p^2) {}^1S^e$	-1.57	790	-0.81

Table 7.1.: List of dipole-allowed transitions between the doubly excited states listed in Tab. 5.1 relevant for the results shown in this section. The dipole-matrix element between the $(2s^2) ({}^1S^e)$ and $(2s2p) ({}^1P^o)$ resonance was obtained by taking the real part of the non-conjugate dot-product $(\phi_{(2s^2)}, \hat{z} \phi_{2s2p})$, where ϕ_a is the eigenfunction of resonance a . The other dipole matrix elements are taken from [68].

The doubly excited states in helium can be interpreted as quasi-bound states within the $\text{He}^+(n = 1)$ continuum and thus can be coupled resonantly with light fields by the same mechanism. Interestingly, the transitions between the energetically lowest states can be driven almost resonantly with infrared or near-infrared light fields, see Tab. 7.1. Nevertheless a driving NIR laser field can not only induce Rabi oscillation, but can also modify the autoionization process itself [44], as the doubly excited states are embedded within the $\text{He}^+(n = 1)$ continuum. The subtle interplay between the strong-field modification of the autoionization process and Rabi flopping has triggered a large number of theoretical and experimental studies [63, 64, 66–69, 147]. The most interesting questions are the disentanglement of Rabi cycling and strong-field ionization, and a detailed understanding of how the autoionization process is influenced by a strong laser field.

In this section we study the residual population in the doubly excited states after the interaction with a few-cycle laser field as function of its wavelength and intensity in a first attempt to disentangle Rabi oscillations and the ionization processes. We use two different wavelengths for the coupling IR field, $\lambda_{\text{IR}} = 500$ nm ($\omega_{\text{IR}} = 2.48$ eV) and $\lambda_{\text{IR}} = 740$ nm ($\omega_{\text{IR}} = 1.67$ eV), see Fig. 7.1a for a sketch of the fields. The two different wavelengths drive different transitions between the doubly excited states resonantly due to their different spectral pulse profile, see Fig. 7.1b. For the numerical details see App. J.2.8.

Similar to the previous chapter we monitor the population in the $(2s2p) {}^1P^o$ resonance 40 fs after its excitation [see also Fig. 6.3b]. For the weakest probe intensity (10^{11} W/cm²) the occupation of the $2s2p$ resonance is depleted by less than 10% for both wavelengths, see Fig. 7.2. Increasing the probe intensity to moderate intensities (10^{12} W/cm²) pronounced differences for the two different wavelengths emerge. For $\lambda = 500$ nm we observe a step-like depletion of the occupation as a function of the time delay superimposed with very weak oscillations. This hints at strong-field ionization being the dominant process for the depletion of the $2s2p$ state. Similar steps can also be observed for $\lambda = 740$ nm, however, on top we observe very pronounced oscillations of the $2s2p$ population which have been linked to the resonant coupling of the three level system consisting of the $(2s2p) {}^1P^o$, $(2p^2) {}^1S^e$ and the $(2s3p) {}^1P^o$ state [68]. The oscillations are even more clearly visible if the two pulses are not overlapping in time. Increasing the probe intensity even further the results

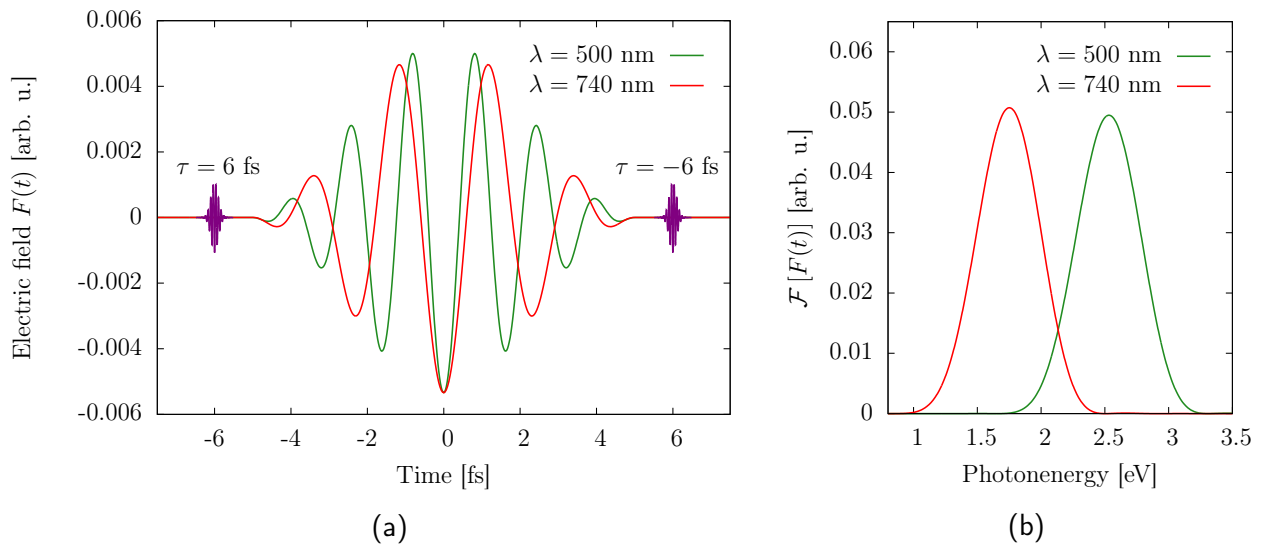


Figure 7.1.: (a) Temporal profile of the probing pulses used in this section with the two employed wavelengths $\lambda_{\text{IR}} = 500 \text{ nm}$ and $\lambda_{\text{IR}} = 740 \text{ nm}$. The purple single attosecond XUV pulses symbolize the full electric field for a time delay of 6 fs (left purple field) and -6 fs (right purple field). Negative time delays correspond to the case that the probing field arrives before the exciting XUV field. The overall amplitude between the XUV and the probe field is not to scale as the XUV intensity is always chosen to be $I_{\text{XUV}} = 10^{11} \text{ W/cm}^2$ and the intensity of the probe is varied from 10^{11} W/cm^2 to $2 \times 10^{13} \text{ W/cm}^2$. (b) Spectral profile of the two probe pulses obtained by Fourier transformation of the IR pulses shown in (a).

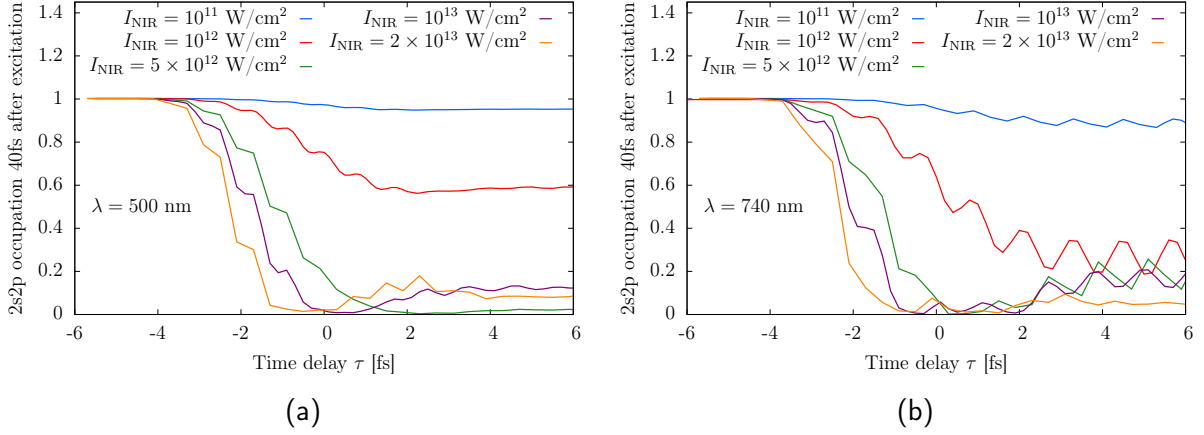


Figure 7.2.: Population of the $(2s2p) \ ^1P^0$ resonance, 40 fs after its excitation by a single attosecond pulse and subsequent probing by a few-cycle laser field with wavelength (a) $\lambda = 500$ nm and (b) $\lambda = 740$ nm, respectively, as a function of the time delay between XUV and probing field and the intensity of the probing NIR field. All curves are normalized such that for negative time delays the residual population is 1. Negative time delays correspond to the case that the probing field arrives before the exciting XUV field.

for the two different wavelengths are very similar within the time delay regime where the XUV and the NIR overlap temporally. The occupation drops rapidly with the time delay even if the system is ionized only by the trailing flank of the NIR pulse. This indicates that strong-field ionization is the dominant process at these intensities as the ionization should depend primarily on the intensity. In line with this hypothesis, the onset of the decay of the occupation shifts to negative time delays with increasing probe intensities.

Turning to the residual occupation of the $(2s3p) \ ^1P^0$ state after the interaction with the NIR fields, much larger oscillation amplitudes of the occupation appear for both probing wavelengths, see Fig. 7.3a and Fig. 7.3b. While for $\lambda = 740$ nm these oscillations might be attributed to the coupling to the $(2p^2) \ ^1S^e$ state, this transition is far off resonant for $\lambda = 500$ nm. Therefore, the strong oscillations for the latter wavelength are either caused by the coupling to other doubly excited states or by the coupling to states which are brought into resonance due to a transient AC Stark shift during the interaction with the strong probe pulse [65, 238, 239]. For $\lambda = 500$ nm the occupation in the $2s3p$ state for large positive time delays decreases monotonically with increasing NIR intensity. This is not the case for $\lambda = 740$ nm where the $2s3p$ occupation shows very large oscillation amplitudes which maximize for $I_{\text{NIR}} = 10^{12}$ W/cm². The increase of the final occupation above the occupation for large negative time delays can be attributed due to occupation transfer from the $2s2p$ state to the $2s3p$ state via the dipole-forbidden $(2p^2) \ ^1S^e$ state. The occupation modulation is maximized for the case where the XUV and the probing field do not overlap in time and hence the XUV excitation and the interaction with the intense

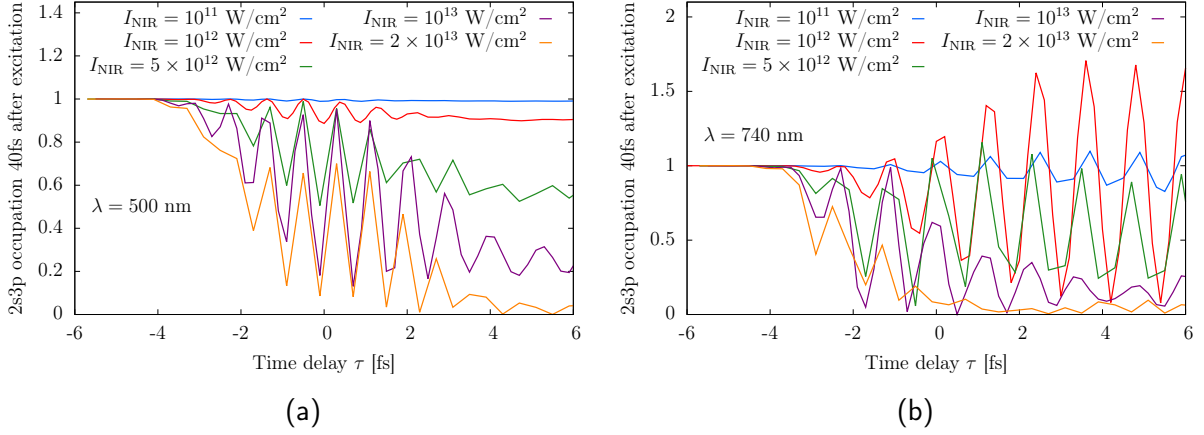


Figure 7.3.: Population of the $(2s3p) \ ^1P^o$ state 40 fs after excitation by a single attosecond pulse and subsequent probing by a few-cycle laser field with wavelength (a) $\lambda = 500$ nm and (b) $\lambda = 740$ nm, respectively, as a function of the time delay between XUV and probing field and the intensity of the probing NIR field. All curves are normalized such that for negative time delays the residual population is 1. Negative time delays correspond to the case that the probing field arrives before the exciting XUV field.

probe field can be clearly separated. For high intensities of the probing field the amplitude of the occupation oscillations with the time delay decreases highlighting the increasing influence of ionization.

Finally, we turn to the occupation of the dipole-forbidden $(2p^2) \ ^1S^e$ state, see Fig. 7.4a and Fig. 7.4b. As expected for large negative time delays this state is not occupied since it can only be excited if another dipole-allowed state is excited before the NIR pulse probes the helium atom. For both wavelengths the final occupation is enhanced if the two pulse overlap temporally as it can be accessed in this case via absorption of one XUV photon and simultaneous absorption or emission of one photon from the probing pulse [65, 160]. Comparing the results for the two wavelengths it becomes clear that the driving field with $\lambda = 740$ nm couples the $(2p^2)$ state more effectively to the dipole-allowed doubly excited states as the final population is larger for a wide range of probing intensities. The oscillation observed for $\lambda_{\text{IR}} = 740$ nm and $I_{\text{NIR}} = 10^{12}$ W/cm² at large positive time delays are almost completely out of phase with the oscillations observed for the $(2s3p) \ ^1P^o$ state for the same probe wavelength and intensity, see Fig. 7.3b. This indicates that we primarily induce Rabi flopping between those two states for a probe pulse with these parameters. Increasing the NIR intensity beyond 10^{13} W/cm² the residual population drops for large negative time delays for $\lambda = 740$ nm, but not for $\lambda = 500$ nm.

Drawing definite conclusions about the interplay between strong-field ionization and Rabi flopping from the discussion above is hard as no real-time information can be obtained by just monitoring the final occupation of the doubly excited states. Experimentally, it is difficult to faithfully measure the occupation of the doubly excited states, as e.g. the

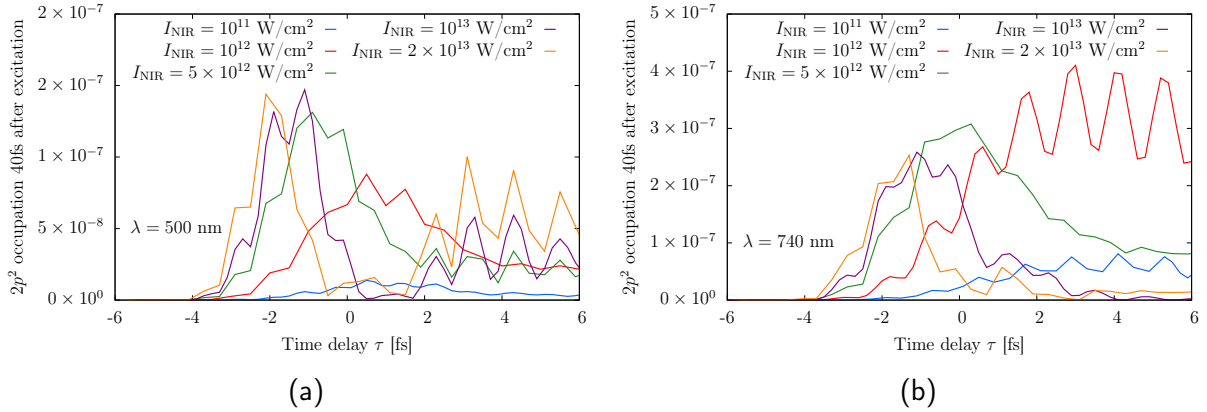


Figure 7.4.: Population in the dipole-forbidden $(2p^2) 1S^e$ state 40 fs after excitation by a single attosecond pulse and subsequent probing by a few-cycle laser field with wavelength (a) $\lambda = 500$ nm and (b) $\lambda = 740$ nm, respectively, as a function of the time delay between XUV and probing field and the intensity of the probing NIR field. Negative time delays correspond to the case that the probing field arrives before the exciting XUV field.

dipole-forbidden states can not be accessed with transient absorption spectroscopy but only from electron spectra.

Therefore, we introduce a new method in the following section that is able to retrieve real-time information on the coupling between the doubly excited states from a single-shot transient absorption measurement.

7.2. Reconstructing the time-dependent dipole moment from a single-shot measurement

Measuring ultrafast atomic processes in the time domain typically relies on observing the nonlinear response of a system to precisely timed interactions with external stimuli [24]. This usually requires two (or more) controlled events, e.g., a triggering pump and a delayed probe pulse. Performing an inter pulse time-delay scan between pump and probe pulses allows to retrieve time-resolved information about the underlying physical processes. Within this section we will generalize this concept and show how to temporally resolve the response of a system in the presence of an additional explicitly time-dependent nonlinear interaction from a single absorption spectrum²³ [70].

As already shown in Sec. 3.3 the attosecond transient absorption spectrum $A(\omega)$ [or cross section $\sigma(\omega)$] is directly proportional to the Fourier transform of the dipole response func-

²³ The results shown in this section were achieved in collaboration with the groups of Thomas Pfeifer and Christoph Keitel at the Max Planck Institute for Nuclear Physics.

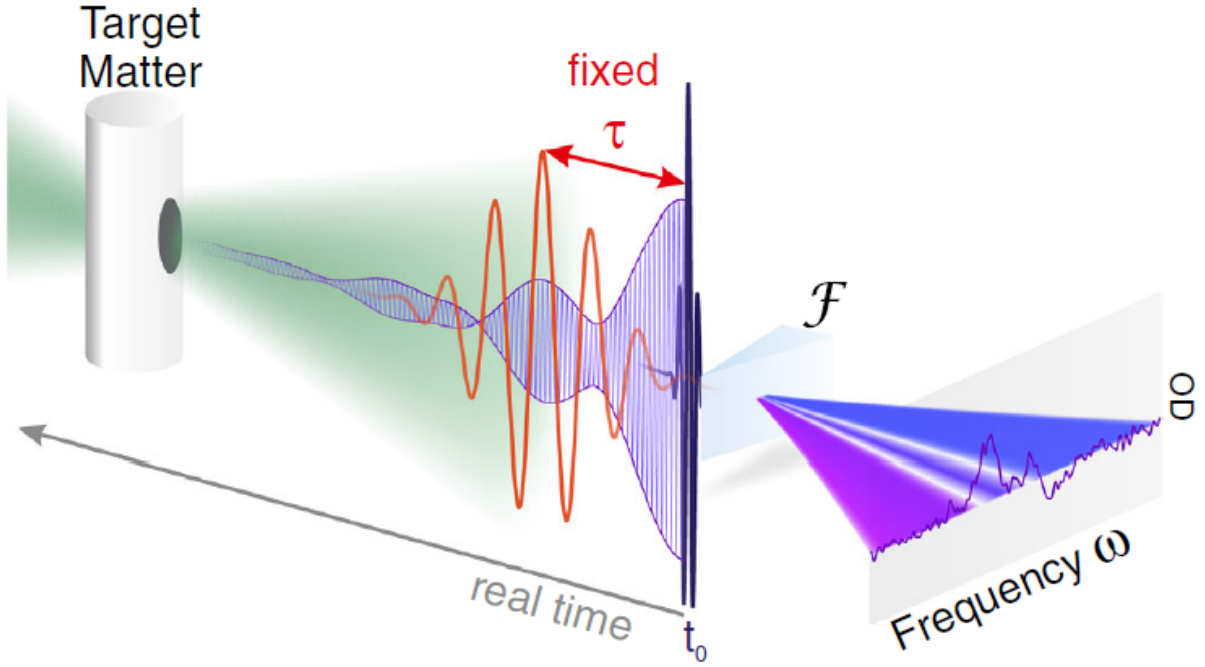


Figure 7.5.: Illustration of the probing of a non-equilibrium state of matter induced by a time-dependent perturbation using an ultrashort laser pulse (black at t_0) to trigger a response (purple), which is then modified e.g. by a strong external time-dependent electric field (red) at a fixed time delay τ . From the measured absorption spectrum [Eq. (7.1)] the strongly driven response can be fully reconstructed if the initial excitation pulse is much shorter than the dynamics of the system using the Fourier transform of the measured spectrum [Eq. (7.2)].

tion $d(t)$ caused by a weakly perturbing field $F_\gamma(t)$ [159, 160],

$$A(\omega) \propto \sigma(\omega) \propto \omega \text{Im} \left(\frac{\mathcal{F}[d(t)]}{\mathcal{F}[F_\gamma(t)]} \right), \quad (7.1)$$

where, in the linear regime $\mathcal{F}[d(t)]$ is linearly proportional to $\mathcal{F}[F_\gamma(t)]$, with \mathcal{F} symbolizing Fourier transformation. For time-translation invariant systems, Eq. (7.1) has in the past frequently provided the starting point of a large number of experiments via linear response theory. Under the condition of weak perturbations and utilizing the connection between amplitude (absorption) and phase (dispersion) owing to causality [240–242], the Fourier transform of the complete linear absorption spectrum corresponds to the response of a system to a (virtual) broadband excitation event. Thus, the spectrum carries information about the internal structure of the system (e.g. resonant excitations) including the natural decay dynamics on the characteristic timescale T_d . The decay times can be extracted for probing fields $F_\gamma(t)$ with pulse duration T_γ much larger than the timescale of the system

($T_\gamma \gg T_d$), simply by tuning the laser frequency through the spectral linewidth. It is even possible to use an incoherent probe field $F_\gamma(t)$, where the system interacts at random points in time with photons of various frequencies resolved by a spectrometer. The reason for this being, that for a time-translation invariant system, the relative phases between frequency components and, subsequently, the arrival time of the probing photons are irrelevant. By contrast, the evolution of a general non-equilibrium state of matter cannot be accessed by incoherent fields, as the system can exhibit explicit time dependence.

7.2.1. Reconstruction of dynamics for non time-translation invariant systems

In the more general case of a system subject to a strong time-dependent interaction $V(t)$, the response function $d(t)$ becomes dependent on both interaction and time $d[V(t), t]$ (see Fig. 7.5 for an illustration). As a consequence, the explicitly time-dependent response can no longer be measured with incoherent light, i.e., photons arriving at random times. To circumvent this limitation, we consider the response to a coherent (laser) pulse $F_\gamma(t)$, followed by an external perturbation $V(t)$.

In the following we assume the duration T_γ of the pulse $F_\gamma(t)$ to be much shorter compared to the timescale T_V of the perturbation $V(t)$ and the decay time T_d of the system ($T_\gamma \ll T_V, T_d$). In this impulsive limit [formally approximated by $F_\gamma(t) = F_\gamma \delta(t)$, with the Dirac $\delta(t)$], the absorption spectrum can be written in analogy to Eq. (7.1)

$$A(\omega) \propto \text{Im} \{ \mathcal{F} [d(V(t), t)] \} \quad \text{for } \omega > 0. \quad (7.2)$$

Such a delta-like excitation can, e.g., be performed by a single attosecond XUV pulse [1, 2]. Therefore we will use $F_\gamma(t) = F_{\text{XUV}}(t)$ in the following. Eq. (7.2) corresponds to the extension of the linear-response expression Eq. (7.1) to the non-linear regime. The reconstruction method presented here aims at extracting the real-time dipole response $d(t)$ initiated at $t_0 = 0$ by the XUV pulse $F_{\text{XUV}}(t)$ in the presence of a subsequent interaction with a few-cycle NIR pulse. In usual linear-response theory, time-translation invariance is assumed, such that the dipole response of the system is not affected by the arrival time of the pulse

$$F_{\text{XUV}}(t) \rightarrow F_{\text{XUV}}(t + \Delta t) \Rightarrow d(t) \rightarrow d(t + \Delta t). \quad (7.3)$$

In a pump-probe setting with NIR interaction at time τ , the time-translation invariance is explicitly broken, and a different dipole response is induced when the initial pulse $F_{\text{XUV}}(t)$ is shifted by Δt .

Even in absence of time-translation invariance, causality [240–242] still implies that the response $d(t)$ vanishes for times $t < 0$ preceding the excitation. This in turn implies that knowledge of the imaginary part of the spectral response $\tilde{d}(\omega)$ is sufficient to fully

reconstruct $d(t)$, because

$$\begin{aligned} \mathcal{F}^{-1}\{i \mathbf{Im}[\tilde{d}(\omega)]\}(t) &= \frac{1}{\sqrt{2\pi}} \int i \mathbf{Im}[\tilde{d}(\omega)] e^{-i\omega t} d\omega = \frac{1}{2}[d(t) - d^*(-t)] \\ \mathcal{F}^{-1}\{i \mathbf{Im}[\tilde{d}(\omega)]\}(t) &= \begin{cases} \frac{d(t)}{2} & \text{if } t > 0 \\ -\frac{d^*(-t)}{2} & \text{if } t < 0 \end{cases} \end{aligned} \quad (7.4)$$

is directly proportional to $d(t)$ for $t > 0$. For an ultrashort excitation field

$$F_{\text{XUV}}(t) \approx F_{\text{XUV}}\delta(t) \quad (7.5)$$

with an approximately constant spectral amplitude

$$\tilde{F}_{\text{XUV}}(\omega) \approx F_{\text{XUV}} = \frac{1}{\sqrt{2\pi}} \int F_{\text{XUV}}(t) e^{i\omega t} dt, \quad (7.6)$$

the absorption spectrum

$$A(\omega) \propto \omega \mathbf{Im} \left[\frac{\tilde{d}(\omega)}{\tilde{F}_{\text{XUV}}(\omega)} \right] \quad (7.7)$$

can hence be used to access the real-time dynamics of the system and to reconstruct the dipole response $d(t)$. In order to focus on the dynamics of one excited state, e.g., $|a\rangle$, and its associated dipole response $d_a(t)$, one selects a spectral range centered on the central energy E_a which is sufficiently broad to access the fine temporal details induced by the subsequent NIR excitation. For absorption spectra of ultrashort XUV pulses, this spectral range is bounded by the bandwidth of the XUV pulse, which in turn implies that the best achievable temporal resolution is given by the duration of the XUV pulse. In general, however, this is not a limitation for accessing the strong-field dynamics induced by the NIR pulse. For an ultrashort excitation $F_{\text{XUV}}(t)$, both ω and $\tilde{F}_{\text{XUV}}(\omega)$ can be assumed to be constant in the selected spectral range, and the absorption spectrum $A(\omega)$ is thus proportional to the imaginary part of the system's frequency response

$$A(\omega) \propto \omega \mathbf{Im} \left[\frac{\tilde{d}(\omega)}{\tilde{F}_{\text{XUV}}(\omega)} \right] \approx \omega_X \frac{\mathbf{Im}[\tilde{d}(\omega)]}{F_{\text{XUV}}}. \quad (7.8)$$

Together with Eq. (7.4) this implies that the absorption spectrum can be used to uniquely reconstruct the time response of the system $d(t)$ for times $t > 0$ following the excitation:

$$d(t) \propto \mathcal{F}^{-1}[iA(\omega)](t) = \frac{i}{\sqrt{2\pi}} \int_{-\infty}^{+\infty} A(\omega) e^{-i\omega t} d\omega \quad \text{for } t > 0. \quad (7.9)$$

Our method as outlined above is closely related to the time-domain method of Peterson and Knight [242], where causality is invoked in the time domain to investigate the response

of a linear, time-translation invariant system. The present work generalizes this approach to access the full response of a system even in the presence of strong interactions which break time-translation invariance. For this we require the coherent broadband spectrum of an ultrashort laser pulse which initiates the dynamics and defines a zero-point in time. In this way, the full response of an explicitly not time-translation invariant system, due to the presence of the additional nonlinear interaction with the NIR pulse can be directly accessed (to all orders), instead of employing a perturbation-theory approach for the treatment of the interaction.

7.3. Application to Rabi flopping between doubly excited states in helium

In the following we first show a theoretical comparison of the retrieved dipole moment with the occupation of doubly excited states for two different NIR wavelengths. Second we show a comparison with experiment [70] where we reconstruct the time-dependent response for the prototypical system of doubly excited states in helium excited by an ultrashort attosecond pulse and subsequently driven by a strong few-cycle NIR laser field. We compare the experimental results to two independent theoretical calculations: a full *ab initio* simulation of the helium atom with the XUV and NIR field and a few-state model which includes only a limited number of doubly excited states.²⁴

7.3.1. Comparison of dipole oscillations with occupations of doubly excited states

We demonstrate now that the above mentioned reconstruction method [Eq. (7.9)] is capable of reconstructing the occupation of the $2s2p$ level during the interaction with an NIR laserfield. The helium atom is excited with an ultrashort XUV and the subsequent NIR pulse has a time delay of $\tau_d = 53.5$ fs ensuring that the exciting XUV pulse has no temporal overlap with the driving NIR field. We simulate the response to two different wavelengths of the NIR field [$\lambda_{\text{NIR}} = 740$ nm ($\omega = 1.67$ eV) and $\lambda_{\text{NIR}} = 538$ nm ($\omega = 2.3$ eV)] to couple the $2s2p$ state near-resonantly with the $(2p^2) \ ^2S^e$ and $(2s^2) \ ^2S^e$ state, respectively [Tab. 5.1]. The total duration of the NIR pulse is chosen long enough to enable the observation of multiple Rabi cycles, see App. J.2.9 for the numerical details.

To be able to resolve the time-dependent dipole moment of just the $2s2p$ resonance from the absorption spectrum we multiply the absorption signal $A(\omega)$ with a Gaussian window function centered at the resonance energy E_a and a width σ of 1 eV

$$A_{\text{filt}}(\omega) = A(\omega)e^{-\frac{(\omega-E_a)^2}{2\sigma^2}}. \quad (7.10)$$

Applying the dipole-reconstruction [Eq. (7.9)] to the spectrally filtered absorption signal $A_{\text{filt}}(\omega)$ we are able to resolve at least four Rabi cycles of the dipole moment d_{rec} for

²⁴ The few-state model was primarily developed by the group of Thomas Pfeifer.

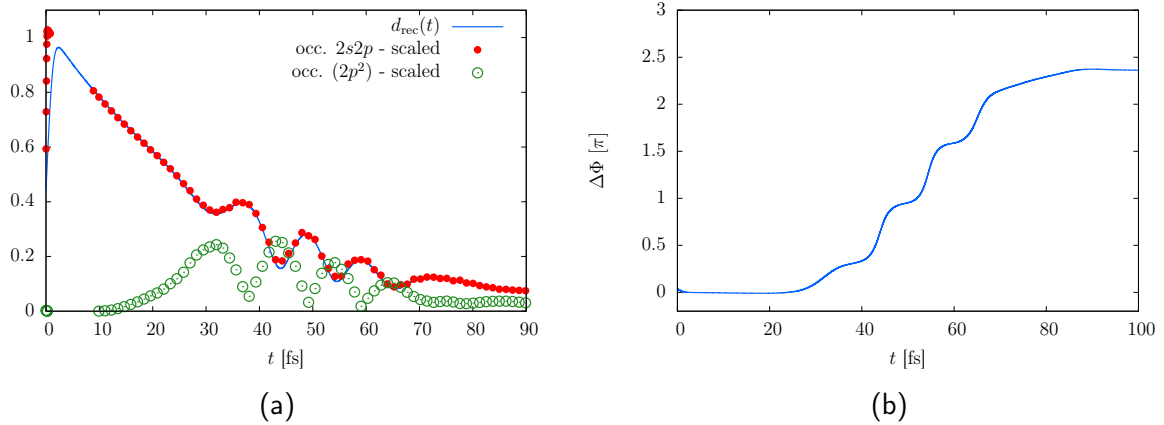


Figure 7.6.: (a) Reconstructed dipole moment (blue line) compared to the scaled occupation of the $2s2p$ (red dots) and the $(2p^2)^2S^e$ (green circles) state. (b) Retrieved phase of the dipole response shown in (a). The intensity of the NIR field is 2 TW/cm^2 with a FWHM duration of $T = 45 \text{ fs}$ and $\lambda_{\text{NIR}} = 740 \text{ nm}$. The time delay between the exciting XUV and probing NIR is $\tau_d = 53.5 \text{ fs}$.

$\lambda_{\text{NIR}} = 740 \text{ nm}$ [Fig. 7.6a]. The oscillations coincide very well with the occupation of the $2s2p$ state. The only free parameter is a global pre-factor corresponding essentially to the dipole matrix element between the groundstate and the doubly excited state. The reconstructed phase shows jumps located at the minima of the amplitude of the dipole response and increases steplike with time, see Fig. 7.6b. As the sign of the phase jump is always positive we can conclude that for this field strength the $2s2p$ state is coupled solely to the energetically higher lying $(2p^2)^2S^e$ resonance and not to the energetically lower $(2s)^2S^e$ state.

Using the same procedure for the case where the $2s2p$ state is coupled to the energetically lower $(2s^2)$ state [$\lambda_{\text{NIR}} = 538 \text{ nm}$], we observe only two Rabi cycles [Fig. 7.7a]. Nevertheless, the time-dependent occupation of the $2s2p$ state coincides almost perfectly with the reconstructed dipole moment $d_{\text{rec}}(t)$. Close to each minimum of $d_{\text{rec}}(t)$ the occupation of the $(2s^2)$ resonance peaks and the phase of the dipole moment drops rapidly as expected for Rabi oscillations, see Fig. 7.7b. Contrary to the case where the $2s2p$ state is coupled to the higher energetic $(2p^2)$ state the phase variation is negative.

These results show that the time-dependent dipole response retrieved from Eq. (7.9) can be used to monitor the occupation of doubly excited states during their interaction with laser fields.

7.3.2. Retrieving dynamics of doubly excited states from experimental data

Before comparing the experimental data to the theoretical calculations, we briefly discuss the experimental setup and introduce a few-state model which we will use to interpret our

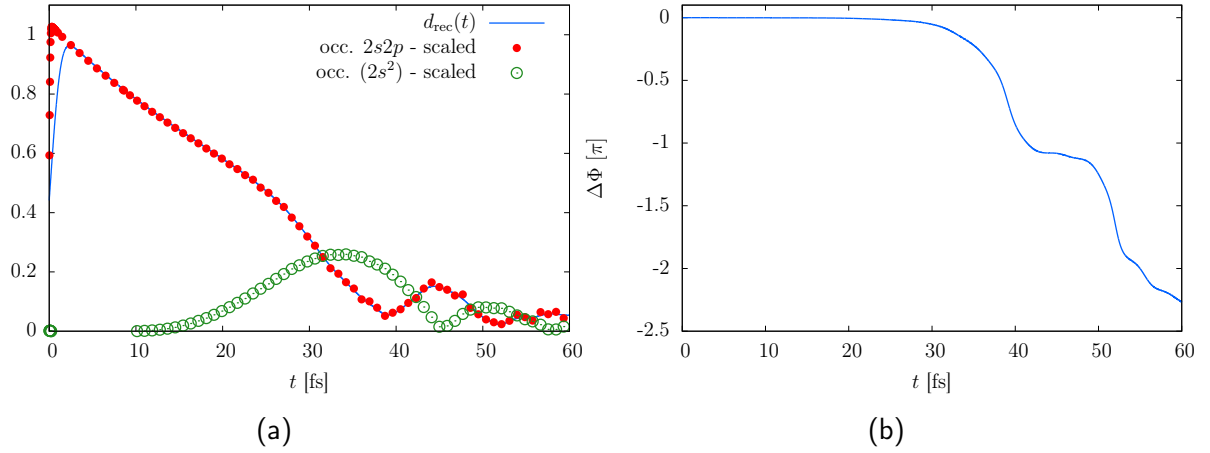


Figure 7.7.: (a) Reconstructed dipole moment (blue line) compared to the scaled occupation of the $2s2p$ (red dots) and the $(2s^2) 2S^e$ (green circles) resonance. (b) Retrieved phase of the dipole response shown in (a). The intensity of the NIR was 2 TW/cm^2 with a FWHM duration of $T = 45 \text{ fs}$ and $\lambda_{\text{NIR}} = 538 \text{ nm}$. The time delay between the exciting XUV and probing NIR is $\tau_d = 53.5 \text{ fs}$.

observations. The parameters for the *ab initio* simulation are given in App. J.2.10.

Experimental setup [70]

The experimental setup as displayed in Fig. 7.8 employs a typical attosecond transient-absorption beam line [44]. The doubly excited states of helium in the $1P^o$ symmetry are coherently excited by XUV attosecond-pulsed light defining the time $t_0 = 0$ for the measurement. The system then interacts with a sub-7-fs (full width at half maximum of intensity) NIR laser pulse ($\omega_{\text{IR}} \approx 1.7 \text{ eV}$) after a fixed time delay of $\tau = 7.4 \pm 0.1 \text{ fs}$. This delay was chosen to minimize the temporal overlap between the NIR and the XUV pulse, while ensuring that the NIR pulse still strongly drives the two-electron excited-state

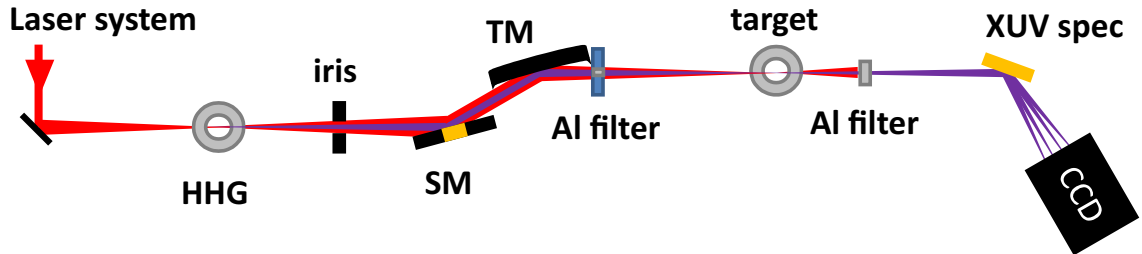


Figure 7.8.: Illustration of the experimental apparatus: High-harmonic generation neon gas target (HHG), split-mirror setup for setting the XUV-NIR time delay (SM), toroidal mirror (TM), XUV flat-field spectrometer (XUV spec).

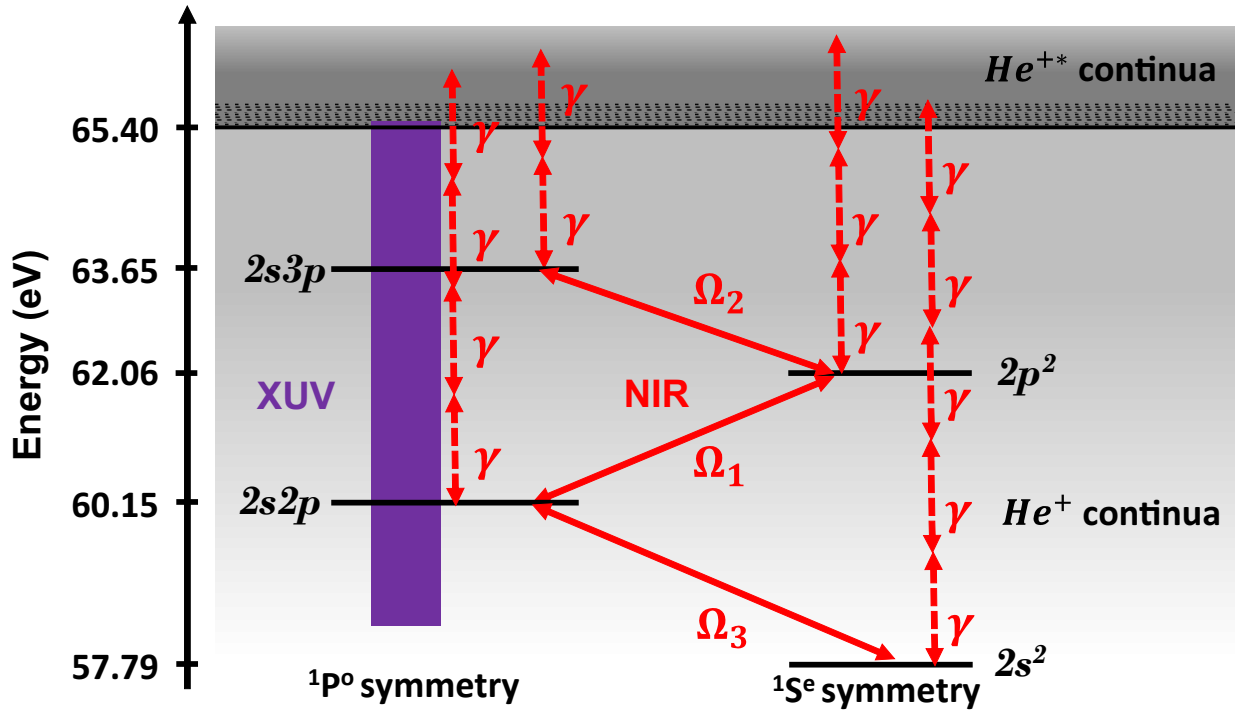


Figure 7.9.: Level scheme of the doubly excited states of helium included in the few-level system (see Tab. 5.1 for the resonance parameters). The violet background highlights the states which can be excited the XUV. The NIR pulse induces resonant couplings Ω_1 , Ω_2 , Ω_3 between the autoionizing doubly excited states, modifies the autoionization, and drives strong-field ionization at the highest intensities as indicated by the dashed red lines.

dynamics on a timescale prior to a significant depletion of the $2s2p$ state. The experiments were performed by the group of Thomas Pfeifer at the Max Planck Institute of Nuclear Physics.

Few-state model

Together with the group of Thomas Pfeifer we extend the few-state model developed in his group [44, 68, 70] to obtain more insights into the Rabi flopping dynamics. While the model is expected to yield good agreement for low NIR intensities where Rabi flopping is the dominating process, for high intensities only the full *ab initio* calculation can be expected to agree with experiment. The reason being the inadequate treatment of strong-field ionization processes in the few-state model.

The few-state model includes all states shown in Fig. 7.9, as well as autoionization and multiphoton ionization rates (orange lines). To be precise, it consists of the ground state $|g\rangle \equiv (1s^2) {}^1S^e$ and the four doubly excited autoionizing states $|a\rangle \equiv (2s^2) {}^1S^e$, $|b\rangle \equiv (2s2p) {}^1P^o$, $|c\rangle \equiv (2p^2) {}^1S^e$ and $|d\rangle \equiv (2s3p) {}^1P^o$ with energies E_g , E_a , E_b , E_c and E_d . The four doubly excited states are coupled to the corresponding continuum states via $V_{a,\epsilon s}$,

$V_{c,\epsilon s}$, and $V_{b,\epsilon p}$, $V_{d,\epsilon p}$ which are assumed to be independent of the energy of the continuum states [38, 63]. The resonance energies and linewidths of all considered resonances are given in Tab. 5.1. The dipole-moment matrix elements between the autoionizing states are $\mu_{ab} = -1.56$ a.u., $\mu_{bc} = 2.17$ a.u. and $\mu_{cd} = -0.81$ a.u. [68], see Tab. 7.1. The quasi-discrete states used to model the relevant continuum states $|\epsilon p\rangle$ and $|\epsilon s\rangle$ have energies ranging from $E_{\min} = 24.8$ eV, to $E_{\max} = 106.7$ eV. The parameters $V_{a,\epsilon s}$, $V_{b,\epsilon p}$, $V_{c,\epsilon s}$, $V_{d,\epsilon p}$, μ_{gb} , μ_{gd} , and $\mu_{g,\epsilon p}$ were set in order to reproduce known experimental and theoretical line shapes. In the absence of an analytical model for nonlinear laser ionization of doubly excited states, we employ in the few-state model state-dependent ionization rates $\Gamma_n = \alpha_n I_{\text{NIR}}(t)^n$. The empirical multi-photon ionization parameters α_2 , α_3 , α_4 and α_5 are determined in order to reach best possible quantitative agreement between the experiment and our calculations for the highest intensity and kept the same for all other intensities. The power n of the NIR intensities corresponds to the number of photons necessary to reach the next ionization threshold in this multi-photon ionization model.

Inserting the ansatz

$$|\psi(t)\rangle = c_g(t) |g\rangle + c_a(t) |a\rangle + c_b(t) |b\rangle + c_c(t) |c\rangle + c_d(t) |d\rangle + c_{\epsilon p}(t) |\epsilon p\rangle + c_{\epsilon s}(t) |\epsilon s\rangle \quad (7.11)$$

for the wavefunction into the time-dependent Schrödinger equation yields

$$\begin{aligned} i\partial_t c_g &= E_g c_g \\ i\partial_t c_a &= [E_a - i\alpha_5 I_{\text{NIR}}^5(t)] c_a - \mu_{ab} F_{\text{NIR}}(t) c_b + V_{a,\epsilon s} c_{\epsilon s} \\ i\partial_t c_b &= -\mu_{gb}^* F_{\text{XUV}}^+(t) c_g - \mu_{ab} F_{\text{NIR}}(t) c_a + [E_b - i\alpha_4 I_{\text{NIR}}^4(t)] c_b - \mu_{bc} F_{\text{NIR}}(t) c_c + V_{b,\epsilon p} c_{\epsilon p} \\ i\partial_t c_c &= -\mu_{bc} F_{\text{NIR}}(t) c_b + [E_c - i\alpha_3 I_{\text{NIR}}^3(t)] c_c - \mu_{cd} F_{\text{NIR}}(t) c_d + V_{c,\epsilon s} c_{\epsilon s} \\ i\partial_t c_d &= -\mu_{gd}^* F_{\text{XUV}}^+(t) c_g - \mu_{cd} F_{\text{NIR}}(t) c_c + [E_d - i\alpha_2 I_{\text{NIR}}^2(t)] c_d + V_{d,\epsilon p} c_{\epsilon p} \\ i\partial_t c_{\epsilon p} &= -\mu_{g,\epsilon p}^* F_{\text{XUV}}^+(t) c_g + V_{b,\epsilon p}^* c_b + V_{d,\epsilon p}^* c_d + \left[\frac{p^2}{2} - i\Gamma_{\epsilon p} \right] c_{\epsilon p} \\ i\partial_t c_{\epsilon s} &= V_{a,\epsilon s}^* c_s + V_{c,\epsilon s}^* c_c + \left[\frac{p^2}{2} - i\Gamma_{\epsilon s} \right] c_{\epsilon s}. \end{aligned} \quad (7.12)$$

The constant line widths $\Gamma_{\epsilon p}$ and $\Gamma_{\epsilon s}$ are employed in order to broaden the quasi-discrete continuum states.

The interaction of the helium atom with the XUV pulse is treated in first-order perturbation theory, thereby assuming that $\partial_t c_g = E_g c_g$, i.e., $[c_g(t)]^2 = 1$. We apply the rotating-wave approximation for the XUV field

$$\begin{aligned} F_{\text{XUV}}(t) &= F_{\text{XUV}}^{(0)} f(t) \cos(\omega_{\text{XUV}} t) = \frac{F_{\text{XUV}}^{(0)} f(t)}{2} (e^{i\omega_{\text{XUV}} t} + e^{-i\omega_{\text{XUV}} t}) \\ F_{\text{XUV}}(t) &\approx \frac{F_{\text{XUV}}^{(0)} f(t)}{2} e^{i\omega_{\text{XUV}} t} = F_{\text{XUV}}^+(t), \end{aligned} \quad (7.13)$$

where $f(t)$ is the XUV pulse envelope and $F_{\text{XUV}}^{(0)}$ is the peak field of the XUV pulse.

Retrieval of dipole dynamics from experimental and theoretical data

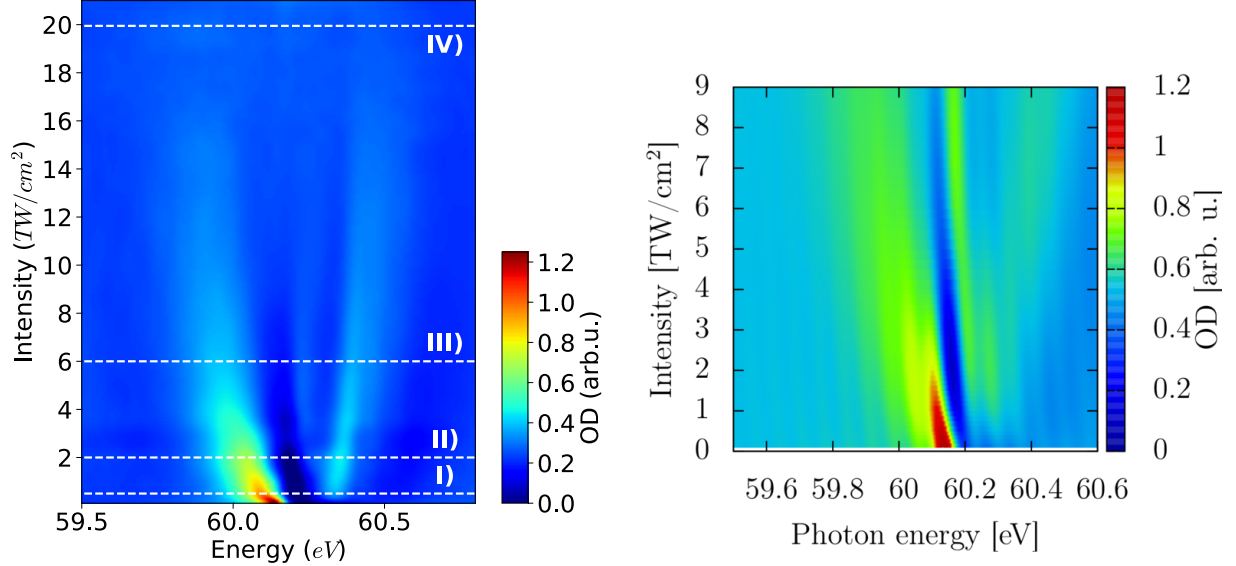


Figure 7.10.: (a) Experimental NIR intensity scan of the Autler-Townes splitting [147] close to the $2s2p$ resonance in helium at fixed time delay $\tau = 7.4 \pm 0.1$ fs. (b) Intensity scan of the Autler-Townes splitting of the $2s2p$ resonance for a fixed time delay $\tau = 7.4$ fs using the *ab initio* simulation. The white dashed lines I-IV in panel (a) show the spectra used in the reconstruction discussed in Fig. 7.11.

The experimentally observed transient absorption spectrum as function of the NIR intensity clearly shows that the $2s2p$ resonance exhibits an Autler-Townes splitting [147], primarily due to the coupling with the $(2p^2)$ $^2S^e$ autoionizing state [Fig. 7.10a]. Even though, there are differences visible between the theoretical prediction obtained from the *ab initio* simulation [Fig. 7.10b] and the experimental data we observe good qualitative agreement for the optical density in the resonance region for both data sets. The remaining differences indicate that most likely the experimentally employed pulse shape and intensity do not perfectly coincide with the parameters used in the simulation.

We reconstruct both the amplitude and the phase of the time-dependent dipole moment (TDDM) $d_{2s2p}(t)$ for four different NIR intensities [white dashed lines in Fig. 7.10a] and normalize all curves to the curve at vanishing NIR intensity, see Fig. 7.11. To isolate the dipole response of the $2s2p$ resonance we apply a Gaussian window function to the absorption spectrum [Eq. (7.10)] with $\sigma = 1$ eV.

The four NIR intensities represent different regimes of strong-field interaction from the weak perturbative regime to the regime of strong coupling and strong-field ionization of autoionizing states. For NIR intensities of $I_{\text{NIR}} = 0.5$ TW/cm² and 2.0 TW/cm², the TDDM amplitude displays increasingly pronounced minima. For even higher NIR inten-

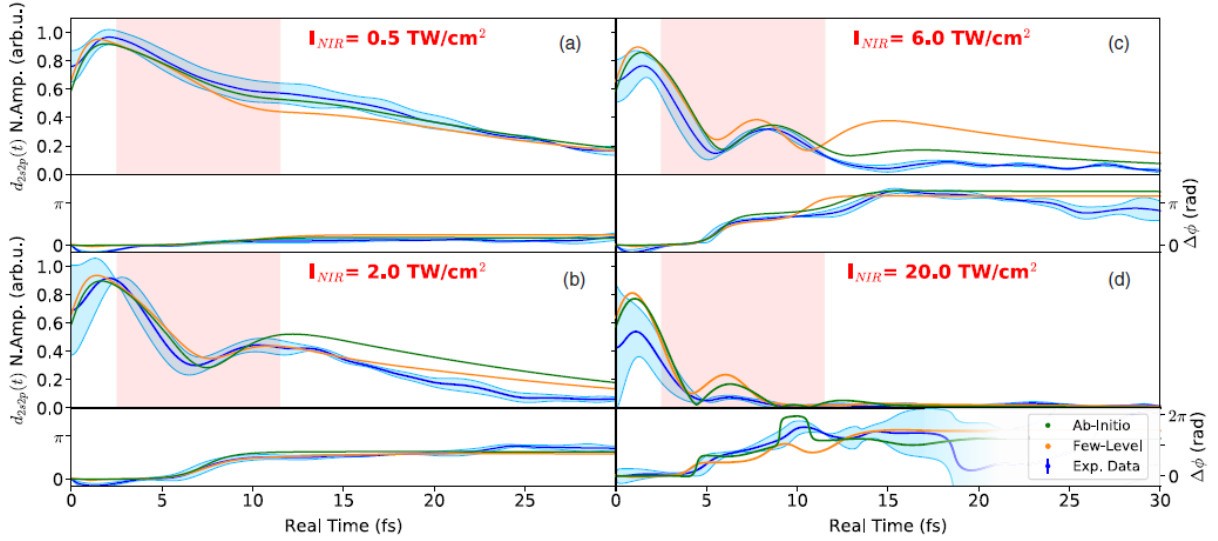


Figure 7.11.: Time-dependent dipole moment (TDDM) $d_{2s2p}(t)$ of the doubly excited helium $2s2p$ state applying a spectral filter [Eq. 7.10] centered at 60.15 eV with a width of 1 eV: Reconstructed TDDM amplitude and phase change (modulo 2π , blue), showing the emerging departure from the simple exponential decay during the interaction with the central part of the NIR pulse (red shaded area) for (a) $I_{\text{NIR}}=0.5$ TW/cm², (b) $I_{\text{NIR}}=2.0$ TW/cm², (c) $I_{\text{NIR}}=6.0$ TW/cm², and (d) $I_{\text{NIR}}=20.0$ TW/cm². The experimental error bars (blue shaded area) show the standard deviations of the reconstructed time-dependent response obtained by employing the data sets measured at time delay $\tau \pm T_{\text{NIR}}/2$ (where $T_{\text{NIR}} = 2.5$ fs is the optical cycle of the NIR field). The orange curves show the calculated amplitude and phase evolution of the TDDMs using a few-state model [Eq. (7.12)]. The green lines represent *ab initio* calculations.

sities of $I_{\text{NIR}} = 6.0 \text{ TW/cm}^2$ and $I_{\text{NIR}} = 20.0 \text{ TW/cm}^2$, several temporal oscillations are observed with rapid phase changes near each minimum of the amplitude. The *ab initio* simulation confirms the reconstructed dipole response for this strongly driven system. Deviations at early (0-1 fs) and late times may result from the non-Gaussian experimental pulse shape and the experimental limitation of the measurement of spectrally very broad and low-signal line shapes, which would require very long measurement times and a more precise determination of the reference spectrum not possible with the current experimental setup.

As the driving NIR pulse is very short the time-dependent dipole response is expected to depend on the carrier-envelope phase (CEP) of the NIR pulse. The *ab initio* calculation allows to explicitly verify this expectation, where we observe that both the amplitude and the phase of the dipole response depend on the CEP, see Fig. 7.12. This result suggests that the dipole reconstruction might also be used to determine the experimental CEP. Comparing the results of the *ab initio* simulation with the experimental data, with undetermined but constant CEP, we achieved the best agreement for a CEP of $\pi/4$.

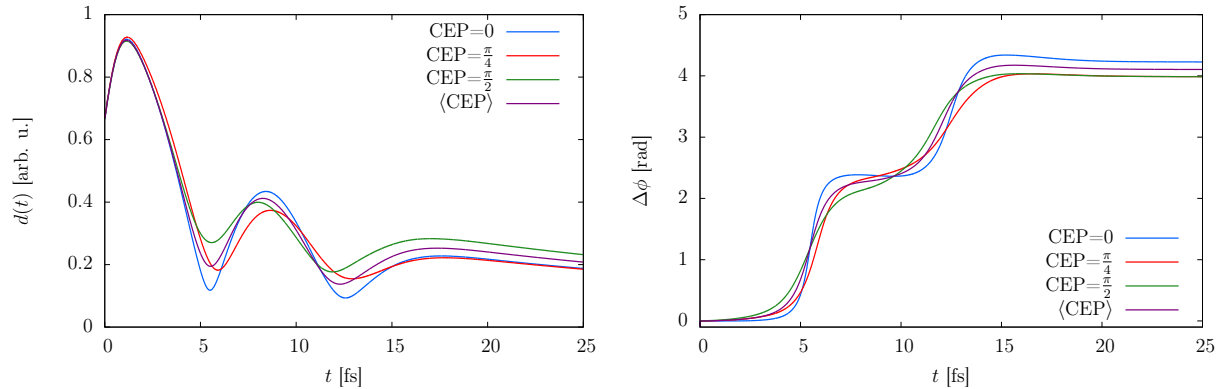


Figure 7.12.: Reconstructed (a) dipole moment and (b) phase for an NIR intensity of 6 TW/cm^2 and time delay $\tau = 7.4 \text{ fs}$ for different carrier envelope phases (CEP) of the NIR field. $\langle \text{CEP} \rangle$ stands for the incoherent average over the CEP.

The *ab initio* simulations allow us to explicitly test the dependence of the retrieved dipole response and phase on the XUV pulse duration (set to 250 as FWHM for the results shown in Fig. 7.11), see Fig. 7.13. Even for the longest pulse duration (4 fs) Rabi oscillations are clearly visible accompanied by rapid phase variations. The overall shape of the reconstructed dipole is not modified drastically, apart from the initial excitation time ($t < T_p$). The reconstructed phase variation yields similar results for all employed pulse durations. These results clearly show that the overall dipole response can be retrieved accurately as long as the excitation time is short compared to the time scale of the driven system.

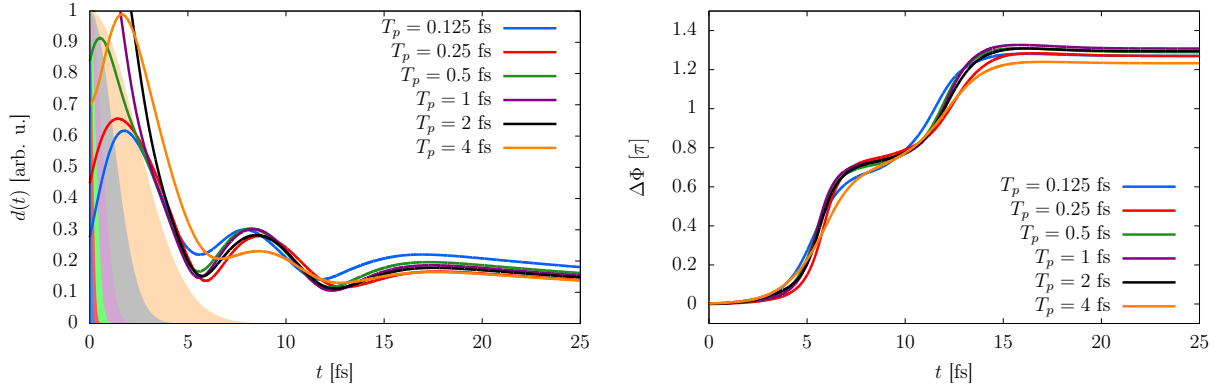


Figure 7.13.: Reconstructed (a) dipole moment and (b) phase for different FWHM pulse durations T_p of the exiting XUV pulse. The time delay between the XUV and IR is $\tau = 7.4$ fs and the NIR intensity is 6 TW/cm^2 for all pulse durations. The shaded areas in (a) represent the intensity envelope of the respective XUV pulses.

7.3.3. Strong field dynamics

Comparison between the few-level model and the *ab initio* calculation allows further insights into the strong-field driven coupling dynamics. For weak XUV excitations and subsequent interactions which leave the ground state unaffected, the dipole is directly related to the amplitude (and thus population, see also Sec. 7.3.1) of the excited state. The minima in the amplitude combined with the associated phase changes, therefore, indicate a significant resonant population transfer due to Rabi oscillations mostly between the $2s2p$ and the $(2p^2)$ states. The increasing number of minima with increasing NIR intensity directly follows from the field dependence of the generalized Rabi frequency $\Omega_{R,ij} = \sqrt{\Delta_{ij}^2 + \Omega_{ij}^2(t)}$ with $\Omega_{ij}(t) = F_{\text{NIR}}(t)\mu_{ij}$, where $\mu_{ij} = \langle i | \hat{\mu} | j \rangle$ is the transition dipole matrix element connecting two doubly excited states, and Δ_{ij} is the respective detuning of the laser from the transition frequency between state $|i\rangle$ and $|j\rangle$.

At higher intensities, the overall decrease in the TDDM amplitude as a function of time shows that contributions of NIR-driven ionization can no longer be neglected. The amplitude evolution of the TDDM predicted by the few-state model shows not quantitative but still qualitative agreement with the dipole moment retrieved from the experimental data and the *ab initio* results at higher NIR intensities.

From the phase evolution at highest intensity shown in Fig. 7.11, even the Rabi cycling to the $(2s^2)$ excited state, albeit not resonantly coupled, can be unambiguously detected by the phase change by about $-\pi$ near 10 fs, visible in both experiment and *ab initio* calculation. This state plays a significant role in the strongly driven quasi-bound state dynamics and has to be accounted for explicitly in the few-state model in order to achieve at least qualitative agreement with the experimental results and the *ab initio* simulation. The presented approach allows to reconstruct the TDDM and to explore the transition from few-level to complex multi-level coupling dynamics for increasing field strength. For

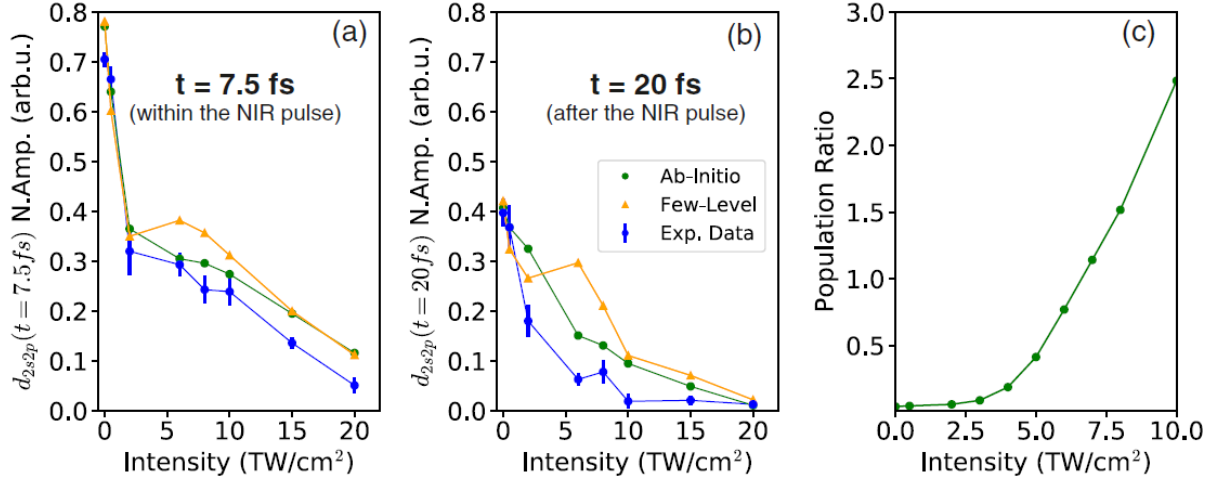


Figure 7.14.: (a) Amplitude of the reconstructed response at time $t=7.5$ fs during the interaction with the NIR pulse (at time delay $\tau = 7.4$ fs). (b) Amplitude of the reconstructed response at real time $t=20$ fs, i.e., after the interaction with the NIR pulse has concluded. (c) The population ratio between the population in 24 excited states excluding the four states used in the few-level simulation and the population in these four states after the strong-field interaction at $t=20$ fs, extracted from the *ab initio* simulation. For a complete list of the states projected on we refer to App. I.

both theory and experiment, Fig. 7.14a, and b show the amplitude of the reconstructed response at real time $t = 7.5$ fs and 20 fs after the excitation, respectively. In both cases, the *ab initio* simulation agrees reasonably well with the experiment. The few-level model, however, starts to disagree significantly, not only quantitatively but also qualitatively, above an intensity threshold of about 2 TW/cm². This result can qualitatively be explained by results obtained from the *ab initio* simulation, shown in Fig. 7.14c. For higher intensities ($I_{\text{NIR}} > 2$ TW/cm²) the number of doubly excited states which are coupled by the NIR field and, thus, participate in the multi-level Rabi dynamics increases drastically. This increased number of relevant states explains the breakdown of the few-state model. Additionally, the *ab initio* simulations clearly show that the assumption in the few-state model of neglecting ionization to the adjacent continua is no longer viable. In other words, the interaction with the NIR field does substantially modify the autoionization process [44]. As the time-domain reconstruction approach described in Eq. (7.9) makes no assumptions about the system under study, it is generally applicable, also to more complex systems. It is viable for single-shot transmission spectra, which could be of use at short-wavelength free-electron lasers. Here, the nonlinear response could be used to uncover the in-situ timing and ensuing dynamics of X-ray and optical pulses which is otherwise often lost due to a temporal jitter.

8. Two-photon double ionization with elliptically polarized light fields

After we have characterized the single ionization continuum in detail we proceed to an investigation of the correlated double continuum in the last part of this thesis. One of the simplest double-ionization processes where correlation induced by the electron-electron interaction plays a significant role, is two-photon double ionization (TPDI) of atomic helium. Thus TPDI has been the focus of many theoretical studies in recent years employing linearly polarized ultrashort XUV pulses, e.g. [89–94, 97, 243–249]. One of the reasons for this being that TPDI for helium can still be handled with virtual exact solutions of the two-electron Schrödinger equation implicating that a detailed understanding of the underlying physics can be obtained. Experimental observation of many of the predicted characteristics, however, has not been possible so far due to the very low double ionization cross section and the limited experimental pulse intensity available. With the recent advent of intense XUV sources based on HHG at ELI-ALPS [250] and increasing number of free-electron lasers (FEL) which produce very intense, high energy photon beams this might change in the near future.

Within this thesis, we will consider TPDI of atomic helium with elliptically polarized light fields, which has only been discussed by very few works [251–254] due to the required high computational effort, and compare to results obtained for linearly polarized pulses. We will start by briefly reviewing the difference between sequential and nonsequential TPDI based on the energy of the ionizing pulse and how this distinction gets blurred for ultrashort pulses. We then discuss similarities and differences observed for total cross sections and angular distributions depending on the ellipticity of the lights fields. Finally, we will show how interference patterns in the doubly differential energy distribution can be controlled for XUV-XUV pump-probe sequences employing elliptically polarized light fields. In the spirit of previous studies with linearly polarized fields [243, 245–247, 255, 256], we show that the joint angular distribution of the ejected electrons allows to distinguish between electrons emitted nonsequentially within one pulse, or sequentially by absorbing one photon out of each pulse.

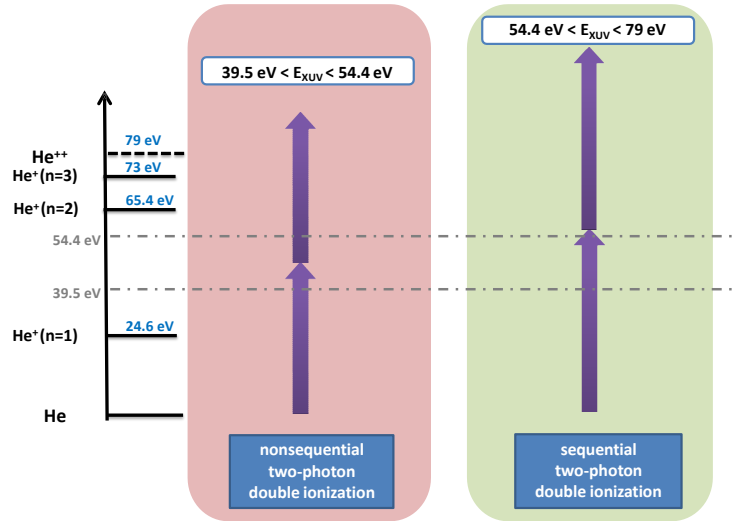


Figure 8.1.: Sketch of the difference between nonsequential (red) and sequential (green) two-photon double ionization (TPDI). For photon energies between 39.5 eV and 54.4 eV two-photon double ionization can only occur for near-simultaneous absorption of both photons giving rise to nonsequential TPDI. For photon energies > 54.4 eV the absorption of either of the photons can happen at any time during the interaction of the atom with the laser pulse via intermediate on-shell transitions in the $\text{He}^+(n > 2)$ manifold giving rise to sequential TPDI. If the photon energy is above the double ionization threshold of 79 eV absorption of one photon is sufficient to doubly ionized helium (one-photon double ionization).

8.1. Sequential and nonsequential two-photon double ionization

In the long pulse limit the distinction between sequential and nonsequential two-photon double ionization has traditionally been based on the central energy of the ionizing pulse, see Fig. 8.1 for a sketch of the two spectral regions. To overcome the double ionization threshold of helium (approximately 79 eV) by absorption of two photons the minimum energy for the ionizing XUV pulse E_{XUV} is roughly 39.5 eV. The total double ionization threshold is the sum of the ionization potential of neutral helium, $I_{p,1} = 24.6$ eV, and the ionization potential of $\text{He}^+(n = 1)$, $I_{p,2} = 54.4$ eV. As the two ionization potentials are quite different from each other it is possible that although the total energy transferred to the atom by absorption of two photons is sufficient to doubly ionize helium, one photon does not provide enough energy to overcome the second ionization potential $I_{p,2} = 54.4$ eV. The electrons can however exchange energy with each other via electron-electron interaction and leave the helium atom at almost the same time. This energy regime between $39.5 \text{ eV} < E_{\text{XUV}} < 54.4 \text{ eV}$ is called nonsequential two-photon double ionization regime. As the ejection of the two electrons cannot happen independently the absorption of the two

photons has to occur near-simultaneous even for long pulses. Contrary, for $E_{\text{XUV}} > 54.4$ eV the ionization of the two electrons does not need to be correlated in time as the photon energy is higher than both the first and the second ionization potential. This regime is thus called sequential two-photon double ionization regime. For photon energies above the double-ionization threshold (79 eV) double ionization can also be triggered by absorption of one photon alone (one-photon double ionization [257]).

A long debated question was the total double-ionization cross section in the non-sequential regime and associated with this also angle-resolved cross sections which provide insight into electron-electron correlation [58, 88–97, 243, 245, 256, 258]. Interestingly, even for XUV pulses in the spectrally sequential regime with central energies above $I_{p,2}$, TPDI becomes nonsequential in the time domain as the first electron is still in the vicinity of the ion when the second absorption process takes place. Exchange of energy and angular momentum between the departing electrons, referred to in the following as dynamical Coulomb correlation, persists which strongly depends on the duration of the ionizing pulse [244, 245].

8.2. Cross sections for TPDI

We start by comparing two-photon double-ionization cross sections for atomic helium obtained for ionization by perfectly circularly and linearly polarized pulses. The two-photon double ionization yield is given by [89]

$$\sigma_2 \approx \left(\frac{\omega}{I_0}\right)^2 \frac{1}{T_{\text{eff},2}} \int dE_1 dE_2 d\Omega_2 d\Omega_1 P(E_1, E_2, \Omega_1, \Omega_2), \quad (8.1)$$

where I_0 is the peak intensity, ω the central frequency of the XUV pulse and the effective time $T_{\text{eff},2}$ for the two-photon absorption is given by

$$T_{\text{eff},2} = \int dt \left(\frac{I(t)}{I_0}\right)^2. \quad (8.2)$$

Eq. (8.1) becomes exact for infinite pulse durations. The triply differential cross section (TDCS) for emitting one electron with energy E_1 into direction Ω_1 , while the other electron is emitted into direction Ω_2 is given by

$$\frac{d\sigma_2}{dE_1 d\Omega_1 d\Omega_2} \approx \left(\frac{\omega}{I_0}\right)^2 \frac{1}{T_{\text{eff},2}} \int dE_2 P(E_1, E_2, \Omega_1, \Omega_2). \quad (8.3)$$

Another distribution frequently referred to in this thesis is the joint angular distribution which is the cross section for one electron emitted in direction Ω_1 , while the other one is emitted in direction Ω_2

$$P(\theta_1, \theta_2, \phi_1, \phi_2) = \frac{d\sigma_2}{d\Omega_1 d\Omega_2} \approx \left(\frac{\omega}{I_0}\right)^2 \frac{1}{T_{\text{eff},2}} \int dE_1 dE_2 P(E_1, E_2, \Omega_1, \Omega_2), \quad (8.4)$$

integrated over both electron energies E_1 and E_2 . The joint angular distribution is a very effective way to characterize electron correlations [97, 244, 259].

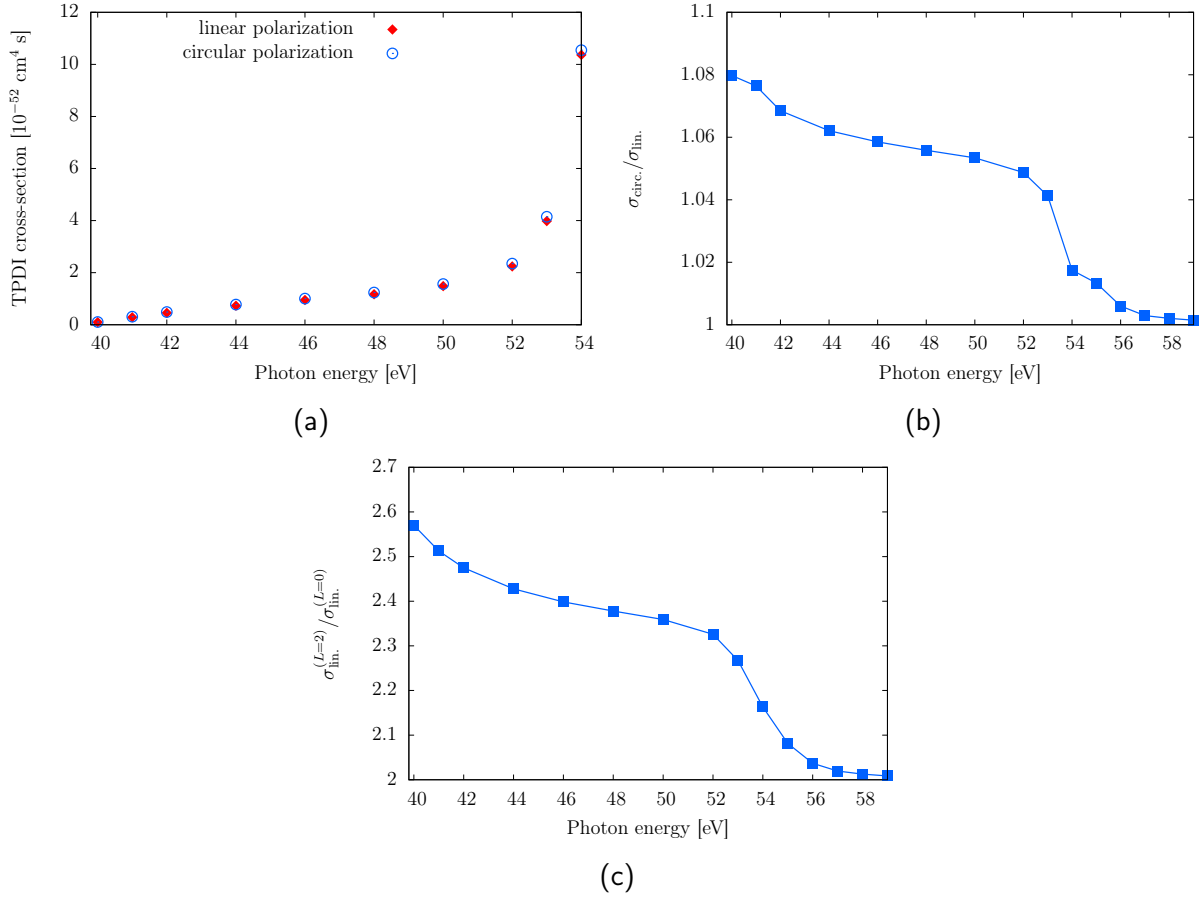


Figure 8.2.: Comparison of the total two-photon double ionization cross section [Eq. 8.3] for linearly $\sigma_{\text{lin.}}$ and right-circularly polarized light fields $\sigma_{\text{circ.}}$ in the spectrally non-sequential regime. (a) Total TPDI cross section. (b) Ratio of the cross section for ionization by circularly and linearly polarized light fields. The FWHM pulse duration was $T_p = 2$ fs and the total peak intensity of the XUV pulse was $1 \times 10^{12} \text{ W/cm}^2$ for all employed pulses. (c) Ratio of the total TPDI cross section in the $L = 2$ and $L = 0$ channel for linearly polarized light fields. The values for linear polarization coincide with the results shown in [89]. Some of the calculations were performed in collaboration with Manuel Ederer during his master thesis.

To obtain converged results for the lowest photon energies the wave function was propagated up to 12 fs after the end of the pulse [98]. The close coupling expansion ($L_{\text{max}} = 3, \ell_1 = \ell_2 = 5$) employed for results shown in (a)-(c) is sufficient to obtain converged fully integrated TPDI cross section, but is not sufficient for converged TDCS or angular distributions [89].

Employed pulse parameters

For linearly polarized pulses, propagating along the \hat{x} axis and polarized along \hat{z} , the vector potential is given by

$$\mathbf{A}(t) = A_0 f(t) \begin{pmatrix} 0 \\ 0 \\ \sin(\omega(t - t_{\text{XUV}})) \end{pmatrix}, \quad (8.5)$$

with being t_{XUV} the peak time of the XUV pulse. The elliptical vector potential, propagating along the \hat{z} axis and polarized in the $\hat{x} - \hat{y}$ plane, is defined by

$$\mathbf{A}(t) = A_0 f(t) \begin{pmatrix} \sin(\omega(t - t_{\text{XUV}})) \\ -\epsilon \cos(\omega(t - t_{\text{XUV}})) \\ 0 \end{pmatrix}, \quad (8.6)$$

where ϵ is the ellipticity of the laser field. More details are given in App. J.2.11.

8.2.1. Spectrally nonsequential two-photon double ionization

Two-photon double ionization of helium in the spectrally nonsequential regime is one of the few examples where the effect of electron correlation on the dynamics is crucial while at the same time being computationally accessible with *ab initio* calculations. Especially the total cross section [Eq. (8.1)] has been investigated with many different methods resulting in considerably different results, e.g. [58, 89, 95, 243, 256, 258]. Consistency between the different approaches and an understanding of necessary requirements to correctly describe the double continuum has only been achieved in the years 2008 to 2010. We extend these studies by comparing the TPDI cross sections for linearly polarized σ_{lin} and circularly polarized fields σ_{circ} .

The total TPDI cross section for circularly polarized pulses is very similar to the cross section calculated for linearly polarized fields [89, 90] for a FWHM duration of 2 fs, see Fig. 8.2a. Close to the nonsequential threshold (39.5 eV) we find slightly larger values for σ_{circ} . The relative difference with respect to σ_{lin} gradually decreases with increasing photon energy and converges rapidly to zero close to the sequential threshold (54.4 eV). In the spectrally sequential regime the cross sections are almost identical for ionization with linearly or circularly polarized light fields, see Fig. 8.2b. Interestingly, the shape of the ratio of the cross sections $\sigma_{\text{circ}}/\sigma_{\text{lin}}$ closely resembles the ratio of the TPDI cross sections to the $L = 2$ and $L = 0$ channels, respectively, $\sigma_{\text{lin}}^{(L=2)}/\sigma_{\text{lin}}^{(L=0)}$ [Fig. 8.2c]. For purely sequential TPDI this ratio is given by the absolute square of the ratio of the respective Clebsch-Gordan coefficients

$$\left| \frac{\langle 1, 1, 1, 0 | 2, 0 \rangle}{\langle 1, 1, 1, 0 | 2, 0 \rangle} \right|^2 = \left| -\sqrt{\frac{2/3}{1/3}} \right|^2 = 2. \quad (8.7)$$

Similar as in Fig. 8.2b the largest deviation for $\sigma_{\text{lin}}^{(L=2)}/\sigma_{\text{lin}}^{(L=0)}$ is found close to the non-sequential threshold. This deviation decreases towards the sequential threshold where it

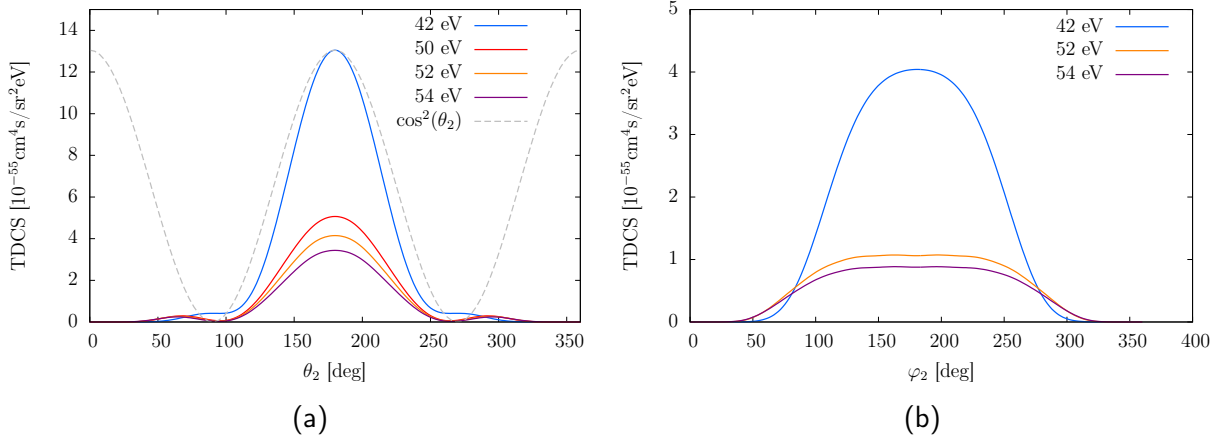


Figure 8.3.: Triply differential two-photon double ionization cross section (TDCS) [Eq. 8.1] for linearly and right-circularly polarized light fields in the nonsequential energy regime. (a) TDCS for ionization by a linearly polarized pulse along \hat{z} . The direction of the first electron was chosen to be $\theta_1 = 0^\circ$. The two azimuthal angles were set to $\varphi_1 = \varphi_2 = 0^\circ$. For ionization by linearly polarized fields the TDCS are independent of the azimuthal angles. The grey dashed line symbolizes the dipolar emission pattern [$\approx \cos^2(\theta_2)$] imprinted onto the TDCS for linearly polarized XUV pulses. (b) TDCS for ionization by a right-circularly polarized ($\epsilon = -1$) light field. The direction of the first electron was chosen to be $\varphi_1 = 0^\circ$. We report the TDCS within the polarization plane ($\hat{x} - \hat{y}$), resulting in $\theta_1 = \theta_2 = \pi/2$. The energy of the first electron E_1 was chosen to be half the excess energy (i.e. 2.5 eV for $\omega = 42$ eV, 10.5 eV for $\omega = 50$ eV, 12.5 eV for $\omega = 52$ eV, 14.5 eV for $\omega = 54$ eV) and we integrate over the energy of the second electron E_2 . The pulse duration was $T_p = 2$ fs and the peak intensity of the XUV pulse was 10^{12} W/cm² for all employed pulses.

drops rapidly and converges to the expected value of 2.

In contrast to the small differences found for the total TPDI cross sections, we expect more pronounced differences with respect to different XUV polarizations for the triply differential cross sections [Eq. (8.3)]. While for ionization by linearly polarized fields a dipolar emission pattern is clearly imprinted onto the TDCS, such an effect is absent for circular polarization. Thus any deviations from a straight line are caused by electron correlation. We fix the emission angles $\theta_1 = 0^\circ, \varphi_1 = \varphi_2 = 0^\circ$ ($\theta_1 = \theta_2 = 90^\circ, \varphi_1 = 0^\circ$) and monitor the TDCS as function of the remaining free angle θ_2 (φ_2) for ionization by linearly (circularly) polarized light fields. The energy of the first electron E_1 is set to half the total excess energy ($2 \times E_{\text{XUV}} - 79$ eV) and we integrate over the energy of the second electron, Eq. (8.3). While the TDCS for linearly polarized fields [Fig. 8.3a] are very narrow with respect to θ_2 due to the dipolar emission pattern [$\approx \cos^2(\theta_2)$] the TDCS for circularly polarized light fields [Fig. 8.3b] are very flat close to their maximum, which is for back-to-back emission ($\theta_2 = 180^\circ$ and $\phi_2 = 180^\circ$, respectively) for both cases. As the photon energy increases the TDCS decrease monotonically independent of the XUV polarization. For the case of circularly polarized fields the plateau like structure close to $\phi_2 = 180^\circ$ broadens with increasing XUV energy. The overall decrease of the TDCS can be explained by comparing the angle-integrated double ionization probabilities

$$P(E_1, E_2) = \int d\Omega_1 d\Omega_2 P(E_1, E_2, \Omega_1, \Omega_2). \quad (8.8)$$

for the different pulse energies, see Fig. 8.4. Close to the nonsequential threshold the double ionization probability is almost independent of the difference between the electron energies $\Delta E = E_1 - E_2$. Differently, $P(E_1, E_2)$ close to the sequential threshold is largest for very asymmetric energy sharing, where one electron is much more energetic than the other one [94]. Hence, even though the total TPDI cross section increases from 42 eV to 52 eV, the cross section at equal-energy sharing ($\Delta E = 0$) decreases.

8.2.2. Temporally nonsequential two-photon double ionization for elliptically polarized light fields

In the following we will investigate the regime of spectrally sequential but temporally nonsequential two-photon double ionization. We monitor the joint angular distributions [Eq. (8.4)] as a function of the ellipticity from the limit of linear polarization along \hat{x} to circular polarization for ultrashort pulses with energy of 70 eV. The pulse durations $T_p \lesssim 2$ fs correspond to a Fourier bandwidth $\Delta\omega_{\text{XUV}} \approx 2\pi/T_p > 2$ eV. Despite this considerable width, the spectral overlap with the energetically nonsequential regime ($\hbar\omega_{\text{XUV}} < I_{p,2} = 54.4$ eV) is still negligible. For TPDI by ultrashort XUV pulses electron-electron interactions in the double continuum leave a strong imprint on the energy and angular distribution of the emitted electron pair [94, 244, 245].

Within the polarization plane ($\theta_1 = \theta_2 = 90^\circ$) and for one electron emitted along the \hat{x} -axis, the joint angular distribution $P(\phi_2) = P(\theta_1 = \theta_2 = 90^\circ, \phi_1 = 0^\circ, \phi_2)$ strongly varies

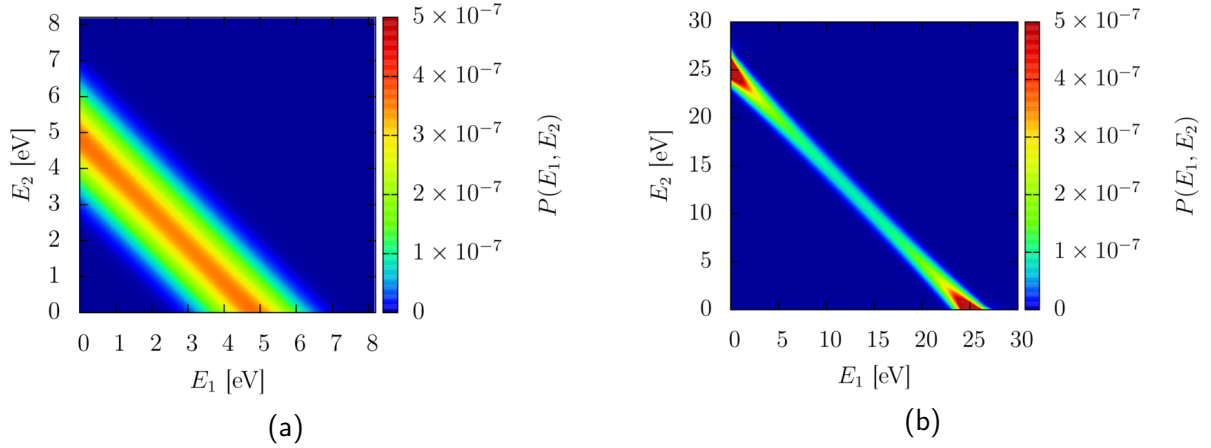


Figure 8.4.: Angle-integrated double ionization spectrum $P(E_1, E_2)$ [Eq. (8.8)] for ionization by a right-circularly polarized ($\epsilon = -1$) pulse with duration $T_p = 2$ fs with peak intensity 10^{12} W/cm² along \hat{x} for XUV energies of (a) 42 eV, and (b) 52 eV.

with the ellipticity. For linear polarization along \hat{x} ($\epsilon=0$), $P(\phi_2)$ displays the previously observed “fish-like” angular distribution [Fig. 8.5 (a)]. With increasing ϵ , the dip due to the nodal line at $\phi=90^\circ$ disappears. The ratio $P(\phi_2=90^\circ)/P(\phi_2=180^\circ)$ approximately scales with ϵ^2 [Fig. 8.5 (b)]. In the limit of circular polarization, the only structure remaining is the suppression of electron emission into the same direction ($\phi_2=0^\circ$) (side-by-side) relative to the back-to-back emission ($\phi_2=180^\circ$). The pronounced minimum for emission of both electrons in the same direction is not affected by the variation of ϵ . The obvious reason for the strong suppression is the repulsive electron-electron interaction, when the two-electron emission is temporally confined to a fraction of a femtosecond and is a prototypical case of dynamical Coulomb correlation.

Performing a scan of the pulse duration T_p [244] we find that with increasing pulse duration the dip in the angular distributions becomes less and less pronounced and in the limit of very long pulses it approaches a purely circular distribution (grey dashed lines), see Fig. 8.6 (a). This dynamical Coulomb correlation can be quantified by the dependence of the ratio $P(\phi_2=0^\circ)/P(\phi_2=180^\circ)$ on T_p [Fig. 8.6 (b)]. In the limit $T_p \rightarrow 0$, Coulomb repulsion tends to completely block the side-by-side emission.

For circular polarization, the side-by-side suppression is the dominant structure in the joint angular distribution, while for linear polarization additional pronounced minima due to the nodal plane may overshadow this effect in the experiment. Circularly polarized XUV’s are therefore the preferred experimental setting to unambiguously establish the dynamical correlation in TPDI for ultrashort pulses. Moreover, unlike for linear polarization the joint angular distribution is rotationally invariant $P(\phi_1 = 0^\circ, \phi_2) = P(\phi_1 = \alpha, \phi_2 + \alpha)$ for circular pulses, see Fig. 8.6c. Consequently, the correlation dip will persist when integrating the experimental angular distribution over the azimuthal angle α while keeping the relative angle $\phi_1 - \phi_2$ fixed, thereby improving the experimental signal-to-noise ratio.

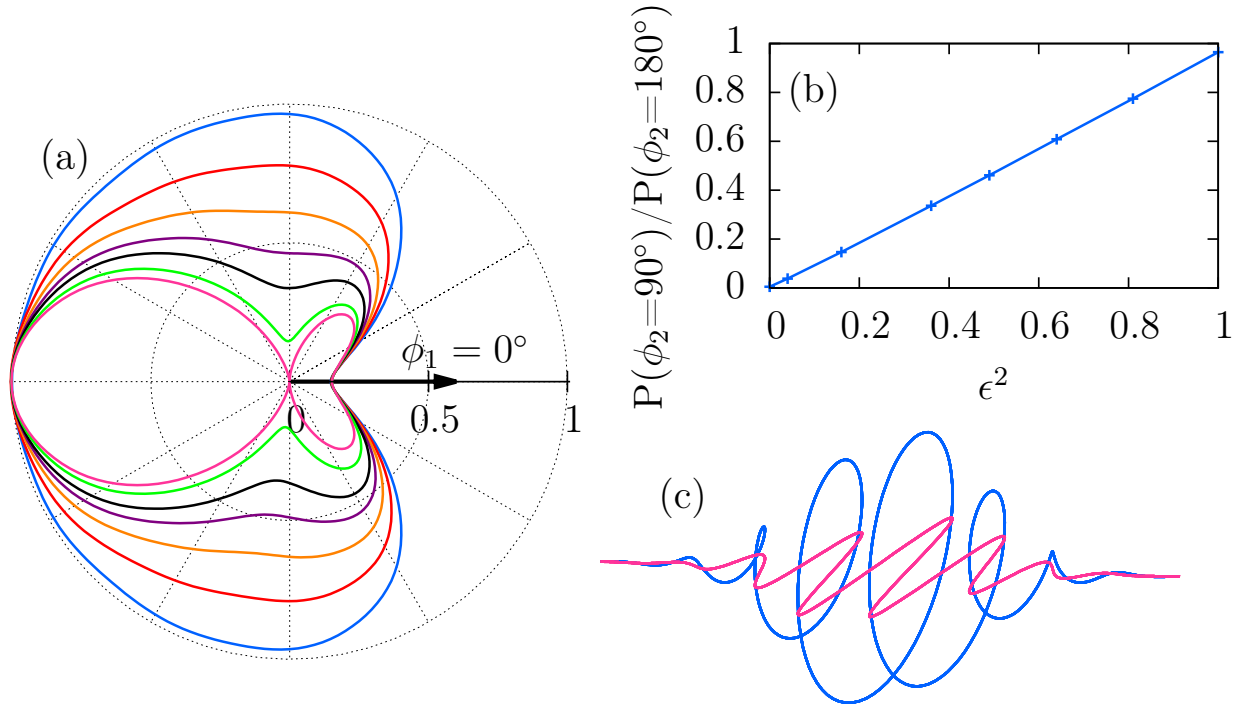


Figure 8.5.: (a) Joint angular distribution $P(\theta_1 = \theta_2 = 90^\circ, \phi_1 = 0^\circ, \phi_2)$ [Eq. (8.4)] of the ejected electrons for a pulse duration $T_p = 150$ as at $E_{\text{xuv}} = 70$ eV for different ellipticities ϵ . The innermost line (pink) corresponds to the previously investigated case of linear polarization along \hat{x} ($\epsilon = 0$), whereas the successive outer curves correspond to $\epsilon = 0.4, 0.6, 0.7, 0.8, 0.9$, and 1 (circular polarization). All distributions are normalized to a maximum value of one. (b) Ratio of probability for emission of the second electron with an angle of $\phi_2 = 90^\circ$ to the probability for emission into the opposite direction (back-to-back) for the different ellipticities shown in (a). (c) Sketch of a laser field with $\epsilon = 1$ (blue) and 0 (pink).

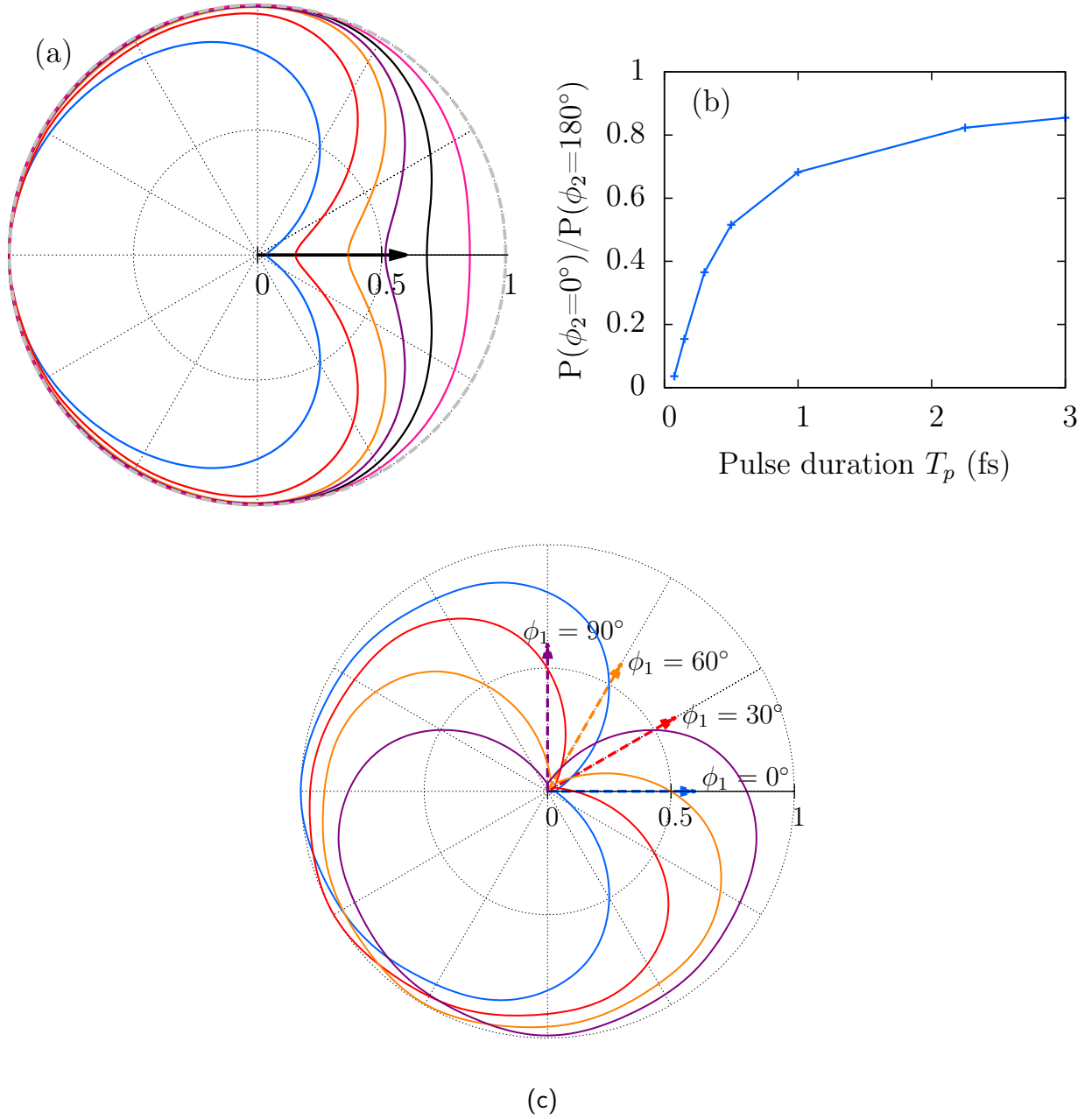


Figure 8.6.: (a) Joint angular distributions $P(\theta_1 = \theta_2 = 90^\circ, \phi_1 = 0^\circ, \phi_2)$ [Eq. (8.4)] of the ejected electrons for different pulse durations at $E_{\text{xuv}} = 70$ eV. The innermost line (blue) is for $T_p = 75$ as, with successive outer lines for $T_p = 150, 300, 500, 1000, 3000$ as. The grey dashed line is the unit circle. All distributions are normalized to the maximum value of the angular distribution at $\phi_2 = 180^\circ$. (b) Ratio of emission of the two electrons into the same (side-by-side) and into the opposite direction (back-to-back) for the different pulse durations shown in (a). (c) Joint angular distributions $P(\theta_1 = \theta_2 = 90^\circ, \phi_1 = \alpha, \phi_2)$ of the ejected electrons for a pulse duration of $T_p = 75$ as and photon energy $E_{\text{xuv}} = 70$ eV for different ejections angles $\alpha \in \{0^\circ, 30^\circ, 60^\circ, 90^\circ\}$ of the first electron. The distributions are normalized to the maximum value of the angular distribution at $\phi_2 = 180^\circ + \alpha$ for $\alpha = 0^\circ$.

8.3. XUV-XUV pump-probe sequence with elliptically polarized pulses

XUV-XUV pump-probe sequences have been theoretically investigated for linearly polarized pulses in the past, e.g. [243, 245–247, 255, 256]. Palacios et al. [243, 245] investigated an XUV-XUV sequence for pulses with different energies and varying time delays and found an interference pattern in the angle integrated, but energy resolved double ionization probability $P(E_1, E_2)$ as a function of the energy difference $\Delta E = E_1 - E_2$ between the electrons. XUV-XUV pulse sequences have also been used to explore double ionization via doubly excited resonances as intermediate states of interfering pathways [246]. Recently there has been the proposal to generate and control spiral interference patterns in the angular distributions of photoelectrons created by single ionization with pairs of counter-rotating time delayed XUV pulses [260] and also in the joint momentum distribution for two-photon double ionization in helium [253]. The latter work shows possibilities to extract information on the dynamics of the doubly excited states which are populated transiently in the two-photon double ionization process.

We explore in the following double ionization by a sequence of two ultrashort XUV pulses with, in general, different ellipticities $\epsilon_{1,2}$. We show that polarization tagging allows to distinguish ionization events occurring in the first and the second pulse and, thus, temporal (non)sequential ionization. Using the ellipticity of the XUV pulses as control knob interferences between the temporally sequential emission events can be switched on and off. The two XUV pulses used for the results shown in the following have an identical central energy of 65 eV and a Fourier width corresponding to $T_p = 1$ fs. The time delay between the pulses is sufficiently large ($\tau = 2.5$ fs) that the two pulses are temporally well separated.

8.3.1. Doubly differential energy distributions

We first consider the angle-integrated double ionization probability $P(E_1, E_2)$ [Eq. (8.8)] as a function of the two electron energies. In the $E_1 - E_2$ plane two well separated peaks signifying sequential double ionization and a faint ridge connecting the two indicating a weak non-sequential contribution can be identified. For opposite polarizations [$\epsilon_1 = 1, \epsilon_2 = -1$, Fig. 8.7 (a)] the peaks are structureless. By contrast, for two pulses with the same ellipticity ($\epsilon_1 = \epsilon_2 = 1$) $P(E_1, E_2)$ displays an intricate interference pattern [Fig. 8.7 (b)]. This pattern results from different pathways in the time domain to reach the same final two-electron state with energies (E_1, E_2) in the double continuum: absorption of two photons from the first pulse, absorption of two photons from the second pulse and absorption of one photon from each pulse, the latter amounting to two paths due to the indistinguishability of the two electrons (see Fig. 8.8). Closer inspection shows that the interference pattern near the sequential peaks is checker-board like while it appears stripe-like near the non-sequential ridge.

Employing second-order perturbation theory (see, e.g., [94, 243, 256, 258]) the interference

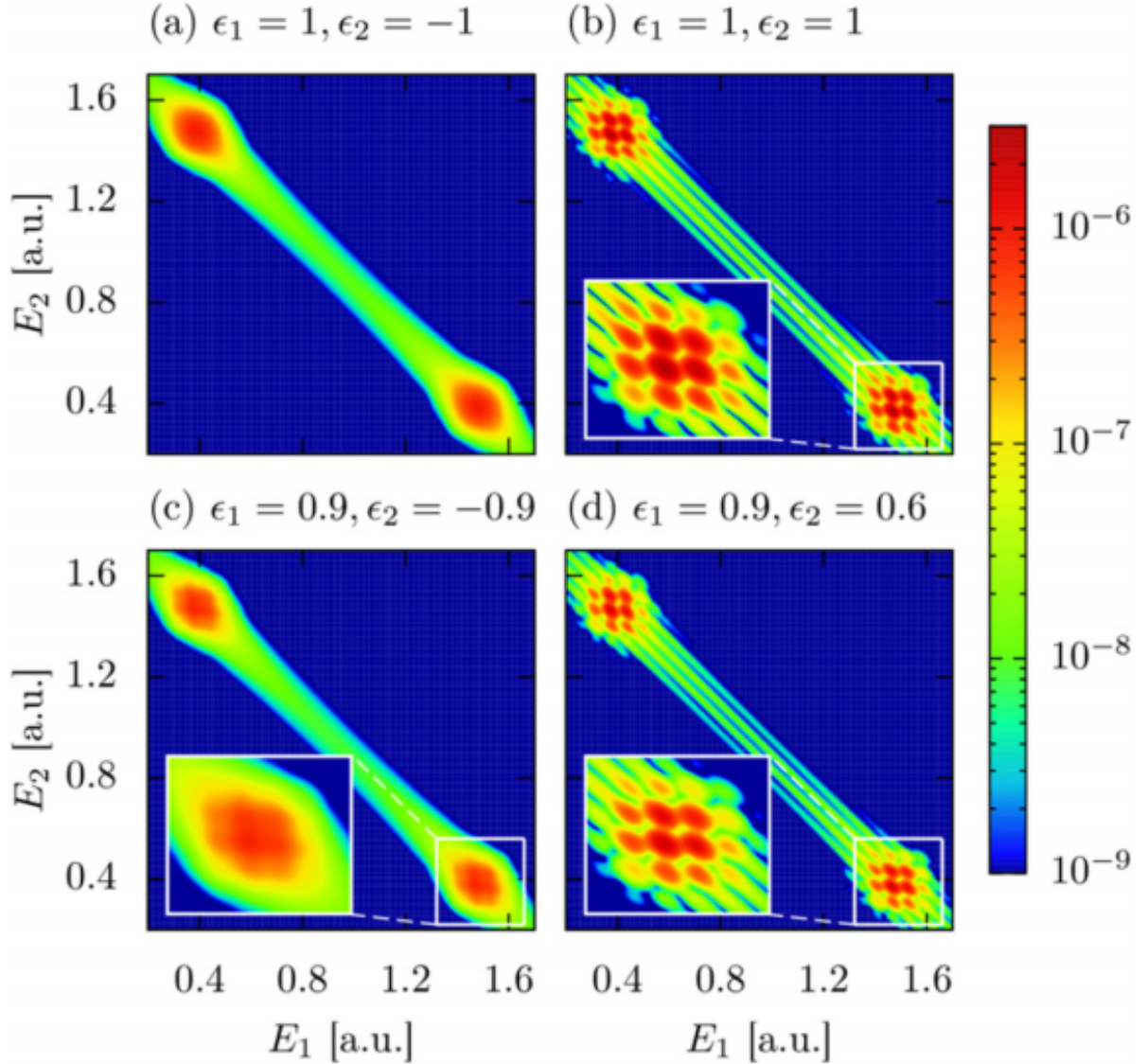


Figure 8.7.: Double ionization spectrum $P(E_1, E_2)$ [Eq. (8.8)] in atomic units (log-scale) as a function of E_1 and E_2 for XUV-XUV sequences with different ellipticities. The corresponding total two-photon double ionization probabilities are (a) 3.4×10^{-8} , (b) 4.6×10^{-8} , (c) 2.8×10^{-8} and (d) 2.8×10^{-8} . The central photon energy of both pulses is 65 eV, their duration is $T_p = 1$ fs and the pulse delay $\tau = 2.5$ fs. The peak intensity of each pulse in \hat{x} direction is 10^{12} W/cm².

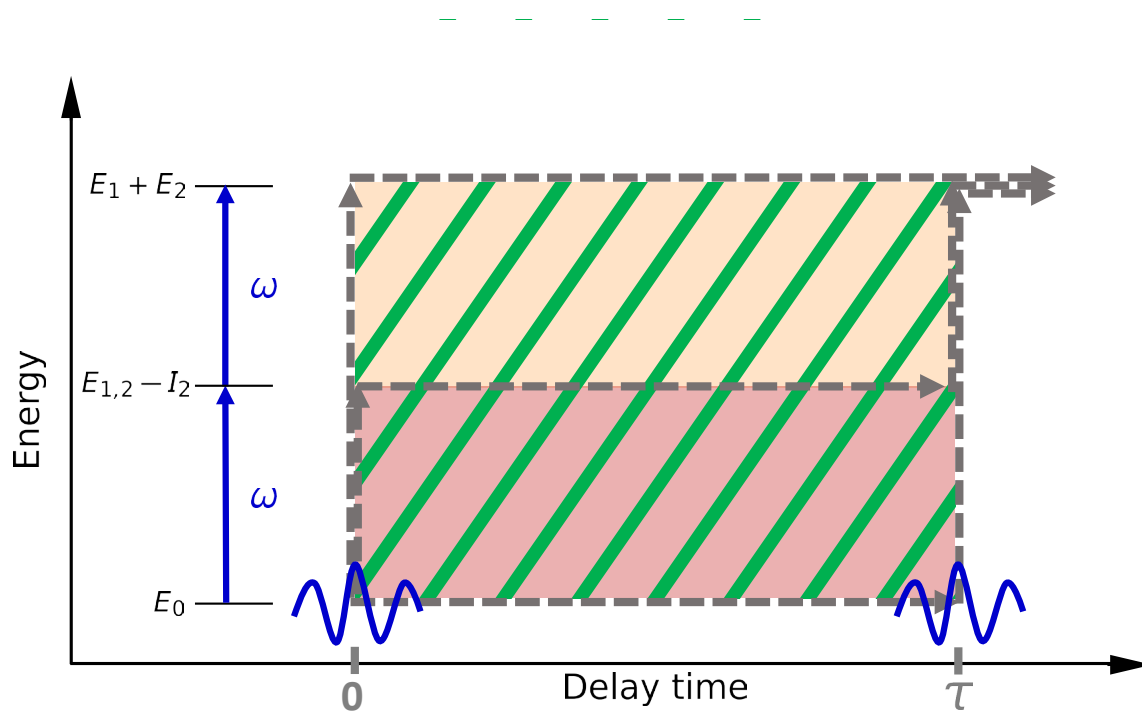


Figure 8.8.: Energy-delay time diagram of the interfering pathways in an XUV-XUV pump-probe sequence. The shaded areas signify the enclosed interference phases giving rise to the stripes (striped area) and to the checkerboard pattern (red, yellow shaded area and striped area) in Fig. 8.7. For details see text.

pattern for two identical time-delayed XUV pulses can be quantitatively accounted for. The angle integrated two-photon double ionization probability is given by the incoherent sum of the transition probabilities $\left[t_{i \rightarrow f}^{(2)} \right]_{L,M}^2$ to all accessible (L, M) channels [94]

$$P(E_1, E_2) = \sum_{L,M=(2,2),(2,0),(2,-2),(0,0)} \left| \left[t_{i \rightarrow f}^{(2)} \right]_{L,M} \right|^2. \quad (8.9)$$

For a pump-probe sequence where the first pulse has ellipticity ϵ_1 and the second ϵ_2 the amplitudes are given by

$$\begin{aligned} \left[t_{i \rightarrow f}^{(2)} \right]_{2,\pm 2} &\propto (1 \pm \epsilon_1)^2 \mathcal{S}^{(2)}(\Delta E) e^{-i(E_1+E_2)\tau} \\ &\quad + (1 \pm \epsilon_2)^2 \mathcal{S}^{(2)}(\Delta E) e^{-iE_0\tau} \\ &\quad + (1 \pm \epsilon_1)(1 \pm \epsilon_2) \mathcal{G}^{(1)}(\Delta E) e^{-i(E_1-I_{p,2})\tau} \\ &\quad + (1 \pm \epsilon_1)(1 \pm \epsilon_2) \mathcal{G}^{(1)}(-\Delta E) e^{-i(E_2-I_{p,2})\tau}, \end{aligned} \quad (8.10)$$

$$\begin{aligned} \left[t_{i \rightarrow f}^{(2)} \right]_{2/0,0} &\propto (1 - \epsilon_1^2) \mathcal{S}^{(2)}(\Delta E) e^{-i(E_1+E_2)\tau} \\ &\quad + (1 - \epsilon_2^2) \mathcal{S}^{(2)}(\Delta E) e^{-iE_0\tau} \\ &\quad + (1 - \epsilon_1\epsilon_2) \mathcal{G}^{(1)}(\Delta E) e^{-i(E_1-I_{p,2})\tau} \\ &\quad + (1 - \epsilon_1\epsilon_2) \mathcal{G}^{(1)}(-\Delta E) e^{-i(E_2-I_{p,2})\tau}, \end{aligned} \quad (8.11)$$

where $\mathcal{S}^{(2)}$ is a generalized shape function for absorption of two photons within one pulse and $\mathcal{G}^{(1)}$ is the shape function for absorbing one photon in each pulse (for details see Appendix H). $E_0 = -(I_{p,1} + I_{p,2})$ is the groundstate energy and $E_{1,2} - I_{p,2}$ is the intermediate state energy if the first (second) electron is ionized by the first pulse while the second (first) electron is bound in the 1s state of He^+ . Eq. (8.10) represents the coherent superposition of ionization paths involving either absorption of two photons with the same polarization from the same pulse (terms proportional to $\mathcal{S}^{(2)}$) and absorption of photons from different pulses (terms proportional to $\mathcal{G}^{(1)}$) with, in general different polarizations $\epsilon_1 \neq \epsilon_2$. The interference pattern depends on (E_1, E_2) or, equivalently, on $\Delta E = E_1 - E_2$ and $E_{\text{tot}} = E_1 + E_2$. Accordingly, the interference oscillations $\sim \cos[(E_1 + E_2 - E_0)\tau]$ along the lines $\Delta E = \text{const.}$ are due to the mixed terms in $\mathcal{S}^{(2)}$ in Eq. (8.10) and are, in principle, present in the entire (E_1, E_2) plane. They appear, however, only when the polarizations of the first and the second pulse agree. The corresponding interference phase $(E_1 + E_2 - E_0)\tau$ is marked in Fig. 8.8 by green stripes. Near the sequential peaks additional interference terms due to the $\mathcal{G}^{(1)}$ terms contribute (marked by red and yellow shaded areas in Fig. 8.8). These interference terms give rise to oscillations $\sim \cos((E_{1/2} + I_{p,2})\tau)$ [$\sim \cos((E_{1/2} + I_{p,1})\tau)$] resulting from interferences between the third/fourth with the first [second] term in Eq. (8.10) and, hence to the checkerboard pattern when the two polarizations agree. The third and fourth term do not interfere with each other since the spectral overlap between $\mathcal{G}^{(1)}(\Delta E)$ and $\mathcal{G}^{(1)}(-\Delta E)$ vanishes.

Eq. (8.11) contains terms that have significant weight only if the polarizations are sufficiently different and are strictly zero for $\epsilon_1 = \epsilon_2 = 1$. Thus by switching the polarizations of the pulses, path interferences can be switched on and off.

The interference in the double ionization spectrum $P(E_1, E_2)$ can be shown to be quite robust relative to variation of ϵ of the XUV pulses employed, as can be seen in Fig. 8.7 (c) for two pulses with $\epsilon_1 = 0.9$, $\epsilon_2 = -0.9$. The interference pattern starts to emerge, but is hardly visible. Similarly, using two pulses with slightly different ellipticity, e.g., $\epsilon_1 = 0.9$, $\epsilon_2 = 0.6$ results in a very similar interference pattern as $\epsilon_1 = \epsilon_2 = 1$ [compare Fig. 8.7 (b) and (d)].

8.3.2. Singly differential energy distributions

Integrating $P(E_1, E_2)$ along the total energy $E_{\text{tot}} = E_1 + E_2$ yields the double ionization probability as a function of the energy difference $\Delta E = E_1 - E_2$ of the two electrons

$$P(\Delta E) = \frac{1}{2} \int_0^\infty dE_{\text{tot}} P(E_1, E_2). \quad (8.12)$$

Since all interference terms contain $\cos(E_{\text{tot}}\tau)$, see Eq. (8.10) and (8.11), integration over E_{tot} damps out all these terms. Conversely, interferences due to the superposition of the terms $\sim \mathcal{S}^{(2)} \sim \cos[(E_{\text{tot}} - E_0)\tau]$ survive when $P(E_1, E_2)$ is integrated over ΔE .

The singly differential spectrum [Eq. (8.12)] can be analyzed by making use of the polarization tagging. This becomes possible because of the perfect locking of the magnetic quantum number of the two-electron wavepacket to the two ellipticities $\epsilon_{1,2} = 1, -1$. The electronic wavepacket with total $M=2$ (or -2) must have absorbed both photons from the first (second) pulse. $M=0$ is reached only when one photon is absorbed from each pulse. While the photoelectron spectrum of the $M=2$ (-2) electrons is influenced by dynamical electron-electron correlation, the $M=0$ electrons stem from a purely sequential process. This is clearly visible in $P(\Delta E)$ [Fig. 8.9 (a)]. Summing over all M results in a $P(\Delta E)$ closely resembling the distribution for a single linearly polarized XUV pulse [94] with a spectrally very flat plateau-like structure in the equal energy sharing ($\Delta E \approx 0$) region. Analyzing $P(\Delta E)$ separately for the different M channels, we observe that for $M=\pm 2$ the probability distribution is very similar to the full spectrum. This is due to the fact that either channel consists of electrons emitted by the absorption of two photons within the same pulse and, thus, has the signatures of both temporal sequential and nonsequential two-photon double ionization. For $M=0$ [dash-dotted line in Fig. 8.9 (a)], $P(\Delta E)$ features two well-separated peaks at $\Delta E \approx \pm 1.1$ a.u. while the equal-energy sharing plateau-like structure is completely missing as expected for a purely sequential ionization process. Moreover, much smaller peaks near $\Delta E \approx \pm 1.9$ a.u. corresponding to shake-up processes with excited ionic states become visible [94].

The decomposition of TPDI into contributions with different total magnetic quantum number M of the two-electron wavepacket is straightforward in theory, but such a separation is not easily accomplished in experiment. We therefore explore the signatures of polarization

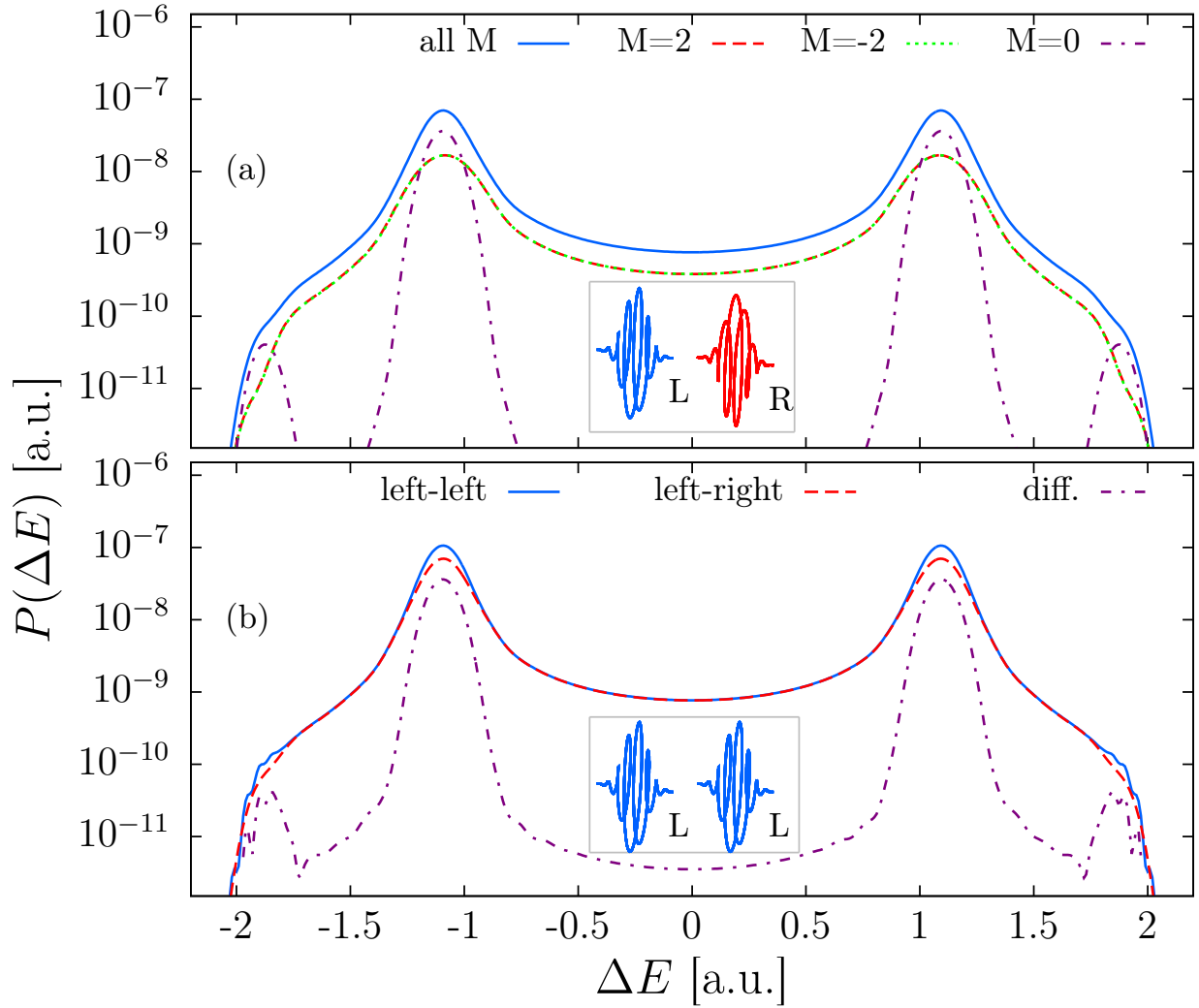


Figure 8.9.: (a) $P(\Delta E)$ for a pump-probe sequence with $\epsilon_1 = 1$ (L), $\epsilon_2 = -1$ (R) (see inset). $P(\Delta E)$ is resolved for the three different M values of the final state. (b) $P(\Delta E)$ for a pump-probe sequence with two left-circularly polarized pulses ($\epsilon_1 = \epsilon_2 = 1$, see inset) and one left- and one right-circularly polarized pulse ($\epsilon_1 = 1$, $\epsilon_2 = -1$). The dashed dotted line shows the difference of the two sequences. The central photon energy of the pulses is 65 eV, their duration is $T_p = 1$ fs and their delay is $\tau = 2.5$ fs.

tagging in the experimentally directly accessible energy- and angular distributions of TPDI. To this end, we compare the energy-differential double-ionization probability, $P(\Delta E)$ for two polarization scenarios: A left-left ($L-L$) pulse sequence ($\epsilon_1 = \epsilon_2 = 1$) with an $L-R$ sequence ($\epsilon_1 = 1, \epsilon_2 = -1$). The absolute value of $P(\Delta E = \pm 1.1 \text{ a.u.})$ near the sequential peak is found to be larger for the $L-L$ sequence than for the $L-R$ sequence. By subtracting $P(\Delta E)$ of the $L-R$ sequence from $P(\Delta E)$ of the $L-L$ sequence [dash-dotted line in Fig. 8.9 (b)] the structure of the two well-separated sequential peaks emerges. This difference spectrum coincides very well with the $M=0$ spectrum of the $L-R$ sequence [Fig. 8.9 (a)] and gives access to the polarization tagged spectrum without actually resolving M . This selectivity can be easily understood from angular momentum coupling arguments. After absorbing the first left-handed photon, the singly ionized state lies in the $L=1, M=1$ channel. During the second pulse the transition amplitude for absorbing another photon is the same irrespective of the polarization apart from the pre-factor which is given by a Clebsch-Gordon coefficient. If the second pulse is also left-circularly polarized the only relevant Clebsch-Gordon coefficient for coupling to $M=2$ is $\langle 1, 1, 1, 1 | 2, 2 \rangle = 1$. For a right circularly-polarized second pulse there are two pathways to $M=0$ with Clebsch-Gordon coefficients $\langle 1, 1, 1, -1 | 2, 0 \rangle = 1/\sqrt{6}$ and $\langle 1, 1, 1, -1 | 0, 0 \rangle = 1/\sqrt{3}$. Squaring and adding those coefficients the probability to absorb one photon out of each pulse from an $L-R$ sequence is half of the $L-L$ sequence. Consequently, by subtracting the $L-R$ from the $L-L$ signal the yield of the electrons is exactly the same as if we would have selected just the electrons which absorbed one photon out of each pulse in the $L-R$ scenario resulting in electrons with $M = 0$.

8.3.3. Joint angular distributions

In the following we investigate the joint angular distributions [Eq. (8.4)] of photoelectrons emitted in the XUV-XUV pulse sequences in the polarization plane ($\theta_1 = \theta_2 = 90^\circ$) and fix the emission direction of the first electron to $\phi_1 = 0^\circ$. We compare

$$P(\phi_2) = P(\theta_1 = \theta_2 = 90^\circ, \phi_1 = 0^\circ, \phi_2) \quad (8.13)$$

for the $L-L$ and $L-R$ pulse sequences [Fig. 8.10 (a) and (b) respectively]. The angular distribution for an $L-L$ sequence [Fig. 8.10 (a)] closely resembles $P(\phi_2)$ of a single pulse of comparable duration (Fig. 8.6a). The distribution features a modest suppression due to dynamical Coulomb correlation for side-by-side emission but is otherwise close to rotationally symmetric. Since the $L-L$ sequence has the propensity to populate $M=2$, the distribution from summation over all M is essentially indistinguishable from the distribution for $M=2$ alone. An entirely different picture emerges for the $L-R$ sequence [Fig. 8.10 (b)]. The angular distribution $P(\phi_2)$ is peanut shaped. Its origin can be traced to the contributions from different M channels which contribute to $P(\phi_2)$ in the $L-R$ sequence. While the $M = \pm 2$ components mirror the distributions for the $L-L$ sequence, the $M=0$ component features a dipolar pattern with a nodal line along $\phi_2 = 90^\circ$ causing the indentation of $P(\phi_2)$.

This particular shape allows to associate the emission direction with the (non)sequential timing of the two-electron emission. The joint probability near $P(\phi_2 = 90^\circ)$ is exclusively due to the quasi-simultaneous emission from the same pulse. Conversely, the joint probability near $P(\phi_2 = 0^\circ)$ is predominantly due to sequential emission of the two electrons spaced in time by $\tau = 2.5$ fs. In the present case of a relatively long pulse of $T_p = 1$ fs the sequential contribution is well above 50%. In the limit of even shorter pulses ($T_p \rightarrow 0$) $P(\phi_2 = 0^\circ)$ tends to become completely sequential [see Fig. 8.6 (b)].

To check for the robustness of our results against imperfection of circular polarization, we also perform simulations for a sequence with $\epsilon_1 = 0.9$, $\epsilon_2 = -0.9$. While the overall yield decreases with decreasing ellipticity, the characteristic shape of the angular distribution remains largely unchanged and structurally stable [Fig. 8.10 (c)]. It should be noted that the angular distribution for $\epsilon \neq \pm 1$ does not only depend on the relative angle $\phi_1 - \phi_2$, but on both azimuthal angles explicitly.

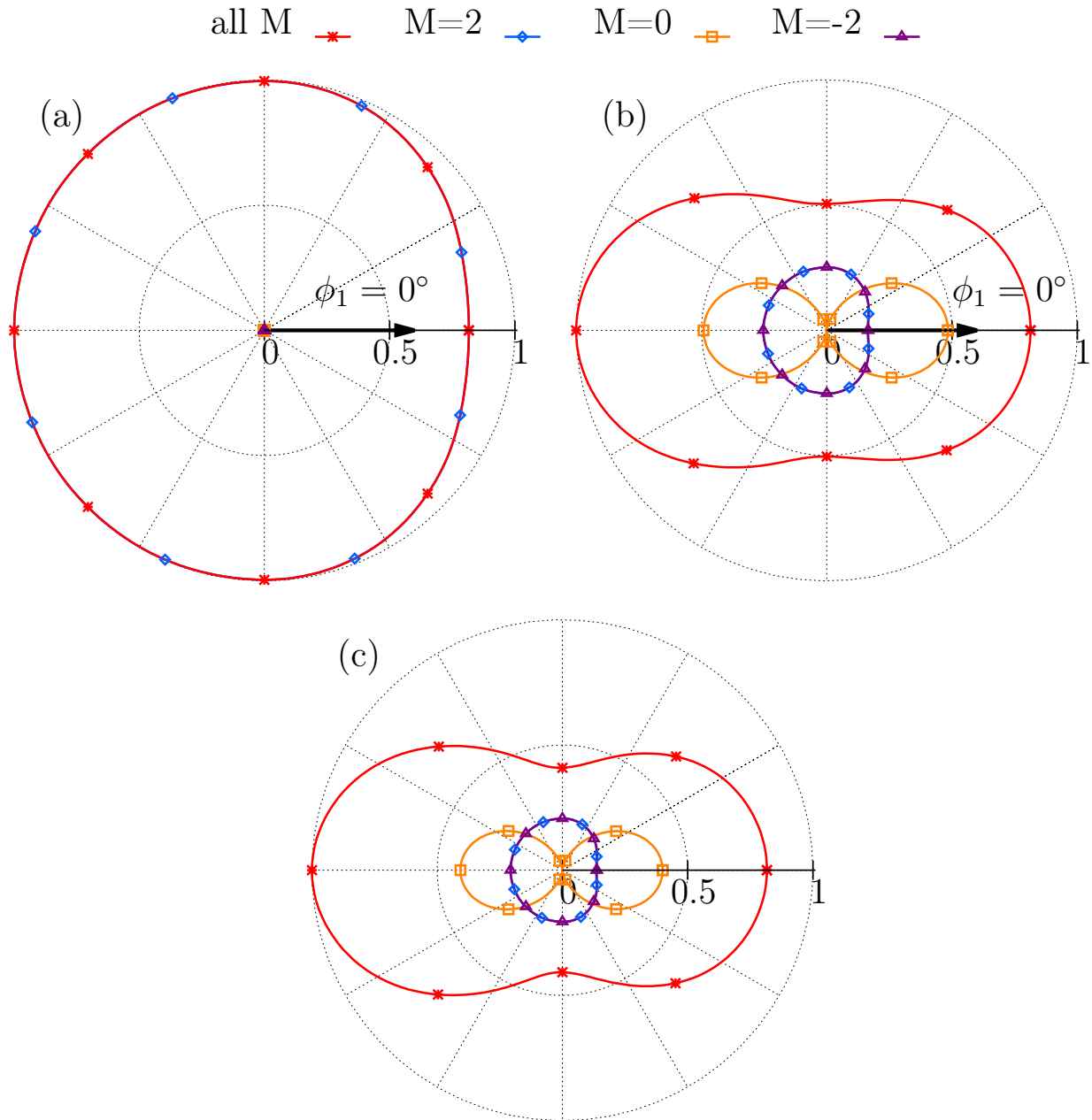


Figure 8.10.: Joint angular distributions $P(\theta_1 = \theta_2 = 90^\circ, \phi_1 = 0^\circ, \phi_2)$ [Eq. (8.4)] of the ejected electrons for an XUV pulse with polarization $\epsilon_1 = 1$ followed by an XUV pulse with (a) $\epsilon_2 = 1$ or (b) $\epsilon_2 = -1$. (c) same as (b) for $\epsilon_1 = 0.9$ and $\epsilon_2 = -0.9$. All pulses have photon energy $E_{\text{XUV}} = 65$ eV and a pulse duration of $T_p = 1$ fs. The different lines correspond to different values of M of the final state. All distributions are normalized to the maximum value of the total probability distribution shown in (a) summed over all M .

9. Summary & Outlook

In summary, we have performed detailed studies of single-photon and multi-photon single and double ionization of small atomic systems by ultrashort multi-color laser pulses. Photoemission of electrons is a quantum mechanical process whose amplitude and phase encodes many interesting physical effects. While the total yield of photoemission has been routinely measured since decades, only recently it became possible to measure also the phase information involved in photoemission through attosecond metrology. In this thesis we have studied the electronic phases and correlations for single ionization processes in the spectral region of resonances (structured continuum), single ionization to the unstructured (flat) continuum, and double ionization via the nonresonant single continuum employing *ab initio* simulations. In addition, we have put forward new measurement schemes (in close collaboration with experimental groups) to obtain parts of this information in actual experiments. While we focus mostly on full *ab initio* simulations of atomic helium the methods studied can be extended to more complicated targets. The helium atom, thus, serves as a benchmark system where electronic correlations are fully included.

Photoionization close to resonant structures has been investigated in great detail since their detection. Whereas the spectral shape of Fano resonances has been studied in great detail employing synchrotron radiation, their imprint on the continuum phases has only been accessible within theoretical studies until recently. Several RABBITT experiments have started to bridge this gap and measured the variation of the two-photon continuum phase modified due to Fano resonances in the intermediate or final state [52–55]. Within this thesis, we have advanced further and have proposed two independent schemes to directly measure the one-photon phase of autoionizing resonances [56] using angle-resolved photoelectron detection. Complementary to the spectral phase we have also proposed a scheme to monitor the temporal formation of the transient build-up of a Fano resonance which has been realized using attosecond transient absorption spectroscopy [57, 103].

Whereas the perturbative interaction of autoionizing resonances with light fields is well understood, the detailed understanding of the non-perturbative interaction of multiple quasi-bound states with strong few-cycle fields is still an open problem [63, 64, 67–69]. Contrary to conventional quantum optics where multi-level Rabi dynamics is the dominant process, the strong light field leads also to a significant modification of the autoionization process. We have introduced a new method based on causality [240–242] which allows to retrieve the time-dependent response of an isolated resonance to a non-perturbative interaction from a single-shot absorption spectrum, and have applied this method to study the NIR driven dynamics of doubly excited states in helium. By using both the time-dependent amplitude and phase of the dipole response we progressed substantially in disentangling

Rabi flopping from strong-field ionization in this prototypical example [70].

One key observable to characterize the unstructured single ionization continuum is the phase an photoelectron acquires during the photoionization process. Employing attosecond chronoscopy techniques it has been possible to measure even the time it takes for a liberated electron to leave its parent ion which is encoded in the phase of the emitted electrons. This time delay has in previous experiments primarily been determined either from electrons emitted into one specific direction, or from angle-integrated measurements. The angular variation and the information encoded in it was, thus, lost completely. More recent experiments, however, are able to retrieve the full angular distribution of emitted electrons and, thus, allow an investigation of interferences between different partial waves. We have determined that the recently found dependence of the photoionization delay [34] on the electron emission angle in RABBITT is caused by mixing of different partial waves within each sideband. Furthermore, we have been able to quantify the dependence of the phase acquired within a free-free transition on the final angular momentum, separately for emission or absorption of a photon for the prototypical system of helium [101].

Investigation of the double ionization continuum for atomic helium has been an integral part of theoretical atomic physics over the past decades. The reason being that helium serves as benchmark system to study the double continuum, and to examine which observables are sensitive to electronic correlations. For the case of two-photon double ionization a large number of calculations have made detailed predictions on electronic correlation features observable in the joint angular distribution of the ionized electrons. Unfortunately, these predictions have not yet been confirmed by experiment due to the very low double ionization cross section of helium. In light of the increasing number of free-electron lasers and high power HHG based laser sources, however, we are confident that experimental investigations of two-photon double ionization in helium are possible over the next years. Within this thesis we have shown that for the case of temporally nonsequential two-photon double ionization [90, 244] (both electrons are ionized simultaneously by an attosecond XUV pulse), the imprint of dynamical Coulomb correlation on the joint angular distribution appears more prominently for ionization by circularly polarized pulses, compared to ionization with a linearly polarized XUV. The reason for this is that the distortion due to the nodal structure of a dipolar emission pattern is absent for ionization by circularly polarized fields. Furthermore, we have shown that for XUV-XUV pump-probe sequences the ellipticity of the light fields allows to control interferences in the double ionization spectrum, and to map the timing of the emission events onto the joint angular distribution [104].

Despite several insights, some questions raised in this thesis are still not answered satisfactory. The first remaining challenge is a quantitative description of the angle dependence of the continuum-continuum phase. For double ionization the most obvious avenue for future research is to time-resolve one- and two-photon double ionization with RABBITT. While the latter one has already been addressed with streaking [248], the time structure of one-photon double ionization is still unexplored. RABBITT provides a better energy

resolution as compared to streaking and allows to retrieve timing information close to the double ionization threshold.

On a broader perspective, we will continue to investigate attosecond metrology techniques where states with different parity interfere with each other. Examples for such protocols are the proposal to measure photoionization time delays for above threshold ionization [166] using an $\omega - 2\omega$ setup with both fields close to the visible regime, or $\omega - 2\omega$ setups with XUV fields [261]. A deep theoretical understanding of these new protocols is essential to fully foster their potential and to extend our knowledge about light-matter interaction.

Acknowledgements

This work would not have been possible without the countless number of people who helped, supported, and encouraged me over the last four years. I want to thank my supervisor Iva Březinová who was always available for my tedious questions, and endured all my rants about physics, life and the universe in general. Her comments, questions and answers showed me everything I did not know, but should have known, thereby considerably enhancing my knowledge and the quality of my research. I am indebted to my supervisor Joachim Burgdörfer who gave me the opportunity to conduct research within his group without very strong boundaries on the topics I want to look into, and for constantly asking for explanations of the results I showed him. His critical feedback on the scientific content and presentation of all my results was always helpful and certainly pushed me forward.

Most of the calculations performed in this thesis were done with the helium code developed by Johannes Feist more than ten years ago. I want to thank Johannes for still answering to all my questions in an extremely timely manner. I really enjoyed my stay in Madrid, to extend the code to arbitrary polarization. This endeavor would not have been possible without his help.

One of the biggest thanks is reserved for Luca Argenti, whom I had the pleasure to visit for five months at the University of Central Florida in Orlando. I cannot thank him enough for his supervision since then, his advise on physics and life, and for letting me live in his house during my stay in the US. Florida was truly a unique experience on a scientific and personal level, and I want to thank Nicolas, Bejan, Crystal, Coleman, Saad and Didar for significantly contributing to my wellbeing in Florida.

I want to thank the groups of Thomas Pfeifer, C. D. Lin, Christoph Keitel, Louis DiMauro, Guillaume Laurent, and Ursula Keller with which I had the joy to collaborate with over the course of the last years. Especially I want to express my gratitude to Alexander Blättermann and Veit Stooß, for all their effort to explain their experimental setup to me, to Tim Gorman and Tim Scarborough, for many productive Skype discussions and to Jaco Fuchs, for his unstoppable interest and enthusiasm for physics.

It was a pleasure to work with the talented students Sebastian Bichelmaier, Ralf Wanzenböck, and especially Manuel Ederer, who is brave enough to conduct his master thesis under my supervision. I enjoyed every event of the International Max Planck Research School on Advanced Photon Science in Munich and in Ringberg Castle. Especially I want to thank Nick Karpowicz, Hanieh Fattahi, Monika Wild and Kerstin Schmidt for organizing all those great events.

I want to thank Stefan Nagele, Florian Libisch, Christoph Lemell, Shuhei Yoshida, Hongcheng Ni, Wei-Chao Jiang and Xiang Gao for being always available for physics and computational questions and for contributing to the great atmosphere in our group. Fur-

ther, I want to thank all former and current (or adopted) PhD students. I enjoyed every discussion we had, and would not want to miss any time I spent with Larisa Chizhova, Paul Tiwald, Georg Wachter, Thomas Fabian, Lukas Linhart, Xin Zhao, Mahdi Kourehpaz, and Christoph Schattauer. Not to forget, I am grateful to Florian Aigner for writing amazing press releases on my work and for great discussions in our coffee breaks. A special thanks goes to Valerie Smejkal and Isabella Floss for all the times we spent on various trains and conferences. It was always fun and good to have someone to complain about unimportant things (e.g. Valerie's taste in music) during the miserable parts of PhD life. In addition I thank Fabian Lackner for many great conferences and discussions on everything one can imagine and more. Predictability is totally overrated. A warm thanks goes to our secretaries Heike Höller, Sylvia Riedler and Ingrid Unger for their support and help in all administrative tasks.

Surviving PhD life would have been a whole lot harder (or even impossible) without the support, distractions and good times I had with all my friends. I apologize for not naming all of you and for all the times I complained about my work. Thanks for always being around in times of need.

There is no way to thank Renate enough for answering all my questions on the helium code and attosecond physics and for always having my back, both in physics and in the real world outside of the ivory tower which theoretical physics constitutes.

Last but definitely not least, I want to thank my mother and aunt for supporting me throughout my studies in all possible ways and for always being curious about what I was actually doing at university, without expecting me to give a comprehensible answer.

Wir betraten die Arena - das war kein Zuckerschlecken.
Wir machten ein paar Fehler - den Rest haben wir vergessen.
Wir gingen nie in Deckung. Wollten uns nie verstecken.
Wir sind dafür geboren wie Gladiatoren.

Die Fantastischen Vier - Wie Gladiatoren

A. Lowest-order perturbation theory for the angle-integrated photoelectron spectrum in RABBITT

In this appendix we briefly describe how to obtain the characteristic beating formula for angle-integrated RABBITT [Eq. 3.9] from Eq. (3.4) [27, 31, 158].

Starting from the factorization of the two-photon transition $\mathcal{A}_{f \leftarrow i}^{(2)}$ [27, 31, 32, 158, 173] given in Eq. (3.4)

$$\mathcal{A}_{H_{2n \pm 1} \mp \omega_{\text{IR}}}^{(2)} = \sum_{\lambda} \sum_{\ell = \lambda \pm 1} \left| \mathcal{A}_{H_{2n \pm 1} \mp \omega_{\text{IR}}, \lambda \ell}^{(2)} e^{i\eta_{\lambda}(\varepsilon_{2n \pm 1})} e^{i\phi_{cc, \lambda \ell}^{\mp}} e^{\mp i\omega_{\text{IR}}\tau} e^{i\pi(1-\lambda/2)} Y_{\ell}^m(\theta, \varphi) \right|, \quad (\text{A.1})$$

the probability distribution at $E = H_{2n}$ is given by

$$|\psi(E = H_{2n}, \theta)|^2 = \left| \mathcal{A}_{2n-1+\omega_{\text{IR}}}^{(2)} + \mathcal{A}_{2n+1-\omega_{\text{IR}}}^{(2)} \right|^2. \quad (\text{A.2})$$

For simplicity we consider only the excitation to an intermediate p state ($\lambda = 1$), for emission from an s -shell electron yielding

$$\begin{aligned} |\psi(E = H_{2n}, \theta)|^2 &= \\ &= \left| \sum_{\ell=0,2} \left[\left| \mathcal{A}_{2n-1+\omega_{\text{IR}}, p \ell}^{(2)} \right| e^{i\eta_p(\varepsilon_{2n-1})} e^{i\phi_{cc, p \ell}^+} e^{i\omega_{\text{IR}}\tau} + \left| \mathcal{A}_{2n+1-\omega_{\text{IR}}, p \ell}^{(2)} \right| e^{i\eta_p(\varepsilon_{2n+1})} e^{i\phi_{cc, p \ell}^-} e^{-i\omega_{\text{IR}}\tau} \right] Y_{\ell}^0(\theta) \right|^2 \\ &= \left| \left[\left| \mathcal{A}_{2n-1+\omega_{\text{IR}}, p s}^{(2)} \right| e^{i\phi_{cc, p s}^+} Y_0^0(\theta) + \left| \mathcal{A}_{2n-1+\omega_{\text{IR}}, p d}^{(2)} \right| e^{i\phi_{cc, p d}^+} Y_2^0(\theta) \right] e^{i\eta_p(\varepsilon_{2n-1})} e^{i\omega_{\text{IR}}\tau} \right. \\ &\quad \left. + \left[\left| \mathcal{A}_{2n+1-\omega_{\text{IR}}, p s}^{(2)} \right| e^{i\phi_{cc, p s}^-} Y_0^0(\theta) + \left| \mathcal{A}_{2n+1-\omega_{\text{IR}}, p d}^{(2)} \right| e^{i\phi_{cc, p d}^-} Y_2^0(\theta) \right] e^{i\eta_p(\varepsilon_{2n+1})} e^{-i\omega_{\text{IR}}\tau} \right|^2, \quad (\text{A.3}) \end{aligned}$$

for the probability distribution. Integrating Eq. (A.3) with respect to θ we obtain

$$\begin{aligned} |\psi(E = H_{2n})|^2 &= \int d\theta \sin(\theta) |\psi(E = H_{2n}, \theta)|^2 \\ &= A + B_s \cos(2\omega_{\text{IR}}\tau - [\eta_p(\varepsilon_{2n+1}) - \eta_p(\varepsilon_{2n-1})] - [\phi_{cc, p s}^- - \phi_{cc, p s}^+]) \\ &\quad + B_d \cos(2\omega_{\text{IR}}\tau - [\eta_p(\varepsilon_{2n+1}) - \eta_p(\varepsilon_{2n-1})] - [\phi_{cc, p d}^- - \phi_{cc, p d}^+]) \\ &= A + B \cos(2\omega_{\text{IR}}\tau + \Delta\phi) \\ &= A + B \cos(2\omega_{\text{IR}}[\tau - \tau_R]). \quad (\text{A.4}) \end{aligned}$$

The angle-integrated RABBITT spectrum [Eq. (A.4)] can be separated into a delay dependent and delay independent part, where the latter contains the approximate time delay $\tau_R = -\frac{\Delta\phi}{2\omega_{\text{IR}}}$ as retrieved by RABBITT.

Assuming that each harmonic H_q has a spectral phase ϕ_q^{XUV} the two-photon matrix elements [Eq. A.1] are modified to

$$\mathcal{A}_{H_{2n\pm 1\mp\omega_{\text{IR}}}}^{(2)} = \sum_{\lambda} \sum_{\ell=\lambda\pm 1} \left| \mathcal{A}_{H_{2n\pm 1\mp\omega_{\text{IR}}}, \lambda\ell}^{(2)} \right| e^{i\eta_{\lambda}(\varepsilon_{2n\pm 1})} e^{i\phi_{cc, \lambda\ell}^{\pm}} e^{\pm i\omega_{\text{IR}}\tau} e^{i\pi(1-\lambda/2)} e^{i\phi_{2n\pm 1}^{\text{XUV}}} Y_{\ell}^m(\theta, \varphi). \quad (\text{A.5})$$

Accordingly the angle-integrated electron spectrum [Eq. (A.4)] changes to

$$\begin{aligned} |\psi(E = H_{2n})|^2 &= \int d\theta \sin(\theta) |\psi(E = H_{2n}, \theta)|^2 \\ &= A + B_s \cos(2\omega_{\text{IR}}\tau - [\eta_p(\varepsilon_{2n+1}) - \eta_p(\varepsilon_{2n-1})] - [\phi_{cc,ps}^- - \phi_{cc,ps}^+] - [\phi_{2n+1}^{\text{XUV}} - \phi_{2n-1}^{\text{XUV}}]) \\ &\quad + B_d \cos(2\omega_{\text{IR}}\tau - [\eta_p(\varepsilon_{2n+1}) - \eta_p(\varepsilon_{2n-1})] - [\phi_{cc,pd}^- - \phi_{cc,pd}^+] - [\phi_{2n+1}^{\text{XUV}} - \phi_{2n-1}^{\text{XUV}}]) \\ &= A + B \cos(2\omega_{\text{IR}}\tau + \Delta\tilde{\phi}) \\ &= A + B \cos(2\omega_{\text{IR}}[\tau - \tilde{\tau}_R]), \end{aligned} \quad (\text{A.6})$$

for ionization of an s electron.

B. Differences and similarities between RABBITT and streaking

In this appendix we discuss the connection between the continuum-continuum delay encountered in RABBITT [27] and the Coulomb-laser coupling encountered in attosecond streaking [33]. In addition we directly compare the time delays obtained from RABBITT and streaking for shake-up ionization of helium.

B.1. Relation between the continuum-continuum delay and the Coulomb-laser coupling

The asymptotic expression for the continuum-continuum phase [Eq. (3.5)] has been derived by Dahlström and co-workers [27, 31, 32] to interpret the phase shift observed in RABBITT experiments [27, 186, 187]. As indicated in Eq. (3.4) it has been found that the two-photon phase can be separated [30, 31] into the one-photon phase acquired within ionization and an additional universal contribution induced by the interaction of the electron propagating in the Coulomb potential with the NIR laser field [Eq. (3.5)]. In RABBITT measurements, however, the absolute two-photon phase has not been measured so far but only the difference

$$\begin{aligned}\Delta\phi_{cc}(E) &= \phi_{cc,+} - \phi_{cc,-} \\ &= \phi_{cc}\left(\sqrt{2E}, \sqrt{2E - \omega_{\text{IR}}}\right) - \phi_{cc}\left(\sqrt{2E}, \sqrt{2E + \omega_{\text{IR}}}\right).\end{aligned}\quad (\text{B.1})$$

The ratio

$$\tau_{cc} = \frac{\Delta\phi_{cc}(E)}{2\omega_{\text{IR}}}\quad (\text{B.2})$$

has been interpreted as continuum-continuum time delay and from its knowledge it has become possible to retrieve the one-photon time delay τ_{EWS} of photoionization from RABBITT measurements, e.g. [27].

Similarly, in streaking the IR field used in the measurement protocol induces an additional time delay in addition to the scattering delay τ_{EWS} [175]. The logarithmic part of the Coulomb phaseshift is responsible for this additional time delay [30, 33, 262] and is called Coulomb-laser coupling (CLC)

$$\tau_{\text{CLC}}(E) = \frac{Z}{(2E)^{3/2}} \left[2 - \ln\left(\frac{2\pi E}{\omega_{\text{IR}}}\right) \right].\quad (\text{B.3})$$

Although Eqs. (B.2) and (B.3) are derived from two different perspectives, they agree almost perfectly for high photoelectron energies [100]. This is in line with the observation that RABBITT and streaking yield the same results for photoionization time delays [30, 220, 263]. For low photoelectron energies, however, neither of the two analytic formulas [Eq. (B.2) and (B.3)] is accurate to determine the time delay caused by the interaction with the IR field.

B.2. Comparing time delays for shake-up ionization in helium using RABBITT and streaking

In this appendix we compare the retrieved time delays for shake-down and shake-up ionization of atomic helium by streaking and RABBITT. Previously this has also been investigated for photoionization of argon [220] and photoionization of solids [263] where good agreement has been achieved.

There are two fundamental differences between RABBITT and streaking. First, RABBITT has a priori no preferred direction and until very recently most experiments were performed using just the fully angle integrated photoelectron spectrum, e.g. [27, 187]. In streaking the photoionization time delay is directly mapped to a momentum shift into the laser polarization direction. This implicates that streaking spectra can, without any further assumptions, only be evaluated for electrons propagating into the polarization direction of IR laser field²⁵. Second, while RABBITT measures the difference between two-photon phases and the photoionization time delay is accessed via a finite difference approximation of the energy derivative [31, 32], streaking directly retrieves the photoionization time delay [30].

The question which arises naturally is whether or not the delays retrieved with the two methods are the same or not for explicitly angle-dependent time delays. For photoionization of an *s* electron and a residual ion with negligible polarization (ionization of hydrogen, shake-down ionization for helium) this question can trivially be answered with yes, given that the angle-dependence of the retrieved delays [Fig. 4.1] only occurs for large emissions angles of the electron relative to the laser polarization ($\theta > 60^\circ$) which do not contribute significantly to the angle-integrated signal. Therefore the delay retrieved from angle-integrated RABBITT spectra and streaking is the same for this specific case.

If the residual ion is easily polarizable this argument is not valid anymore as the dipole delay [Eq. (4.6)] is explicitly dependent on the electron emission angle. Thus, we compare the delays obtained from RABBITT and streaking for $n = 2$ shake-up ionization in helium. In this case the residual ion is a superposition of $\text{He}^+(2s)$ and $\text{He}^+(2p)$ and thus polarizable within the IR field [28, 29]. Comparing the delays obtained for photoelectrons which are emitted along the polarization direction ($\theta = 0^\circ$) we find near perfect agreement between the RABBITT and streaking simulations, Fig. B.1. The data points for the streaking sim-

²⁵ In turn, this means that for non-collinear XUV and IR fields the time delay into the relative polarization angle is detected [190, 191]

ulations are taken from [28, 29]. For the RABBITT calculations we use an IR field with $\lambda_{IR} = 800$ nm, intensity of 2×10^9 W/cm² and a FWHM duration of 16 fs. The APT has a FWHM duration of 9 fs and the harmonics have intensities ranging from 5×10^9 to 2×10^{12} W/cm². Both, the APT as well as the IR are within the perturbative regime.

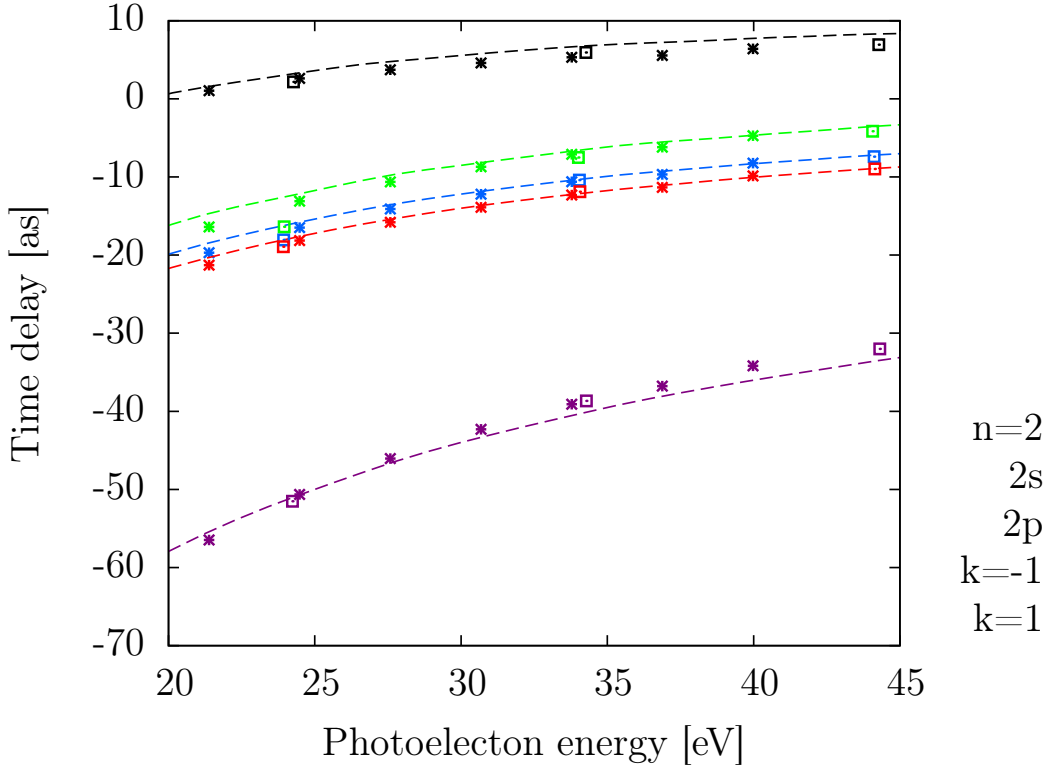


Figure B.1.: Comparison of the retrieved photoemission time delay for RABBITT (crosses) and streaking (boxes) spectra evaluated into $\theta = 0^\circ$ with the analytic expectation Eq. (4.1) (dashed line) for the full $n = 2$ shell and also the different sub-shells and shake-up states resolved. The fundamental IR pulse has a wavelength of $\lambda_{IR} = 800$ nm.

C. Calculation of the electron spectrum close to resonances

To extract the single ionization spectrum close to resonances we partition the wave function after the end of the pulse into an “outer” and an “inner” region using a smooth switch-on or switch-off function (i.e. a Gauss error function) around a partition radius r_{part} for both spatial directions, see Fig. C.1 for a sketch. In the “outer” region the single ionization spectra are extracted via projection onto products of bound He^+ states and Coulomb waves [89], Sec. 2.2.2. The spectra in the “inner” region are computed using exterior complex scaling (ECS) [60]. We sum the two spectra coherently to obtain the full spectrum. Unless stated otherwise we partitioned the wave function at $r_{part} = 20$ a.u. in both spatial dimensions for all results shown in this thesis. Comparing the single ionization spectrum obtained via this partition method with calculating the single ionization spectrum in the full spatial range via exterior complex scaling we find near perfect agreement for the results shown in this thesis.

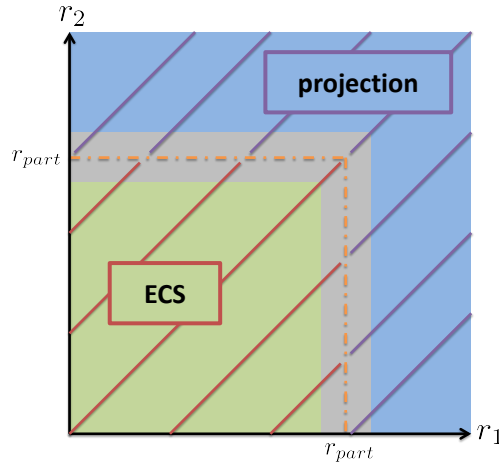


Figure C.1.: Sketch of the different radial regions the wave function is partitioned in. The green and blue area represent the unmasked inner and outer region, respectively. The grey area is the area where we apply the smooth masking function which is centered at the partition radius r_{part} (orange dashed-dotted line). In the area marked with red stripes (“inner” region) the electron spectrum is calculated using ECS [60]. The parts of wave function in the area marked with purple stripes (“outer” region) are projected onto products of bound He^+ states and Coulomb waves to obtain the electron spectra [89], Sec. 2.2.2.

D. Additional information on RABBITT with even and odd harmonics

In this appendix we discuss several aspects of RABBITT with even and odd harmonic in more detail.

D.1. Beating of the asymmetry \mathcal{C} in RABBITT with even and odd harmonics

To obtain an analytic expression for the beating of the asymmetry \mathcal{C} for RABBITT with even and odd harmonics with respect to ω_{IR} we insert the wave function Eq. (5.23)

$$\begin{aligned}
 \psi(E, \tau) &= \mathcal{A}_{E \leftarrow i}^{(1)} + \mathcal{A}_{E \leftarrow E + \omega_{\text{IR}} \leftarrow i}^{(2)} e^{-i\omega_{\text{IR}}\tau} + \mathcal{A}_{E \leftarrow E - \omega_{\text{IR}} \leftarrow i}^{(2)} e^{i\omega_{\text{IR}}\tau} \\
 &= \sum_{L=\lambda \pm 1} \sum_{\lambda} \left| \mathcal{A}_{E \leftarrow i, \lambda}^{(1)} \right| e^{i\phi_{\lambda}^{(1)}(E)} Y_{\lambda}^0(\theta) \\
 &\quad + \left| \mathcal{A}_{E, L \leftarrow E + \omega_{\text{IR}}, \lambda \leftarrow i}^{(2)} \right| e^{i[\phi_{\lambda, L}^{(2-)}(E) - \omega_{\text{IR}}\tau]} Y_L^0(\theta) \\
 &\quad + \left| \mathcal{A}_{E, L \leftarrow E - \omega_{\text{IR}}, \lambda \leftarrow i}^{(2)} \right| e^{i[\phi_{\lambda, L}^{(2+)}(E) + \omega_{\text{IR}}\tau]} Y_L^0(\theta)
 \end{aligned} \tag{D.1}$$

into Eq. (5.22)

$$\begin{aligned}
 \mathcal{C}(E, \tau) &= P_{\text{up}} - P_{\text{down}} \\
 &= \int_0^{2\pi} d\Omega |\psi(E, \tau)|^2 - \int_{2\pi}^{4\pi} d\Omega |\psi(E, \tau)|^2 \\
 &= 2\pi \left\{ \int_0^{\pi/2} d\theta \sin(\theta) |\psi(E, \tau)|^2 - \int_{\pi/2}^{\pi} d\theta \sin(\theta) |\psi(E, \tau)|^2 \right\}.
 \end{aligned} \tag{D.2}$$

λ and L are the angular momenta of the intermediate and the final state. The first term in Eq. (D.2) [P_{up}] is given by

$$\begin{aligned}
\int_0^{\pi/2} d\theta \sin(\theta) |\psi(E, \tau)|^2 &= \sum_{L=\lambda\pm 1} \sum_{L'=\lambda'\pm 1} \sum_{\lambda, \lambda'} \int_0^{\pi/2} d\theta \sin(\theta) \\
&\left| \mathcal{A}_{E\leftarrow i, \lambda}^{(1)} \right| e^{i\phi_\lambda^{(1)}(E)} Y_\lambda^0(\theta) \left| \mathcal{A}_{E\leftarrow i, \lambda'}^{(1)} \right| e^{-i\phi_{\lambda'}^{(1)}(E)} Y_{\lambda'}^0(\theta) \\
&+ \left| \mathcal{A}_{E, L\leftarrow E+\omega_{\text{IR}}, \lambda\leftarrow i}^{(2)} \right| e^{i[\phi_{\lambda, L}^{(2-)}(E) - \omega_{\text{IR}}\tau]} Y_L^0(\theta) \left| \mathcal{A}_{E, L'\leftarrow E+\omega_{\text{IR}}, \lambda'\leftarrow i}^{(2)} \right| e^{-i[\phi_{\lambda', L'}^{(2-)}(E) - \omega_{\text{IR}}\tau]} Y_{L'}^0(\theta) \\
&+ \left| \mathcal{A}_{E, L\leftarrow E-\omega_{\text{IR}}, \lambda\leftarrow i}^{(2)} \right| e^{i[\phi_{\lambda, L}^{(2+)}(E) + \omega_{\text{IR}}\tau]} Y_L^0(\theta) \left| \mathcal{A}_{E, L'\leftarrow E-\omega_{\text{IR}}, \lambda'\leftarrow i}^{(2)} \right| e^{-i[\phi_{\lambda', L'}^{(2+)}(E) + \omega_{\text{IR}}\tau]} Y_{L'}^0(\theta) \\
&+ \left| \mathcal{A}_{E\leftarrow i, \lambda}^{(1)} \right| e^{i\phi_\lambda^{(1)}(E)} Y_\lambda^0(\theta) \left| \mathcal{A}_{E, L'\leftarrow E+\omega_{\text{IR}}, \lambda'\leftarrow i}^{(2)} \right| e^{-i[\phi_{\lambda', L'}^{(2-)}(E) - \omega_{\text{IR}}\tau]} Y_{L'}^0(\theta) \\
&+ \left| \mathcal{A}_{E\leftarrow i, \lambda}^{(1)} \right| e^{i\phi_\lambda^{(1)}(E)} Y_\lambda^0(\theta) \left| \mathcal{A}_{E, L'\leftarrow E-\omega_{\text{IR}}, \lambda'\leftarrow i}^{(2)} \right| e^{-i[\phi_{\lambda', L'}^{(2+)}(E) + \omega_{\text{IR}}\tau]} Y_{L'}^0(\theta) \\
&+ \left| \mathcal{A}_{E, L\leftarrow E+\omega_{\text{IR}}, \lambda\leftarrow i}^{(2)} \right| e^{i[\phi_{\lambda, L}^{(2-)}(E) - \omega_{\text{IR}}\tau]} Y_L^0(\theta) \left| \mathcal{A}_{E, L'\leftarrow E-\omega_{\text{IR}}, \lambda'\leftarrow i}^{(2)} \right| e^{-i[\phi_{\lambda', L'}^{(2-)}(E) + \omega_{\text{IR}}\tau]} Y_{L'}^0(\theta) \\
&+ c.c. \tag{D.3}
\end{aligned}$$

Eq. (D.2) is a superposition of the different pathways [Eq. (D.1)] giving rise to terms which have a $\cos(2\omega_{\text{IR}}\tau)$ modulation, a $\cos(\omega_{\text{IR}}\tau)$ modulation and, no modulation with the time delay. Performing the integration with respect to θ the terms oscillating with $\cos(2\omega_{\text{IR}}\tau)$ [seventh line of Eq. (D.3)] and the terms which show no modulation with τ [second, third and fourth line of Eq. (D.3)] are the same for P_{up} and P_{down} . The asymmetry \mathcal{C} is thus solely given by

$$\begin{aligned}
\mathcal{C} &= \sum_{L=\lambda\pm 1} \sum_{\lambda, \lambda'} C_{L, \lambda} \\
&\times \left\{ \left| \mathcal{A}_{E\leftarrow i, \lambda}^{(1)} \right| \left| \mathcal{A}_{E, L\leftarrow E+\omega_{\text{IR}}, \lambda'\leftarrow i}^{(2)} \right| \cos \left[\omega_{\text{IR}}\tau + \left(\phi_\lambda^{(1)} - \phi_{\lambda', L}^{(2-)} \right) \right] \right. \\
&\quad \left. + \left| \mathcal{A}_{E\leftarrow i, \lambda}^{(1)} \right| \left| \mathcal{A}_{E, L\leftarrow E-\omega_{\text{IR}}, \lambda'\leftarrow i}^{(2)} \right| \cos \left[-\omega_{\text{IR}}\tau + \left(\phi_\lambda^{(1)} - \phi_{\lambda', L}^{(2+)} \right) \right] \right\}, \tag{D.4}
\end{aligned}$$

where the angular momentum dependent coefficients $C_{L, \lambda}$ are given by

$$\begin{aligned}
C_{L, \lambda} &= 8\pi \int_0^{\pi/2} d\theta \sin(\theta) Y_L^0(\theta) Y_\lambda^0(\theta) \\
&= 8\pi \sqrt{\frac{(2L+1)(2\lambda+1)}{4\pi}} \sum_J \sqrt{2J+1} \begin{pmatrix} L & \lambda & J \\ 0 & 0 & 0 \end{pmatrix} \begin{pmatrix} L & \lambda & J \\ 0 & 0 & 0 \end{pmatrix} \int_0^{\pi/2} d\theta \sin(\theta) Y_J^0(\theta) \\
&= 8\pi \sqrt{\frac{(2L+1)(2\lambda+1)}{4\pi}} \sum_J \sqrt{2J+1} \begin{pmatrix} L & \lambda & J \\ 0 & 0 & 0 \end{pmatrix} \begin{pmatrix} L & \lambda & J \\ 0 & 0 & 0 \end{pmatrix} \sqrt{\frac{2J+1}{4\pi}} (-1)^{\frac{J-1}{2}} \frac{J!!}{J(J+1)!!} \\
&= 2\sqrt{(2L+1)(2\lambda+1)} \sum_J (-1)^{\frac{J-1}{2}} (2J+1) \left[\begin{pmatrix} L & \lambda & J \\ 0 & 0 & 0 \end{pmatrix} \right]^2 \frac{J!!}{J(J+1)!!}. \tag{D.5}
\end{aligned}$$

D.2. Phases retrieved by RABBITT with even and odd harmonics as function of the intensity of the harmonics

In this appendix we try to understand the discrepancy between the retrieved phase close to the $2s2p$ resonance in helium and a pure Fano phase [Eq. (5.17)] seen in Fig. 5.5b in more detail. We systematically study the retrieved phase as function of the intensity of the harmonics neighboring the harmonic resonant with the $2s2p$ resonance in helium.

To do so, we set the fundamental wavelength to $\lambda_{\text{IR}} = 742\text{nm}$ and employ an APT consisting out of the 35^{th} to 37^{th} harmonic with intensities $I_{35} = 10^{11} \text{ W/cm}^2$, $I_{36} = 2.5 \times 10^{10} \text{ W/cm}^2$ and $I_{37} = \eta I_{35}$. For the chosen fundamental wavelength $\lambda_{\text{IR}} = 742\text{nm}$ the energy of the 36^{th} harmonic coincides with the energy of the $2s2p$ resonance in helium. The ratio $\eta = I_{37}/I_{35}$ is varied smoothly within $\eta \in [0 : 100]$. The FWHM duration of the IR pulse and the APT are approximately 15 fs and 12.5 fs. We choose a radial box spanning 2220 a.u. (40 a.u.) in the larger (smaller) direction and 11 basis function for every finite element spanning 5 a.u.. We obtained converged results for a close-coupling expansion of $L_{\text{max}} = 3$, $\ell_1 = \ell_2 = 4$ employing length gauge. The spectrum was calculated using the method described in App. C.

For the case of two isolated harmonics ($\eta = 0$) we retrieve the expected Fano phase variation [Fig. D.1a]. Similarly, if the intensity of the harmonic above compared to the one below the resonant harmonic is much larger ($I_{37} \gg I_{35}$), i.e. $\eta = 100$, an inverted Fano phase profile is retrieved from the oscillation of the asymmetry \mathcal{C} . For intermediate values of η a smooth transition between the two extrema ($\eta = 0$ and $\eta = 100$) can be observed. When both harmonics are identical in amplitude ($\eta = 1$) the retrieved phase is drastically distorted from the expected profile. When the energetically higher harmonic dominates over the lower harmonic, the sign of the phase variation changes. Interestingly, the retrieved phase at the resonance energy ($E_R = 60.15 \text{ eV}$) is half the amplitude of the total phase variation, i.e. $\pi/2$ for all values of η . Similarly, for all explored values of η the retrieved phase jumps by π at $\epsilon + q = 0$. Since the energy-resolved phase is different for different intensity ratios η we expect also a difference if the phase is extracted from the asymmetry integrated in energy over the harmonic width, see Fig. D.1b. As the intensity of the above harmonic (I_{37}) is increased the retrieved phase increases monotonically. Comparing the values for $\eta = 0$ and $\eta = 5$ we observe a difference of approximately 1 rad.

Furthermore, we characterize the influence of the intensity ratio on the retrieved phase for the case where one of the two two-photon transitions interfering with the direct one-photon transition has the $2s2p$ resonance as intermediate state. Thus, we employ the same parameters as before but with an APT consisting out of the 34^{th} to 36^{th} harmonic of the fundamental $\lambda_{\text{IR}} = 742\text{nm}$, with intensities $I_{34} = \eta I_{36}$, $I_{35} = 2.5 \times 10^{10} \text{ W/cm}^2$ and $I_{36} = 10^{11} \text{ W/cm}^2$. Within the nonresonant harmonic 35 the superposition of three contributions gives rise to two different oscillations of the asymmetry

$$\mathcal{C} = A_1 \cos(-\omega_{\text{IR}}\tau + \phi_1) + A_2 \cos(\omega_{\text{IR}}\tau + \phi_2).$$

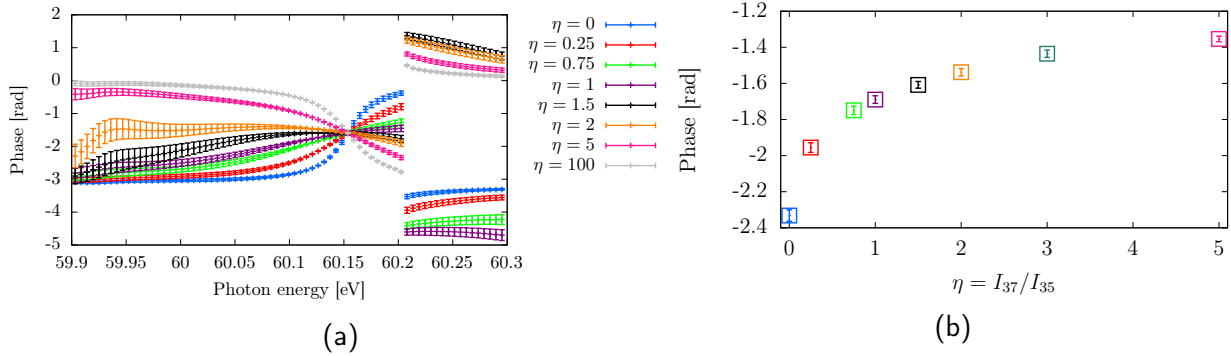


Figure D.1.: (a) Retrieved phase of the oscillation of the asymmetry \mathcal{C} for various ratios $\eta = I_{37}/I_{35}$ of the adjacent harmonics. (b) Same as (a), but the phase is now retrieved from the asymmetry integrated over the full harmonic width from 60 eV to 60.3 eV photon energy. The energy of the 36th harmonic coincides with the resonance energy of the 2s2p resonance in helium.

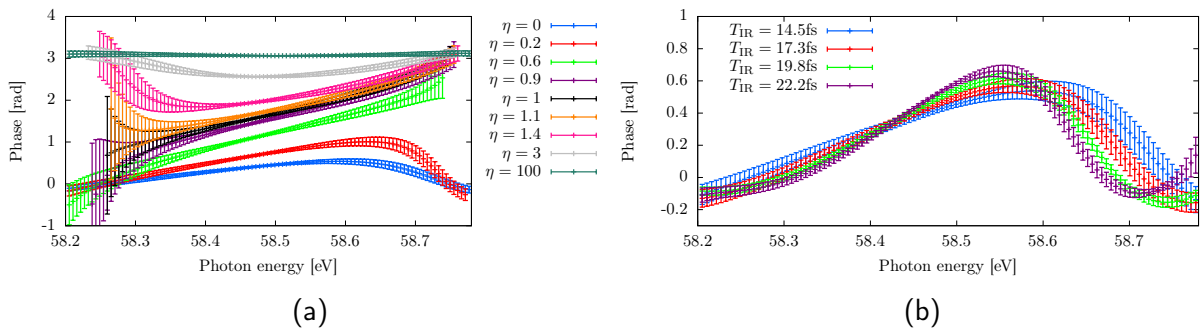


Figure D.2.: (a) Retrieved phase of the oscillation of the asymmetry \mathcal{C} in the 35th harmonic neighboring the resonant 36th harmonic, for various ratios $\eta = I_{34}/I_{36}$ of the harmonics. (b) Retrieved phase of the asymmetry \mathcal{C} oscillation in the 35th harmonic for $\eta = 0$ and four different durations of the fundamental IR T_{IR} . The FWHM duration of the APT was 12.5 fs.

The contribution oscillating with $-\omega_{\text{IR}}\tau$ is due to the interference of the non-resonant one-photon transition to harmonic 35 and the two-photon transition to harmonic 35 via the non-resonant harmonic 34. The contribution oscillating with $\omega_{\text{IR}}\tau$ is created by the interference of the non-resonant one-photon transition to harmonic 35 with the two-photon transition to harmonic 35 via the resonant harmonic 36. While for the former path the phase difference ϕ_1 is expected to be almost constant across the harmonic width the latter path will feature a pronounced phase variation ϕ_2 across the harmonic width due to the intermediate resonant state [52, 53, 176].

This expectation is, indeed, confirmed by varying the intensity ratio of the lowest harmonic with respect to the resonant harmonic $\eta = \frac{I_{34}}{I_{36}}$, see Fig. D.2a. The retrieved phase varies smoothly as a function of the intensity ratio η from the pronounced two-photon phase variation via a resonant transition ($\eta = 0$) to a fully flat phase ($\eta = 100$) as the contribution from the interference of two non-resonant transitions is dominant. For the scenario where both paths contribute significantly, $\eta \approx 1$, the retrieved phase variation is much larger and completely different compared to the phase for either of the two limiting cases. As was already shown in [176] the phase excursion of the two-photon phase via a resonant transition does depend strongly on the spectral width (and thus its duration) of the IR causing the second transition, see Fig. D.2b. In other words, for a spectrally very narrow IR field one can expect to observe a phase variation which is very close to the one-photon phase in the resonant harmonic [53].

D.3. Angle-integrated RABBITT with even and odd harmonics

To perform a theoretical consistency check for RABBITT with even and odd harmonics (RABBITT-evo), we analyze the fully angle-integrated electron spectrum

$$P_{\text{tot}}(E, \tau) = P_{\text{up}}(E, \tau) + P_{\text{down}}(E, \tau) = \int_0^{4\pi} d\Omega P(E, \tau, \Omega), \quad (\text{D.6})$$

which is the same observable as exploited in traditional RABBITT. $P_{\text{tot}}(E, \tau)$ shows a $2\omega_{\text{IR}}$ beating, which contrary to conventional RABBITT is not produced by interference of three paths, but by four paths, see Fig. D.3a. Path 2 and 3 are also present in conventional angle-integrated RABBITT spectra and induce a $2\omega_{\text{IR}}$ beating in the main bands [Fig. D.3b]. The phases of this $2\omega_{\text{IR}}$ beating agree very well with phases extracted with RABBITT for the sidebands (corresponding to the even harmonics for RABBITT-evo) [Figs. D.4a and b], as well as for the mainbands (corresponding to the odd harmonics for RABBITT-evo) [Figs. D.4c and d].

The small discrepancies visible in the phases extracted from RABBITT and RABBITT-evo can most likely be explained by the additional interference path [Path 4 in Fig. D.3a].

The results shown in Fig. D.4 were calculated using a fundamental field with a FWHM duration of approximately 22 fs and an APT duration of roughly 14.5 fs, resulting in

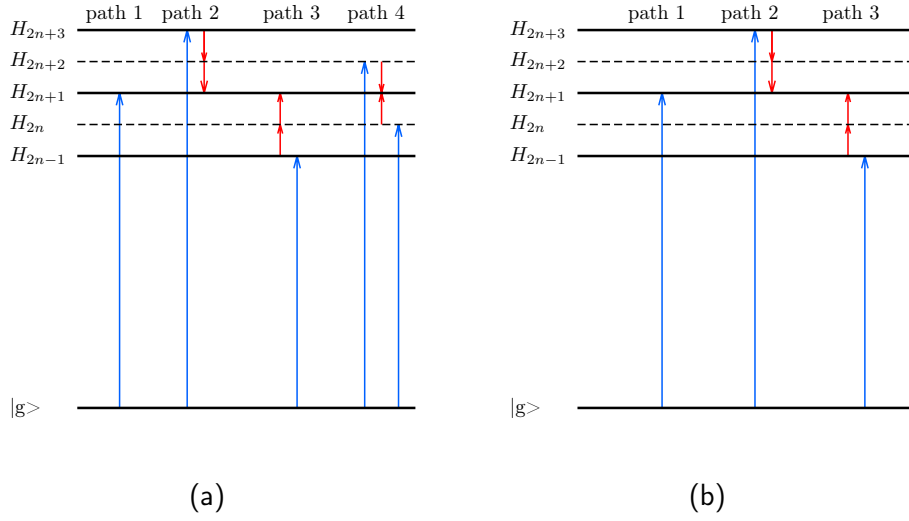


Figure D.3.: (a) Sketch to illustrate the interference paths resulting in a $2\omega_{\text{IR}}$ beating of the harmonics for RABBITT with even and odd harmonics. (b) Sketch to illustrate the interference paths resulting in a $2\omega_{\text{IR}}$ beating of the mainbands for RABBITT.

spectrally broad harmonics, see Fig. 5.5a for the spectrum of the APT used for RABBITT with even and odd harmonics. For the RABBITT simulations the APT consisted only of the odd harmonics 67, 69, 71, 75. The fundamental wavelength λ_{IR} is smoothly varied from 1456nm to 1472nm. For $\lambda_{\text{IR}} = 1464$ nm the 71st harmonic is almost resonant with the 2s2p resonance in helium.

Energy-resolved $2\omega_{\text{IR}}$ phase in RABBITT and RABBITT with even and odd harmonics

The phase of the $2\omega_{\text{IR}}$ beating of $P_{\text{tot}}(E, \tau)$ within the mainband centered at the 2s2p resonance for RABBITT and within the resonant harmonic for RABBITT with even and odd harmonics clearly reveals the characteristic Fano phase variation Φ_F [Eq. (5.17)], see Fig. D.5a. Both techniques yield almost the same result implicating that either of them could be used to directly measure Φ_F within the angle-integrated photoelectron spectrum.

Numerical parameters In the *ab initio* simulation we use an asymmetric radial box where the larger (smaller) radial coordinate extends up to 3410 a.u. (20 a.u.) and we use 11 basis function for every finite element spanning 5 a.u. in the FEDVR expansion. An absorbing boundary prevents the influence of reflected parts of the wave packet starting at 3324.8 and 15 a.u., respectively. Employing velocity gauge we achieve converged results

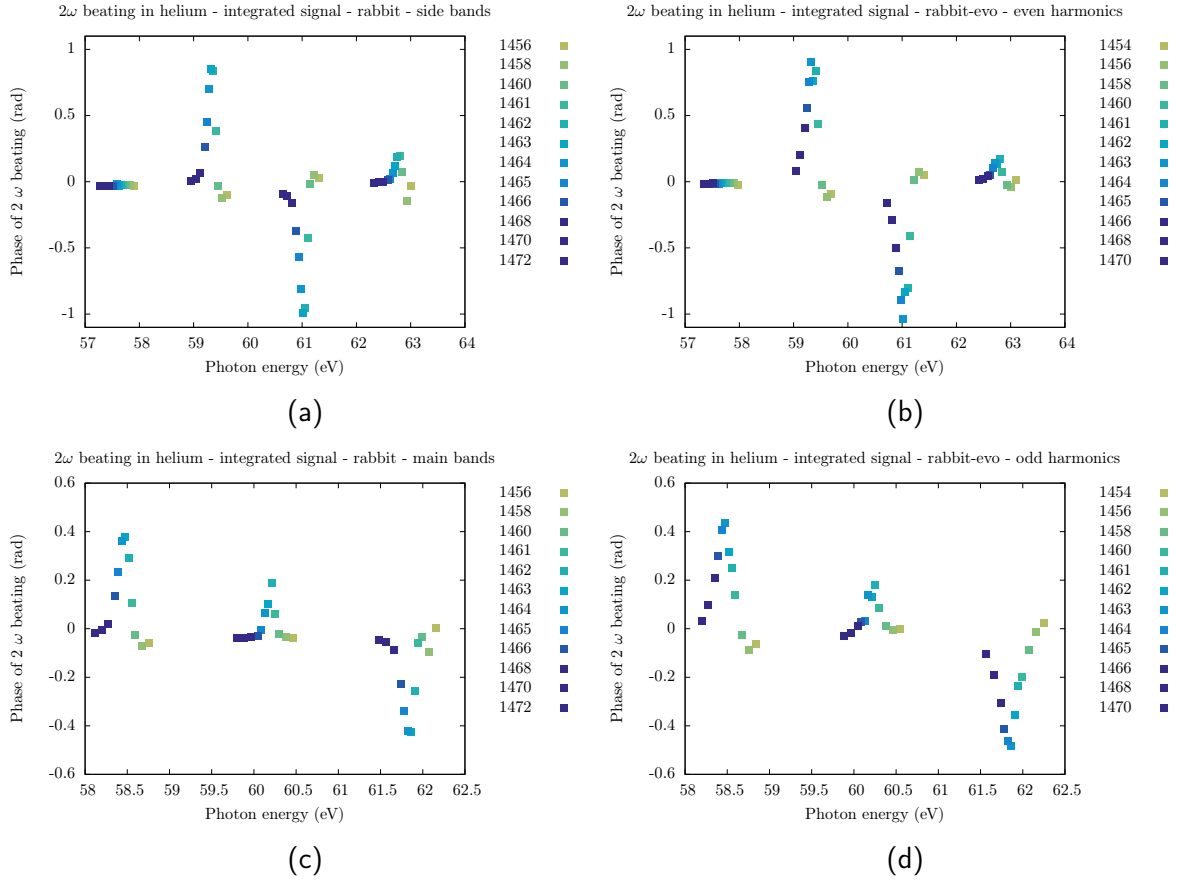
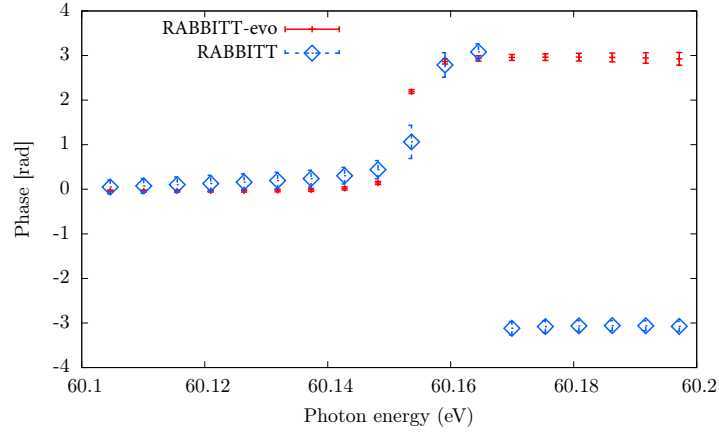


Figure D.4.: (a) Retrieved $2\omega_{\text{IR}}$ phase in the side bands using conventional RABBITT for a scan of the fundamental wavelength λ_{IR} . (b) Retrieved $2\omega_{\text{IR}}$ phase in the even harmonics using RABBITT with even and odd harmonics (RABBITT-evo) for a scan of the fundamental wavelength λ_{IR} . (c) Retrieved $2\omega_{\text{IR}}$ phase in the main bands using traditional RABBITT for a scan of the fundamental wavelength λ_{IR} . (d) Retrieved $2\omega_{\text{IR}}$ phase in the odd harmonics using RABBITT-evo for a scan of the fundamental wavelength λ_{IR} .



(a)

Figure D.5.: Energy resolved phase of the $2\omega_{IR}$ beating of the fully angle-integrated photoelectron spectrum P_{tot} in the 71^{st} harmonic for $\lambda_{IR}=1464$ nm for RABBITT (this is the beating in the main band) and RABBITT with even and odd harmonics (RABBITT-evo). The energy of the 71^{st} harmonic coincides with the resonance energy of the $2s2p$ resonance.

with a close-coupling expansion of $L_{max} = 3$, $\ell_1 = \ell_2 = 4$. The single-ionization spectra are obtained using the method described in App. C.

E. Derivation of the CHIP beating formula and the phase shear term

In this appendix we discuss some more details of the circular holographic ionization phase meter (CHIP) discussed in Sec. 5.2.2.

E.1. Lowest-order perturbation theory for CHIP

The emergence of different interference patterns in the angularly resolved energy distribution at the energy of the $3n + k$ harmonic, $\mathcal{P}_k^{\nu_{\text{IR}}}(E, \Omega)$, which is the key observable in CHIP can be explained within lowest-order perturbation theory. For simplicity we consider only the interference in the upper harmonic $3n + 2$. In the excitation of helium to a superposition of $|1sE\ell m\rangle$ continuum states, the photoelectron anisotropy results from the interference between the p -wave one-photon amplitude $\mathcal{A}_{Ep, \nu_k}^{(1)}$ by absorption of an XUV photon from the $3n + 2$ harmonic with helicity ν_k and the two-photon amplitude $\mathcal{A}_{E\ell, -\nu_k + \nu_{\text{IR}}}^{(2)}$ for either an s -wave ($\ell = 0$) or d -wave ($\ell = 2$) by absorption of one photon each from the harmonic $3n + 1$ (helicity $-\nu_k$) and the IR pulse (helicity ν_{IR}). The angular distribution takes the form

$$\mathcal{P}_k^{\nu_{\text{IR}}}(E, \Omega) = |\mathcal{A}_{Ep, \nu_k}^{(1)} Y_1^{\nu_k} + \sum_{\ell=0,2} \mathcal{A}_{E\ell, -\nu_k + \nu_{\text{IR}}}^{(2)} Y_\ell^{-\nu_k + \nu_{\text{IR}}}|^2. \quad (\text{E.1})$$

Either two, or three partial waves interfere, depending on whether the IR and the lower harmonic are co- or counter-rotating, respectively. The interference signal is strongest in the light polarization plane and vanishes along the light propagation direction. The one-photon amplitude $\mathcal{A}_{Ep, \nu_k}^{(1)}$ is proportional to the dipole ionization matrix element and the Fourier transform of the XUV field \tilde{F}_{XUV} , i.e.

$$\mathcal{A}_{Ep, \nu_k}^{(1)} \propto \tilde{F}_{\text{XUV}}(E - E_g) \langle 1sEp\nu_k | \hat{D}_1^{\nu_k} | g \rangle, \quad (\text{E.2})$$

where $\hat{D}_1^{\nu_k}$ is the dipole operator for light helicity ν_k , and the continuum states $|1sE\ell m\rangle$ satisfy incoming boundary conditions [132] and their outgoing component coincides asymptotically with that of a regular Coulomb function. In the limit of infinitely long IR pulses (finite-pulse effects are discussed latter), the two-photon amplitude initiated by the $3n + 1$ harmonic is proportional to

$$\begin{aligned} \mathcal{A}_{E\ell, -\nu_k + \nu_{\text{IR}}}^{(2)} &\propto \tilde{F}_{\text{IR}} \tilde{F}_{\text{XUV}}(E - E_g - \omega_{\text{IR}}) \times \\ &\times \int dE' \frac{\langle 1sE\ell, -\nu_k + \nu_{\text{IR}} | \hat{D}_1^{\nu_{\text{IR}}} | 1sE'p, -\nu_k \rangle \langle 1sE'p, -\nu_k | \hat{D}_1^{-\nu_k} | g \rangle}{E - E' - \omega_{\text{IR}} + i0^+}, \end{aligned} \quad (\text{E.3})$$

where \tilde{F}_{IR} is the Fourier transform of the IR field [172]. The angular resolved photoelectron distribution in the polarization plane ($\theta = \pi/2$) is a function of E and a harmonic function of the azimuthal angle φ ,

$$\mathcal{P}_k^{\nu_{\text{IR}}}(E, \varphi) = \mathcal{W}_k^{\nu_{\text{IR}}}(E) + |\mathcal{S}_k^{\nu_{\text{IR}}}(E)| \cos[\beta_k^{\nu_{\text{IR}}}\varphi + \Delta_k^{\nu_{\text{IR}}}(E)], \quad (\text{E.4})$$

with the angular frequency $\beta_k^{\nu_{\text{IR}}} = 2\nu_k - \nu_{\text{IR}}$. For the case $\nu_k = -1$ $\beta_k = -3$, or -1 for co- or counter-rotating lower harmonic and IR field. For the case $\nu_k = 1$ $\beta_k = 3$, or 1 for co- or counter-rotating lower harmonic and IR field. The parameters $\mathcal{W}_k^{\nu_{\text{IR}}}$, $\mathcal{S}_k^{\nu_{\text{IR}}}$, and $\Delta_k^{\nu_{\text{IR}}}$ do not depend on the azimuthal angle φ . The parameters describing the oscillatory part are given by:

$$\mathcal{S}_k^{\nu_{\text{IR}}}(E) = \mathcal{A}_{Ep, \nu_k}^{(1)} [b_k^{\nu_{\text{IR}}} \mathcal{A}_{Es, -\nu_k + \nu_{\text{IR}}}^{(2)*} + \mathcal{A}_{Ed, -\nu_k + \nu_{\text{IR}}}^{(2)*} a_k^{\nu_{\text{IR}}} \sqrt{15/4\pi}] \quad (\text{E.5})$$

$$\Delta_k^{\nu_{\text{IR}}}(E) = \arg[\mathcal{S}_k^{\nu_{\text{IR}}}(E)], \quad (\text{E.6})$$

where $a_k^{\nu_{\text{IR}}} = \nu_k/\sqrt{2}$ and $b_k^{\nu_{\text{IR}}} = -\nu_k\sqrt{3/8\pi^2}$ for $\beta_k = -1$ and $a_k^{\nu_{\text{IR}}} = -\nu_k\sqrt{3/4}$ and $b_k^{\nu_{\text{IR}}} = 0$ for $\beta_k = -3$.

E.2. Effects of non vanishing time delay between the APT and the IR and finite IR pulse duration

To derive the shear term visible for finite IR pulse duration [Eq. (5.35)] we focus on the case of the absorption of an XUV photon, followed by the absorption of a co-rotating IR photon with the same polarization vectors $\hat{\epsilon}$, that leads to a state in the continuum with energy E . The amplitude for this process is [176],

$$\mathcal{A}_{E \leftarrow g}^{(2)} = -i \int d\omega \tilde{F}_{\text{IR}}(E - E_g - \omega) \tilde{F}_{\text{XUV}}(\omega) \mathcal{M}_{E \leftarrow g}^{(2)}(\omega) \quad (\text{E.7})$$

where \tilde{F}_{XUV} and \tilde{F}_{IR} are the Fourier transform of the pump (XUV) and probe (IR) electric fields, and $\mathcal{M}_{E \leftarrow g}^{(2)}(\omega)$ is the two-photon matrix element

$$\mathcal{M}_{E \leftarrow g}^{(2)}(\omega) = \int dE' \frac{\langle E | \hat{\mu} | E' \rangle \langle E' | \hat{\mu} | g \rangle}{E_g + \omega - E' + i0^+}, \quad (\text{E.8})$$

where we replaced $|1sEl \nu_k \pm \nu_{\text{IR}}\rangle$ of Eq. (E.3) with $|E\rangle$ for simplicity. The operator $\hat{\mu} = \hat{\vec{D}} \cdot \hat{\epsilon}$ is the projection of the dipole operator on the polarization vector. In the present context, we can simplify Eq. (E.8) by using the fact that the continuum-continuum dipole matrix element is approximately diagonal in the energy, $\langle E | \hat{\mu} | E' \rangle \approx \bar{\mu}(E) \delta(E - E')$ (*on-shell* approximation), and that the folding with the XUV and IR spectra samples only frequencies far from the pole in the integrand of Eq. (E.8),

$$\mathcal{M}_{E \leftarrow g}^{(2)}(\omega) \approx \frac{\bar{\mu}(E) \mu_{Eg}}{E_g + \omega - E}. \quad (\text{E.9})$$

Since the denominator is non-zero, we can conveniently rewrite it by introducing the new variables $\xi_e = E - (E_g + \omega_{\text{XUV}} + \omega_{\text{IR}})$, $\xi_\omega = \omega - \omega_{\text{XUV}}$, and $\xi = \xi_\omega - \xi_e$,

$$\frac{1}{E_g + \omega - E} = \frac{-1}{\omega_{\text{IR}}} \exp[-\log(1 - \xi/\omega_{\text{IR}})]. \quad (\text{E.10})$$

To second order in ξ/ω_{IR} ,

$$\frac{1}{E_g + \omega - E} \approx \frac{-1}{\omega_{\text{IR}}} \exp\left[\xi/\omega_{\text{IR}} + \frac{1}{2}\left(\frac{\xi}{\omega_{\text{IR}}}\right)^2\right]. \quad (\text{E.11})$$

Let's assume that the XUV and the IR spectra have a Gaussian profile,

$$\tilde{F}_{\text{XUV}}(\omega) \propto \exp\left[-\frac{(\omega - \omega_{\text{XUV}})^2}{2\sigma_{\text{XUV}}^2}\right], \quad (\text{E.12})$$

$$\tilde{F}_{\text{IR}}(\omega) \propto \exp\left[-\frac{(\omega - \omega_{\text{IR}})^2}{2\sigma_{\text{IR}}^2} - i\omega\tau\right]. \quad (\text{E.13})$$

$$(\text{E.14})$$

Then, up to irrelevant constant factors,

$$\mathcal{A}_{E \leftarrow g}^{(2)} \propto e^{-i\omega_{\text{IR}}\tau} \exp\left(-\frac{\xi_e^2}{2\sigma_{\text{XUV}}^2}\right) \int d\xi \exp\left[-\xi^2 \frac{\sigma_{\text{IR}}^{-2} + \sigma_{\text{XUV}}^{-2} - \omega_{\text{IR}}^{-2}}{2} + \xi(i\tau + \omega_{\text{IR}}^{-1} - \xi_e \sigma_{\text{XUV}}^{-2})\right] \quad (\text{E.15})$$

the integral over ξ is readily evaluated yielding

$$\mathcal{A}_{E \leftarrow g}^{(2)} \propto e^{-i\omega_{\text{IR}}\tau} \exp\left\{\frac{1}{2} \frac{[i\tau\sigma_{\text{XUV}} + \omega_{\text{IR}}^{-1}\sigma_{\text{XUV}} - \xi_e\sigma_{\text{XUV}}^{-1}]^2}{1 + \sigma_{\text{XUV}}^2(\sigma_{\text{IR}}^{-2} - \omega_{\text{IR}}^{-2})} - \frac{\xi_e^2}{2\sigma_{\text{XUV}}^2}\right\}. \quad (\text{E.16})$$

The expression comprises an amplitude modulation as well as a phase modulation scaling linear with the delay, which, up to a constant is

$$\arg\left[\mathcal{A}_{E \leftarrow g}^{(2)}\right] = \left[1 - \frac{\sigma_{\text{XUV}}^2}{\omega_{\text{IR}}^2 + \sigma_{\text{XUV}}^2(\omega_{\text{IR}}^2\sigma_{\text{IR}}^{-2} - 1)}\right] \omega_{\text{IR}}\tau - \frac{\sigma_{\text{IR}}^2}{\sigma_{\text{IR}}^2 + \sigma_{\text{XUV}}^2 - \sigma_{\text{IR}}^2\sigma_{\text{XUV}}^2/\omega_{\text{IR}}^2} \xi_e\tau. \quad (\text{E.17})$$

The first term, i.e., the standard modulation of the beating with the delay, does not depend on the final energy and it includes the red shift in the beating frequency due to the finite duration of the pump and probe pulses, which was demonstrated already in [176]. In practical cases, however, this red shift is of the order of one part in thousand and hence it is hardly observable at all. The second term is linear in both time delay and energy, and corresponds to a shear of the phase with energy. Typically the IR pulse is an order of magnitude longer than the IR period. The phase shear with energy, $\partial^2 \arg\left[\mathcal{A}_{E \leftarrow g}^{(2)}\right] / \partial E \partial \tau$, therefore, is approximately

$$\frac{\partial^2}{\partial E \partial \tau} \arg\left[\mathcal{A}_{E \leftarrow g}^{(2)}\right] \simeq \frac{-1}{1 + \sigma_{\text{XUV}}^2/\sigma_{\text{IR}}^2}. \quad (\text{E.18})$$

For a fixed time delay corresponding to one IR period starting at zero, therefore, the excursion of the phase $\Delta\phi$ (and hence, in CHIP of angle) across one harmonic is

$$\Delta\phi \leq 2\pi \frac{\sigma_{\text{XUV}}/\omega_{\text{IR}}}{1 + \sigma_{\text{XUV}}^2/\sigma_{\text{IR}}^2}. \quad (\text{E.19})$$

The APT is typically half as short as the IR or shorter extending over a few IR cycles. In this case Eq. E.19 predicts $\Delta\phi \leq 30^\circ$. If long acquisition times are necessary, therefore, the laser system must have high CEP and time-delay stability.

F. Theoretical basis employed for wavelength scanning in argon

To treat the single ionization process underlying the observed RABBITT spectra for photoionization of argon we use the `newstock` suite described in section 2.2.3 and [102]. For the results presented in Sec. 5.3 we use two different sets of configuration-state function (CSF) bases, tailored to either the low-energy part of the spectrum (CSF-low) or the mid-energy part, above the $3s^{-1}3p^6$ threshold (CSF-mid). The CSF-mid space of the argon atom comprises all the configurations of the form $[\text{Ne}]3s^{\nu_1}3p^{\nu_2}3d^{\nu_3}4s^{\nu_4}4p^{\nu_5}$, in which the K and L shells are fully occupied ($[\text{Ne}] = 1s^22s^22p^6$), only two electrons at most are promoted to the N shells, $\nu_4 + \nu_5 \leq 2$, and no $4d$ or $4f$ orbital is populated. Among these configurations, we selected those that are most representative for the doublet ions with energy within approximately 36 eV above the ground state. These configurations are $[\text{Ne}]3s^23p^5$, $[\text{Ne}]3s^13p^6$, $[\text{Ne}]3s^13p^5nl$, $[\text{Ne}]3p^53dnl$, $[\text{Ne}]3p^6nl$, $[\text{Ne}]3s^23p^4nl$, $[\text{Ne}]3s3p^43dnl$, $[\text{Ne}]3s^23p^3nl'n'l'$, and $[\text{Ne}]3s^23p^23d^2nl$, where nl can be $3d$, $4s$, $4p$. The maximal angular momentum of the free electron was chosen to be 6. These configurations can give rise to various total symmetries. Here we considered the following parent-ion symmetries: $^2S^e$, $^2S^o$, $^2P^o$, $^2P^e$, $^2D^e$, $^2D^o$, $^2F^o$, $^2F^e$, and $^2G^e$. Both the radial part of the atomic orbitals $1s$, $2s$, $2p$, $3s$, $3p$, $3d$, $4s$, $4p$, and the configuration-interaction coefficients are determined with a Multi-Configuration Hartree-Fock calculation (MCHF) performed using the ATSP2K package by Charlotte Froese-Fischer and co-workers [141]. The smaller CSF basis (CSF-low) that specifically targets the low-energy part of the spectrum comprises a subset of CSF-mid, as well as a smaller orbital angular momentum (4) for the photoelectron. To be more precise, we exclude the configurations $[\text{Ne}]3p^6nl$, $[\text{Ne}]3p^53d4l$, $[\text{Ne}]3s23p^23d^24s$ in the CSF-low basis and consider only a limited number of parent-ion symmetries: $^2S^e$, $^2P^o$, $^2P^e$, $^2D^e$.

Since we are interested in reproducing RABBITT spectra in the perturbative limit and for linearly polarized light, we have limited the expansion of the total symmetry to $^1S^e$, $^1P^o$, and $^1D^e$. Each total symmetry comprises a localized channel constructed by adding, in all possible ways, an electron to a CSF configuration in any of the $3s$, $3p$, $3d$, $4s$, and $4p$ active orbitals. There are 82 (63), 159 (150), and 207 (158) such states for the $^1S^e$, $^1P^o$, and $^1D^e$ symmetries for the CSF-mid (CSF-low) basis, respectively. Each close coupling space comprises all channels deemed essential to describe photoionization up to approximately 34 eV above the ground-state energy. This results in 7 (5), 17 (11), and 23 (13) partial wave channels (PWCs) in $^1S^e$, $^1P^o$, and $^1D^e$ symmetry for the CSF-mid (CSF-low) basis. We use B-splines of order 7 with asymptotic separation between consecutive nodes of 0.4 a.u., up to a maximum radius of 500 a.u. Details about the CSF-mid and CSF-low bases can

Table F.1.: Energy of the parent ions n^2L^π obtained from the MCHF (see text for details) for the CSF-mid basis as compared with the experimental value for the energy of the highest angular momentum J state in the corresponding n^2L^π multiplet. The absolute *ab initio* energy of the ground $[\text{Ne}]2s^22p^5$ ($^2P^\circ$) state is $E_1^{2P^\circ} = -526.377339$ a.u.. In forming the close-coupling space, the energy of the parent ions is shifted with respect to its *ab initio* value to reproduce more closely the experimental differences.

State a	Dominant CSF	NIST E_a	MCHF E_a	Δ_a
I $^2P^\circ$	$[\text{Ne}]3s^23p^5$	0	0	-0.023 47
I $^2S^e$	$[\text{Ne}]3s3p^6$	0.495 372	0.471 898	0.
I $^2P^e$	$[\text{Ne}]3s^23p^4(^3P)4s$	0.629 884	0.619 725	-0.013 30
II $^2P^e$	$[\text{Ne}]3s^23p^4(^3P)3d$	0.663 716	0.699 406	-0.059 16
I $^2D^e$	$[\text{Ne}]3s^23p^4(^1D)4s$	0.678 176	0.677 970	-0.023 26
I $^2F^e$	$[\text{Ne}]3s^23p^4(^3P)3d$	0.684 123	0.747 823	-0.087 17
II $^2D^e$	$[\text{Ne}]3s^23p^4(^3P)3d$	0.688 404	0.728 334	-0.063 40
I $^2G^e$	$[\text{Ne}]3s^23p^4(^3P)3d$	0.702 503	0.754 436	-0.075 40
I $^2D^\circ$	$[\text{Ne}]3s^23p^4(^3P)4p$	0.723 228	0.715 706	-0.015 95
II $^2P^\circ$	$[\text{Ne}]3s^23p^4(^3P)4p$	0.730 105	0.725 268	-0.018 63
I $^2S^\circ$	$[\text{Ne}]3s^23p^4(^3P)4p$	0.733 977	0.725 896	-0.015 39
II $^2F^e$	$[\text{Ne}]3s^23p^4(^1D)3d$	0.744 991	0.825 046	-0.103 53
II $^2S^e$	$[\text{Ne}]3s^23p^4(^1S)4s$	0.762 311	0.757 771	-0.018 87

Table F.2.: Energy of the parent ions n^2L^π obtained from the MCHF (see text for details) for the CSF-low basis as compared with the experimental value for the energy of the highest angular momentum J term in the corresponding n^2L^π multiplet. The absolute *ab initio* energy of the ground $[\text{Ne}]2s^22p^5$ ($^2P^\circ$) state is $E_1^{2P^\circ} = -526.390684$ a.u.. In forming the close-coupling space, the energy of the parent ions is shifted with respect to its *ab initio* value to reproduce more closely the experimental differences.

State a	Dominant CSF	NIST E_a	MCHF E_a	Δ_a
I $^2P^\circ$	$[\text{Ne}]3s^23p^5$	0	0	-0.017 4
I $^2S^e$	$[\text{Ne}]3s3p^6$	0.495 372	0.477 943	0.
I $^2P^e$	$[\text{Ne}]3s^23p^4(^3P)4s$	0.629 884	0.621 415	-0.009 0
II $^2P^e$	$[\text{Ne}]3s^23p^4(^3P)3d$	0.663 716	0.724 892	-0.074 0
I $^2D^e$	$[\text{Ne}]3s^23p^4(^1D)4s$	0.678 176	0.680 509	-0.020 8
II $^2D^e$	$[\text{Ne}]3s^23p^4(^3P)3d$	0.688 404	0.759 509	-0.091 3
II $^2P^\circ$	$[\text{Ne}]3s^23p^4(^3P)4p$	0.730 105	0.869 935	-0.159 7
II $^2S^e$	$[\text{Ne}]3s^23p^4(^1S)4s$	0.762 311	0.807 098	-0.062 2

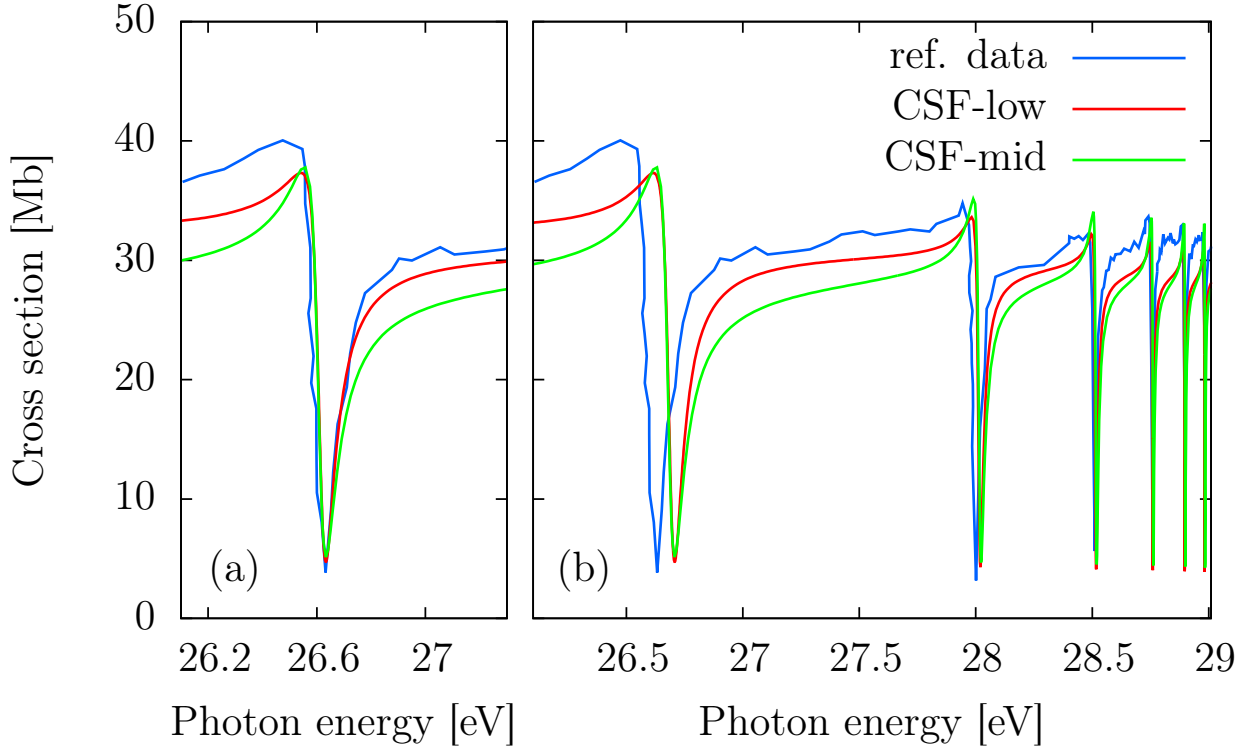


Figure F.1.: Calculated cross section σ for the two different bases with the newstock code compared against experimental reference data taken from [264]. To compare directly the cross section close to the $3s^{-1}4p$ resonance in (a) the results were shifted upward in energy by 0.443 eV for the CSF-low and 0.378 eV for the CSF-mid basis. To compare cross section for the energetically higher $3s^{-1}np$ resonances in (b) the results were shifted upward in energy by 0.517 eV for the CSF-low and 0.452 eV for the CSF-mid basis such the second ionization threshold coincides between the reference data and both theoretical bases. The results shown are obtained within length gauge.

be found in Tab. F.1 and Tab. F.2, respectively.

All results shown obtained from the time propagation employ velocity gauge.

F.1. Determination of basis quality

The total cross section for the fundamental ion ${}^2\text{P}^{\circ}$ agrees reasonably well with experimental results obtained from photoelectron spectroscopy experiments [264] for both bases, see Fig. F.1. Overall we observe a slightly better agreement of the cross section in this region between experimental data and the CSF-low basis. This is no surprise as this basis was optimized just for the energy region below the second ionization threshold (approximately 29.24 eV). To be able to directly compare the cross section for the $3s^{-1}4p$ resonance we

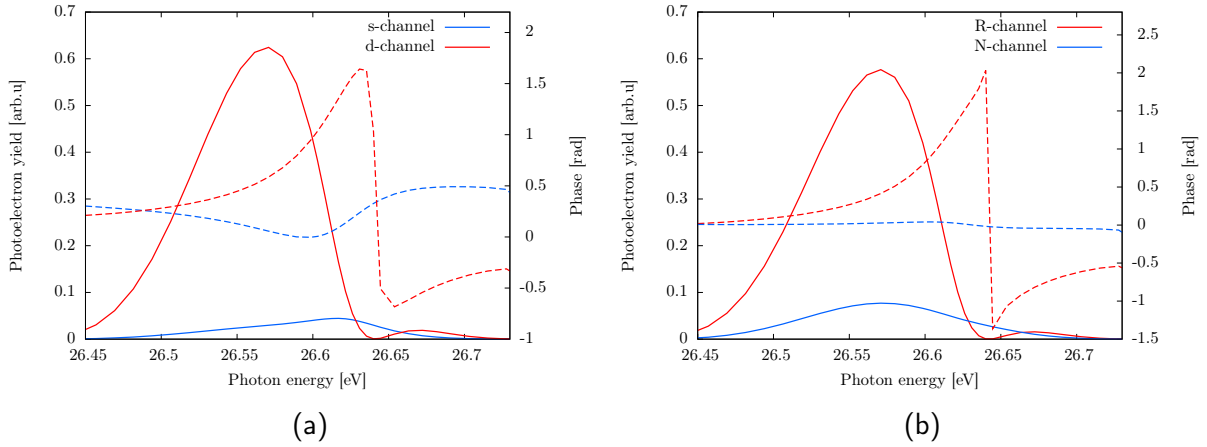


Figure F.2.: Channel resolved photoelectron spectrum for ionization of argon with a single attosecond pulse centered at the $3s^{-1}4p$ resonance in argon. (a) Amplitude (solid line) and phase (dashed line) of the $3s^{-1}4p$ resonance in argon for the ionized electron angular momentum $\ell = 0$ (s-channel) and $\ell = 2$ (channel) separately. (b) Amplitude (solid line) and phase (dashed line) of the resonant (R) and nonresonant (N) channel $3s^{-1}4p$ resonance in argon applying the unitary transformation shown in Eq. (5.18) to the $\ell = 0$ and $\ell = 2$ channels.

have to shift the energies for both bases. Doing so, we observe that for both theoretical bases the width and amplitude modulation due to the resonance are accurately captured by the theoretical calculations. Shifting the energies of the theoretical calculations in order for the second ionization threshold to coincide with experiment we find that the energy of the two energetically lowest resonances ($3s^{-1}4p$ and $3s^{-1}5p$) differ from experimental results. The energy of the higher lying resonances is, however, very accurately reproduced. This can be explained by the fact that the lowest resonances are more influenced by electronic correlations. Thus the inclusion of more CSF channels would be necessary to achieve agreement with the experimental resonance energies.

The amplitude and phase variation across the $3s^{-1}4p$ resonance is completely different for the $\ell = 0$ (s) and $\ell = 2$ (d) channel of the ionized photoelectron. Using the parameters $C_{s,N} = 0.0656 - 0.984i$ and $C_{d,N} = -0.0614 - 0.152i$ [265] for the unitary transformation described in Eq. (5.18) the angular momentum eigenchannels can be decoupled, see Fig. F.2b. The resonant channel (R) shows a phase jump of π close to 26.65 eV and the non-resonant channel shows almost no phase variation within the full energy region of the harmonic. The non-resonant channel (N) features a very symmetric electron yield inline with the expectation for a non-resonant channel. Close inspection of Fig. F.2a shows that the d-channel is dominating over the s-channel in the considered energy region and is also almost the resonant channel (as it features already a very large phase variation).

F.2. Pulse parameters

The theoretically used APTs and IR fields for the results shown in Sec. 5.3 have a full width at half maximum duration of 3.5 cycles and 7 cycles of the fundamental IR field. The pulse parameters used for $\lambda_{\text{IR}}=1500$ nm employing the CSF-mid basis are given in Tab. F.3. The deviation of the energy of the n^{th} harmonic from $n\omega_{\text{IR}}$ is chosen to compensate the error in the energy of the first ionization threshold. As the energy of the first ionization threshold is slightly different for the CSF-low and the CSF-mid basis the pulse parameters for the same IR wavelength are slightly different for the two bases.

λ [nm]	ω [eV]	Peak intensity [W/cm ²]	FWHM duration [fs]	CEP [π]	harmonic #
1500	0.83	1×10^9	35	0	-
58.70	21.12	2×10^{10}	17.8	0	25 th
54.45	22.77	4×10^{10}	17.8	0	27 th
50.77	24.42	6×10^{10}	17.8	0	29 th
47.54	26.08	8×10^{10}	17.8	0	31 st
44.71	27.73	1.2×10^{11}	17.8	0	33 rd
42.18	29.39	1.7×10^{11}	17.8	0	35 th
39.94	31.04	1.3×10^{11}	17.8	0	37 th
37.92	32.69	1.18×10^{11}	17.8	0	39 th
36.09	34.35	8×10^{10}	17.8	0	41 st
34.44	36.00	5×10^{10}	17.8	0	43 rd
32.93	37.65	4×10^{10}	17.8	0	45 th
31.55	39.30	3×10^{10}	17.8	0	47 th

Table F.3.: Pulse parameters used in the simulation shown in Sec. 5.3 for the CSF-mid basis for $\lambda_{\text{IR}} = 1500\text{nm}$.

G. Derivation of the time-dependent dipole moment for an impulsively excited Fano resonance

In this appendix we derive the time-dependent dipole moment for an impulsively excited Fano resonance [Eq. (6.7)] using Eqs. (6.4) and (6.5). The time-dependent dipole moment $d(t)$ is given by

$$\begin{aligned}
d(t) &= \langle \psi(t) | z | \psi(t) \rangle \\
&= C_a(t) e^{iE_0 t} \langle a | z | g \rangle^* + \int d\epsilon C_\epsilon(t) e^{iE_0 t} \langle \epsilon | z | g \rangle + c.c. \\
&= C_a^{(0)} \langle a | z | g \rangle^* e^{-i(E_a - E_0)t} \left\{ \left(1 - \frac{i}{q} \right) e^{-\frac{\Gamma_a}{2}t} + \frac{1}{(\pi V_{ae} q)^2} \right. \\
&\quad \left. \int d\epsilon \frac{(q + \epsilon) e^{-i\frac{\Gamma_a}{2}\epsilon} - (q - i) e^{-\frac{\Gamma_a}{2}t}}{\epsilon + i} \right\} + c.c. \quad (\text{G.1})
\end{aligned}$$

To calculate the transient absorption spectrum we Fourier transform the dipole moment $d(t)$. Within the Fourier transform only the term proportional to $e^{-i(E_a - E_0)t}$ will contribute significantly. Therefore, the complex conjugate term proportional to $e^{i(E_a - E_0)t}$ (c.c. in Eq. G.1) will be dropped in the following (rotating-wave approximation). Using further $\oint \frac{1}{\xi + i} d\xi = -i\pi$ we evaluate Eq. (G.1)

$$\begin{aligned}
d(t) &= C_a^{(0)} \langle a | z | g \rangle^* \frac{e^{-i(E_a - E_0)t}}{q^2} \left\{ q(q - i) e^{-\frac{\Gamma_a}{2}t} + \frac{2}{\pi \Gamma_a} \int d\epsilon \frac{(q + \epsilon + i - i) e^{-i\frac{\Gamma_a}{2}\epsilon} - (q - i) e^{-\frac{\Gamma_a}{2}t}}{\epsilon + i} \right\} \\
&= C_a^{(0)} \langle a | z | g \rangle^* \frac{e^{-i(E_a - E_0)t}}{q^2} \left\{ q(q - i) e^{-\frac{\Gamma_a}{2}t} + \frac{1}{\pi} \int d\epsilon e^{-i\frac{\Gamma_a}{2}\epsilon} + \frac{q - i}{\pi} \int d\epsilon \frac{e^{-i\frac{\Gamma_a}{2}\epsilon} - e^{-\frac{\Gamma_a}{2}t}}{\epsilon + i} \right\} \\
&= C_a^{(0)} \langle a | z | g \rangle^* \frac{e^{-i(E_a - E_0)t}}{q^2} \left\{ q(q - i) e^{-\frac{\Gamma_a}{2}t} + \frac{2}{\pi \Gamma_a} 2\pi \delta(t) + \frac{q - i}{\pi} \left[\int d\epsilon \frac{e^{-i\frac{\Gamma_a}{2}\epsilon}}{\epsilon + i} - e^{-\frac{\Gamma_a}{2}t} \int d\epsilon \frac{1}{\epsilon + i} \right] \right\} \\
&= C_a^{(0)} \langle a | z | g \rangle^* \frac{e^{-i(E_a - E_0)t}}{q^2} \left\{ q(q - i) e^{-\frac{\Gamma_a}{2}t} + \frac{4}{\Gamma_a} \delta(t) - \frac{q - i}{\pi} e^{-\frac{\Gamma_a}{2}t} 2\pi i + \frac{q - i}{\pi} e^{-\frac{\Gamma_a}{2}t} \pi i \right\} \\
d(t) &= C_a^{(0)} \langle a | z | g \rangle^* \frac{1}{q^2} \left\{ \frac{4}{\Gamma_a} \delta(t) + (q - i)^2 e^{-i(E_a - E_0)t} e^{-\frac{\Gamma_a}{2}t} \right\}. \quad (\text{G.2})
\end{aligned}$$

Both, $|a\rangle$ and $|g\rangle$ are quasi-bound states and hence $\langle a|z|g\rangle$ can be assumed to be a real quantity. Assuming further that the exciting XUV field is delta-like and, accordingly $C_a(0)$ purely imaginary within first-order perturbation theory the dipole moment is given by

$$d(t) \propto i \left\{ 2\delta(t) + \frac{\Gamma_a}{2} (q - i)^2 e^{-i(E_a - E_0)t} e^{-\frac{\Gamma_a}{2}t} \right\}. \quad (\text{G.3})$$

H. Interference pattern in the TPDI energy distribution for XUV-XUV pump-probe sequences

In this appendix we derive the equations describing the interference pattern in the double differential two-photon double ionization (TPDI) energy distribution for XUV-XUV pump probe sequences with arbitrary ellipticities of the two pulses ϵ_1 and ϵ_2 [Eqs. (8.10) and (8.11)], see [104] Employing second-order time-dependent perturbation theory (see, e.g., [94, 243, 256, 258]) the interference pattern observed in the angle-integrated double ionization spectrum $P(E_1, E_2)$ for a pump-probe sequence can be described quantitatively. The transition amplitude for two-photon double ionization is accordingly given by

$$t_{i \rightarrow f}^{(2)} = -\sum_n \int_{-\infty}^{t_f} dt_1 \int_{-\infty}^{t_1} dt_2 e^{iE_{fn}t_1} e^{iE_{ni}t_2} \times \langle f | V(t_1) | n \rangle \langle n | V(t_2) | i \rangle, \quad (\text{H.1})$$

with $E_{fn} = E_f - E_n$ and $E_{ni} = E_n - E_i$. The initial state $|i\rangle$ is the ground state and the final state $|f\rangle = |E_1\Omega_1, E_2\Omega_2\rangle$ is the double continuum. The sum runs over all intermediate two-electron states $|n\rangle$.

To calculate the transition amplitude to the final state for the different (L, M) channels $\left[t_{i \rightarrow f}^{(2)} \right]_{L,M}$ we project onto the final state $|E_1, E_2, L, M\rangle$. The two-photon double ionization probability is then given by

$$P(E_1, E_2) = \sum_{L,M=(2,2),(2,0),(2,-2),(0,0)} \left| \left[t_{i \rightarrow f}^{(2)} \right]_{L,M} \right|^2. \quad (\text{H.2})$$

We employ the velocity gauge, i.e. $\hat{V}(t) = (\hat{\mathbf{p}}_1 + \hat{\mathbf{p}}_2) \cdot \mathbf{A}(t) \equiv \hat{\boldsymbol{\mu}} \cdot \mathbf{A}(t)$. Expanding $\hat{\boldsymbol{\mu}} \cdot \mathbf{A}(t)$ in spherical tensor components yields

$$\hat{\boldsymbol{\mu}} \cdot \mathbf{A}(t) = \sum_{q=-1}^1 (-1)^q \hat{\mu}_q A_{-q}, \quad (\text{H.3})$$

where the spherical tensor components are defined as $\hat{T}_{+1} = -(\hat{T}_x + i\hat{T}_y)/\sqrt{2}$, $\hat{T}_{-1} = (\hat{T}_x - i\hat{T}_y)/\sqrt{2}$, $\hat{T}_0 = \hat{T}_z$. Using the vector potential [Eq. (8.6)] in rotating-wave approximation $[\mathbf{A}(t) \approx \frac{A_0}{2} f(t) e^{-i\omega t} (i\hat{x} - \epsilon\hat{y})]$ the spherical components of the field are $A_{+1} =$

$-i(1-\epsilon)A_0f(t)e^{-i\omega t}/\sqrt{8}$, $A_{-1} = i(1+\epsilon)A_0f(t)e^{-i\omega t}/\sqrt{8}$, $A_0 = 0$. Inserting the spherical components of the field A_q into Eq. (H.3) yields

$$\begin{aligned}\hat{\boldsymbol{\mu}} \cdot \mathbf{A}(t) &= [-\hat{\mu}_{+1}(1+\epsilon) + \hat{\mu}_{-1}(1-\epsilon)] i \frac{A_0}{\sqrt{8}} f(t) e^{-i\omega t} \\ &= \hat{\mu}_\epsilon \bar{A}(t).\end{aligned}\quad (\text{H.4})$$

Within the rotating-wave approximation $\hat{\mu}_\epsilon$ can be expanded as a function of spherical harmonics

$$\hat{\mu}_\epsilon \propto -(1+\epsilon)Y_1^1 + (1-\epsilon)Y_1^{-1}.\quad (\text{H.5})$$

Using Eq. (H.4) we can simplify Eq. (H.1):

$$\begin{aligned}\left[t_{i \rightarrow f}^{(2)} \right]_{L,M} &= - \sum_n \langle E_1, E_2, L, M | \hat{\mu}_\epsilon | n \rangle \langle n | \hat{\mu}_\epsilon | i \rangle \\ &\quad \times \mathcal{G} [E_{fn}, E_{ni}, \bar{A}(t)],\end{aligned}\quad (\text{H.6})$$

with

$$\begin{aligned}\mathcal{G} [E_{fn}, E_{ni}, \bar{A}(t)] &= \\ &\int_{-\infty}^{t_f} dt_1 \int_{-\infty}^{t_1} dt_2 e^{iE_{fn}t_1} e^{iE_{ni}t_2} \bar{A}(t_1) \bar{A}(t_2).\end{aligned}\quad (\text{H.7})$$

We note that the shape function \mathcal{G} is fully determined by the temporal envelope $f(t)$ and the central frequency of the pulse. To leading order only the intermediate state with one electron in the p continuum and the other electron bound in the $1s$ state of He^+ contributes ($|n_0\rangle = |E_1p, 1s\rangle$). The contribution of shake-up intermediate states is small compared to the intermediate ground state (see Fig. 8.9).

Assuming only the on-shell intermediate state by absorbing the first photon with ellipticity ϵ_I and the second with ellipticity ϵ_{II} the matrix element in Eq. H.6 is given by

$$\begin{aligned}M_{2,2} &= -(1+\epsilon_{II})(1+\epsilon_I)C_{2,2;1,1} \\ M_{2,0} &= (1+\epsilon_{II})(1-\epsilon_I)C_{2,0;1,-1} \\ &\quad + (1-\epsilon_{II})(1+\epsilon_I)C_{2,0;1,1} \\ &= 2(1-\epsilon_I\epsilon_{II})C_{2,0;1,1} \\ M_{2,-2} &= -(1-\epsilon_{II})(1-\epsilon_I)C_{2,2;1,-1} \\ M_{0,0} &= (1+\epsilon_{II})(1-\epsilon_I)C_{0,0;1,-1} \\ &\quad + (1-\epsilon_{II})(1+\epsilon_I)C_{0,0;1,1} \\ &= 2(1-\epsilon_I\epsilon_{II})C_{0,0;1,1},\end{aligned}\quad (\text{H.8})$$

with $C_{L,M;L',M'}$ being the product of Clebsch-Gordon coefficients and the reduced matrix elements containing the momentum operators \hat{p}_{+1} and \hat{p}_{-1} . (L', M') are the total angular momentum and magnetic quantum number of the intermediate state $|n_0\rangle$ and $C_{2,0;1,-1} =$

$$C_{2,0;1,+1}, C_{0,0;1,-1} = C_{0,0;1,+1}.$$

To calculate the shape function \mathcal{G} [Eq. (H.7)] we distinguish whether both photons are absorbed within one pulse [$\mathcal{G}^{(2)}$] or one photon out of each pulse is absorbed [$\mathcal{G}^{(1)}$]. $\mathcal{G}^{(1)}$ can be easily calculated since the integration limits in Eq. (H.7) are independent

$$\begin{aligned} \mathcal{G}^{(1)} [E_{fn}, E_{ni}, \bar{A}(t)] = \\ \int_{-\infty}^{t_f} dt_1 e^{iE_{fn}t_1} \bar{A}(t_1) \int_{-\infty}^{t_f} dt_2 e^{iE_{ni}t_2} \bar{A}(t_2). \end{aligned} \quad (\text{H.9})$$

Inserting the envelope of the pulse we obtain

$$\begin{aligned} \mathcal{G}^{(1)} (E_{fn}, E_{ni}, A_0, T_p) = \frac{A_0^2}{8} \\ \int_{-T_p}^{T_p} dt_1 e^{i(E_{fn}-\omega)t_1} \cos^2 \left(\frac{\pi t_1}{2T_p} \right) \\ \int_{-T_p}^{T_p} dt_2 e^{i(E_{ni}-\omega)t_2} \cos^2 \left(\frac{\pi t_2}{2T_p} \right). \end{aligned} \quad (\text{H.10})$$

For long pulses the total energy of the final state is accurately determined to be $E_1 + E_2 = 2\omega + E_0$ and we can write $\mathcal{G}^{(1)}$ as function of $(E_{\text{tot}}, \Delta E)$

$$\begin{aligned} \mathcal{G}^{(1)} (\Delta E) = \frac{A_0^2}{8} \\ \int_{-T_p}^{T_p} dt_1 e^{i(\Delta E + I_{p,1} - I_{p,2})t_1/2} \cos^2 \left(\frac{\pi t_1}{2T_p} \right) \\ \int_{-T_p}^{T_p} dt_2 e^{i(-\Delta E + I_{p,2} - I_{p,1})t_2/2} \cos^2 \left(\frac{\pi t_2}{2T_p} \right). \end{aligned} \quad (\text{H.11})$$

$\mathcal{G}^{(1)} (\Delta E)$ depends only on ΔE but not on E_{tot} . Furthermore, for sufficiently long pulses $\mathcal{G}^{(1)} (\Delta E)$ and $\mathcal{G}^{(1)} (-\Delta E)$ appearing in Eqs. (8.10) and (8.11) have vanishing spectral overlap. Consequently mixed terms of the form $\mathcal{G}^{(1)} (\Delta E) [\mathcal{G}^{(1)} (-\Delta E)]^*$ vanish.

$\mathcal{G}^{(2)}$ is given by [94]

$$\begin{aligned} \mathcal{G}^{(2)} (\Delta E_{fn}, \Delta E_{ni}, A_0, T_p) \\ = \frac{A_0^2}{8} \int_{-T_p}^{T_p} dt_1 \int_{-T_p}^{t_1} dt_2 \mathcal{F} (\Delta E_{fn}, t_1, T_p) \mathcal{F} (\Delta E_{ni}, t_2, T_p), \end{aligned} \quad (\text{H.12})$$

with

$$\mathcal{F} (\xi, t, T) = e^{i\xi t} \cos^2 \left(\frac{\pi t}{2T} \right), \quad (\text{H.13})$$

where $\Delta E_{fn} = E_{fn} - \omega$ and $\Delta E_{ni} = E_{ni} - \omega$. As for $\mathcal{G}^{(1)}$ we use that for long pulses the total energy of the final state is accurately determined to be $E_1 + E_2 = 2\omega + E_0$. This

enforces $\Delta E_{fn} = -\Delta E_{ni}$. Changing the variables from (E_1, E_2) to $(E_{\text{tot}}, \Delta E)$ one obtains

$$\begin{aligned} \mathcal{G}^{(2)}(\Delta E_{fn}, \Delta E_{ni}, A_0, T_p) = \\ \mathcal{G}^{(2)}((I_{p,2} - I_{p,1} - \Delta E)/2, -(I_{p,2} - I_{p,1} - \Delta E)/2, A_0, T_p). \end{aligned} \quad (\text{H.14})$$

Not only the shape function $\mathcal{G}^{(1)}$ but also $\mathcal{G}^{(2)}$ depend only on ΔE and not on E_{tot} . As shown in [94] the amplitude of two-photon absorption within one pulse is given by $\mathcal{S}^{(2)} = \mathcal{G}^{(2)}(\Delta E) + \mathcal{G}^{(2)}(-\Delta E)$.²⁶

For a pump-probe sequence where the first pulse has ellipticity ϵ_1 and the second ϵ_2 the transition amplitudes are given by

$$\begin{aligned} \left[t_{i \rightarrow f}^{(2)} \right]_{2,2} \propto (1 + \epsilon_1)^2 \mathcal{S}^{(2)}(\Delta E) e^{-i(E_1 + E_2)\tau} \\ + (1 + \epsilon_2)^2 \mathcal{S}^{(2)}(\Delta E) e^{-iE_0\tau} \\ + (1 + \epsilon_1)(1 + \epsilon_2) \mathcal{G}^{(1)}(\Delta E) e^{-i(E_1 - I_{p,2})\tau} \\ + (1 + \epsilon_1)(1 + \epsilon_2) \mathcal{G}^{(1)}(-\Delta E) e^{-i(E_2 - I_{p,2})\tau}, \end{aligned} \quad (\text{H.15})$$

$$\begin{aligned} \left[t_{i \rightarrow f}^{(2)} \right]_{2,-2} \propto (1 - \epsilon_1)^2 \mathcal{S}^{(2)}(\Delta E) e^{-i(E_1 + E_2)\tau} \\ + (1 - \epsilon_2)^2 \mathcal{S}^{(2)}(\Delta E) e^{-iE_0\tau} \\ + (1 - \epsilon_1)(1 - \epsilon_2) \mathcal{G}^{(1)}(\Delta E) e^{-i(E_1 - I_{p,2})\tau} \\ + (1 - \epsilon_1)(1 - \epsilon_2) \mathcal{G}^{(1)}(-\Delta E) e^{-i(E_2 - I_{p,2})\tau}, \end{aligned} \quad (\text{H.16})$$

$$\begin{aligned} \left[t_{i \rightarrow f}^{(2)} \right]_{2,0} \propto (1 - \epsilon_1^2) \mathcal{S}^{(2)}(\Delta E) e^{-i(E_1 + E_2)\tau} \\ + (1 - \epsilon_2^2) \mathcal{S}^{(2)}(\Delta E) e^{-iE_0\tau} \\ + (1 - \epsilon_1\epsilon_2) \mathcal{G}^{(1)}(\Delta E) e^{-i(E_1 - I_{p,2})\tau} \\ + (1 - \epsilon_1\epsilon_2) \mathcal{G}^{(1)}(-\Delta E) e^{-i(E_2 - I_{p,2})\tau}, \end{aligned} \quad (\text{H.17})$$

$$\begin{aligned} \left[t_{i \rightarrow f}^{(2)} \right]_{0,0} \propto (1 - \epsilon_1^2) \mathcal{S}^{(2)}(\Delta E) e^{-i(E_1 + E_2)\tau} \\ + (1 - \epsilon_2^2) \mathcal{S}^{(2)}(\Delta E) e^{-iE_0\tau} \\ + (1 - \epsilon_1\epsilon_2) \mathcal{G}^{(1)}(\Delta E) e^{-i(E_1 - I_{p,2})\tau} \\ + (1 - \epsilon_1\epsilon_2) \mathcal{G}^{(1)}(-\Delta E) e^{-i(E_2 - I_{p,2})\tau}. \end{aligned} \quad (\text{H.18})$$

²⁶ We use the notation $\mathcal{S}^{(2)}$ instead of $\mathcal{A}^{(2)}$ as employed in [94, 104] to avoid confusion, as we use $\mathcal{A}^{(2)}$ frequently throughout this thesis for the two-photon matrix element associated with single ionization by an APT assisted by an IR field in RABBITT.

For the $L - L$ and the $L - R$ sequence these equations simplify drastically .

For the $L - L$ sequence

$$\begin{aligned} \left[t_{i \rightarrow f}^{(2)} \right]_{2,2} &\propto \mathcal{S}^{(2)}(\Delta E) (e^{-i(E_1+E_2)\tau} + e^{-iE_0\tau}) \\ &\quad + \mathcal{G}^{(1)}(\Delta E) e^{-i(E_1-I_{p,2})\tau} \\ &\quad + \mathcal{G}^{(1)}(-\Delta E) e^{-i(E_2-I_{p,2})\tau} \end{aligned}$$

while

$$\left[t_{i \rightarrow f}^{(2)} \right]_{2,0} = \left[t_{i \rightarrow f}^{(2)} \right]_{2,-2} = \left[t_{i \rightarrow f}^{(2)} \right]_{0,0} = 0.$$

Consequently the $\left[t_{i \rightarrow f}^{(2)} \right]_{2,2}$ terms fully account for the interferences. For the $L - R$ sequence we have:

$$\begin{aligned} \left[t_{i \rightarrow f}^{(2)} \right]_{2,2} &\propto \mathcal{S}^{(2)}(\Delta E) e^{-i(E_1+E_2)\tau}, \\ \left[t_{i \rightarrow f}^{(2)} \right]_{2,-2} &\propto \mathcal{S}^{(2)}(\Delta E) e^{-iE_0\tau}, \\ \left[t_{i \rightarrow f}^{(2)} \right]_{2,0} &\propto \mathcal{G}^{(1)}(\Delta E) e^{-i(E_1-I_{p,2})\tau} \\ &\quad + \mathcal{G}^{(1)}(-\Delta E) e^{-i(E_2-I_{p,2})\tau}, \\ \left[t_{i \rightarrow f}^{(2)} \right]_{0,0} &\propto \mathcal{G}^{(1)}(\Delta E) e^{-i(E_1-I_{p,2})\tau} \\ &\quad + \mathcal{G}^{(1)}(-\Delta E) e^{-i(E_2-I_{p,2})\tau}. \end{aligned}$$

Since $\mathcal{G}^{(1)}(\Delta E)$ and $\mathcal{G}^{(1)}(-\Delta E)$ have vanishing spectral overlap the only interfering terms in $\left[t_{i \rightarrow f}^{(2)} \right]_{2,0}$ and $\left[t_{i \rightarrow f}^{(2)} \right]_{0,0} \sim \mathcal{G}^{(1)}(\Delta E) [\mathcal{G}^{(1)}(-\Delta E)]^*$ vanish. Consequently there are effectively no interfering paths and hence no interference pattern in $P(E_1, E_2)$ for the $L - R$ sequence.

I. Doubly excited states in helium

To obtain the occupation ratio shown in Fig. 7.14c we project the time-dependent wave function onto the bound part of the double excited states specified in Tab. I.1 using the non-hermitian dot product. The four “named” states are they ones which where included in the few-state model shown in Sec. 7.3.2. The eigenstates where obtained using exterior complex scaling [60]. For consistency the doubly excited states for $L = 0, 1, 2$ are listed with a classification very close to the one proposed by C.D. Lin [266].

Table I.1.: Doubly excited states with their respective resonance energy E_R and lifetime τ on which the time-dependent wave function for the dipole reconstruction was projected on to obtain Fig. 7.14c.

L	Class	E_R [a.u.]	E_R [eV]	τ [fs]	“name”
0	L0_2+	-0.777867	57.84	5.3	$(2s^2)$
0	L0_3+	-0.589894	62.96	17.8	
0	L0_4+	-0.544881	64.18	49.2	
0	L0_5+	-0.526687	64.68	110.6	
0	L0_6+	-0.517641	64.93	213.1	
0	L0_2-	-0.621898	62.09	112.0	$(2p^2)$
0	L0_3-	-0.548082	64.10	322.5	
0	L0_4-	-0.527715	64.65	522.4	
0	L0_5-	-0.518104	64.91	809.8	
1	L1_22+	-0.693125	60.15	17.7	$2s2p$
1	L1_23+	-0.564083	63.66	80.4	$2s3p$
1	L1_24+	-0.534362	64.47	188.4	
1	L1_25+	-0.521504	64.82	367.6	
1	L1_23-	-0.597074	62.76	6365	
1	L1_24-	-0.546493	64.14	11927	
1	L1_25-	-0.527298	64.66	24637	
2	L2_102	-0.701937	59.91	10.2	
2	L2_103	-0.569218	63.52	43.5	
2	L2_104	-0.536726	64.41	75.6	
2	L2_013	-0.556429	63.87	1209	
2	L2_014	-0.531512	64.55	2199	
2	L2_-104	-0.529292	64.61	2×10^6	
3	L3_1	-0.558282	63.82	1890	
3	L3_2	-0.532257	64.53	3383	
3	L3_3	-0.531482	64.55	1.4×10^6	
3	L3_4	-0.520492	64.85	5000	
3	L3_5	-0.520124	64.86	2.7×10^6	
3	L3_6	-0.519402	64.88	8.5×10^{10}	

J. Parameters for the different simulations

In this appendix we list all numerical parameters used for the simulations presented in the main part of this thesis.

J.1. Single-active electron calculations

In the following we give the parameters used for the single-active electron calculations [Sec. 2.2.1] performed within in this thesis.

J.1.1. Parameters for Fig. 4.1

We use a radial box spanning 4417 a.u. and $L_{\max} = 5$. We use 11 finite elements for each FEDVR element spanning 4 a.u. close to the core and 5 a.u. for $r > 24$ a.u.. An absorbing boundary starting at 4284.5 a.u. was used to avoid reflections of the wave function at the boundary. The pulse parameters are given in Tab. J.1. The short-ranged Yukawa potential is defined as

$$V(r) = \frac{1.90831}{r} e^{-r}, \quad (\text{J.1})$$

and has an ionization potential of 0.5 a.u..

λ [nm]	ω [eV]	Peak intensity [W/cm ²]	FWHM duration [fs]	CEP [π]	harmonic #
740	1.68	2×10^9	20	0	-
49.33	25.13	1×10^{11}	15	0	15 th
43.53	28.48	1×10^{11}	15	0	17 th
38.95	31.83	1×10^{11}	15	0	19 th
35.24	35.18	1×10^{11}	15	0	21 st
32.17	38.54	1×10^{11}	15	0	23 rd
29.60	41.89	1×10^{11}	15	0	25 th

Table J.1.: Pulse parameters used for the results shown in Fig. 4.1.

J.1.2. Parameters for Fig. 4.3

We use a radial box spanning 4417 a.u. and $L_{\max} = 8$ for $\lambda_{\text{IR}} = 500$ nm and 1480 nm. We use 11 finite elements for each FEDVR element spanning 4 a.u. close to the core and 5 a.u. for $r > 24$ a.u.. An absorbing boundary starting at 4284.5 a.u. was used to avoid reflections of the wave function at the boundary. The pulse parameters for $\lambda_{\text{IR}} = 500$ nm are given in Tab. J.2. The pulse parameters for $\lambda_{\text{IR}} = 1480$ nm are given in Tab. J.3.

λ [nm]	ω [eV]	Peak intensity [W/cm ²]	FWHM duration [fs]	CEP [π]	harmonic #
500	2.47	2×10^9	20	0	-
55.55	22.32	1×10^{11}	15	0	9 th
45.45	27.28	1×10^{11}	15	0	11 th
38.46	32.24	1×10^{11}	15	0	13 th
33.33	37.20	1×10^{11}	15	0	15 th
29.41	42.16	1×10^{11}	15	0	17 th

Table J.2.: Pulse parameters used for the results shown in Fig. 4.3.

λ [nm]	ω [eV]	Peak intensity [W/cm ²]	FWHM duration [fs]	CEP [π]	harmonic #
1480	0.84	2×10^9	20	0	-
51.03	24.30	1×10^{11}	15	0	29 th
47.74	25.97	1×10^{11}	15	0	31 st
44.85	27.64	1×10^{11}	15	0	33 rd
42.29	29.32	1×10^{11}	15	0	35 th
40.00	31.00	1×10^{11}	15	0	37 th
37.95	32.67	1×10^{11}	15	0	39 th
36.10	34.34	1×10^{11}	15	0	41 st
34.42	36.02	1×10^{11}	15	0	43 rd
32.89	37.70	1×10^{11}	15	0	45 th

Table J.3.: Pulse parameters used for the results shown in Fig. 4.3

J.1.3. Parameters for Fig. 4.6

We use a radial box spanning 3002 a.u. and $L_{\max} = 5$. We use 11 finite elements for each FEDVR element spanning 4 a.u. close to the core and 5 a.u. for $r > 24$ a.u.. An absorbing boundary starting at 2762 a.u. was used to avoid reflections of the wave function at the boundary. We use the model potential described in [114] to describe single ionization of neon. The pulse parameters are given in Tab. J.4.

λ [nm]	ω [eV]	Peak intensity [W/cm ²]	FWHM duration [fs]	CEP [π]	harmonic #
800	1.55	2×10^9	13	0	-
29.63	41.84	1.5625×10^{10}	10	0	27 th
27.59	44.94	1.5625×10^{10}	10	0	29 th

Table J.4.: Pulse parameters used for the results shown in Fig. 4.6.

J.2. Two-active electron calculations

In the following we write down the parameters used for the two-active electron calculations for helium [Sec. 2.2.2] performed within in this thesis.

J.2.1. Parameters for Fig. 4.9

We use an asymmetric box where the bigger (smaller) radial size is 3857 a.u. (37 a.u.) with 11 basis function for every finite element spanning 4 a.u. close to the core and 5 a.u. for $r > 24$ a.u.. To avoid reflection at the boundary an absorbing potential is used which starts at 3703 a.u. and 20 a.u. respectively. Employing velocity gauge we achieve converged results for an angular momentum expansion of $L_{\max} = 3$, $\ell_1 = \ell_2 = 9$. The pulse parameters are given in Tab. J.5.

λ [nm]	ω [eV]	Peak intensity [W/cm ²]	FWHM duration [fs]	CEP [π]	harmonic #
740	1.68	2×10^9	20	0	-
13.45	92.15	9.4×10^{10}	15	0	55 th
12.98	95.50	1.4×10^{11}	15	0	57 th
12.54	98.85	1.58×10^{11}	15	0	59 th
12.13	102.20	1.642×10^{11}	15	0	61 st
11.75	105.55	1.265×10^{11}	15	0	63 rd

Table J.5.: Pulse parameters used for the results shown in Fig. 4.9.

J.2.2. Parameters for Fig. 4.16

In the numerical simulation we use an IR with $\lambda_{IR} = 656.064\text{nm}$ together with an APT consisting of the 45th, 47th, 49th and 51st harmonic of the fundamental with a FWHM duration of 10 fs and 6 fs, see Tab. J.6. The intensity of the IR and each harmonic of the APT were chosen to be in the purely perturbative limit. We use an asymmetric radial box spanning 2592 a.u. (64 a.u.) for the larger (smaller) direction where we use 11 finite elements for each region of 4 a.u.. To avoid reflection at the boundary an absorbing potential starts at 2397.6 a.u. (49 a.u.) for the bigger (smaller) radial component. Employing

velocity gauge we obtain convergent results with a close-coupling expansion of $L_{\max} = 3$, $\ell_1 = \ell_2 = 7$.

λ [nm]	ω [eV]	Peak intensity [W/cm ²]	FWHM duration [fs]	CEP [π]	harmonic #
656.064	1.89	2×10^9	10	0	-
14.58	85.04	1×10^{10}	6	0	45 th
13.96	88.82	1×10^{10}	6	0	47 th
13.39	92.60	1×10^{10}	6	0	49 th
12.86	96.38	12×10^{10}	6	0	51 st

Table J.6.: Pulse parameters used used for the results shown in Fig. 4.16.

J.2.3. Parameters for the simulations in section 4.3

The single-active electron calculations²⁷ employ a model potential for helium [114], are based on a finite-difference scheme and employ the Crank-Nicolson method [267, 268] for the time propagation. For the *ab initio* two-active electron simulations we use an asymmetric box which spans 2417 a.u. (37 a.u.) in the larger (smaller) radial direction. For each finite element of size 4 a.u. close to the core and of size 5 a.u. for $r > 24$ a.u. we use 11 basis functions. A complex absorption potential starts at 2296.15 a.u. and 22 a.u. for the larger and smaller radial direction, respectively, to avoid reflection of the wave function at the boundary of the numerical box. Employing velocity gauge we achieve converged results for an angular momentum expansion of $L_{\max} = 4$, $\ell_1 = 6$, $\ell_2 = 8$. The exact parameters of the APT (see Tab. J.7) for the single-active electron and the *ab initio* simulation were chosen to match the experimental XUV spectra and are the same for the single-active electron calculations and the two-active electron simulation. The IR field in the experiment has a FWHM duration of 29 fs which is approximately 3.5 times longer than the IR used in the simulations (FWHM duration of 8 fs) to make the full *ab initio* calculations possible. To rule out any influence of the IR pulse duration we also perform SAE simulations for an IR pulse duration of 20 fs, which give practically identical results to the simulations shown in Fig. 4.18 where the IR pulse duration is 8 fs.

In addition to the results for helium, we report calculations for the hydrogen atom, for which harmonics from the 9th to the 17th order are used to generate the XUV spectrum, such that the electron kinetic energy remains in the same range as for helium.

J.2.4. Parameters for Fig. 5.4a

The fundamental laser field has a wavelength of $\lambda = 1485$ nm, a FWHM duration of roughly 22 fs (corresponding to 4.5 cycles) and a peak intensity of 2×10^9 W/cm². The APT

²⁷ Performed by Nicolas Douguet at the University of Central Florida.

λ [nm]	ω [eV]	Peak intensity [W/cm ²]	FWHM duration [fs]	CEP [π]
790	1.57	1×10^{11}	8	0
53.01	23.39	1.04×10^{10}	3.6	-0.11
46.68	26.56	3.40×10^{10}	2.6	-0.06
41.60	29.80	6.38×10^{10}	2.0	-0.04
37.67	32.91	5.01×10^{10}	1.9	-0.06
34.33	36.11	3.65×10^{10}	2.0	-0.11
31.50	39.36	3.16×10^{10}	1.8	-0.18
29.22	42.43	1.46×10^{10}	1.6	-0.29
27.35	45.33	0.47×10^{10}	1.5	-0.44

Table J.7.: Pulse parameters used for the results shown in section 4.3. All but the first pulse form the attosecond pulse train (APT) used to ionize the helium atom.

consisting of the 71st and 72nd harmonic has a total duration of 17 fs, see Tab. J.8. We use an asymmetric radial box where the larger (smaller) radial coordinate extends up to 2550 a.u. (20 a.u.) and we use 11 basis functions for every finite element spanning 5 a.u. in the FEDVR expansion. An absorbing boundary prevents the influence of reflected parts of the wave packet starting at 2422.5 a.u. and 15 a.u., respectively. Employing velocity gauge we achieve converged results with a close-coupling expansion of $L_{\max} = 3$, $\ell_1 = \ell_2 = 4$. The single-ionization spectra are obtained using the method described in App. C.

λ [nm]	ω [eV]	Peak intensity [W/cm ²]	FWHM duration [fs]	CEP [π]	harmonic #
1485	1.57	2×10^9	22.2	0	-
20.92	59.27	1×10^{11}	8.5	0	71 st
20.63	60.11	1×10^{11}	8.5	0	72 nd

Table J.8.: Pulse parameters for the results shown Fig. 5.4a.

J.2.5. Parameters for Fig. 5.5b

In the *ab initio* simulation we use an asymmetric radial box where the larger (smaller) radial coordinate extends up to 3410 a.u. (20 a.u.) and we use 11 basis function for every finite element spanning 5 a.u. in the FEDVR expansion. An absorbing boundary prevents the influence of reflected parts of the wave packet starting at 3324.8 and 15 a.u., respectively. Employing velocity gauge we achieve converged results with a close-coupling expansion of $L_{\max} = 3$, $\ell_1 = \ell_2 = 4$. The single-ionization spectra are obtained using the method described in App. C. Most of the results shown, were computed by fitting the asymmetry only within $\tau \in [-0.5T_{\text{IR}} : 0.5T_{\text{IR}}]$. We ensured that this does not alter the

results by comparing to the fitting interval $\tau \in [-2T_{\text{IR}} : 2T_{\text{IR}}]$ for one wavelength. The fundamental field has a FWHM duration of approximately 22 fs and the APT duration is roughly 14.5 fs, resulting in spectrally broad harmonics, see Tab. J.9 for the pulses used for $\lambda_{\text{IR}} = 1464$ nm. The fundamental wavelength is smoothly varied from λ_{IR} from 1456 nm to 1470 nm.

λ [nm]	ω [eV]	Peak intensity [W/cm ²]	FWHM duration [fs]	CEP [π]	harmonic #
1464	0.85	2×10^9	21	0	-
21.85	56.74	9.4×10^{10}	15	0	67 th
21.53	57.59	3.5×10^{10}	6	0	68 th
21.22	58.44	1.4×10^{11}	6	0	69 th
20.91	59.28	4×10^{10}	6	0	70 th
20.62	60.13	1.58×10^{11}	6	0	71 st
20.33	60.98	4.3×10^{10}	6	0	72 nd
20.05	61.83	1.642×10^{11}	6	0	73 rd
19.78	62.78	3.8×10^{10}	6	0	74 th
19.52	63.52	1.265×10^{11}	6	0	75 th

Table J.9.: Pulse parameters for the results shown Fig. 5.5b.

J.2.6. Parameters for section 5.2.2

Employing velocity gauge we achieve converged results for a close coupling expansion with intensity dependent number of enclosed partial waves: total angular momentum $L_{\text{max}} = 3$ (4), and angular momentum of the two electrons $\ell_1 = \ell_2 = 6$ (8) for $I_{\text{IR}} = 10^9$ W/cm² ($I_{\text{IR}} = 10^{11}$ W/cm²). We use an asymmetric radial box where the spatial grid for the larger (smaller) radial component extends up to 3010 (20) a.u.. To avoid reflections at the boundary we use a complex absorbing boundary in both spatial directions. Within this section we use a \cos^4 envelope for the vector potential with a total duration of 50 fs for the IR and 19 fs for the XUV corresponding to a full-width half maximum (FWHM) duration of $\tau_{\text{IR}} \approx 13$ fs and $\tau_{\text{XUV}} \approx 5$ fs.

J.2.7. Parameters for section 6.3

For the theoretical calculation of the dipole moment $d(t)$ needed to obtain the transient absorption cross section [Eq. (3.16)] we use a radial box of 128 a.u. where an absorbing boundary starts at 102 a.u. For the XUV pulse we use a central energy of 60 eV, with a Gaussian envelope for the intensity profile (160 as FWHM), and a peak intensity of 10^{11} W/cm². For the NIR pulse, we use a wavelength of 740 nm with a Gaussian envelope for the intensity profile (7 fs FWHM) and peak intensity up to 2×10^{13} W/cm². Propagation effects are not considered since the probability for reabsorption of photons is negligible in

the investigated energy region. In velocity gauge an angular momentum expansion with $L_{\max} = \ell_1 = \ell_2 = 10$ was sufficient to achieve converged results for the highest intensities show in this section. The occupation of the 2s2p resonance was obtained by projecting the wave function contained within the small box onto the bound part of the 2s2p scattering eigenstate using the non-hermitian dot product. The doubly excited states were calculated using exterior complex scaling [60].

J.2.8. Parameters for section 7.1

We employ an ultrashort single attosecond pulse (FWHM duration of 160 as with intensity $I_{\text{XUV}} = 10^{11}$ W/cm²) centered at the 2s2p resonance to broadly excite all doubly excited states within the ¹P^o symmetry below the He⁺ ($n = 2$) threshold. After excitation by the single attosecond pulse the system is probed by a few-cycle light pulse with a total duration of 10 fs (cos² envelope) for two different wavelengths separately, $\lambda_{\text{IR}} = 500$ nm ($\omega_{\text{IR}} = 2.48$ eV) and $\lambda_{\text{IR}} = 740$ nm ($\omega_{\text{IR}} = 1.67$ eV). The two different wavelengths drive different transitions between the doubly excited states resonantly due to their different spectral pulse profile.

All calculations are performed within a radial box spanning 128 a.u. in both directions with an absorbing boundary starting at 102.4. a.u.. We use 11 basis function for every finite element spanning 4 a.u.. For the highest employed probe intensity we achieve converged results for a close coupling expansion of $L_{\max} = 7$, $\ell_1 = 6$ and $\ell_2 = 7$ employing velocity gauge. The occupations of the doubly excited states after the interaction with the laser pulses shown within this chapter are obtained by projecting the wavefunction $|\psi(t)\rangle$ onto the eigenfunctions $|\phi_i\rangle$ of the corresponding states, using the non-conjugate dot-product $(\phi_i, \psi(t)) = \int d\vec{r}_1 d\vec{r}_2 \phi_i \cdot \psi(t)$ ²⁸. The eigenfunctions are obtained using exterior complex scaling [60].

J.2.9. Parameters for section 7.3.1

We chose to a rather weak NIR pulse ($I_{\text{NIR}} = 10^{12}$ W/cm²) with long total duration (FWHM 45 fs with a cos² envelope) enabling the observation of multiple Rabi cycles. The NIR pulse has a time delay of $\tau_d = 53.5$ fs with respect to the XUV ensuring that the exciting XUV pulse has no temporal overlap with the driving NIR field. We simulate the response to two different wavelengths of the NIR field $\lambda_{\text{NIR}} = 740$ nm ($\omega = 1.67$ eV) and $\lambda_{\text{NIR}} = 538$ nm ($\omega = 2.3$ eV) to couple the 2s2p state resonantly with the ($2p^2$) ²S^e and ($2s^2$) ²S^e state respectively, see Tab. 5.1. Employing length gauge we use a close-coupling expansion of $L_{\max} = \ell_1 = \ell_2 = 10$. To obtain the occupation of the doubly excited states we use the procedure described in Sec. J.2.8 projecting the time-dependent wave function at times of the zero crossing of the electric field.

²⁸ We use the non-conjugate dotproduct since the eigenfunctions for the resonances are only quasi-bound states. Thus they have complex eigen energies and the left- and right eigenvalues and eigenfunctions are different.

J.2.10. Parameters for section 7.3.2

We use 11 basis functions for each radial element of size 4 a.u.. In the present simulation, we use an angular momentum expansion with $L_{\max} = 10$, $l_1 = 10$, $l_2 = 10$ for the close-coupling scheme. We have verified that length and velocity gauge give equivalent results. For the XUV pulse we use a central energy of 60.15 eV, a Gaussian envelope for the intensity profile with a pulse duration of 250 as FWHM, and a peak intensity of 10^{12} W/cm². We verified the validity of the impulsive excitation approximation underlying the reconstruction algorithm by varying the pulse duration showing that the results are independent of the XUV pulse duration as long as the pulse is on the attosecond scale and short compared to time scales governing the dynamics of the auto-ionizing states. For the NIR pulse, we use a wavelength of 740 nm with a Gaussian envelope for the intensity profile (7 fs FWHM), a carrier envelope phase of $\frac{\pi}{4}$ and varying peak intensity. The carrier envelope phase was chosen to match best with experiment, as will be discussed later. For the calculation of the time-dependent dipole moment $d(t)$, the wave function is used within a relatively small radial box of 128 a.u. where an absorbing boundary starts at 102 a.u. We verified that reconstructing the dipole moment $d(t)$ from the dipole acceleration yields the same results, assuring that the presented results are not influenced by the finite box size. Propagation effects are not considered since the probability for reabsorption of photons is negligible in the investigated energy region.

To calculate the occupation of the doubly excited states we use the same procedure as described in Sec. J.2.8.

J.2.11. Parameters for chapter 8

For linearly polarized pulses, propagating along the \hat{x} axis and polarized along \hat{z} , the vector potential is given by

$$\mathbf{A}(t) = A_0 f(t) \begin{pmatrix} 0 \\ 0 \\ \sin(\omega(t - t_{\text{XUV}})) \end{pmatrix}, \quad (\text{J.2})$$

with being t_{XUV} the peak time of the XUV pulse. The elliptical vector potential, propagating along the \hat{z} axis and polarized in the $\hat{x} - \hat{y}$ plane, is defined by

$$\mathbf{A}(t) = A_0 f(t) \begin{pmatrix} \sin(\omega(t - t_{\text{XUV}})) \\ -\epsilon \cos(\omega(t - t_{\text{XUV}})) \\ 0 \end{pmatrix}, \quad (\text{J.3})$$

where ϵ is the ellipticity of the laser field. The light field is called left(right)-circularly polarized if $\epsilon = 1(-1)$. We employ a \cos^2 envelope $f(t)$ for the vector potential given by $f(t) = \cos^2\left(\frac{\pi}{2T_p}(t - t_{\text{XUV}})\right)$ for $-T_p < (t - t_{\text{XUV}}) < T_p$ where T_p is the full-width at half maximum duration of the vector potential. Typically we achieve converged results for a close-coupling expansion of $L_{\max} = 3$, $l_1 = l_2 = 12$ employing velocity gauge. The box size is chosen large enough to keep the full doubly ionized part of the wavefunction within

the box, where the largest box we employed spanned 800 a.u. in both radial directions. A complex absorbing boundary potential close to the boundary was used to avoid any reflections of the singly ionized parts of the wavefunctions.

To ensure converged results with the propagation time we projected all wavefunctions 3 fs after the end of the laser pulses, unless states otherwise [89]. We use XUV pulses with central photon energies between 40 and 70 eV and peak intensities up to 2×10^{12} W/cm², which is in the purely perturbative regime for these photon energies.

Bibliography

- [1] T. Brabec and F. Krausz. *Intense few-cycle laser fields: Frontiers of nonlinear optics*. Rev. Mod. Phys. **72**, 545 (2000).
- [2] F. Krausz and M. Ivanov. *Attosecond physics*. Rev. Mod. Phys. **81**, 163 (2009).
- [3] J. J. Macklin, J. D. Kmetec, and C. L. Gordon. *High-order harmonic generation using intense femtosecond pulses*. Physical Review Letters **70**, 766 (1993).
- [4] A. L'Huillier and P. Balcou. *High-order harmonic generation in rare gases with a 1-ps 1053-nm laser*. Physical Review Letters **70**, 774 (1993).
- [5] A. McPherson, G. Gibson, H. Jara, U. Johann, T. S. Luk, I. A. McIntyre, K. Boyer, and C. K. Rhodes. *Studies of multiphoton production of vacuum-ultraviolet radiation in the rare gases*. JOSA B **4**, 595 (1987).
- [6] M. Ferray, A. L'Huillier, X. F. Li, L. A. Lompre, G. Mainfray, and C. Manus. *Multiple-harmonic conversion of 1064 nm radiation in rare gases*. Journal of Physics B: Atomic, Molecular and Optical Physics **21**, L31 (1988).
- [7] K. C. Kulander and B. W. Shore. *Calculations of Multiple-Harmonic Conversion of 1064-nm Radiation in Xe*. Phys. Rev. Lett. **62**, 524 (1989).
- [8] F. Brunel. *Harmonic generation due to plasma effects in a gas undergoing multiphoton ionization in the high-intensity limit*. JOSA B **7**, 521 (1990).
- [9] J. L. Krause, K. J. Schafer, and K. C. Kulander. *High-order harmonic generation from atoms and ions in the high intensity regime*. Physical Review Letters **68**, 3535 (1992).
- [10] P. B. Corkum. *Plasma perspective on strong field multiphoton ionization*. Phys. Rev. Lett. **71**, 1994 (1993).
- [11] M. Lewenstein, P. Balcou, M. Y. Ivanov, A. L'Huillier, and P. B. Corkum. *Theory of high-harmonic generation by low-frequency laser fields*. Phys. Rev. A **49**, 2117 (1994).
- [12] M. Hentschel, R. Kienberger, C. Spielmann, G. A. Reider, N. Milosevic, T. Brabec, P. Corkum, U. Heinzmann, M. Drescher, and F. Krausz. *Attosecond metrology*. Nature **414**, 509 (2001).

- [13] M. Drescher, M. Hentschel, R. Kienberger, G. Tempea, C. Spielmann, G. A. Reider, P. B. Corkum, and F. Krausz. *X-ray Pulses Approaching the Attosecond Frontier*. *Science* **291**, 1923 (2001).
- [14] R. López-Martens, K. Varjú, P. Johnsson, J. Mauritsson, Y. Mairesse, P. Salières, M. B. Gaarde, K. J. Schafer, A. Persson, S. Svanberg, C.-G. Wahlström, and A. L’Huillier. *Amplitude and Phase Control of Attosecond Light Pulses*. *Phys. Rev. Lett.* **94**, 033001 (2005).
- [15] M. Lein. *Attosecond Probing of Vibrational Dynamics with High-Harmonic Generation*. *Phys. Rev. Lett.* **94**, 053004 (2005).
- [16] S. Baker, J. S. Robinson, C. A. Haworth, H. Teng, R. A. Smith, C. C. Chirilă, M. Lein, J. W. G. Tisch, and J. P. Marangos. *Probing Proton Dynamics in Molecules on an Attosecond Time Scale*. *Science* **312**, 424 (2006).
- [17] T. T. Luu, Z. Yin, A. Jain, T. Gaumnitz, Y. Pertot, J. Ma, and H. J. Wörner. *Extreme-ultraviolet high-harmonic generation in liquids*. *Nature Communications* **9**, 3723 (2018).
- [18] S. Ghimire and D. A. Reis. *High-harmonic generation from solids*. *Nature Physics* **15**, 10 (2019).
- [19] H. Liu, Y. Li, Y. S. You, S. Ghimire, T. F. Heinz, and D. A. Reis. *High-harmonic generation from an atomically thin semiconductor*. *Nature Physics* **13**, 262 (2017).
- [20] T. Popmintchev, M.-C. Chen, D. Popmintchev, P. Arpin, S. Brown, S. Ališauskas, G. Andriukaitis, T. Balčiunas, O. D. Mücke, A. Pugzlys, A. Baltuška, B. Shim, S. E. Schrauth, A. Gaeta, C. Hernández-García, L. Plaja, A. Becker, A. Jaron-Becker, M. M. Murnane, and H. C. Kapteyn. *Bright Coherent Ultrahigh Harmonics in the keV X-ray Regime from Mid-Infrared Femtosecond Lasers*. *Science* **336**, 1287 (2012).
- [21] S. L. Cousin, N. Di Palo, B. Buades, S. M. Teichmann, M. Reduzzi, M. Devetta, A. Kheifets, G. Sansone, and J. Biegert. *Attosecond Streaking in the Water Window: A New Regime of Attosecond Pulse Characterization*. *Phys. Rev. X* **7**, 041030 (2017).
- [22] T. Gaumnitz, A. Jain, Y. Pertot, M. Huppert, I. Jordan, F. Ardana-Lamas, and H. J. Wörner. *Streaking of 43-attosecond soft-X-ray pulses generated by a passively CEP-stable mid-infrared driver*. *Opt. Express* **25**, 27506 (2017).
- [23] J. Li, X. Ren, Y. Yin, K. Zhao, A. Chew, Y. Cheng, E. Cunningham, Y. Wang, S. Hu, Y. Wu, M. Chini, and Z. Chang. *53-attosecond X-ray pulses reach the carbon K-edge*. *Nature Communications* **8**, 1 (2017).
- [24] A. H. Zewail. *Femtochemistry: Atomic-Scale Dynamics of the Chemical Bond*. *The Journal of Physical Chemistry A* **104**, 5660 (2000).

- [25] P. M. Paul, E. S. Toma, P. Breger, G. Mullot, F. Audebert, P. Balcou, H. G. Muller, and P. Agostini. *Observation of a Train of Attosecond Pulses from High Harmonic Generation*. *Science* **292**, 1689 (2001).
- [26] M. Schultze, M. Fieß, N. Karpowicz, J. Gagnon, M. Korbman, M. Hofstetter, S. Neppl, A. L. Cavalieri, Y. Komninos, T. Mercouris, C. A. Nicolaides, R. Pazourek, S. Nagele, J. Feist, J. Burgdörfer, A. M. Azzeer, R. Ernstorfer, R. Kienberger, U. Kleineberg, E. Goulielmakis, F. Krausz, and V. S. Yakovlev. *Delay in Photoemission*. *Science* **328**, 1658 (2010).
- [27] K. Klünder, J. M. Dahlström, M. Gisselbrecht, T. Fordell, M. Swoboda, D. Guénot, P. Johnsson, J. Caillat, J. Mauritsson, A. Maquet, R. Taieb, and A. L’Huillier. *Probing Single-Photon Ionization on the Attosecond Time Scale*. *Physical Review Letters* **106**, 143002 (2011).
- [28] M. Ossiander, F. Siegrist, V. Shirvanyan, R. Pazourek, A. Sommer, T. Latka, A. Guggenmos, S. Nagele, J. Feist, J. Burgdörfer, R. Kienberger, and M. Schultze. *Attosecond correlation dynamics*. *Nature Physics* **13**, 280 (2017).
- [29] R. Pazourek, J. Feist, S. Nagele, and J. Burgdörfer. *Attosecond Streaking of Correlated Two-Electron Transitions in Helium*. *Physical Review Letters* **108**, 163001 (2012).
- [30] R. Pazourek, S. Nagele, and J. Burgdörfer. *Attosecond chronoscopy of photoemission*. *Rev. Mod. Phys.* **87**, 765 (2015).
- [31] J. M. Dahlström, A. L’Huillier, and A. Maquet. *Introduction to attosecond delays in photoionization*. *Journal of Physics B: Atomic, Molecular and Optical Physics* **45**, 183001 (2012).
- [32] J. M. Dahlström, D. Guénot, K. Klünder, M. Gisselbrecht, J. Mauritsson, A. L’Huillier, A. Maquet, and R. Taieb. *Theory of attosecond delays in laser-assisted photoionization*. *Chemical Physics* **414**, 53 (2013).
- [33] R. Pazourek, S. Nagele, and J. Burgdörfer. *Time-resolved photoemission on the attosecond scale: opportunities and challenges*. *Faraday Discussions* **163**, 353 (2013).
- [34] S. Heuser, A. Jimenez Galan, C. Cirelli, C. Marante, M. Sabbar, R. Boge, M. Lucchini, L. Gallmann, I. Ivanov, A. S. Kheifets, J. M. Dahlström, E. Lindroth, L. Argenti, F. Martin, and U. Keller. *Angular dependence of photoemission time delay in helium*. *Physical Review A* **94**, 063409 (2016).
- [35] A. W. Bray, F. Naseem, and A. S. Kheifets. *Simulation of angular-resolved RABBITT measurements in noble-gas atoms*. *Phys. Rev. A* **97**, 063404 (2018).

- [36] H. Beutler. *Über Absorptionsenergien von Argon, Krypton und Xenon zu Termen zwischen den beiden Ionisierungsenergien ${}^2P_{3/2}^o$ und ${}^2P_{1/2}^o$* . Zeitschrift für Physik **93**, 177 (1935).
- [37] U. Fano. *Sullo spettro di assorbimento dei gas nobili presso il limite dello spettro d'arco*. Il Nuovo Cimento (1924-1942) **12**, 154 (1935).
- [38] U. Fano. *Effects of Configuration Interaction on Intensities and Phase Shifts*. Physical Review **124**, 1866 (1961).
- [39] X. Fan, W. Zheng, and D. J. Singh. *Light scattering and surface plasmons on small spherical particles*. Light: Science & Applications **3**, e179 (2014).
- [40] M. Galli, S. Portalupi, M. Belotti, L. C. Andreani, L. O'Faolain, and T. Krauss. *Light scattering and Fano resonances in high-Q photonic crystal nanocavities*. Applied Physics Letters **94**, 071101 (2009).
- [41] S. Rotter, F. Libisch, J. Burgdörfer, U. Kuhl, and H.-J. Stöckmann. *Tunable Fano resonances in transport through microwave billiards*. Phys. Rev. E **69**, 046208 (2004).
- [42] S. Orrigo, H. Lenske, F. Cappuzzello, A. Cunsolo, A. Foti, A. Lazzaro, C. Nociforo, and J. Winfield. *Core excited Fano-resonances in exotic nuclei*. Physics Letters B **633**, 469 (2006).
- [43] A. E. Miroshnichenko, S. Flach, and Y. S. Kivshar. *Fano resonances in nanoscale structures*. Rev. Mod. Phys. **82**, 2257 (2010).
- [44] C. Ott, A. Kaldun, P. Raith, K. Meyer, M. Laux, J. Evers, C. H. Keitel, C. H. Greene, and T. Pfeifer. *Lorentz Meets Fano in Spectral Line Shapes: A Universal Phase and Its Laser Control*. Science **340**, 716 (2013).
- [45] K. P. Heeg, C. Ott, D. Schumacher, H.-C. Wille, R. Röhlberger, T. Pfeifer, and J. Evers. *Interferometric phase detection at x-ray energies via Fano resonance control*. Phys. Rev. Lett. **114**, 207401 (2015).
- [46] M. Reduzzi, W.-C. Chu, C. Feng, A. Dubrouil, J. Hummert, F. Calegari, F. Frassetto, L. Poletto, O. Kornilov, M. Nisoli, C.-D. Lin, and G. Sansone. *Observation of autoionization dynamics and sub-cycle quantum beating in electronic molecular wave packets*. Journal of Physics B: Atomic, Molecular and Optical Physics **49**, 065102 (2016).
- [47] B. Xu, E. Cappelluti, L. Benfatto, B. P. P. Mallett, P. Marsik, E. Sheveleva, F. Lyzwa, T. Wolf, R. Yang, X. G. Qiu, Y. M. Dai, H. H. Wen, R. P. S. M. Lobo, and C. Bernhard. *Scaling of the Fano Effect of the In-Plane Fe-As Phonon and the Superconducting Critical Temperature in $Ba_{1-x}K_xFe_2As_2$* . Phys. Rev. Lett. **122**, 217002 (2019).

- [48] N. Caselli, F. Intonti, F. L. China, F. Biccari, F. Riboli, A. Gerardino, L. Li, E. H. Linfield, F. Pagliano, A. Fiore, and M. Gurioli. *Generalized Fano lineshapes reveal exceptional points in photonic molecules*. *Nature Communications* **9**, 396 (2018).
- [49] K. Thyagarajan, J. Butet, and O. J. F. Martin. *Augmenting Second Harmonic Generation Using Fano Resonances in Plasmonic Systems*. *Nano Letters* **13**, 1847 (2013).
- [50] K. Baumann, N. Q. Burdick, M. Lu, and B. L. Lev. *Observation of low-field Fano-Feshbach resonances in ultracold gases of dysprosium*. *Physical Review A* **89**, 020701 (2014).
- [51] I. Mazumdar, A. R. P. Rau, and V. S. Bhasin. *Efimov States and their Fano Resonances in a Neutron-Rich Nucleus*. *Physical Review Letters* **97**, 062503 (2006).
- [52] M. Kotur, D. Guénot, A. Jiménez-Galán, D. Kroon, E. W. Larsen, M. Louisy, S. Bengtsson, M. Miranda, J. Mauritsson, C. L. Arnold, S. E. Canton, M. Gisselbrecht, T. Carette, J. M. Dahlström, E. Lindroth, A. Maquet, L. Argenti, F. Martin, and A. L’Huillier. *Spectral phase measurement of a Fano resonance using tunable attosecond pulses*. *Nature Communications* **7**, 10566 (2016).
- [53] V. Gruson, L. Barreau, A. Jimenez-Galan, F. Risoud, J. Caillat, A. Maquet, B. Carre, F. Lepetit, J.-F. Hergott, T. Ruchon, L. Argenti, R. Taieb, F. Martín, and P. Salieres. *Attosecond dynamics through a Fano resonance: Monitoring the birth of a photoelectron*. *Science* **354**, 734 (2016).
- [54] D. Busto, L. Barreau, M. Isinger, M. Turconi, C. Alexandridi, A. Harth, S. Zhong, R. J. Squibb, D. Kroon, S. Plogmaker, M. Miranda, A. Jimenez-Galan, L. Argenti, C. L. Arnold, R. Feifel, F. Martin, M. Gisselbrecht, A. L’Huillier, and P. Salieres. *Time-frequency representation of autoionization dynamics in helium*. *Journal of Physics B: Atomic, Molecular and Optical Physics* **51**, 044002 (2018).
- [55] L. Barreau, C. L. M. Petersson, M. Klinker, A. Camper, C. Marante, T. Gorman, D. Kiesewetter, L. Argenti, P. Agostini, J. González-Vázquez, P. Salières, L. F. DiMauro, and F. Martín. *Disentangling Spectral Phases of Interfering Autoionizing States from Attosecond Interferometric Measurements*. *Phys. Rev. Lett.* **122**, 253203 (2019).
- [56] S. Donsa, N. Douguet, J. Burgdörfer, I. Březinová, and L. Argenti. *Circular Holographic Ionization-Phase Meter*. *Phys. Rev. Lett.* **123**, 133203 (2019).
- [57] A. Kaldun, A. Blättermann, V. Stooß, S. Donsa, H. Wei, R. Pazourek, S. Nagele, C. Ott, C. D. Lin, J. Burgdörfer, and T. Pfeifer. *Observing the ultrafast buildup of a Fano resonance in the time domain*. *Science* **354**, 738 (2016).

- [58] L. A. A. Nikolopoulos and P. Lambropoulos. *Time-dependent theory of double ionization of helium under XUV radiation*. Journal of Physics B: Atomic, Molecular and Optical Physics **40**, 1347 (2007).
- [59] W.-C. Chu and C. D. Lin. *Theory of ultrafast autoionization dynamics of Fano resonances*. Physical Review A **82**, 053415 (2010).
- [60] L. Argenti, R. Pazourek, J. Feist, S. Nagele, M. Liertzer, E. Persson, J. Burgdörfer, and E. Lindroth. *Photoionization of helium by attosecond pulses: Extraction of spectra from correlated wave functions*. Physical Review A **87**, 053405 (2013).
- [61] M. Wickenhauser, J. Burgdörfer, F. Krausz, and M. Drescher. *Time Resolved Fano Resonances*. Physical Review Letters **94**, 023002 (2005).
- [62] M. Wickenhauser, J. Burgdörfer, F. Krausz, and M. Drescher. *Attosecond streaking of overlapping Fano resonances*. Journal of Modern Optics **53**, 247 (2006).
- [63] P. Lambropoulos and P. Zoller. *Autoionizing states in strong laser fields*. Physical Review A **24**, 379 (1981).
- [64] H. Bachau, P. Lambropoulos, and R. Shakeshaft. *Theory of laser-induced transitions between autoionizing states of He*. Physical Review A **34**, 4785 (1986).
- [65] X. M. Tong and C. D. Lin. *Double photoexcitation of He atoms by attosecond xuv pulses in the presence of intense few-cycle infrared lasers*. Phys. Rev. A **71**, 033406 (2005).
- [66] W.-C. Chu, S.-F. Zhao, and C. D. Lin. *Laser-assisted-autoionization dynamics of helium resonances with single attosecond pulses*. Physical Review A **84**, 033426 (2011).
- [67] S. I. Themelis, P. Lambropoulos, and M. Meyer. *Ionization dynamics in double resonance involving autoionizing states in helium: the effect of pulse shapes*. Journal of Physics B: Atomic, Molecular and Optical Physics **37**, 4281 (2004).
- [68] C. Ott, A. Kaldun, L. Argenti, P. Raith, K. Meyer, M. Laux, Y. Zhang, A. Blättermann, S. Hagstotz, T. Ding, R. Heck, J. Madroñero, F. Martín, and T. Pfeifer. *Reconstruction and control of a time-dependent two-electron wave packet*. Nature **516**, 374 (2014).
- [69] S. Gilbertson, M. Chini, X. Feng, S. Khan, Y. Wu, and Z. Chang. *Monitoring and Controlling the Electron Dynamics in Helium with Isolated Attosecond Pulses*. Physical Review Letters **105**, 263003 (2010).
- [70] V. Stooß, S. M. Cavaletto, S. Donsa, A. Blättermann, P. Birk, C. H. Keitel, I. Březinová, J. Burgdörfer, C. Ott, and T. Pfeifer. *Real-Time Reconstruction of the Strong-Field-Driven Dipole Response*. Phys. Rev. Lett. **121**, 173005 (2018).

- [71] A. Fleischer, O. Kfir, T. Diskin, P. Sidorenko, and O. Cohen. *Spin angular momentum and tunable polarization in high-harmonic generation*. Nature Photonics **8**, 543 (2014).
- [72] D. B. Milošević. *Circularly polarized high harmonics generated by a bicircular field from inert atomic gases in the p state: A tool for exploring chirality-sensitive processes*. Physical Review A **92**, 043827 (2015).
- [73] D. Baykusheva, M. S. Ahsan, N. Lin, and H. J. Wörner. *Bicircular High-Harmonic Spectroscopy Reveals Dynamical Symmetries of Atoms and Molecules*. Physical Review Letters **116**, 123001 (2016).
- [74] F. Mauger, A. D. Bandrauk, and T. Uzer. *Circularly polarized molecular high harmonic generation using a bicircular laser*. Journal of Physics B: Atomic, Molecular and Optical Physics **49**, 10LT01 (2016).
- [75] D. M. Reich and L. B. Madsen. *Illuminating Molecular Symmetries with Bicircular High-Order-Harmonic Generation*. Physical Review Letters **117**, 133902 (2016).
- [76] L. Medišauskas, J. Wragg, H. van der Hart, and M. Y. Ivanov. *Generating Isolated Elliptically Polarized Attosecond Pulses Using Bichromatic Counterrotating Circularly Polarized Laser Fields*. Physical Review Letters **115**, 153001 (2015).
- [77] O. Kfir, P. Grychtol, E. Turgut, R. Knut, D. Zusin, D. chev, T. Popmintchev, H. Nembach, J. M. Shaw, A. Fleischer, H. Kapteyn, M. Murnane, and O. Cohen. *Generation of bright phase-matched circularly-polarized extreme ultraviolet high harmonics*. Nature Photonics **9**, 99 (2015).
- [78] T. Fan, P. Grychtol, R. Knut, C. Hernandez-Garcia, D. D. Hickstein, D. Zusin, C. Gentry, F. J. Dollar, C. A. Mancuso, C. W. Hogle, O. Kfir, D. Legut, K. Carva, J. L. Ellis, K. M. Dorney, C. Chen, O. G. Shpyrko, E. E. Fullerton, O. Cohen, P. M. Oppeneer, D. B. Milosevic, A. Becker, A. A. Jaron-Becker, T. Popmintchev, M. M. Murnane, and H. C. Kapteyn. *Bright circularly polarized soft X-ray high harmonics for X-ray magnetic circular dichroism*. Proceedings of the National Academy of Sciences **112**, 14206 (2015).
- [79] C. Chen, Z. Tao, C. Hernández-Garcia, P. Matyba, A. Carr, R. Knut, O. Kfir, D. Zusin, C. Gentry, P. Grychtol, O. Cohen, L. Plaja, A. Becker, A. Jaron-Becker, H. Kapteyn, and M. Murnane. *Tomographic reconstruction of circularly polarized high-harmonic fields: 3D attosecond metrology*. Science Advances **2**, e1501333 (2016).
- [80] P.-C. Huang, C. Hernández-Garcia, J.-T. Huang, P.-Y. Huang, C.-H. Lu, L. Rego, D. D. Hickstein, J. L. Ellis, A. Jaron-Becker, A. Becker, S.-D. Yang, C. G. Durfee, L. Plaja, H. C. Kapteyn, M. M. Murnane, A. H. Kung, and M.-C. Chen. *Polarization control of isolated high-harmonic pulses*. Nature Photonics **12**, 349 (2018).

- [81] D. D. Hickstein, F. J. Dollar, P. Grychtol, J. L. Ellis, R. Knut, C. Hernández-García, D. Zusin, C. Gentry, J. M. Shaw, T. Fan, K. M. Dorney, A. Becker, A. Jaron-Becker, H. C. Kapteyn, M. M. Murnane, and C. G. Durfee. *Non-collinear generation of angularly isolated circularly polarized high harmonics*. Nature Photonics **9**, 743 (2015).
- [82] P.-C. Huang, C. Hernández-García, J.-T. Huang, P.-Y. Huang, C.-H. Lu, L. Rego, D. D. Hickstein, J. L. Ellis, A. Jaron-Becker, A. Becker, S.-D. Yang, C. G. Durfee, L. Plaja, H. C. Kapteyn, M. M. Murnane, A. H. Kung, and M.-C. Chen. *Polarization control of isolated high-harmonic pulses*. Nature Photonics **12**, 349 (2018).
- [83] Z.-Y. Chen and A. Pukhov. *Bright high-order harmonic generation with controllable polarization from a relativistic plasma mirror*. Nature Communications **7**, 12515 (2016).
- [84] G. Ma, W. Yu, M. Y. Yu, B. Shen, and L. Veisz. *Intense circularly polarized attosecond pulse generation from relativistic laser plasmas using few-cycle laser pulses*. Optics Express **24**, 10057 (2016).
- [85] E. Allaria, B. Diviacco, C. Callegari, P. Finetti, B. Mahieu, J. Viefhaus, M. Zangrando, G. De Ninno, G. Lambert, E. Ferrari, J. Buck, M. Ilchen, B. Vodungbo, N. Mahne, C. Svetina, C. Spezzani, S. Di Mitri, G. Penco, M. Trovó, W. M. Fawley, P. R. Rebernik, D. Gauthier, C. Grazioli, M. Coreno, B. Ressel, A. Kivimäki, T. Mazza, L. Glaser, F. Scholz, J. Seltmann, P. Gessler, J. Grünert, A. De Fanis, M. Meyer, A. e. Knie, S. P. Moeller, L. Raimondi, F. Capotondi, E. Pedersoli, O. Plekan, M. B. Danailov, A. Demidovich, I. Nikolov, A. Abrami, J. Gautier, J. Lüning, P. Zeitoun, and L. Giannessi. *Control of the Polarization of a Vacuum-Ultraviolet, High-Gain, Free-Electron Laser*. Physical Review X **4**, 041040 (2014).
- [86] A. A. Lutman, J. P. MacArthur, M. Ilchen, A. O. Lindahl, J. Buck, R. N. Coffee, G. L. Dakovski, L. Dammann, Y. Ding, H. A. Dürr, L. Glaser, J. Grünert, G. Hartmann, N. Hartmann, D. Higley, K. Hirsch, Y. I. Levashov, A. Marinelli, T. Maxwell, A. Mitra, S. Moeller, T. Osipov, F. Peters, M. Planas, I. Shevchuk, W. F. Schlotter, F. Scholz, J. Seltmann, J. Viefhaus, P. Walter, Z. R. Wolf, Z. Huang, and H.-D. Nuhn. *Polarization control in an X-ray free-electron laser*. Nature Photonics **10**, 468 (2016).
- [87] C. von Korff Schmising, D. Weder, T. Noll, B. Pfau, M. Hennecke, C. Strüber, I. Radu, M. Schneider, S. Staeck, C. M. Günther, J. Lüning, A. e. d. Merhe, J. Buck, G. Hartmann, J. Viefhaus, R. Treusch, and S. Eisebitt. *Generating circularly polarized radiation in the extreme ultraviolet spectral range at the free-electron laser FLASH*. Review of Scientific Instruments **88**, 053903 (2017).
- [88] J. Colgan and M. S. Pindzola. *Core-Excited Resonance Enhancement in the Two-Photon Complete Fragmentation of Helium*. Physical Review Letters **88**, 173002 (2002).

- [89] J. Feist, S. Nagele, R. Pazourek, E. Persson, B. I. Schneider, L. A. Collins, and J. Burgdörfer. *Nonsequential two-photon double ionization of helium*. Physical Review A **77**, 043420 (2008).
- [90] A. Palacios, T. N. Rescigno, and C. W. McCurdy. *Time-dependent treatment of two-photon resonant single and double ionization of helium by ultrashort laser pulses*. Phys. Rev. A **79**, 033402 (2009).
- [91] S. Laulan and H. Bachau. *Correlation effects in two-photon single and double ionization of helium*. Physical Review A **68**, 013409 (2003).
- [92] S. X. Hu, J. Colgan, and L. A. Collins. *Triple-differential cross-sections for two-photon double ionization of He near threshold*. Journal of Physics B: Atomic, Molecular and Optical Physics **38**, L35 (2005).
- [93] A. S. Kheifets and I. A. Ivanov. *Convergent close-coupling calculations of two-photon double ionization of helium*. Journal of Physics B: Atomic, Molecular and Optical Physics **39**, 1731 (2006).
- [94] R. Pazourek, J. Feist, S. Nagele, E. Persson, B. I. Schneider, L. A. Collins, and J. Burgdörfer. *Universal features in sequential and nonsequential two-photon double ionization of helium*. Physical Review A **83**, 053418 (2011).
- [95] L. Feng and H. van der Hart. *Two-photon double ionization of He*. Journal of Physics B: Atomic, Molecular and Optical Physics **36**, L1 (2002).
- [96] X. Guan, K. Bartschat, and B. I. Schneider. *Dynamics of two-photon double ionization of helium in short intense xuv laser pulses*. Phys. Rev. A **77**, 043421 (2008).
- [97] Z. Zhang, L.-Y. Peng, M.-H. Xu, A. F. Starace, T. Morishita, and Q. Gong. *Two-photon double ionization of helium: Evolution of the joint angular distribution with photon energy and two-electron energy sharing*. Physical Review A **84**, 043409 (2011).
- [98] J. Feist. *Two-photon double ionization of helium*. PhD thesis, Vienna University of Technology (2009).
- [99] S. Nagele. *Theoretical investigation of attosecond electronic dynamics in atoms*. PhD thesis, Vienna University of Technology (2012).
- [100] R. Pazourek. *Time-resolved photoemission in one- and two-electron atoms*. PhD thesis, Vienna University of Technology (2013).
- [101] J. Fuchs, N. Douguet, S. Donsa, F. Martín, J. Burgdörfer, L. Argenti, L. Cattaneo, and U. Keller. *Time delays from one-photon transitions in the continuum*. arXiv:1907.03607 [physics] (2019). ArXiv: 1907.03607.

- [102] T. Gorman, T. Scarborough, D. Keisewetter, P. Agostini, S. Mehmood, E. Lindroth, S. Donsa, J. Burgdörfer, L. Argenti, and L. F. DiMauro. *High-lying autoionization resonances in argon revealed through wavelength scanning*. to be submitted (2019).
- [103] A. Blättermann, A. Kaldun, V. Stooß, S. Donsa, H. Wei, R. Pazourek, S. Nagele, C. Ott, C.-D. Lin, J. Burgdörfer, and T. Pfeifer. *Watching the emergence of a Fano resonance in doubly excited helium*. Journal of Physics: Conference Series **875**, 012010 (2017).
- [104] S. Donsa, I. Březinová, H. Ni, J. Feist, and J. Burgdörfer. *Polarization tagging of two-photon double ionization by elliptically polarized XUV pulses*. Phys. Rev. A **99**, 023413 (2019).
- [105] A. Ludwig, J. Maurer, B. W. Mayer, C. R. Phillips, L. Gallmann, and U. Keller. *Breakdown of the Dipole Approximation in Strong-Field Ionization*. Phys. Rev. Lett. **113**, 243001 (2014).
- [106] S. Brennecke and M. Lein. *High-order above-threshold ionization beyond the electric dipole approximation*. Journal of Physics B: Atomic, Molecular and Optical Physics **51**, 094005 (2018).
- [107] S. Brennecke and M. Lein. *High-order above-threshold ionization beyond the electric dipole approximation: Dependence on the atomic and molecular structure*. Phys. Rev. A **98**, 063414 (2018).
- [108] M.-X. Wang, H. Liang, X.-R. Xiao, S.-G. Chen, W.-C. Jiang, and L.-Y. Peng. *Nondipole effects in atomic dynamic interference*. Phys. Rev. A **98**, 023412 (2018).
- [109] M. Klaiber, E. Yakaboylu, H. Bauke, K. Z. Hatsagortsyan, and C. H. Keitel. *Under-the-Barrier Dynamics in Laser-Induced Relativistic Tunneling*. Phys. Rev. Lett. **110**, 153004 (2013).
- [110] A. Bandrauk, F. Fillion-Gourdeau, and E. Lorin. *Atoms and molecules in intense laser fields: gauge invariance of theory and models*. Journal of Physics B: Atomic, Molecular and Optical Physics **46**, 153001 (2013).
- [111] M. S. Pindzola, F. Robicheaux, S. D. Loch, J. C. Berengut, T. Topcu, J. Colgan, M. Foster, D. C. Griffin, C. P. Ballance, D. R. Schultz, T. Minami, N. R. Badnell, M. C. Witthoef, D. R. Plante, D. M. Mitnik, J. A. Ludlow, and U. Kleiman. *The time-dependent close-coupling method for atomic and molecular collision processes*. Journal of Physics B: Atomic, Molecular and Optical Physics **40**, R39 (2007).
- [112] A. Scrinzi. *Time-Dependent Schrödinger equation*. In T. Schultz and M. Vrakking (eds.), *Attosecond and XUV physics*. Wiley-VCH (2014).
- [113] K. L. Ishikawa and T. Sato. *A Review on Ab Initio Approaches for Multielectron Dynamics*. IEEE Journal of Selected Topics in Quantum Electronics **21**, 1 (2015).

- [114] X. Tong and C. Lin. *Empirical formula for static field ionization rates of atoms and molecules by lasers in the barrier-suppression regime*. Journal of Physics B: Atomic, Molecular and Optical Physics **38**, 2593 (2005).
- [115] R. H. Garvey, C. H. Jackman, and A. E. S. Green. *Independent-particle-model potentials for atoms and ions with $36 < Z < 54$ and a modified Thomas-Fermi atomic energy formula*. Phys. Rev. A **12**, 1144 (1975).
- [116] X.-M. Tong and S.-I. Chu. *Theoretical study of multiple high-order harmonic generation by intense ultrashort pulsed laser fields: A new generalized pseudospectral time-dependent method*. Chemical Physics **217**, 119 (1997). Dynamics of Driven Quantum Systems.
- [117] T. N. Rescigno and C. W. McCurdy. *Numerical grid methods for quantum-mechanical scattering problems*. Physical Review A **62**, 032706 (2000).
- [118] C. W. McCurdy, D. A. Horner, and T. N. Rescigno. *Practical calculation of amplitudes for electron-impact ionization*. Physical Review A **63**, 022711 (2001).
- [119] B. I. Schneider and L. A. Collins. *The discrete variable method for the solution of the time-dependent Schrödinger equation*. Journal of Non-Crystalline Solids **351**, 1551 (2005).
- [120] B. I. Schneider, L. A. Collins, and S. X. Hu. *Parallel solver for the time-dependent linear and nonlinear Schrödinger equation*. Physical Review E **73**, 036708 (2006).
- [121] X. Tang, H. Rudolph, and P. Lambropoulos. *Nonperturbative time-dependent theory of helium in a strong laser field*. Phys. Rev. A **44**, R6994 (1991).
- [122] A. Scrinzi and B. Piraux. *Two-electron atoms in short intense laser pulses*. Phys. Rev. A **58**, 1310 (1998).
- [123] G. Lagmago Kamta and A. F. Starace. *Angular Distributions for Double Ionization of Li^- by an Ultrashort, Intense Laser Pulse*. Phys. Rev. Lett. **86**, 5687 (2001).
- [124] G. Lagmago Kamta and A. F. Starace. *Multielectron system in an ultrashort, intense laser field: A nonperturbative, time-dependent two-active-electron approach*. Phys. Rev. A **65**, 053418 (2002).
- [125] M. S. Pindzola and F. Robicheaux. *Time-dependent close-coupling calculations of correlated photoionization processes in helium*. Phys. Rev. A **57**, 318 (1998).
- [126] E. S. Smyth, J. S. Parker, and K. T. Taylor. *Numerical integration of the time-dependent Schrödinger equation for laser-driven helium*. Computer Physics Communications **114**, 1 (1998).

- [127] R. Hasbani, E. Cormier, and H. Bachau. *Resonant and non-resonant ionization of helium by XUV ultrashort and intense laser pulses*. Journal of Physics B: Atomic, Molecular and Optical Physics **33**, 2101 (2000).
- [128] K. J. Meharg, J. S. Parker, and K. T. Taylor. *Beyond the dipole approximation for helium and hydrogen in intense laser fields*. Journal of Physics B: Atomic, Molecular and Optical Physics **38**, 237 (2005).
- [129] T. J. Park and J. C. Light. *Unitary quantum time evolution by iterative Lanczos reduction*. The Journal of Chemical Physics **85**, 5870 (1986).
- [130] C. Leforestier, R. H. Bisseling, C. Cerjan, M. D. Feit, R. Friesner, A. Guldberg, A. Hammerich, G. Jolicard, W. Karrlein, H. D. Meyer, N. Lipkin, O. Roncero, and R. Kosloff. *A comparison of different propagation schemes for the time dependent Schrödinger equation*. Journal of Computational Physics **94**, 59 (1991).
- [131] H. Friedrich. *Theoretical Atomic Physics*. Springer International Publishing AG (2017).
- [132] G. Breit and H. A. Bethe. *Ingoing Waves in Final State of Scattering Problems*. Phys. Rev. **93**, 888 (1954).
- [133] L. Argenti and E. Lindroth. Unpublished (2018).
- [134] T. Carette, J. M. Dahlström, L. Argenti, and E. Lindroth. *Multiconfigurational Hartree-Fock close-coupling ansatz: Application to the argon photoionization cross section and delays*. Phys. Rev. A **87**, 1 (2013).
- [135] U. Becker, R. Wehlitz, O. Hemmers, B. Langer, and A. Menzel. *Observation of participator Auger decay following valence photoionization with excitation*. Phys. Rev. Lett. **63**, 1054 (1989).
- [136] C. deBoor. *A Pratical Guide to Splines*. Springer-Verlag (1978).
- [137] H. Bachau, E. Cormier, P. Decleva, J. E. Hansen, and F. Martín. *Applications of B-splines in atomic and molecular physics*. Rep. Prog. Phys. **64**, 1815 (2001).
- [138] L. Argenti and R. Colle. *On the B-splines effective completeness*. Computer Physics Communications **180**, 1442 (2009).
- [139] C. Froese Fischer. *Hartree-Fock Method for Atoms: A Numerical Approach*. Wiley (1977).
- [140] C. Froese Fischer, T. Brage, and P. Jönsson. *Computational Atomic Structure: An MCHF Approach*. Tayler & Francis (1997).

- [141] C. Froese Fischer, G. Tachiev, G. Gaigalas, and M. R. Godefroid. *An MCHF atomic-structure package for large-scale calculations*. Computer Physics Communications **176**, 559 (2007).
- [142] F. Calegari, G. Sansone, S. Stagira, C. Vozzi, and M. Nisoli. *Advances in attosecond science*. Journal of Physics B: Atomic, Molecular and Optical Physics **49**, 062001 (2016).
- [143] M. Chini, B. Zhao, H. Wang, Y. Cheng, S. X. Hu, and Z. Chang. *Subcycle ac Stark Shift of Helium Excited States Probed with Isolated Attosecond Pulses*. Phys. Rev. Lett. **109**, 073601 (2012).
- [144] X. Feng, S. Gilbertson, H. Mashiko, H. Wang, S. D. Khan, M. Chini, Y. Wu, K. Zhao, and Z. Chang. *Generation of Isolated Attosecond Pulses with 20 to 28 Femtosecond Lasers*. Phys. Rev. Lett. **103**, 183901 (2009).
- [145] M. Swoboda, T. Fordell, K. Klünder, J. M. Dahlström, M. Miranda, C. Buth, K. J. Schafer, J. Mauritsson, A. L’Huillier, and M. Gisselbrecht. *Phase Measurement of Resonant Two-Photon Ionization in Helium*. Phys. Rev. Lett. **104**, 103003 (2010).
- [146] P. Johnsson, J. Mauritsson, T. Remetter, A. L’Huillier, and K. J. Schafer. *Attosecond Control of Ionization by Wave-Packet Interference*. Phys. Rev. Lett. **99**, 233001 (2007).
- [147] Z.-H. Loh, C. H. Greene, and S. R. Leone. *Femtosecond induced transparency and absorption in the extreme ultraviolet by coherent coupling of the He 2s2p (1Po) and 2p2 (1Se) double excitation states with 800nm light*. Chemical Physics **350**, 7 (2008).
- [148] G. Sansone, E. Benedetti, F. Calegari, C. Vozzi, L. Avaldi, R. Flammini, L. Poletto, P. Villoresi, C. Altucci, R. Velotta, S. Stagira, S. De Silvestri, and M. Nisoli. *Isolated Single-Cycle Attosecond Pulses*. Science **314**, 443 (2006).
- [149] W. Li, X. Zhou, R. Lock, S. Patchkovskii, A. Stolow, H. C. Kapteyn, and M. M. Murnane. *Time-Resolved Dynamics in N₂O₄ Probed Using High Harmonic Generation*. Science **322**, 1207 (2008).
- [150] P. M. Kraus, B. Mignolet, D. Baykusheva, A. Rupenyan, L. Horný, E. F. Penka, G. Grassi, O. I. Tolstikhin, J. Schneider, F. Jensen, L. B. Madsen, A. D. Bandrauk, F. Remacle, and H. J. Wörner. *Measurement and laser control of attosecond charge migration in ionized iodoacetylene*. Science **350**, 790 (2015).
- [151] U. Keller. *Recent developments in compact ultrafast lasers*. Nature **424**, 831 (2003).
- [152] E. Goulielmakis, M. Schultze, M. Hofstetter, V. S. Yakovlev, J. Gagnon, M. Uiberacker, A. L. Aquila, E. M. Gullikson, D. T. Attwood, R. Kienberger, F. Krausz, and U. Kleineberg. *Single-Cycle Nonlinear Optics*. Science **320**, 1614 (2008).

- [153] M. T. Hassan, T. T. Luu, A. Moulet, O. Raskazovskaya, P. Zhokhov, M. Garg, N. Karpowicz, A. M. Zheltikov, V. Pervak, F. Krausz, and E. Goulielmakis. *Optical attosecond pulses and tracking the nonlinear response of bound electrons*. Nature **530**, 66 (2016).
- [154] V. Shumakova, P. Malevich, S. Ališauskas, A. Voronin, A. M. Zheltikov, D. Faccio, D. Kartashov, A. Baltuška, and A. Pugžlys. *Multi-millijoule few-cycle mid-infrared pulses through nonlinear self-compression in bulk*. Nature Communications **7**, 12877 (2016).
- [155] J. Itatani, F. Quéré, G. L. Yudin, M. Y. Ivanov, F. Krausz, and P. B. Corkum. *Attosecond Streak Camera*. Phys. Rev. Lett. **88**, 173903 (2002).
- [156] R. Kienberger, E. Goulielmakis, M. Uiberacker, A. Baltuska, V. Yakovlev, F. Bammer, A. Scrinzi, T. Westerwalbesloh, U. Kleineberg, U. Heinzmann, M. Drescher, and F. Krausz. *Atomic transient recorder*. Nature **427**, 817 (2004).
- [157] H. Muller. *Reconstruction of attosecond harmonic beating by interference of two-photon transitions*. Applied Physics B **74**, s17 (2002).
- [158] V. Vénier, R. Taieb, and A. Maquet. *Phase dependence of $(N+1)$ -color ($N>1$) ir-uv photoionization of atoms with higher harmonics*. Physical Review A **54**, 721 (1996).
- [159] M. B. Gaarde, C. Buth, J. L. Tate, and K. J. Schafer. *Transient absorption and reshaping of ultrafast XUV light by laser-dressed helium*. Physical Review A **83**, 013419 (2011).
- [160] M. Wu, S. Chen, S. Camp, K. J. Schafer, and M. B. Gaarde. *Theory of strong-field attosecond transient absorption*. Journal of Physics B: Atomic, Molecular and Optical Physics **49**, 062003 (2016).
- [161] A. Beck, D. Neumark, and S. Leone. *Probing ultrafast dynamics with attosecond transient absorption*. Chemical Physics Letters **624**, 119 (2015).
- [162] J. M. Schins, P. Breger, P. Agostini, R. C. Constantinescu, H. G. Muller, G. Grillon, A. Antonetti, and A. Mysyrowicz. *Observation of Laser-Assisted Auger Decay in Argon*. Phys. Rev. Lett. **73**, 2180 (1994).
- [163] T. E. Glover, R. W. Schoenlein, A. H. Chin, and C. V. Shank. *Observation of Laser Assisted Photoelectric Effect and Femtosecond High Order Harmonic Radiation*. Phys. Rev. Lett. **76**, 2468 (1996).
- [164] D. Azoury, O. Kneller, S. Rozen, B. D. Bruner, A. Clergerie, Y. Mairesse, B. Fabre, B. Pons, N. Dudovich, and M. Krüger. *Electronic wavefunctions probed by all-optical attosecond interferometry*. Nature Photonics **13**, 54 (2019).

- [165] N. Dudovich, O. Smirnova, J. Levesque, Y. Mairesse, M. Y. Ivanov, D. M. Villeneuve, and P. B. Corkum. *Measuring and controlling the birth of attosecond XUV pulses*. Nature Physics **2**, 781 (2006).
- [166] L. J. Zipp, A. Natan, and P. H. Bucksbaum. *Probing electron delays in above-threshold ionization*. Optica **1**, 361 (2014).
- [167] P. Eckle, A. N. Pfeiffer, C. Cirelli, A. Staudte, R. Dörner, H. G. Muller, M. Büttiker, and U. Keller. *Attosecond Ionization and Tunneling Delay Time Measurements in Helium*. Science **322**, 1525 (2008).
- [168] U. S. Sainadh, H. Xu, X. Wang, A. Atia-Tul-Noor, W. C. Wallace, N. Douguet, A. Bray, I. Ivanov, K. Bartschat, A. Kheifets, R. T. Sang, and I. V. Litvinyuk. *Attosecond angular streaking and tunnelling time in atomic hydrogen*. Nature p. 1 (2019).
- [169] N. Eicke and M. Lein. *Attoclock with counter-rotating bicircular laser fields*. Phys. Rev. A **99**, 031402 (2019).
- [170] M. Uiberacker, T. Uphues, M. Schultze, A. J. Verhoef, V. Yakovlev, M. F. Kling, J. Rauschenberger, N. M. Kabachnik, H. Schröder, M. Lezius, K. L. Kompa, H.-G. Muller, M. J. J. Vrakking, S. Hendel, U. Kleineberg, U. Heinzmann, M. Drescher, and F. Krausz. *Attosecond real-time observation of electron tunnelling in atoms*. Nature **446**, 627 (2007).
- [171] Y. Mairesse, A. d. Bohan, L. J. Frasinski, H. Merdji, L. C. Dinu, P. Monchicourt, P. Breger, M. Kovac, R. Taieb, B. Carre, H. G. Muller, P. Agostini, and P. Salieres. *Attosecond Synchronization of High-Harmonic Soft X-rays*. Science **302**, 1540 (2003).
- [172] A. Jiménez-Galán, L. Argenti, and F. Martín. *Modulation of Attosecond Beating in Resonant Two-Photon Ionization*. Phys. Rev. Lett. **113**, 263001 (2014).
- [173] D. Busto, J. Vinbladh, S. Zhong, M. Isinger, S. Nandi, S. Maclot, P. Johnsson, M. Gisselbrecht, A. L’Huillier, E. Lindroth, and J. M. Dahlström. *Fano’s Propensity Rule in Angle-Resolved Attosecond Pump-Probe Photoionization*. Phys. Rev. Lett. **123**, 133201 (2019).
- [174] U. Fano. *Propensity rules: An analytical approach*. Phys. Rev. A **32**, 617 (1985).
- [175] S. Nagele, R. Pazourek, J. Feist, K. Doblhoff-Dier, C. Lemell, K. Tokési, and J. Burgdörfer. *Time-resolved photoemission by attosecond streaking: extraction of time information*. Journal of Physics B: Atomic, Molecular and Optical Physics **44**, 081001 (2011).
- [176] A. Jimenez-Galan, F. Martin, and L. Argenti. *Two-photon finite-pulse model for resonant transitions in attosecond experiments*. Physical Review A **93**, 023429 (2016).

- [177] C. Cirelli, C. Marante, S. Heuser, C. L. M. Petersson, A. J. Galan, L. Argenti, S. Zhong, D. Busto, M. Isinger, S. Nandi, S. Maclot, L. Rading, P. Johnsson, M. Gisselbrecht, M. Lucchini, L. Gallmann, J. M. Dahlström, E. Lindroth, A. L’Huillier, F. Martin, and U. Keller. *Anisotropic photoemission time delays close to a Fano resonance*. Nature Communications **9**, 955 (2018).
- [178] M. Swoboda, J. M. Dahlström, T. Ruchon, P. Johnsson, J. Mauritsson, A. L’Huillier, and K. J. Schafer. *Intensity dependence of laser-assisted attosecond photoionization spectra*. Laser Physics **19**, 1591 (2009).
- [179] I. A. Ivanov and A. S. Kheifets. *Angle-dependent time delay in two-color XUV+IR photoemission of He and Ne*. Phys. Rev. A **96**, 013408 (2017).
- [180] J. C. Baggesen and L. B. Madsen. *On the dipole, velocity and acceleration forms in high-order harmonic generation from a single atom or molecule*. Journal of Physics B: Atomic, Molecular and Optical Physics **44**, 115601 (2011).
- [181] H. Wang, M. Chini, S. Chen, C.-H. Zhang, F. He, Y. Cheng, Y. Wu, U. Thumm, and Z. Chang. *Attosecond Time-Resolved Autoionization of Argon*. Phys. Rev. Lett. **105**, 143002 (2010).
- [182] V. Stooß, M. Hartmann, P. Birk, G. D. Borisova, T. Ding, A. Blättermann, C. Ott, and T. Pfeifer. *XUV-beamline for attosecond transient absorption measurements featuring a broadband common beam-path time-delay unit and in situ reference spectrometer for high stability and sensitivity*. Review of Scientific Instruments **90**, 053108 (2019).
- [183] M. F. Jager, C. Ott, P. M. Kraus, C. J. Kaplan, W. Pouse, R. E. Marvel, R. F. Haglund, D. M. Neumark, and S. R. Leone. *Tracking the insulator-to-metal phase transition in VO₂ with few-femtosecond extreme UV transient absorption spectroscopy*. Proceedings of the National Academy of Sciences **114**, 9558 (2017).
- [184] E. Goulielmakis, Z.-H. Loh, A. Wirth, R. Santra, N. Rohringer, V. S. Yakovlev, S. Zherebtsov, T. Pfeifer, A. M. Azzeer, M. F. Kling, S. R. Leone, and F. Krausz. *Real-time observation of valence electron motion*. Nature **466**, 739 (2010).
- [185] A. L. Cavalieri, N. Müller, T. Uphues, V. S. Yakovlev, A. Baltuska, B. Horvath, B. Schmidt, L. Blümel, R. Holzwarth, S. Hendel, M. Drescher, U. Kleineberg, P. M. Echenique, R. Kienberger, F. Krausz, and U. Heinzmann. *Attosecond spectroscopy in condensed matter*. Nature **449**, 1029 (2007).
- [186] D. Guenot, D. Kroon, E. Balogh, E. W. Larsen, M. Kotur, M. Miranda, T. Fordell, P. Johnsson, J. Mauritsson, M. Gisselbrecht, K. Varju, C. L. Arnold, T. Carette, A. S. Kheifets, E. Lindroth, A. L’Huillier, and J. M. Dahlström. *Measurements of relative photoemission time delays in noble gas atoms*. Journal of Physics B: Atomic, Molecular and Optical Physics **47**, 245602 (2014).

- [187] C. Palatchi, J. M. Dahlström, A. S. Kheifets, I. A. Ivanov, D. M. Canaday, P. Agostini, and L. F. DiMauro. *Atomic delay in helium, neon, argon and krypton*. Journal of Physics B: Atomic, Molecular and Optical Physics **47**, 245003 (2014).
- [188] M. Sabbar, S. Heuser, R. Boge, M. Lucchini, T. Carette, E. Lindroth, L. Gallmann, C. Cirelli, and U. Keller. *Resonance Effects in Photoemission Time Delays*. Phys. Rev. Lett. **115**, 133001 (2015).
- [189] P. Hockett. *Angle-resolved RABBITT: theory and numerics*. Journal of Physics B: Atomic, Molecular and Optical Physics **50**, 154002 (2017).
- [190] A. Schumer. *Angle-dependent attosecond streaking*. Bachelor thesis, Vienna University of Technology (2014).
- [191] A. Schumer. *Angle-dependent attosecond streaking*. Projectwork, Vienna University of Technology (2016).
- [192] J. C. Baggesen and L. B. Madsen. *Polarization Effects in Attosecond Photoelectron Spectroscopy*. Physical Review Letters **104**, 043602 (2010).
- [193] J. Feist, O. Zatsarinny, S. Nagele, R. Pazourek, J. Burgdörfer, X. Guan, K. Bartschat, and B. I. Schneider. *Time delays for attosecond streaking in photoionization of neon*. Phys. Rev. A **89**, 033417 (2014).
- [194] S. Sukiasyan, K. L. Ishikawa, and M. Ivanov. *Attosecond cascades and time delays in one-electron photoionization*. Phys. Rev. A **86**, 033423 (2012).
- [195] L. R. Moore, M. A. Lysaght, J. S. Parker, H. W. van der Hart, and K. T. Taylor. *Time delay between photoemission from the 2p and 2s subshells of neon*. Phys. Rev. A **84**, 061404 (2011).
- [196] M. Isinger, R. J. Squibb, D. Busto, S. Zhong, A. Harth, D. Kroon, S. Nandi, C. L. Arnold, M. Miranda, J. M. Dahlström, E. Lindroth, R. Feifel, M. Gisselbrecht, and A. L’Huillier. *Photoionization in the time and frequency domain*. Science **358**, 893 (2017).
- [197] G. Laurent, W. Cao, H. Li, Z. Wang, I. Ben-Itzhak, and C. L. Cocke. *Attosecond Control of Orbital Parity Mix Interferences and the Relative Phase of Even and Odd Harmonics in an Attosecond Pulse Train*. Phys. Rev. Lett. **109**, 083001 (2012).
- [198] S. A. Aseyev, Y. Ni, L. J. Frasinski, H. G. Muller, and M. J. J. Vrakking. *Attosecond Angle-Resolved Photoelectron Spectroscopy*. Phys. Rev. Lett. **91**, 223902 (2003).
- [199] L. H. Haber, B. Doughty, and S. R. Leone. *Energy-dependent photoelectron angular distributions of two-color two-photon above threshold ionization of atomic helium*. Phys. Rev. A **84**, 013416 (2011).

- [200] S. Nagele, R. Pazourek, J. Feist, and J. Burgdörfer. *Time shifts in photoemission from a fully correlated two-electron model system*. Phys. Rev. A **85**, 033401 (2012).
- [201] H. Ehrhardt, M. Schulz, T. Tekaats, and K. Willmann. *Ionization of Helium: Angular Correlation of the Scattered and Ejected Electrons*. Phys. Rev. Lett. **22**, 89 (1969).
- [202] U. Heinzmann and J. H. Dil. *Spin-orbit-induced photoelectron spin polarization in angle-resolved photoemission from both atomic and condensed matter targets*. Journal of Physics: Condensed Matter **24**, 173001 (2012).
- [203] U. Heinzmann. *Attosecond Physics*, volume 177 of *Springer Series in Optical Sciences*. Springer Berlin Heidelberg, Berlin, Heidelberg (2013).
- [204] M. Fanciulli, H. Volfová, S. Muff, J. Braun, H. Ebert, J. Minár, U. Heinzmann, and J. H. Dil. *Spin Polarization and Attosecond Time Delay in Photoemission from Spin Degenerate States of Solids*. Phys. Rev. Lett. **118**, 067402 (2017).
- [205] J. J. More. *Numerical analysis*. Springer (1978).
- [206] R. Dörner and V. Mergel and O. Jagutzki and L. Spielberger and J. Ullrich and R. Moshhammer and H. Schmidt-Böcking. *Cold Target Recoil Ion Momentum Spectroscopy: a 'momentum microscope' to view atomic collision dynamics*. Physics Reports **330**, 95 (2000).
- [207] M. Sabbar, S. Heuser, R. Boge, M. Lucchini, L. Gallmann, C. Cirelli, and U. Keller. *Combining attosecond XUV pulses with coincidence spectroscopy*. Review of Scientific Instruments **85**, 103113 (2014).
- [208] M. Lucchini, A. Ludwig, T. Zimmermann, L. Kasmi, J. Herrmann, A. Scrinzi, A. S. Landsman, L. Gallmann, and U. Keller. *Anisotropic emission in quantum-beat spectroscopy of helium excited states*. Phys. Rev. A **91**, 063406 (2015).
- [209] V. Vénierard and B. Piraux. *Continuum-continuum dipole transitions in femtosecond-laser-pulse excitation of atomic hydrogen*. Phys. Rev. A **41**, 4019 (1990).
- [210] U. Fano and J. W. Cooper. *Line Profiles in the Far-uv Absorption Spectra of the Rare Gases*. Phys. Rev. **137**, A1364 (1965).
- [211] C. A. Nicolaides, T. Mercouris, and Y. Komninos. *Attosecond dynamics of electron correlation in doubly excited atomic states*. Journal of Physics B: Atomic, Molecular and Optical Physics **35**, L271 (2002).
- [212] R. P. Madden and K. Codling. *New Autoionizing Atomic Energy Levels in He, Ne, and Ar*. Physical Review Letters **10**, 516 (1963).
- [213] M. Domke, K. Schulz, G. Remmers, G. Kaindl, and D. Wintgen. *High-resolution study of $^1P^0$ double-excitation states in helium*. Phys. Rev. A **53**, 1424 (1996).

- [214] Z.-H. Loh, M. Khalil, R. E. Correa, R. Santra, C. Buth, and S. R. Leone. *Quantum State-Resolved Probing of Strong-Field-Ionized Xenon Atoms Using Femtosecond High-Order Harmonic Transient Absorption Spectroscopy*. Physical Review Letters **98**, 143601 (2007).
- [215] A. Bürgers, D. Wintgen, and J.-M. Rost. *Highly doubly excited S states of the helium atom*. Journal of Physics B: Atomic, Molecular and Optical Physics **28**, 3163 (1995).
- [216] K. Schulz, G. Kaindl, M. Domke, J. D. Bozek, P. A. Heimann, A. S. Schlachter, and J. M. Rost. *Observation of New Rydberg Series and Resonances in Doubly Excited Helium at Ultrahigh Resolution*. Phys. Rev. Lett. **77**, 3086 (1996).
- [217] E. Lindroth. *Calculation of doubly excited states of helium with a finite discrete spectrum*. Phys. Rev. A **49**, 4473 (1994).
- [218] S. L. Sorensen, T. Åberg, J. Tulkki, E. Rachlew-Källne, G. Sundström, and M. Kirm. *Argon 3s autoionization resonances*. Phys. Rev. A **50**, 1218 (1994).
- [219] N. Berrah, B. Langer, J. Bozek, T. W. Gorczyca, O. Hemmers, D. W. Lindle, and O. Toader. *Angular-distribution parameters and R-matrix calculations of Ar resonances*. Journal of Physics B: Atomic, Molecular and Optical Physics **29**, 5351 (1996).
- [220] L. Cattaneo, J. Vos, M. Lucchini, L. Gallmann, C. Cirelli, and U. Keller. *Comparison of attosecond streaking and RABBITT*. Optics Express **24**, 29060 (2016).
- [221] J. Mauritsson, P. Johnsson, E. Gustafsson, A. L’Huillier, K. J. Schafer, and M. B. Gaarde. *Attosecond Pulse Trains Generated Using Two Color Laser Fields*. Phys. Rev. Lett. **97**, 013001 (2006).
- [222] D. Ray, Z. Chen, S. De, W. Cao, I. V. Litvinyuk, A. T. Le, C. D. Lin, M. F. Kling, and C. L. Cocke. *Momentum spectra of electrons rescattered from rare-gas targets following their extraction by one- and two-color femtosecond laser pulses*. Phys. Rev. A **83**, 013410 (2011).
- [223] G. Laurent, W. Cao, I. Ben-Itzhak, and C. L. Cocke. *Attosecond pulse characterization*. Opt. Express **21**, 16914 (2013).
- [224] S. Skruszewicz, J. Tiggesbäumker, K.-H. Meiwes-Broer, M. Arbeiter, T. Fennel, and D. Bauer. *Two-Color Strong-Field Photoelectron Spectroscopy and the Phase of the Phase*. Phys. Rev. Lett. **115**, 043001 (2015).
- [225] V. Lorient, A. Marciniak, G. Karras, B. Schindler, G. Renois-Predelus, I. Compagnon, B. Concina, R. Brédy, G. Celep, C. Bordas, E. Constant, and F. Lépine. *Angularly resolved RABBITT using a second harmonic pulse*. Journal of Optics **19**, 114003 (2017).

- [226] J. Ullrich, R. Moshhammer, A. Dorn, R. Dörner, L. P. H. Schmidt, and H. Schmidt-Böcking. *Recoil-ion and electron momentum spectroscopy: reaction-microscopes*. Reports on Progress in Physics **66**, 1463 (2003).
- [227] C. E. Rallis, T. G. Burwitz, P. R. Andrews, M. Zohrabi, R. Averin, S. De, B. Bergues, B. Jochim, A. V. Voznyuk, N. Gregerson, B. Gaire, I. Znakovskaya, J. McKenna, K. D. Carnes, M. F. Kling, I. Ben-Itzhak, and E. Wells. *Incorporating real time velocity map image reconstruction into closed-loop coherent control*. Review of Scientific Instruments **85**, 113105 (2014).
- [228] L. Barreau, K. Veyrinas, V. Gruson, S. J. Weber, T. Auguste, J.-F. Hergott, F. Lepetit, B. Carré, J.-C. Houver, D. Dowek, and P. Salières. *Evidence of depolarization and ellipticity of high harmonics driven by ultrashort bichromatic circularly polarized fields*. Nature Communications **9**, 4727 (2018).
- [229] D. Azoury, O. Kneller, M. Krüger, B. D. Bruner, O. Cohen, Y. Mairesse, and N. Dudovich. *Interferometric attosecond lock-in measurement of extreme-ultraviolet circular dichroism*. Nature Photonics **13**, 198 (2019).
- [230] M. Sabbar, S. Heuser, R. Boge, M. Lucchini, T. Carette, E. Lindroth, L. Gallmann, C. Cirelli, and U. Keller. *Erratum: Resonance Effects in Photoemission Time Delays [Phys. Rev. Lett. 115, 133001 (2015)]*. Phys. Rev. Lett. **119**, 219901 (2017).
- [231] M. Wickenhauser. *Ionization Dynamics of Atoms in Femto- and Attosecond Pulses*. PhD thesis, Vienna University of Technology (2006).
- [232] C. A. Nicolaides, T. Mercouris, and Y. Komninos. *Time-dependent formation of the profile of resonance atomic states and its dependence on the duration of ultrashort pulses from free-electron lasers*. Physical Review A **80**, 055402 (2009).
- [233] T. Mercouris, Y. Komninos, and C. A. Nicolaides. *Time-dependent formation of the profile of the He 2s2p state excited by a short laser pulse*. Physical Review A **75**, 013407 (2007).
- [234] T. Mercouris, Y. Komninos, and C. A. Nicolaides. *Theory and computation of the attosecond dynamics of pairs of electrons excited by high-frequency short light pulses*. Physical Review A **69**, 032502 (2004).
- [235] L. Argenti and E. Lindroth. *Ionization Branching Ratio Control with a Resonance Attosecond Clock*. Phys. Rev. Lett. **105**, 053002 (2010).
- [236] I. I. Rabi. *Space Quantization in a Gyration Magnetic Field*. Phys. Rev. **51**, 652 (1937).
- [237] M. O. Scully and M. S. Zubairy. *Quantum Optics*. Cambridge University Press, 6th edition (2008).

- [238] S. I. Themelis. *The Stark effect in autoionizing doubly excited states of helium below the He^+ ($n=2$) threshold*. *Physica Scripta* **83**, 045302 (2011).
- [239] S. Kar and Y. K. Ho. *Strong dc electric-field effects on the lowest doubly excited singlet states of helium using highly correlated exponential wavefunctions*. *Journal of Physics B: Atomic, Molecular and Optical Physics* **43**, 135003 (2010).
- [240] R. d. L. Kronig. *On the Theory of Dispersion of X-Rays*. *J. Opt. Soc. Am.* **12**, 547 (1926).
- [241] R. Kubo. *Statistical-Mechanical Theory of Irreversible Processes. I. General Theory and Simple Applications to Magnetic and Conduction Problems*. *Journal of the Physical Society of Japan* **12**, 570 (1957).
- [242] C. W. Peterson and B. W. Knight. *Causality calculations in the time domain: An efficient alternative to the Kramers–Kronig method*. *J. Opt. Soc. Am.* **63**, 1238 (1973).
- [243] A. Palacios, T. N. Rescigno, and C. W. McCurdy. *Two-Electron Time-Delay Interference in Atomic Double Ionization by Attosecond Pulses*. *Physical Review Letters* **103**, 253001 (2009).
- [244] J. Feist, S. Nagele, R. Pazourek, E. Persson, B. I. Schneider, L. A. Collins, and J. Burgdörfer. *Probing Electron Correlation via Attosecond xuv Pulses in the Two-Photon Double Ionization of Helium*. *Physical Review Letters* **103**, 063002 (2009).
- [245] A. Palacios, D. A. Horner, T. N. Rescigno, and C. W. McCurdy. *Two-photon double ionization of the helium atom by ultrashort pulses*. *Journal of Physics B: Atomic, Molecular and Optical Physics* **43**, 194003 (2010).
- [246] J. Feist, S. Nagele, C. Ticknor, B. I. Schneider, L. A. Collins, and J. Burgdörfer. *Attosecond Two-Photon Interferometry for Doubly Excited States of Helium*. *Physical Review Letters* **107**, 093005 (2011).
- [247] W.-C. Jiang, W.-H. Xiong, T.-S. Zhu, L.-Y. P. Peng, and Q. Gong. *Double ionization of He by time-delayed attosecond pulses*. *Journal of Physics B: Atomic, Molecular and Optical Physics* **47**, 091001 (2014).
- [248] R. Pazourek, S. Nagele, and J. Burgdörfer. *Probing time-ordering in two-photon double ionization of helium on the attosecond time scale*. *Journal of Physics B: Atomic, Molecular and Optical Physics* **48**, 061002 (2015).
- [249] W.-C. Jiang, S. Nagele, and J. Burgdörfer. *Observing electron-correlation features in two-photon double ionization of helium*. *Physical Review A* **96**, 053422 (2017).

- [250] S. Kühn, M. Dumergue, S. Kahaly, S. Mondal, M. Füle, T. Csizmadia, B. Farkas, B. Major, Z. Várallyay, E. Cormier, M. Kalashnikov, F. Calegari, M. Devetta, F. Frassetto, E. Månsson, L. Poletto, S. Stagira, C. Vozzi, M. Nisoli, P. Rudawski, S. Maclot, F. Campi, H. Wikmark, C. L. Arnold, C. M. Heyl, P. Johnsson, A. L’Huillier, R. Lopez-Martens, S. Haessler, M. Bocoum, F. Boehle, A. Vernier, G. Iaquaniello, E. Skantzakis, N. Papadakis, C. Kalpouzos, P. Tzallas, F. Lépine, D. Charalambidis, K. Varjú, K. Osvay, and G. Sansone. *The ELI-ALPS facility: the next generation of attosecond sources*. Journal of Physics B: Atomic, Molecular and Optical Physics **50**, 132002 (2017).
- [251] J. Ngoko Djiokap, N. Manakov, A. Meremianin, S. Hu, L. Madsen, and A. F. Starace. *Nonlinear Dichroism in Back-to-Back Double Ionization of He by an Intense Elliptically Polarized Few-Cycle Extreme Ultraviolet Pulse*. Physical Review Letters **113**, 223002 (2014).
- [252] M. S. Pindzola, Y. Li, and J. Colgan. *Multiphoton double ionization of helium using femtosecond laser pulses*. Journal of Physics B: Atomic, Molecular and Optical Physics **49**, 215603 (2016).
- [253] J. M. Ngoko-Djiokap and A. F. Starace. *Doubly-excited state effects on two-photon double ionization of helium by time-delayed, oppositely circularly-polarized attosecond pulses*. Journal of Optics **19**, 124003 (2017).
- [254] A. Y. Istomin, E. A. Pronin, N. L. Manakov, S. I. Marmo, and A. F. Starace. *Elliptic and Circular Dichroism Effects in Two-Photon Double Ionization of Atoms*. Phys. Rev. Lett. **97**, 123002 (2006).
- [255] T. Morishita, S. Watanabe, and C. D. Lin. *Attosecond Light Pulses for Probing Two-Electron Dynamics of Helium in the Time Domain*. Phys. Rev. Lett. **98**, 083003 (2007).
- [256] E. Fomouo, P. Antoine, H. Bachau, and B. Piraux. *Attosecond timescale analysis of the dynamics of two-photon double ionization of helium*. New Journal of Physics **10**, 025017 (2008).
- [257] T. A. Carlson. *Double Electron Ejection Resulting from Photo-Ionization in the Outermost Shell of He, Ne, and Ar, and Its Relationship to Electron Correlation*. Phys. Rev. **156**, 142 (1967).
- [258] D. A. Horner, F. Morales, T. N. Rescigno, F. Martín, and C. W. McCurdy. *Two-photon double ionization of helium above and below the threshold for sequential ionization*. Phys. Rev. A **76**, 030701 (2007).
- [259] A. Liu and U. Thumm. *Laser-assisted XUV few-photon double ionization of helium: Joint angular distributions*. Phys. Rev. A **89**, 063423 (2014).

- [260] J. Ngoko Djiokap, S. Hu, L. Madsen, N. Manakov, A. Meremianin, and A. F. Starace. *Electron Vortices in Photoionization by Circularly Polarized Attosecond Pulses*. Physical Review Letters **115**, 113004 (2015).
- [261] D. You, K. Ueda, E. V. Gryzlova, A. N. Grum-Grzhimailo, M. M. Popova, E. I. Staroselskaya, O. Tugs, Y. Orimo, T. Sato, K. L. Ishikawa, P. A. Carpeggiani, T. Csizmadia, M. Füle, G. Sansone, P. K. Maroju, A. D’Elia, T. Mazza, M. Meyer, C. Callegari, M. Di Fraia, O. Plekan, R. Richter, L. Giannessi, E. Allaria, G. De Ninno, M. Trov’o, L. Badano, B. Diviacco, D. Gauthier, N. Mirian, G. Penco, P. R. Ribič, S. Spampinati, C. Spezzani, G. Gaio, and K. C. Prince. *A new quantum clock for measuring photoemission delay times*. arXiv:1811.05341 [physics] (2019). ArXiv: 1907.13605.
- [262] C. W. Clark. *Coulomb phase shift*. American Journal of Physics **47**, 683 (1979).
- [263] A. Gebauer, S. Neb, W. Enns, B. Stadtmüller, M. Aeschlimann, and W. Pfeiffer. *Equivalence of RABBITT and Streaking Delays in Attosecond-Time-Resolved Photoemission Spectroscopy at Solid Surfaces*. Applied Sciences **9**, 592 (2019).
- [264] J. Samson and W. Stolte. *Precision measurements of the total photoionization cross-sections of He, Ne, Ar, Kr, and Xe*. Journal of Electron Spectroscopy and Related Phenomena **123**, 265 (2002).
- [265] A. Jiménez-Galán, L. Argenti, and F. Martín. *private communication* .
- [266] C. D. Lin. *Classification and supermultiplet structure of doubly excited states*. Phys. Rev. A **29**, 1019 (1984).
- [267] N. Douguet, A. N. Grum-Grzhimailo, E. V. Gryzlova, E. I. Staroselskaya, J. Venzke, and K. Bartschat. *Photoelectron angular distributions in bichromatic atomic ionization induced by circularly polarized VUV femtosecond pulses*. Phys. Rev. A **93**, 033402 (2016).
- [268] A. N. Grum-Grzhimailo, M. N. Khaerdinov, and K. Bartschat. *Effects of numerical approximations in the treatment of short-pulse strong-field ionization of atomic hydrogen*. Phys. Rev. A **88**, 055401 (2013).